Design of the Aerobic HAIL Reactor - Towards Improved Energy Efficiency

Gianluca Sasha Salvatore Ganter Shaer

In fulfilment of the requirements for the degree of
Master of Science

Supervisor: Susan T. L. Harrison
Co-Supervisors: Siew Tai
Marijke Fagan-Endres

Department of Chemical Engineering
Faculty of Engineering and the Built Environment
University of Cape Town

University of Cape Town

The copyright of this thesis vests in the author. No quotation from it or information derived from it is to be published without full acknowledgement of the source. The thesis is to be used for private study or non-commercial research purposes only.

Published by the University of Cape Town (UCT) in terms of the non-exclusive license granted to UCT by the author.

University of Cape Town

Plagiarism Declaration

1. I know that plagiarism is wrong. Plagiarism is to use another's work and to pretend that it is one's own.
2. I have used the Harvard system for citation and referencing. Each significant contribution to, and quotation in, this report from the work, or works, of other people has been attributed, and has been cited and referenced.
3. This report is my own unaided work, except for assistance received from the teaching staff.
4. I have not allowed, and will not allow, anyone to copy my work with the intention of passing it off as his or her own work.

Signed by candidate

Signature

Abstract

This dissertation presents the results of an investigation into the design of a novel low aspect ratio reactor, dubbed the HAIL (horizontal air-injected loop) reactor. Current industrial high cell density aerobic reactors for cultivation of bacteria and yeast are typically either stirred tank reactors (STR's), bubble column reactors (BCR's) or airlift reactors (ALR's). These systems can attain high mass transfer rates and short mixing times; however, their energy efficiency remains a concern. Many studies have attempted to further optimise these reactors, but they are ultimately limited by their high aspect ratios. These lead to large pressure heads that the air compressor needs to overcome on sparging, contributing significantly to energy costs.

Low aspect ratio (LAR) reactors, such as the wave bag, orbital shaker and raceway reactors offer an alternative to these systems, providing superior energy efficiency for both mixing and aeration. However, each has core issues preventing their usage in high cell density aerobic culture. Their maximum mass transfer coefficient is typically too low to support high cell density cultures. Additionally, these reactors tend to have poor scalability, making them unfeasible for large scale industrial usage. To overcome these challenges, the HAIL reactor makes use of a tubular loop design. The anticipated benefit of the loop design was that it forces the air to travel the length of the reactor before leaving the system, enabling significant surface aeration and residence time in the reactor. These both impact the mass transfer coefficient. Additionally, the loops can be stacked upon one another, overcoming the scalability issue. The reactor would also be energy efficient based on its LAR.

To establish target performance ranges, a literature review on the gas-liquid mass transfer coefficient, mixing time and efficiency of current low and high aspect ratio (HAR) reactors was conducted. This was supplemented with experimental results (including mass transfer coefficients, cell density and viscosity) from the fed-batch STR cultivation of *Saccharomyces cerevisiae*, an easy to work with highly aerobic yeast. A fed-batch feeding profile was developed for this. To better compare reactor performance, a term was introduced called the mass transfer energy efficiency, with units $m^3 \cdot h^{-1} \cdot W^{-1}$, obtained via the quotient of the k_La and the power input per unit volume.

The literature mass transfer energy efficiency ranges for the STR, BCR and ALR were found to be 0.022-0.236 $m^3 \cdot h^{-1} \cdot W^{-1}$, 0.084-0.317 $m^3 \cdot h^{-1} \cdot W^{-1}$ and 0.142-0.493 $m^3 \cdot h^{-1} \cdot W^{-1}$ respectively, with maximum k_La values ranging up to 1000 h^{-1} depending on the power input. Mixing times for these systems differ depending on scale and configuration, ranging from below a minute up to 20 minutes. Experimental fed-batch and sterile water systems had efficiency ranges of 0.044-0.245 $m^3 \cdot h^{-1} \cdot W^{-1}$ and 0.059-0.285 $m^3 \cdot h^{-1} \cdot W^{-1}$ respectively, with a maximum k_La of 240 h^{-1} and 226 h^{-1}. Based on cellular growth results, the theoretical minimum k_La required was calculated as 372 h^{-1}. The most notable literature efficiencies for LAR reactors were held by the travelling loop, raceway, and wave reactors with ranges of 0.286-0.295 $m^3 \cdot h^{-1} \cdot W^{-1}$, 0.034-0.867 $m^3 \cdot h^{-1} \cdot W^{-1}$, and 0.112-0.742 $m^3 \cdot h^{-1} \cdot W^{-1}$. For the wave and travelling loop reactors, mixing times below a minute were attainable.

A 6.2 L proof-of-concept and 31.4 L laboratory-scale prototype of the HAIL reactor were developed. In the proof-of-concept prototype, preliminary studies were carried out on the impact of sparger depth and angle on circulation time. Using the laboratory-scale system a range of sparger designs, including different angled jets, outlet areas and a circular sparger design, were investigated. The circular sparger design was found to be the ideal sparger type. A mixing time of 7-19 minutes depending on the power input was found for the 31.4 L configuration. The power efficiency range determined was 0.120-0.281 $m^3 \cdot h^{-1} \cdot W^{-1}$; however, the calculation used to determine this is an underapproximation. The maximum k_La of 13.84 h^{-1} is an order of magnitude (between 10 and 100) lower than the values that can be obtained in HAR reactors for industrial aerobic culture. It was found that HAIL reactor performance did not change substantially with an increase in viscosity from 1 to 1.4 cP.

The HAIL reactor did not compete with existing low and high aspect ratio reactors in its current configuration in terms of mass transfer. Additional research on the design is recommended to enhance gas – liquid contacting and associated mass transfer. These ongoing studies will enable the potential relevance and application of the novel reactor to be determined.

Acknowledgements

The author of this dissertation would like to extend his utmost thanks to the following people who assisted greatly with the presented within:

- Prof Sue Harrison, my primary supervisor, who guided me through the difficult early stages of this work and whose kind words and encouragement will be forever appreciated.

- My co-supervisors, Dr Siew Tai and Dr Marijke Fagan-Endres for being there whenever I needed advice and for always being willing to lend a helping hand/ear.

- The students and staff at CeBER, who made my time working on this thesis a pleasure, even when everything seemed to be going wrong.
- I would like to especially thank Sharon Rademeyer for her endless patience with me as I learned the ropes, for never turning me away when I confronted her with an endless barrage of questions and for the enormous amount of help she provided throughout my work.
- I would like to give special mention to Tich Samkange, who despite his many obligations always managed to make time to help me with my endeavours.
- I also would like to give a special shout-out to Ruegshana Ederies, whose friendly conversations, help and baking advice will never be forgotten!

- The good people of the engineering workshop, who assembled the base for my surprisingly large reactor.

- My parents, for supporting and encouraging me throughout this Master's and my Undergraduate degree.

- Alan McDonald, for his industry expertise, his boundless passion for this project and his invigorating encouragement!

- The UCT Brewing team, for the extremely interesting and entertaining application of bioprocess engineering that gave me a passion I did not realise I had!

- Mark Hambrock, for the endless encouragement, banter, and support when I needed it most.

- My stepfather, Tony Mundell, who unfortunately passed due to COVID before I could complete this work. You will forever be missed, and I will never forget the good times we had.

Finally, I would like to thank the Department of Science and Innovation (DSI) and National Research Foundation (NRF) for the financial support I received throughout the preparation of this Master's dissertation through the SARChI research chair in Bioprocess Engineering.

Table of Contents

Abstract i
Acknowledgements iii
Table of Contents v
List of Figures vii
List of Tables xi
Glossary of Terms xiii
Acronyms and Abbreviations xv
1 Introduction 1
1.1 Background 1
1.2 Dissertation Scope and Focus 1
1.3 Dissertation Structure 1
2 Literature Review 3
2.1 Mass Transfer Theory 3
2.1.1 Introductory Theory 3
2.1.2 Mass Transfer in a Bioreactor 5
2.1.3 Dissolved Oxygen Determination Theory 6
2.1.4 k_La Determination Methodology and Theory 7
2.1.5 Factors Influencing Mass Transfer 9
2.2 Reactor Overviews 12
2.2.1 Stirred Tank Reactors 12
2.2.2 Bubble Column Reactors 14
2.2.3 Airlift Reactors 16
2.2.4 Low Aspect Ratio Reactors 17
2.3 Reactor Performance Comparison 21
2.3.1 Mixing Time vs Power Input 22
2.3.2 Mass Transfer Coefficient vs Power Input 25
2.4 Yeast as a Model Organism for Aerobic Culture 32
2.4.1 Overview 32
2.4.2 Growth Characteristics of Baker's Yeast 33
2.4.3 Industrial Feed and Growth Conditions for Baker's Yeast 33
2.4.4 Mass Transfer Requirements for Baker's Yeast Production 33
2.4.5 Typical Industrial Reactor Configurations for Baker's Yeast Production 34
2.5 Concluding Remarks 35
3 Project Definition 37
3.1 Problem Statement 37
3.2 Hypothesis 37
3.3 Key Questions 37
4 Research Approach, STR Methods and Methodology 39
4.1 Experimental Approach to Research 39
4.2 STR Methodology, Materials and Methods 39
4.2.1 Reactor Description 39
4.2.2 k_La Measurement Techniques 40
4.2.3 Power Input Measurement 42
4.2.4 Yeast Fermentation 42
5 STR Results and Discussion 49
5.1 Baseline STR Results 49
5.2 STR Batch Results 49
5.3 STR Fed-Batch Results 50
5.3.1 Cell Growth Trends 50

5.3.2 Accuracy/Reliability of the Fed-batch Feeding Strategy 55
5.4 k_La vs. Power Input per Unit Volume Results 57
5.4.1 Fed-batch STR Results 57
5.4.2 Adjusted Baseline STR Results 60
6 Novel Reactor Design 63
6.1 Literature Discussion and Reactor Ideation 63
6.1.1 LAR Reactor Mixing Time and k_La Range 63
6.1.2 LAR Reactor Energy Efficiency 64
6.1.3 LAR Reactor Scalability 64
6.1.4 The Proposed Design 64
6.2 Proof-of-Concept Prototype 65
6.2.1 Specifying the prototype 65
6.2.2 Potential Configuration Changes – Sparger Design 66
6.2.3 Methodology, Materials and Methods 67
6.2.4 Results and Discussion 67
6.3 Laboratory-scale Prototype 68
6.3.1 Prototype Reactor Design 68
6.3.2 Potential Configurations to Test 69
6.3.3 Methodology, Materials and Methods 70
7 HAIL Reactor Results and Discussion 75
7.1 Initial Test Results 75
7.2 Sparger Comparisons 77
7.2.1 Mixing and Circulation Time Performance 77
7.2.2 Mass Transfer Performance 80
7.3 Investigating the Optimal Sparger Configuration 81
7.3.1 Mixing and Circulation Time Performance 81
7.3.2 Mass Transfer Performance 82
7.3.3 Impact of Viscosity 86
8 Conclusion and Recommendations 89
8.1 Conclusion 89
8.2 Recommendations 90
References 93
Appendix A – Equation Derivation 101
Appendix B – Reactor Configurations 102
Appendix C – STR Data 105
C.1 STR Fed-batch Concentration Data 105
C.2 STR Fed-batch Key Results Tables 106
C.3 STR Fed-batch Prediction Trends 108
C.4 STR Fed-batch Efficiency Data 110
Appendix D – Bubble Calculations 111
Appendix E – Sparger Designs 113
E.1 Sparger Layout 113
E.2 Proof-of-concept Reactor Sparger 3D Models 113
E.3 Laboratory-scale Reactor Sparger 3D Models 115
Appendix F – HAIL Reactor Experiment List 117

List of Figures

Figure 2.1 – Concentration profile across gas-liquid interface according to Two-Film Theory adapted from Whitman (1923) 4
Figure 2.2 – Mass transfer pathway from bubble to cell, adapted from Chisti (1989) 5
Figure 2.3 – Laboratory-scale stirred tank reactor design 13
Figure 2.4 – Simplified bubble column reactor diagram 15
Figure 2.5 – Simplified diagrams of an (a) internal loop ALR and (b) external loop ALR 16
Figure 2.6 – Simplified standard wave bioreactor diagram 18
Figure 2.7 – Simplified orbital shaker diagram 19
Figure 2.8 – Simplified Tubular Loop Diagram 20
Figure 2.9 – Simplified helical reactor diagram adapted from Carvalho et al. (2006) 21
Figure 2.10 – STR power input vs observed k_La for ionic and pure water systems, correlation constants taken from Van't Riet (1979) 26
Figure 2.11 – Variation in observed k_La vs power input for different STR systems at $vs = 0.005\ m/s$ 26
Figure 2.12 – k_La vs power input for BCR's using literature correlations 28
Figure 2.13 – k_La vs power input for ALR's using literature correlations 28
Figure 2.14 – k_La vs power input for orbitally shaken reactors 29
Figure 2.15 – k_La vs power input for wave bag bioreactors 30
Figure 2.16 – Relationship Between Minimum k_La Required and Dry Yeast Cell Biomass at $\mu = 0.25\ h^{-1}$ 34
Figure 2.17 – Typical Industrial Yeast Fermentation Pathway adapted from Bekatorou et al. (2006) 35
Figure 4.1 – Peristaltic pump calibration curve 40
Figure 5.1 – Observed k_La vs. agitation rate in a STR at different volumes in (a) deionised water and (b) media systems at 30 °C and an aeration rate of 1 vvm. 49
Figure 5.2 – Glucose, ethanol and cell concentration vs. time for a single batch STR fermentation growing *S. cerevisiae* 50
Figure 5.3 – Fed-batch STR run 5 ethanol, glucose, and cell concentration profiles over time 51
Figure 5.4 – Glucose concentration vs. time for fed-batch STR run 5 52
Figure 5.5 – Fermentation broth density vs. cell density profiles for fed-batch STR runs for the (a) overall system, (b) 3rd run, (c) 4th run, and (d) 5th run 53
Figure 5.6 – Fermentation broth viscosity vs. cell density profiles for fed-batch STR runs for the overall system (a), 3rd run (b), 4th run (c), and (d) 5th run 53
Figure 5.7 – Observed vs. predicted (a) cell concentration, (b) growth rate, and (c) productivity for fed-batch STR run 5 55
Figure 5.8 – Theoretical minimum k_La requirement vs observed minimum k_La requirement over time for fed-batch STR run 5 using (a) initial growth rates and (b) corrected growth rates 56
Figure 5.9 – k_La vs. power input per unit volume for fed-batch STR (a) run 2, (b) run 3, (c) run 4 and (d) run 5 58
Figure 5.10 – k_La vs power input per unit volume at a constant volume of 9.4 L from post fermentation experiments from fed-batch STR run 4 59
Figure 5.11 – All fed-batch STR k_La results vs. respective power input per unit volume 59
Figure 5.12 – Response time corrected data for a (a) deionised water STR set-up, with (b) fill volume comparisons from the same experiment 60
Figure 6.1 – Proof-of-concept prototype HAIL reactor 66
Figure 6.2 – Prototype sparger 66
Figure 6.3 – Circulation time at different depths for different sparger designs on aeration at 8 LPM in a HAIL reactor filled with 4 L of tap water 68
Figure 6.4 – HAIL reactor 69

Figure 6.5 – Circle sparger with improved guard design 69
Figure 6.6 – Laboratory-scale HAIL reactor fill volume vs. liquid height 71
Figure 6.7 – Sample mixing and circulation time data 72
Figure 7.1 – Circulation time vs gas flow rate in LPM (a) and vvm (b) for the 60d sparger configuration operated at four fill volumes 75
Figure 7.2 – Mixing time vs gas flow rate in LPM (a) and vvm (b) for the 60d sparger configuration at different fill volumes 76
Figure 7.3 – Comparison between mixing time and circulation time for all volumes using the 60d sparger configuration 76
Figure 7.4 – Mass transfer coefficient vs. power input per unit volume at 20 L fill volume for the 60d sparger configuration 77
Figure 7.5 – Circulation time vs. gas flow rate at 20 L fill volume in HAIL Reactor across all sparger designs 78
Figure 7.6 – Mixing time vs. gas flow rate at 20 L fill volume in HAIL Reactor across all sparger designs 78
Figure 7.7 – Mixing time vs. power input per unit volume for the c1, 60s and 90s sparger designs at a fill volume of 20 L in the HAIL reactor 79
Figure 7.8 – Mixing time vs. power input per unit volume for all 10 mm2 sparger designs at a fill volume of 20 L in the HAIL reactor 79
Figure 7.9 – (a) Circulation and (b) mixing time vs. power input data for c1 sparger for 20 L, 23 L and 26 L volumes 81
Figure 7.10 – Mixing time vs reactor fill percentage at a gas flow rate of 30 LPM for c1 HAIL reactor configuration. 82
Figure 7.11 – (a) Liquid surface area vs. liquid level and (b) the ratio between surface area and liquid volume in the laboratory-scale HAIL reactor 82
Figure 7.12 – Mass transfer coefficient vs. power input per unit volume at 20 L fill volume in the laboratory-scale HAIL reactor using the c1 sparger 83
Figure 7.13 – k_La power efficiency vs. reactor fill volume at an aeration rate of 30 LPM in the HAIL reactor using the c1 sparger 84
Figure 7.14 – Circulation and mixing time vs. power input at 20 L volume in the HAIL reactor at 1.0 cP and 1.4 cP using the c1 sparger 87
Figure 7.15 – kLa vs. power input per unit volume at 20 L fill volume in laboratory-scale HAIL reactor at 1.4 cP viscosity 87

Figure A.1 – Plot of k_La vs. power input per unit volume for the baffled travelling loop reactor, adapted from Kaiser et al. (2016b) 101
Figure A.2 – Plot of k_La vs. power input per unit volume for the unbaffled travelling loop reactor, adapted from Kaiser et al. (2016b) 101
Figure C.1 – Substrate and cell concentration data for fed-batch STR run 1 105
Figure C.2 – Substrate and cell concentration data for fed-batch STR run 2 105
Figure C.3 – Substrate and cell concentration data for fed-batch STR run 3 106
Figure C.4 – Substrate and cell concentration data for fed-batch STR run 4 106
Figure C.5 – Observed vs. predicted (a) cell concentration and (b) fed-batch growth rate for fed-batch STR run 1 108
Figure C.6 – Observed vs. predicted (a) cell concentration and (b) fed-batch growth rate for fed-batch STR run 2 108
Figure C.7 – Observed vs. predicted (a) cell concentration and (b) fed-batch growth rate for fed-batch STR run 3 109
Figure C.8 – Observed vs. predicted (a) cell concentration, (b) fed-batch growth rate and (c) productivity for fed-batch STR run 4 109
Figure D.1 – Force diagram over bubble 111
Figure E.1 – Typical sparger experiment cross-section 113

Figure E.2 – Sparger P45-30 113
Figure E.3 – Sparger P45-40 113
Figure E.4 – Sparger P45-50 113
Figure E.5 – Sparger P60-30 114
Figure E.6 – Sparger P60-40 114
Figure E.7 – Sparger P60-50 114
Figure E.8 – Sparger P75-30 114
Figure E.9 – Sparger P75-40 114
Figure E.10 – Sparger P75-50 114
Figure E.11 – Sparger P90-30 115
Figure E.12 – Sparger P90-40 115
Figure E.13 – Sparger P90-50 115
Figure E.14 – 60° laboratory-scale HAIL reactor sparger designs (a) 60d, (b) 60dm, and (c) 60s 115
Figure E.15 – 90° laboratory-scale HAIL reactor sparger designs (a) 90d, (b) 90dm, and (c) 90s 116
Figure E.16 – Non-standard laboratory-scale HAIL reactor sparger designs (a) c1 and (b) surface aerator 116

List of Tables

Table 2.1 – Mixing time for different reactor configurations, volumes and aeration rates at a power input of 2 W/L, adapted from Van't Riet and van der Lans (2011). 23
Table 2.2 – Mass transfer energy efficiency comparison for vertical bioreactors 28
Table 2.3 – Mass transfer energy efficiency in raceway bioreactors 31
Table 2.4 – Oxygen utilisation rates for various yeast species, data from Hagman et al. (2014) 32
Table 4.1 – Media composition for STR fed-batch operation growing *S. cerevisiae* 45
Table 5.1 – Temperature, pH, and DO data for fed-batch STR run 5 51
Table 5.2 – Key Results from fed-batch STR run 5 54
Table 5.3 – Mass transfer energy efficiency across fed-batch STR runs 57
Table 5.4 – Constants and R^2 for fed-batch STR runs 2-5 59
Table 5.5 – Key observations from response time corrected deionised water STR experiment data 60
Table 6.1 – LAR reactor performance comparison 63
Table 6.2 – List of tested spargers in laboratory-scale prototype HAIL reactor 70
Table 7.1 – HAIL reactor mass transfer coefficient results behind the sparger at a fill volume of 20 L and gas flow rate of 20 LPM for all tested spargers 80
Table 7.2 – k_La due to surface aeration in the HAIL reactor with 20 LPM aeration at varying volumes in absence of below-surface liquid sparging 83
Table 7.3 – Mass transfer efficiencies for c1 sparger taken from Figure 7.12 84
Table 7.4 – Overall mass transfer energy efficiency results for HAIL reactor with c1 sparger 84
Table 7.5 – Summary of k_La data from literature review and experimental work results 85

Table B.1 – STR reactor configurations used in Figure 2.11 102
Table B.2 – BCR reactor configurations used in Figure 2.12 103
Table B.3 – ALR reactor configurations used in Figure 2.13 104
Table C.1 – Key fed-batch data from fed-batch STR run 1 106
Table C.2 – Key fed-batch data from fed-batch STR run 2 107
Table C.3 – Key fed-batch data from fed-batch STR run 3 107
Table C.4 – Key fed-batch data from fed-batch STR run 4 107
Table C.5 – Run 1 mass transfer energy efficiency data 110
Table C.6 – Run 2 mass transfer energy efficiency data 110
Table C.7 – Run 3 mass transfer energy efficiency data 110
Table C.8 – Run 4 mass transfer energy efficiency data 110
Table C.9 – Run 5 mass transfer energy efficiency data 110
Table E.1 – 45° proof-of-concept reactor sparger designs 113
Table E.2 – 60° proof-of-concept reactor sparger designs 114
Table E.3 – 75° proof-of-concept reactor sparger designs 114
Table E.4 – 90° proof-of-concept reactor sparger designs 115
Table F.1 – HAIL reactor circulation/mixing time experiment list 117

Glossary of Terms

Circulation Time	The time required for liquid in a loop to travel one length of the loop
DO Dot	An adhesive sensor, in the shape of a circular sticker, to be used with an optical probe
Electrochemical Electrode	Metallic rods with a membrane-coated tip. Used in the detection of the dissolved gas concentration in a liquid.
Gassed Power	The comparatively reduced power input of a stirred tank reactor as a result of the impeller/s when the reactor is aerated
Mass Transfer Coefficient	Denoted by k_La, represents the efficiency at which a gas can be transferred into a liquid system
Mass Transfer Energy Efficiency	The energy efficiency with which a magnitude of k_La is obtained, given by the k_La divided by the associated required power draw
Mixing Time	The time required for a system to reach 95% homogeneity after an input
Optical Probe	A fiber optic cable through which a light is shined at a sensor/object of interest. Information is gathered via reflected light and transferred back through the cable
Oxygen Transfer Rate	The rate at which gaseous oxygen is transferred into a liquid system as a result of various system characteristics.
Power Input per Unit Volume	The power input into a reactor system relative to the system's liquid volume
Power Number	A dimensionless number relating resistance to inertia used in the determination of the ungassed power in a stirred tank reactor
Re-aeration	The process by which gas flow is re-enabled for a system after having been initially terminated, usually as part of a mass transfer experiment
Reynold's Number	A dimensionless number commonly used to denote liquid turbulence
Tracer	An inert injected liquid used to assess mixing profiles within a reactor
Ungassed Power	The power input of a stirred tank reactor as a result of the impeller/s in absence of aeration

Acronyms and Abbreviations

ALR	Airlift Reactor
BCR	Bubble Column Reactor
DO	Dissolved Oxygen
EL-ALR	External Loop Airlift Reactor
HAIL	Horizontal Air-Injected Loop
HAR	High Aspect Ratio
HPLC	High Pressure Liquid Chromatography
IL-ALR	Internal Loop Airlift Reactor
LAR	Low Aspect Ratio
LPM	Liters Per Minute
OD	Optical Density
OTR	Oxygen Transfer Rate
OUR	Oxygen Uptake Rate
STR	Stirred Tank Reactor
YPD	Yeast Peptone Dextrose

1 Introduction

1.1 Background

The industrial production of aerobic micro-organisms predominantly occurs in high aspect ratio (HAR) reactors such as the stirred tank reactor (STR), bubble column reactor (BCR) and airlift reactor (ALR) (Garcia-Ochoa et al., 2011; Jakobsen et al., 2001; Yen et al., 2019). These reactors are reliable and relatively well understood, however they suffer from a major drawback in that the energy requirement for air compression is a significant cost due to the massive pressure drop from bottom to the top of the reactor (Harding, 2008). Oxygen mass transfer tends to be the limiting factor in such reactors owing to the low solubility of oxygen in liquid media, requiring optimal gas sparging.

As this pressure drop is inherent in the design of aerated HAR reactors, the next logical step in the enhancement of aerobic processes is to explore viable low aspect ratio (LAR) reactor designs. By making use of a horizontal orientation, the high pressure drop associated with a high aspect ratio is avoided and superior mass transfer performance as a function of power input per unit volume can potentially be obtained.

There are two major categories of horizontal bioreactor currently being explored in literature: shaken systems and loop systems. Shaken systems include wave and orbital shaker bioreactors whereas loop systems include raceways and horizontal tubular loop reactors, among others. As these are not currently employed in the industry employing aerobic microbial culture, it stands to reason that they have been unable to compete with the more standard HAR’s. It is here that that the motivation behind this Master’s dissertation is found: the design and proposal of a novel LAR reactor capable of high-efficiency oxygen mass transfer and scalability.

1.2 Dissertation Scope and Focus

In this dissertation a thorough review of the existing literature on LAR and HAR reactors was conducted. This information was collated to propose and construct a novel LAR reactor design. Additional experimental information on HAR reactors (limited to the stirred tank reactor owing to time constraints and reactor availability) for comparison between literature and the novel system was gathered. This information included mass transfer energy efficiency and reactor performance with aerobic cultivation of yeast, including change in viscosity, oxygen demand and culture density or cell concentration over time. To this extent a glucose-limited feeding strategy was developed.

Following development of the novel reactor design, a proof-of-concept system was constructed, and basic mixing tests were performed. This was followed by the laboratory-scale system, where the reactor’s mass transfer and mixing performance was determined across a wide range of operating conditions. The novel system was customised by altering the sparger type employed. However additional customisations, such as the inclusion of baffles, could not be followed, nor could live culture experiments be conducted, due to time and resource constraints. The above approach was carried out with the intention of verifying whether the novel system could meet the required gas-liquid mass transfer performance for aerobic production of yeast biomass while delivering improved energy efficiency over either the HAR reactor systems or existing LAR designs.

1.3 Dissertation Structure

Chapter 1 of this dissertation presents its scope and contains all the introductory information necessary for a basic understanding of the topic of this dissertation and its importance. Chapter 2 introduces the literature review and synthesis. This constitutes a significant portion of this dissertation as it sets the framing for the novel reactor design. It begins with an in-depth discussion of pertinent mass transfer theory and the many ways mass transfer can be influenced whether it be chemical or physical. This is followed by a more in-depth analysis of existing bioreactors and their relative strengths and weaknesses, as well as numerical data to quantify the mixing and mass transfer performance of these systems. Finally, the literature review is concluded with a discussion of mass transfer and performance requirements for a model aerobic micro-organism, *Saccharomyces cerevisiae*. Chapter 3 details the dissertation's problem statement, hypothesis, and key questions. This is followed by Chapter 4 wherein the research approach is detailed, in addition to the methodology and methods employed for the STR experiments encompassed by this work. The STR results are then presented and discussed in Chapter 5. In Chapter 6 information from the literature review is used to inform the design of the novel reactor. The results of experiments performed in a proof-of-concept prototype are provided and used to inform the additional experiments and design of the final laboratory-scale prototype. The results for the laboratory-scale prototype are presented in Chapter 7, where the final reactor is compared with literature data as well as the experimental results detailed in Chapter 5. Finally, the relevant conclusions and recommendations are provided in Chapter 8.

2 Literature Review

In the aerobic fermentation industry, reactor design is highly focused upon the maximisation of mass transfer energy efficiency. Cells require significant oxygen supply for sustained aerobic growth but the low solubility of oxygen in water presents a significant challenge. This necessitates that mass transfer rates be kept high. Many aerobic processes, such as the growth of Baker's Yeast, have low profit margins and the energy required to supply air to these bioreactors is one of the most significant costs for plant operation (Harding, 2008). As a result, increasing the efficiency at which a high rate of mass transfer can be obtained remains critical to plant operation and is the focus of continued reactor design and improvement.

2.1 Mass Transfer Theory

The precursor to all reactor design is the fundamentals, and there is nothing more fundamental to an aerobic bioreactor than mass transfer. Depending on the reactor configuration, different hydrodynamics and mass transfer characteristics can be expected during operation. A failure to understand the underlying mass transfer theory before commencing work or research on the matter of reactor design would be fruitless.

2.1.1 Introductory Theory

Mass transfer can be described as the process wherein a mass of one substance is transferred from one system to another. In the case of gas/liquid mass transfer, as the name implies, this indicates the dissolution of gas into a liquid. The initial basis for mass transfer can be established by considering Fick's First Law of Diffusion which provides that the molar flux of a component "A" diffusing across a membrane into a bulk component "B" is given by:

$$J_A = -D_{AB}\frac{dC_A}{dz}$$

Equation (2.1)

Where J_A is the molar flux of component "A" across the membrane in mol/m^{2}s, D_{AB} is the diffusivity of component "A" through "B" in m^2/s, dC_A is the change in concentration of component "A" across the boundary in mol/m^3 and dz is the thickness of the boundary layer in metres. Equation (2.1) accounts for movement across the membrane due to diffusion effects but is insufficient on its own to determine the flux in a real-world system as one still needs to consider the bulk fluid transport of "A" relative to "B". This is given by the following:

$$N_{A,b} = (N_A + N_B)\left(\frac{C_A}{c}\right)$$

Equation (2.2)

Where $N_{A,b}$ is the bulk molar flux of "A", N_A is the total molar flux of "A" across the membrane whilst N_B is the total molar flux of "B" across the membrane, both of which are in mol/m^{2}s, and c is the total molar concentration of the system in mol/m^3.

Combining Equation (2.1) and Equation (2.2) gives the following equation for the net movement of component "A" through a membrane into a bulk component "B":

$$N_A = (N_A + N_B)\left(\frac{C_A}{c}\right) - D_{AB}\left(\frac{\delta c_A}{\delta z}\right)$$

Equation (2.3)

This formula provides the basis for Fick's First Law of Diffusion for Binary Mixtures. It is useful to simplify this term for real world applications. This is done by expanding Equation (2.3) and eliminating terms based on the flow between the bulk regions, such as whether it is unimolecular $(N_B = 0)$ or equimolecular $(N_B = N_A)$. Regardless of the flow, Equation (2.3) can be simplified to the following:

$$N_A = -k_c(C_{Ai} - C_A) \qquad \text{Equation (2.4)}$$

Where C_{Ai} is the concentration of A at the interface in mol/m^3 and k_c is the mass transfer coefficient for the system and is of the general form $\frac{D_{AB}}{\delta z}$. The exact derivation of k_c differs depending on the system conditions, but the general form can always be obtained.

Whilst effective, this method of determining molar flux does not take into consideration resistance effects experienced by components "A" and "B" on both sides of the membrane. Historically, only a single resistance was considered, either from the liquid or gas side of the system (going with whichever system had the best fit with the researcher's data) until Whitman (1923) proposed his Two-Film Theory of Gas Absorption.

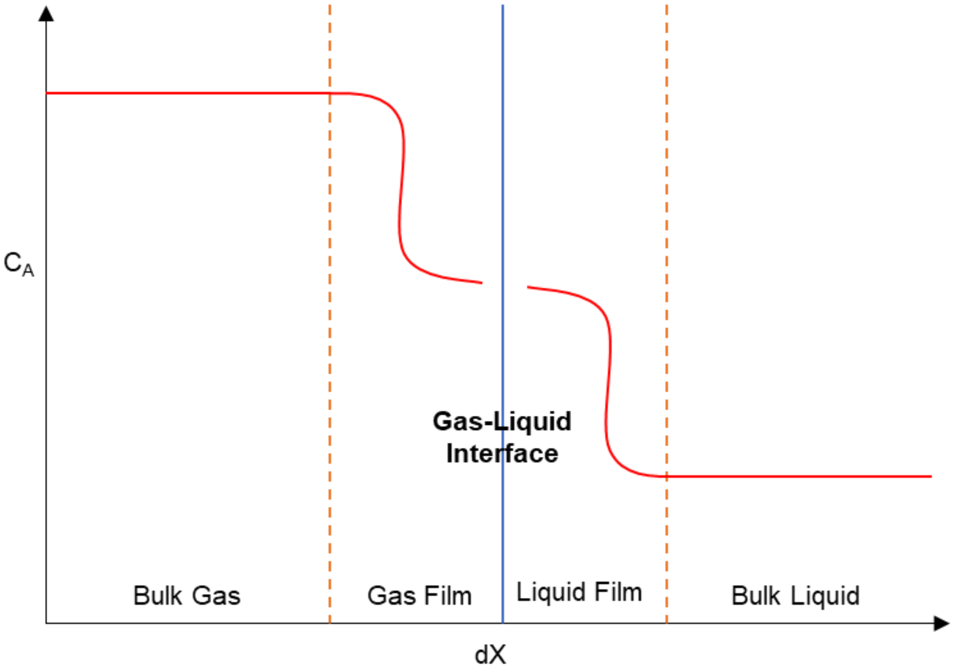

Figure 2.1 – Concentration profile across gas-liquid interface according to Two-Film Theory adapted from Whitman (1923)

Referring to Figure 2.1 above, two separate films can be observed. Each film has their own distinct thickness and an overall mass transfer coefficient (as demonstrated by the term k_c in Equation (2.4)) related to the diffusivity of the relevant components in the bulk fluids. Now one considers the net molar flux across the gas-liquid interface whilst taking both resistances into consideration for mass transfer going across either side of the membrane. This is done by determining the molar flux of component "A" from both the liquid and gas sides of the film then equating them. The exact simplifications and steps followed are based on the bulk fluid flow, as used in the determination of Equation (2.4), but it generally results in the following overall formula:

$$N_A = \left(\frac{1}{k_L} + \frac{1}{H_A k_g}\right)^{-1} (C_A - C_A^*) \qquad \text{Equation (2.5)}$$

Here, k_L represents the overall mass transfer coefficient for the liquid film in s^{-1}, k_g represents the overall mass transfer coefficient for the gas film in s^{-1} and H_A is the Henry's law solubility constant for component "A". C_A^* represents the saturated equilibrium concentration of component "A" in the bulk liquid in mol/m^3.

A simplification is usually made here, such that the new term K_L represents the mass transfer coefficient through both the gas and liquid films on either side of the membrane in s^{-1} resulting in the following equation:

$$N_A = K_L\ (C_A - C_A^*) \qquad \text{Equation (2.6)}$$

2.1.2 Mass Transfer in a Bioreactor

In a conventional bioreactor, air is supplied to the fermentation broth via a sparger. Air bubbles escaping from the sparger quickly rise to the surface, resulting in a very limited time with which the air can transfer into the broth. Once air has dissolved in the liquid broth, it can be utilised by any aerobic micro-organisms present. The entire process can be described by Two Film Theory and general mass transfer and is broken down into eight different mass transfer resistances as described by (Chisti, 1989).

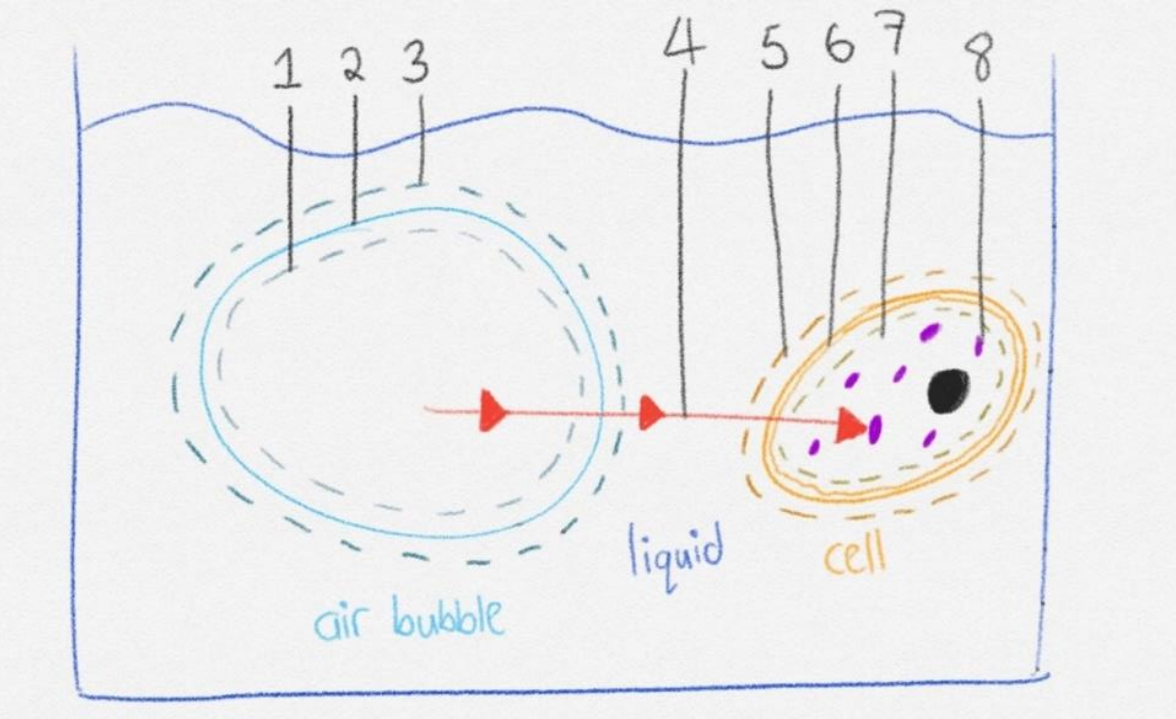

Figure 2.2 – Mass transfer pathway from bubble to cell, adapted from Chisti (1989)

Referring to Figure 2.2, the movement of air/oxygen from an air bubble to a cell can be seen as demonstrated by the red line with arrows. Numerous resistances must be overcome as the oxygen travels from the high concentration present in the bubble to the relatively lower oxygen concentrations in the bulk liquid and then lower still oxygen concentration in the cell. These resistances therefore dictate the rate of mass transfer into the cell. As the gas will predominantly be transferring into the liquid, one considers the pathway from the bulk gas into the bulk liquid.

The first resistance (1) encountered is that of the gas film inside the bubble. This is followed by (2) resistance due to the gas-liquid interface of the bubble itself then (3) the liquid film surrounding the bubble. Once the gas has escaped the bubble, it must now deal with (4) the mass transfer resistance of the bulk liquid itself as it travels through it. When a micro-organism contacts the dissolved gas, the gas must first traverse (5) a liquid film surrounding the cell itself, followed by (6) the cell-liquid interface (typically the cell-wall). Once inside the cell, the gas must overcome (7) resistance due to its movement through the cytoplasm, then finally (8) resistance at the biochemical reaction sites within the cell (such as the mitochondria).

Considering all these resistances would drastically increase the complexity of reactor-based mass transfer calculations. However, the magnitude of most of these resistances is relatively minor in comparison to those due to the gas-liquid interface (resistances 1 through 3 as depicted in Figure 2.2).

This is because reactor system are generally well-agitated (hence bulk fluid flow resistance can be ignored) and transfer effects into the cell are generally rapid (Chisti, 1989). Reflecting on Equation (2.5) and Equation (2.6), it can be noted that the gas film is generally significantly smaller than the liquid film which a much higher diffusivity. As a result, the resistance due to the gas film is generally negligible, hence the overall mass transfer coefficient, K_L, can be approximated to the liquid mass transfer coefficient k_L. This allows for mass transfer phenomena in a bioreactor to be described by Equation (2.7) in the presence of cells, assuming that the utilisation of oxygen by the cells is instantaneous:

$$OTR = -k_L a \left(C_A^* - C_A\right) - OUR \qquad \text{Equation (2.7)}$$

Where OTR and OUR are the oxygen transfer rate into the fermentation broth and oxygen utilisation rate by the cells respectively in mol/s and a is the interfacial area for mass transfer because of the bubble surface area relative to the reactor volume in m^2/m^3 (simplifying to m^{-1}). Due to the difficulty involved in calculating a in a live bioreactor where there are several bubbles of numerous sizes as well as the general difficulty involved in calculating k_L in isolation, the two terms are generally grouped together to form the mass transfer coefficient, herewith referred to as the k_La with units h^{-1}.

2.1.3 Dissolved Oxygen Determination Theory

High accuracy DO measurements are important in industry to ensure that energy is not wasted via excessive agitation/aeration whilst ensuring that the DO never drops below the growing organism's critical level. As a result, there are several different methodologies available for the determination of DO. Each method has unique advantages and disadvantages which differentiate them, however for the industrial usage case any methodologies with a slow response time are entirely non-competitive. Note that the response time is defined as the time at which a sensor reaches 63.2% of its final value when introduced to a step change in concentration (Tribe et al., 1995).

The list of industrially viable DO determination methods is thereby reduced and hence consists largely of different varieties of electrochemical electrodes and optical probes (Kadic and Heindel, 2014).

Electrochemical Electrodes

Electrochemical electrodes are metallic rods with a membrane-coated tip. They are generally favoured owing to the relative ease of their usage in conjunction with low response times and the ability to be autoclaved/steam sterilised.

The membrane at the tip of these probes is gas-permeable, but impermeable to both liquids and ions preventing cross contamination between the electrolyte solution (which lies behind the membrane) and the bulk liquid. The DO concentration is determined via a reduction reaction between DO, having passed into the electrolyte solution across the membrane, and the metallic rod. The current generated by this reaction is proportional to the oxygen partial pressure in the bulk liquid (Doran, 2013a).

This reaction is relatively quick, allowing for response times averaging at 5 seconds for fast commercial probes (Garcia-Ochoa and Gomez, 2009) although the range of response times for different probes (such as those used at laboratory-scale) can be much larger, especially if the probe is autoclavable. Riet and Tramper (1991) indicate that for non-autoclavable probes, the average response time is between 2-3 seconds, whilst for the autoclavable variety the response time increases to between 10-100 seconds. This delay is largely caused by the thickness of the membrane, as the gas takes time to pass through it into the electrolyte.

Optical Probes

Optical probes are still relatively new compared to the more standard electrochemical electrodes. According to Turner and White (2002), the most conventional optical probes work in the following manner: an optical fibre is used to create a system that makes use of fluorescence to monitor the concentration of oxygen in a system. This works by coating the surface of the optical fibre with a special fluorescent dye that changes intensity depending on the concentration of a target analyte in the bulk gas/liquid. A light is emitted from the optical probe, which is reflected by the target analyte back into the optical probe which receives a signal based on the intensity of the fluorescent dye.

Optical probes offer a number of advantages over electrochemical electrodes which make them interesting alternatives, although their few disadvantages have made their wide-spread use more difficult (Kadic and Heindel, 2014). Advantages include rapid response times, as no membrane needs to be traversed, in addition to the fact that no oxygen is consumed in a reaction to take the reading. These probes can also be non-invasive, and some varieties are autoclavable/steam sterilisable. However as they are light-sensitive they are prone to photobleaching, interference of ambient light and suffer from potentially limited DO detection ranges (Turner and White, 2002).

2.1.4 k_La Determination Methodology and Theory

There are two predominant for the determination of the k_La in a liquid system, the oxygen balance method, and the dynamic method. Each has their own disadvantages and advantages, with the most used being the dynamic method and its variations.

Oxygen Balance Method

The oxygen balance method is simple in theory and works off basic mass balance principles. The oxygen entering the target system is known based on a set gas flowrate and composition, hence analysing the gas flowrate and composition of the gas leaving the system allows for a mass balance to be performed, wherein the amount of oxygen “missing” from the exiting gas when compared to the entering gas is regarded as the oxygen which has been transferred to the bulk liquid, i.e., it is the OTR. This is demonstrated in Equation (2.8), which has been adapted from (Doran, 2013a):

$$OTR = \frac{F_i \cdot C_i - F_o \cdot C_o}{V_L} \qquad \text{Equation (2.8)}$$

OTR is the oxygen transfer rate in mol/m^{3}s, F_i and F_o are the inlet and outlet gas flow rates in m^3/s respectively, C_i and C_o are the inlet and outlet concentration of oxygen in the gas streams and V_L is the total liquid volume in m^3.

Using the instantaneous OTR, the live k_La can be determined by knowing both the oxygen concentration in the liquid and the saturated oxygen concentration at equilibrium in a system with no respiring cells, or the OUR in addition to the prior two in the case of a live aerobic culture. This is done via Equation (2.7). The predominant issues with this method are that, despite being the most reliable means of approximating the k_La (Doran, 2013a), exceptionally fast and accurate readings are required for both gas flow rate (and hence also temperature and pressure) measurement and composition. Such equipment can be prohibitively expensive and hence is not considered unless there are additional reasons to motivate for the accurate measurement of gas flow rates (Kadic and Heindel, 2014).

Dynamic Method

The dynamic method is the generally preferred method for k_La determination. This is due to its high accessibility and relatively low cost, as it only requires a DO measurement and a timer. The method was originally definitively proposed by Bandyopadhyay et al. (1967) and many refinements to the method have been proposed over time.

The original method states that, in a typical reactor system, the oxygen transfer rate at any point of time is given by Equation (2.7). As a result, it is dependent on the concentration of oxygen in the gas and bulk liquid, the mass transfer coefficient and the OUR. By restricting airflow to the reactor, the k_La drops to zero and the OTR becomes equal to the OUR. The OUR can additionally be expanded as such:

$$OUR = rX \qquad \text{Equation (2.9)}$$

Where "r" is the oxygen uptake rate in mol/$g_{biomass}$·s and "X" is the instantaneous biomass concentration in the reactor in $g_{biomass}/m^3$.

By following the change in oxygen concentration versus time, the OUR can hence be approximated as the average gradient of the line formed, as the OUR=OTR and the OTR is equivalent to $\frac{dC}{dt}$. By recommencing aeration before the DO drops below the critical level, the resultant trend can be used to determine the OTR in a similar manner as before. However, the OUR must be subtracted from this value as the cells will continue to respire during the re-aeration period. Equation (2.7) is then rearranged as follows, so that a linear plot to determine k_La can be generated:

$$C_L = -\frac{1}{k_L a}\left(\frac{dC}{dt} + rX\right) + C^* \qquad \text{Equation (2.10)}$$

Here, C_L is the true DO concentration at time t in mol/m^3. Equation (2.10) can still be simplified further by assuming that the OTR=OUR at steady state, hence at steady state:

$$rX = \ k_L a(C^* - C) \qquad \text{Equation (2.11)}$$

Substituting Equation (2.11) into Equation (2.10) and rearranging allows for the generation of the following linearised formula:

$$\ln\left(\frac{C_0 - C_L}{C_0 - C_s}\right) = -k_L a(t - t_s) \qquad \text{Equation (2.12)}$$

Where C_0 is the DO concentration at the start of the experiment, C_L is the current DO concentration and C_S is the DO concentration when re-aeration commences. The mass transfer coefficient can then be obtained from the gradient of this relationship. In non-respiring systems, the mass transfer coefficient can still be evaluated by instead using nitrogen sparging to get the DO concentration to zero. In such a scenario the rX would be zero in Equation (2.10). Substituting this in and re-arranging allows for the following linearisation:

$$-k_L a \cdot t = \ln\left(1 - \frac{C_L}{C^*}\right) \qquad \text{Equation (2.13)}$$

The gradient can once again be used to determine the mass transfer coefficient. Unfortunately, this method is only usable for the generation of viable data so long as the k_La of the system remains relatively low in conjunction with a low probe response time (τ_e). For example, Riet and Tramper (1991) indicate that a k_La of up to 0.1 s^{-1} (360 h^{-1}) requires no time correction so long as the probe response time remains between 2-3 seconds. However autoclavable probes typically lie outside this range, indicating the need for response time correction. Gaddis (1999) further expands on this with the following ranges based upon the magnitude of the value of $\frac{1}{k_L a}$ versus τ_e:

1. In scenarios where $\frac{1}{k_L a} \gg \ \tau_e$, response time corrections can be ignored.
2. In scenarios where $\frac{1}{k_L a} \approx \tau_e$, considerable errors in the observed k_La will be observed if τ_e is not taken into consideration, hence the use of adjusted equations is recommended.
3. In scenarios where $\frac{1}{k_L a} \ll \tau_e$, the dynamic method is not recommended at all.

There are several different approaches used to account for the probe response time, however most modern probes can make use of a first-order model to accommodate for the response time and approximate the k_La (Tribe et al., 1995). The exact model used depends on whether the system is respiring (hence OUR is non-zero) or not and varies from author to author. For non-respiring systems, a general first-order approach for determining the k_La as suggested by Garcia-Ochoa and Gomez (2009) is as follows:

$$\frac{dC_m}{dt} = \frac{(C_L - C_m)}{\tau_e} \qquad \text{Equation (2.14)}$$

Where C_m is the DO concentration as reported by the probe at time t in mol/m^3 and τ_e is the probe response time in seconds. Substituting Equation (2.14) back into Equation (2.7) and assuming that the OUR is zero results in the following model:

$$C_m = \mathrm{C}_{\mathrm{sat}} + \frac{C_{sat} - C_0}{1 - \tau_e k_L a} \cdot \left[\tau_e k_L a \cdot e^{-\frac{t-t_0}{\tau_e}} - e^{-k_L a(t-t_0)}\right] \qquad \text{Equation (2.15)}$$

Equation (2.15) can be used to generate a graph that will approximate the true change in DO concentration versus time (with C_0 and t_0 being the initial DO concentration and time at which the experiment is started). In order to obtain the true k_La, an initial guess of the k_La needs to be supplied, then a solver used to minimise the error between the model suggested in Equation (2.15) and the graph obtained experimentally by varying the k_La approximation.

For a respiring system however, the calculation needs to consider the probe response time's impact on the OUR, hence a different method, such as the following first-order approach suggested by Tribe, Briens and Margaritis (1995) needs to be employed:

$$C_m = C_{L_0} - \mathrm{OUR}\left[t - \tau_e\left(1 - e^{-\frac{t}{\tau_e}}\right)\right] \qquad \text{Equation (2.16)}$$

Where C_{L_0} is the DO concentration at the start of the experiment when the gas flowrate is cut. The OUR is first approximated, then the true value is determined by using a solver to match the experimental data with the generated first order model. When re-aeration occurs (the process of re-enabling air flow in the system and aerating it once again), the following formula is proposed to obtain the k_La:

$$C_m = C_{L_0} + OUR \cdot \tau_e\left(e^{\frac{-(t-t_s)}{\tau_e}} - e^{-\frac{t}{\tau_e}}\right) - \mathrm{OUR} \cdot t_s \cdot e^{\frac{-(t-t_s)}{\tau_e}} + \frac{C_{L_0} - C_s}{1 - k_L a \cdot \tau_e}\left(e^{\frac{-(t-t_s)}{\tau_e}} - e^{-k_L a(t-t_s)}\right) \qquad \text{Equation (2.17)}$$

Where t_s is the time at which re-aeration occurs in seconds with respect to the entire experiment. As before, the k_La can then be obtained using a solver to fit the model given by Equation (2.17) to the experimental data. As an alternative to using a solver, Equation (2.14) can be re-arranged to give the following prediction for C_L.

$$C_L = C_m + \frac{dC_m}{dt}\tau_e \qquad \text{Equation (2.18)}$$

Using Equation (2.18) to correct existing concentration data allows for Equation (2.12) and Equation (2.13) to be used in lieu of a solver.

2.1.5 Factors Influencing Mass Transfer

There are several factors that can reduce or enhance the mass transfer in a bioreactor. Referring to Equation (2.7), the only avenues available are to adjust either the k_La, the current concentration of the dissolved gas in the liquid, the equilibrium concentration of the gas in the liquid or the oxygen utilisation rate.

As the OUR is tied to the growth rate/production rate of the microbe in the fermentation media, controlling this is only useful to remain within the design constraints of a reactor. It is of great economic importance to maximise the OUR whilst preventing the DO concentration from dropping below the organisms critical DO level. Exceeding this critical DO level can result in morphological changes in the organism, potentially lowering production of the desired product/biomass or even resulting in cellular death (Kadic and Heindel, 2014). This in turn implies that lowering the DO concentration in the reactor in attempt to create a steeper concentration gradient and increase the OTR is only effective to a certain point.

This leaves the saturated oxygen concentration and oxygen mass transfer coefficient as the only variables that can potentially be adjusted to improve the oxygen transfer rate.

Oxygen Solubility in the Bulk Liquid

Solubility of oxygen in the bulk liquid has a significant impact on the overall oxygen transfer rate. As can be observed from Equation (2.7), increasing the saturated oxygen concentration in the system will increase the concentration gradient between the gas bubble and the bulk liquid, assuming the actual DO concentration in the liquid remains constant. The solubility of oxygen in the bulk liquid is the result of a variety of factors, namely temperature, pressure, chemical composition, and the presence of dissolved solutes.

Different liquid compounds and compositions have unique solubilities for different chemical gasses. This is due to the various inter-molecular forces present between the molecules. In a live culture, micro-organisms often release several metabolites into the fermentation broth which can have either a positive or negative impact on the overall oxygen mass transfer (Ju and Sundararajan, 1995). The potentially beneficial impact of adjusting the liquid composition of the fermentation broth has resulted in research into the improvement of oxygen solubility in fermentation media with the addition of chemicals or organic compounds such as palm oil (Mohd Sauid et al., 2013) or perfluorocarbons (Ju et al., 1991). However, these chemicals can potentially have an impact on the micro-organism being cultivated, in addition to having an associated increase in the cost of production.

The impact of temperature and pressure on the solubility of a gas in a liquid can be described with reference to Henry's Law, which states that the mass of gas which can dissolve in a liquid is proportional to the partial pressure of said gas above the liquid. The formula resulting from this relationship is given by the following:

$$p_A = Hx_A \qquad \text{Equation (2.19)}$$

Where p_A is the partial pressure of component "A" above the liquid in atm, H is Henry's Constant, a value determined experimentally for different gas-liquid systems which is a function of the system's temperature and is given in units atm/mol fraction and where x_A is the mol fraction of component "A" in the liquid (Schaschke, 2014).

Typically, a higher temperature of the bulk liquid directly results in a decrease in oxygen solubility, by means of a reduction in the value of H. For example, at standard state temperature (25 °C) and atmospheric pressure the solubility of oxygen in water is 8.69 mg/L, whilst at a temperature of 30 °C, the solubility of oxygen drops to 8.05 mg/L (Doran, 2013a). This a 7.4% drop in solubility for a 5-degree temperature difference. This is due to the increased heat energy present in the liquid transferring over to the dissolved gas, allowing it to escape more readily. As temperature generally needs to be set at specific values for a fermentation to cater to the micro-organism being sustained, adjusting the oxygen transfer rate by adjusting the temperature is a poor solution. Alternatively, pressure has a directly proportional effect on solubility, increasing it at higher pressures and decreasing it at lower pressures. Unfortunately, increasing the operating pressure is generally a very expensive option both in terms of capital and operating expenditure.

Finally, dissolved solutes in the liquid, typically in the form nutrients and salts, can have both an adverse and beneficial impact on the solubility of oxygen in the bulk liquid. For example, work by Vendruscolo et al. (2012) indicated that a fermentation media containing a variety of sulphate and phosphate salts (in concentrations below or at 2.5 g/L) as well as 20 g/L of glucose and 5 g/L glycine dropped the oxygen solubility from 7.677 mg/L at 30 °C to 6.772 mg/L. This value increased over the course of a fermentation as sugars and salts were consumed, resulting in a final oxygen solubility post-fermentation of 7.743 mg/L. Vendruscolo et al. (2012) reported that, on average, oxygen solubility in fermentation media is between 5% and 25% lower than in distilled water. With regards to enhancement of oxygen solubility, Ho et al. (1990) found that the addition of n-Hexadecane (a hydrocarbon) increased the solubility of oxygen in water. Flourocarbons (such as perfluorodecalin) are similarly beneficial in this regard as an additive, as they also enhance oxygen solubility (Elibol, 2001).

Fluid Rheology, Antifoam, Surfactants and Bubble Size

Liquid composition has a noticeable impact on the oxygen transfer rate in a reactor system. This occurs in one of two ways, either by influencing the way the bulk liquid interacts with the bubbles, or by impacting the bulk fluid flow in the system. A decrease in bubble size will, in practice, increase the available surface area of the gas relative to the liquid, increasing the interfacial mass transfer area and hence the k_La. However, decreasing bubble size will only help to a certain extent as bubbles tend to become increasingly rigid (decreasing k_L) as their size decreases. This effect is even more pronounced in viscous media. As a result, bubbles below 1 mm in diameter are strongly avoided if possible (Doran, 2013a).

For example, the presence of ions in tap water has been found to increase the calculated k_La in a stirred tank reactor by between 5-10% over that of identical experiments when using de-ionised water (Van’t Riet, 1979). This is due to a decrease in the average bubble size in the reactor as a direct result increased coalescence experienced due to the presence of these ions. Several other factors outside of ionic concentration can influence the fluid rheology, however.

Viscosity of the liquid is an important factor to consider when determining mass transfer, as a higher liquid viscosity has a direct impact on the bulk fluid movement in the reactor. The exact impacts of viscosity are often dependent on the exact reactor configuration, however in general a higher viscosity results in a higher required power draw from the reactor system as the bulk fluid becomes more difficult to move which in turn causes a decrease in k_L (de Jesus et al., 2017). Whether this decrease in k_L results in an overall drop in k_La is dependent on the additional impact it has on the interfacial mass transfer area. In general, a higher viscosity causes increased bubble coalescence in the system and additionally causes bubbles to flow in a much more homogenous flow pattern. This would cause the available area to decrease, however the increased viscosity has the additional effect of reducing the overall bubble size, hence the area available for mass transfer can also increase to an extent as a result of a heightened viscosity Kováts et al. (2020). An example of the variability in overall impact is given by Labík et al. (2018), where the authors report on the impact of increased viscosity on an unbaffled stirred tank reactor. Labík et al. (2018) found that an increase in viscosity resulted in a decrease in k_La up until a certain flow regime, wherein a higher viscosity was beneficial for the k_La.

Foam will often form at the fluid surface during bioreactor operation as a direct result of proteins floating in the fermentation broth which are released by the micro-organisms present. This foaming, whilst having no negative impact on mass transfer, can cause significant operational issues due to the tendency to cause overflowing as well as reducing the overall liquid volume (Prins and Van’t Riet, 1987). The solution to this is generally to add an anti-foam, however anti-foams are well-known for causing a significant decrease in the attainable k_La. There are multiple reasons for this. Anti-foam addition causes a sharp increase in the coalescence of the bulk liquid (Prins and Van’t Riet, 1987). Anti-foam also causes an increase in the mass transfer resistance and supresses the mobility of the bubble surface by decreasing surface tension in the bulk liquid. This causes the bubble walls to become more rigid and hence prohibit mass transfer (Kawase and Moo-Young, 1990). As a result, anti-foams should be used sparingly and only as needed.

Surfactants, which also tend to reduce the surface tension in the bulk liquid, can instead have both a positive and negative impact on the system. Despite the potential to increase the rigidity of the bubble wall and hence decrease k_L, they additionally promote the reduction of coalescence in the bulk liquid. This reduces the average bubble size and increases the interfacial area available for mass transfer (Kawase and Moo-Young, 1990).

Cellular Influence on the Bulk Liquid

In addition to biomass, micro-organisms produce a wide variety of metabolites as they consume substrates in the fermentation broth, many of which are leaked into the surrounding media. As a result, as the cellular density increases, so too does their influence on the system's overall mass transfer. Ju and Sundararajan (1995) reported on these phenomena using *S. cerevisiae* as a model. In their report, they specify three potential influences as a direct result of the present micro-organisms.

The first is the metabolic modification of the medium either via the release of proteins, reduction in the concentration of ions or the production of surfactants. The second is the physical presence of the cells as solid particles which influences the rheology of the bulk liquid. The third is the respiration effects of cells at the gas/liquid interface, directly influencing the oxygen transfer rate by lowering the DO concentration immediately near the cells.

The results of their study indicated that the net impact of the live organisms on the oxygen transfer rate in the system was positive with the bulk positive change coming from the metabolic modification of the medium. A minor enhancing effect as a result of cellular respiration was observed and a minor inhibition effect was observed as a result of cellular density. The authors concluded that the exact contributions to the mass transfer rate would be dependent on both the physical system being used (a STR was employed in their study) as well as the organism/product being produced (Ju and Sundararajan, 1995).

Work by Abufalgha et al. (2019) determined that the physical presence of inactive *S. cerevisiae* cells has a significant impact on the superficial gas velocity required to ensure homogeneity in an aerated bubble column reactor. The authors discovered that, despite commonly being neglected in studies, the physical presence of cells significantly decreased the required gas flow rate to induce full homogeneity in the system in an air-water-hydrocarbon system. The authors indicate that this is a result of the impact of these cells on the viscosity and surface tension of the bulk fluid.

Power Input per Unit Volume

The power input per unit volume is commonly used to approximate the k_La obtained in a bioreactor. This is because the typical impact of increasing power input per unit volume an observed increase in k_La. This is due to increased turbulence/energy in the system and decreasing bubble coalescence which enable the mass transfer coefficient k_L to increase by decreasing film thickness around the bubbles (Kadic and Heindel, 2014). The turbulence also serves to keep the system well mixed and aids in the breakage of bubbles, enabling them to remain small and thereby increase the interfacial area available for mass transfer. The net positive effect of an increasing power input however is typically the result of the large gains in interfacial area as opposed to the slight increases in the mass transfer coefficient k_L (Stenberg and Andersson, 1988).

The exact means of increasing the power transferred to the medium depends on the reactor itself. For example, a STR uses a combination of aeration and agitation to supply power to the fluid, whereas BCR's and ALR's forgo agitation in favour of a higher air flow rate. With all these systems, the gain of k_La with increasing power input is not strictly linear and is scenario dependent. In some circumstances increasing power input can actually have negligible impact on the observed k_La (de Jesus et al., 2017).

2.2 Reactor Overviews

2.2.1 Stirred Tank Reactors

General Overview

The primary benefits of stirred tank reactors (STR'S) include enhanced control and superior mixing in viscous environments, as due to their similarity to reactors conventionally used in the long-standing chemical industry their basic design and hydrodynamics are very well understood (Kadic and Heindel, 2014). Whilst there are many different configurations for STR's as a result of this, the basic form is generally consistent. An example of a laboratory-scale STR is depicted in Figure 2.3.

The main draw of these reactors is the mechanically driven impeller. There are two main reasons for this. The first is the introduction of turbulence in the system via the impeller, which enhances mixing.

The second is the breaking up of bubbles by the high-shear region around the impeller blades. Breaking up the bubbles increases their overall surface area, enhancing mass transfer. To aid this, the sparger is located directly below the impeller shaft.

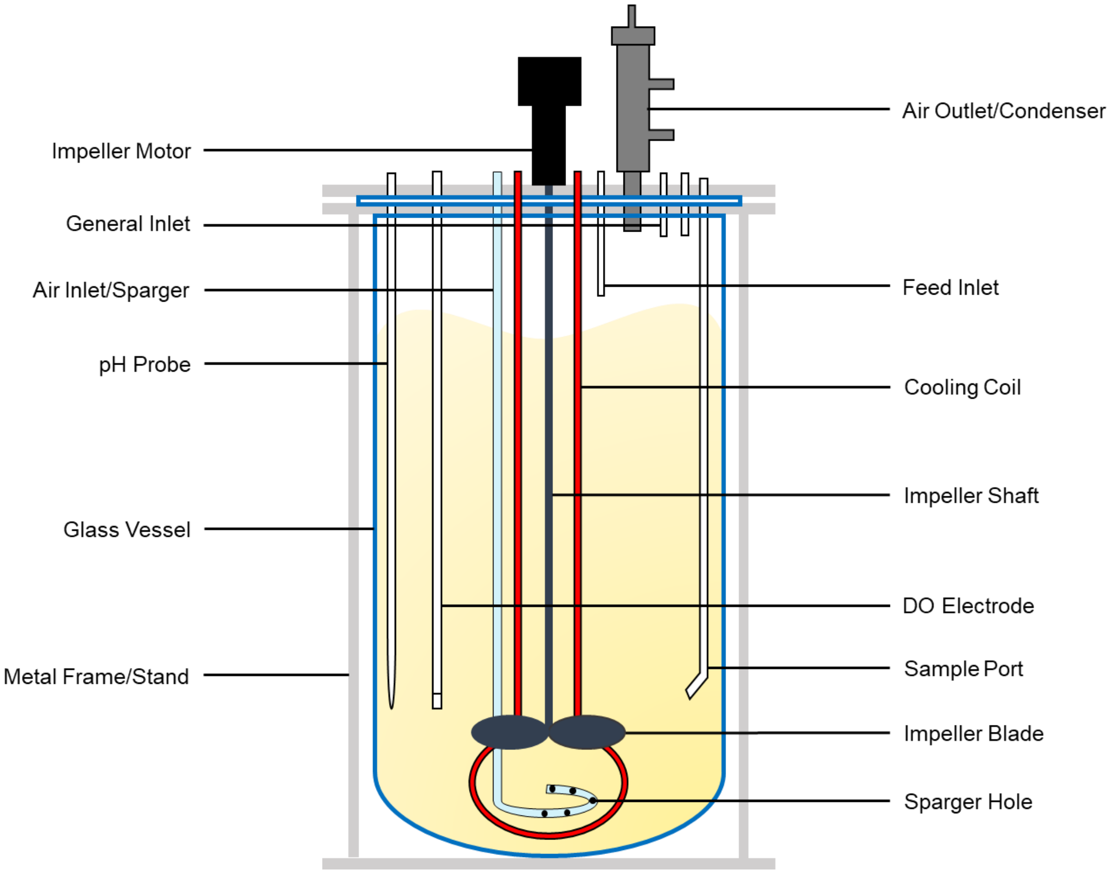

Figure 2.3 – Laboratory-scale stirred tank reactor design

Customisation Options for Performance Enhancement

The most notable avenue for performance enhancement of STR’s is the customisation afforded by the various available impeller set up. The first basis of impeller customisation lies within the impeller shape, either axial or radial. This classification is based on the flow pattern around the impeller blade they generate. Axial impellers offer superior solid suspension and mixing of the bulk-liquid when compared to radial impellers and offer a relatively lower shear environment than radial. Radial impellers, which generate high-shear environments around their blade edges, are superior for the enhancement of gas-liquid mass transfer due to the enhanced disruption of rising bubbles that encounter the blades (Tatterson, 1991).

Outside of impeller type, multiple impeller systems (two or more impellers on one shaft) are often considered. The most frequently encountered configurations make use of two impellers, most typically Rushton turbines (radial flow). Two-impeller systems generally experience better mass transfer at the same power input per unit volume as single-impeller systems (Karimi et al., 2013), however adding a third, or more, impellers to the shaft provides diminishing returns (Gagnon et al., 1998). The contradicting effects of radial and axial impeller types has led some researchers to experiment with dual-impeller systems by using one of each type. Buffo et al. (2016) found notably enhanced mixing and mass transfer by using a combination of Rushton turbine and Elephant Ear impellers. When using a dual-impeller system, special care must be taken to ensure that the spacing between impellers is correct (dependent on tank dimensions), else any performance enhancement effect might be nullified (Nishikawa et al. (1984); Linek et al. (1996)).

STR construction also allows for the customisation of sparger design. However, significant variance in sparger design typically has a negligible impact on bioreactor performance so long as a radial impeller is utilised. To this end a ring sparger with a lower diameter than the impeller is generally used (García-Ochoa and Gómez, 1998). On the contrary, Birch and Ahmed (1997) found that sparger location can have a noticeable impact on performance. Their work has shown that gas hold-up and power draw can potentially be increased for Rushton turbines by placing the sparger in-line with the impeller (hence having a larger diameter than the impeller) such that the bubbles are directed into the impeller discharge stream. Despite the discrepancy between these two authors, and in fact several others, more recent work by Karimi et al. (2013) confirms the findings of García-Ochoa and Gómez (1998) in that the influence of sparger design is inconsequential in an STR.

A final area of customisation is the choice to include baffles in a system. The most commonly used baffles are a set of 4 or 8 equidistant flat blades that are placed inside a STR and run along the length of the reactor, from the bottom to the surface. They serve two primary functions. The first is to prevent the whirlpool effect in a STR, an effect caused when the impeller speed is too high and a whirlpool forms which reduces mixing ability in the STR. The presence of baffles changes the flow patterns in the system and prevents the formation of whirlpools entirely. The second function is a result of the first, in that the liquid that contacts the impeller is “pushed around”. This causes turbulent eddies to form at the surface of the STR, enabling superior surface mass transfer and improving turbulence/mixing of the system. Whilst a large number of different baffle designs exist, the exact benefits offered by designing unique baffles typically fail to outweigh the additional capital and research cost, especially considering the reliability in using the standardised design (Kadic and Heindel, 2014).

2.2.2 Bubble Column Reactors

General Overview

Bubble column reactors (BCR’s), as depicted in Figure 2.4, are entry-level pneumatic reactors, simple in their construction and operation but complex in their design due to the difficulty encountered in understanding their hydrodynamic behaviour. However, simplicity combined with a relatively low operating cost makes these reactors very popular (Shah et al., 1982). As such, they are commonly employed in the production of Baker’s Yeast (George et al., 1998). To accommodate for the lack of agitation present in these bioreactors, gas is bubbled through the bottom and the height of the vessel is maximised. This increases the residence time of gas bubbles in the system as they take longer to reach the surface, at the cost of a larger pressure head that must be overcome. The complex hydrodynamics in these reactors are a direct result of the bubble motion. Depending on the speed at which the bubbles leave the sparger, as well as the type/location of the sparger and the physical characteristics of the bioreactor, different flow regimes will form in the BCR. There are two primary flow regimes utilised in industrial BCR’s. These are the homogenous and heterogenous flow regimes. Additional regimes include the transition regime and slug flow. The transition regime lies between the homogenous and heterogenous regimes and is generally avoided due to its high instability (Kadic and Heindel, 2014). Slug flow is exclusive to BCR’s with a small internal diameter (Shah et al., 1982) and hence is not typical in industrial bio-processes where the reactors used are very large.

The homogenous flow regime is the most beneficial for reactor operation and is characterised by weak mixing and low turbulence (and hence low shear) as well as great mass transfer capability. The low bubble rise velocity results in low bubble coalescence, maximising the interfacial area and allowing for a high oxygen transfer rate.

The heterogenous flow regime is obtained in several different ways, the most common of which is to increase the gas flow velocity beyond a critical threshold. This threshold is unique to each bubble column design/set of reactor conditions (Thorat and Joshi, 2004). It can additionally be obtained by varying the sparger type used, as some spargers are incapable of supporting the homogenous flow regime (Sharaf et al., 2016), as well as by increasing the BCR’s diameter and height. This forces the flow into the heterogeneous regime at lower superficial gas velocities (Ruzicka et al., 2001). As most large-scale industrial bioreactors are tall and relatively wide, it can be stated that the most encountered flow regime in industry is the heterogenous flow regime. The increased turbulence of the heterogeneous regime results in a decrease in the available interfacial area due to increased bubble coalescence. This reduces the efficiency with which the k_La can be improved with increasing superficial gas velocity/power input (Krishna and Van Baten, 2003) but offers a significant improvement to mixing performance.

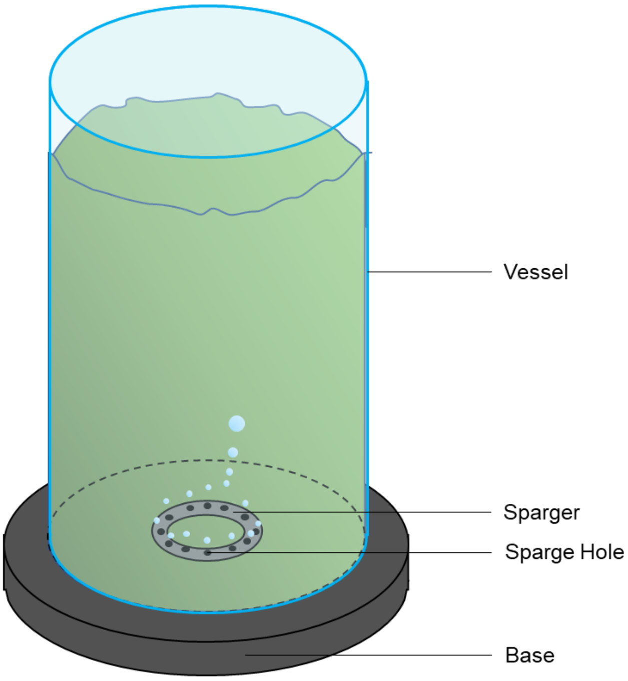

Figure 2.4 – Simplified bubble column reactor diagram

Customisation Options for Performance Enhancement

BCR’s make use of neither baffles nor impeller system. Customisation options and the research direction for improvement on the BCR design are hence limited to the column shape and the design of the gas sparger. With regards to the vessel geometry, the mass transfer tends to decrease with increasing diameter up until a threshold value of approximately 0.15 m, whereupon any additional increase has a negligible impact (Shah et al., 1982). Increasing the bubble column height whilst maintaining a constant diameter results in an increase in the height/diameter ratio. A ratio below 2-5 tends to result in the bubble flow not being fully realised by the time the bubbles reach the surface and in such instances the design and positioning of the sparger is of high importance (Haque et al., 1986). It is important to note that sparger design has limited to no impact on mass transfer performance in bubble column reactors that operate with high superficial gas velocity and hence in the heterogenous regime (Liu et al., 2013) or have aspect ratios greater than 5. Hence for such reactors sparger customisation/design is of relative unimportance (Thorat et al., 1998).

In homogenous systems, different sparger positioning/shape can greatly impact the mass transfer and gas residence time in a system as the initial shape of the bubble tends to remain constant owing to the non-turbulent flow (Sharaf et al., 2016). Furthermore, in the homogenous regime, the achievable mass transfer in porous distributors such as sintered plates has been observed to be superior to single-orifice/multi-nozzle spargers, hence they are the most commonly used sparger type in bubble columns (Shah et al., 1982) .

2.2.3 Airlift Reactors

General Overview

Airlift reactors (ALR's) are also pneumatic reactors and are an adaption of the existing BCR design, of which there are two predominant variations. These are referred to as Internal-Loop Airlift Reactors (IL-ALR's) and External-Loop Airlift Reactors (EL-ALR's). The basic shape of both reactors can be seen by referring to Figure 2.5.

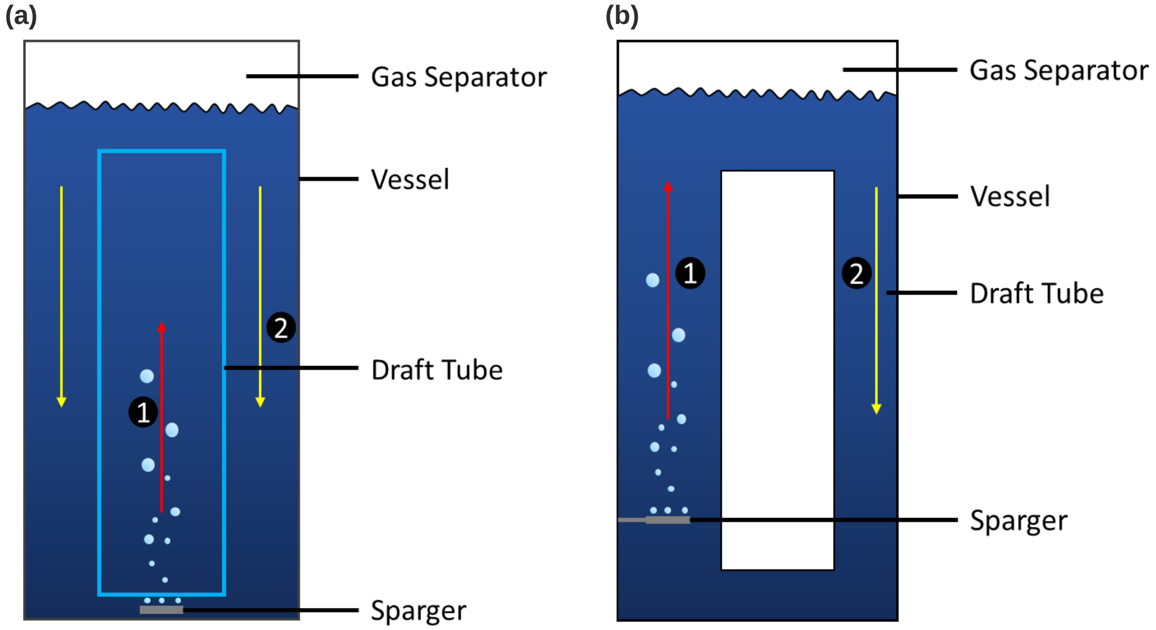

Figure 2.5 – Simplified diagrams of an (a) internal loop ALR and (b) external loop ALR

Their operation is akin to that of a BCR in principle. A gas sparger (generally located at the bottom) is used to aerate a reactor vessel, encouraging both mixing and gas-liquid mass transfer. The operation differs because of the introduction of the draft tube, located either internally or externally depending on the type of ALR being employed. This in turn generates a circulating liquid flow, which can be described in two parts: the riser and downcomer. This can be observed in Figure 2.5 as numbers 1 and 2 respectively. Gas entrained in the riser liquid is released once the liquid reaches the surface, increasing the density of the liquid and forcing it into the downcomer. This mixing is highly efficient and scales very well with size, in addition to generating low shear, offering steep competition to STR's even if the mixing itself is not as vigorous (Chen, 1990).

The bulk of mass transfer in ALR's occurs in the riser on account of the sparger location. Both designs are HAR bioreactors as, for flow to fully develop and to maximise gas-liquid contact time, a taller column is largely beneficial. As a result, overcoming a large pressure head remains a core issue with ALR's much like with BCR's. Similarly to BCR's, ALR's experience the same three general flow regimes: homogeneous, transition and heterogeneous (Šijački et al., 2013). Once again, the homogeneous regime is present at low superficial gas velocity and is characterised by small bubbles with low coalescence. However, the expected limited mixing is offset by the basic operating principle of the ALR making it more useful than in BCR's. The heterogeneous regime is reached once a threshold superficial gas velocity is surpassed.

Customisation Options for Performance Enhancement

When designing and customising ALR's, there are two primary areas that can be influenced: the structural design of the reactor itself, such as internal diameters and/or loop placement, and sparger type/position. The choice between internal loop or external loop is the first choice to make. Industrially, the most commonly employed of these designs is the IL-ALR (Chen, 1990). The reason for this is that, despite being able to better direct the downcomer flow and the higher liquid circulation velocity and hence improved mixing times in EL-ALR’s, IL-ALR’s generally have a higher gas hold-up in both the riser and downcomer, which lends itself directly to an improved k_La (Chisti, 1989).

Both systems can be further customised by varying their dimensions, specifically with regards to the downcomer/riser area, height of the draft tube and area of the gas separator. An overview of the effects of these design variables is given by Mehrnia et al. (2004). A decrease in the downcomer/riser area ratio tends to result in an increase in gas hold-up which in turn results in an increase in the observed k_La and improves mixing in the system due to increased liquid flow velocity in the downcomer. Increasing the height/length of the draft tube results in a slight increase to gas hold-up at the cost of increased mixing time. An increase in the gas separator area improves gas disengagement but reduces the observed k_La.

In so far as sparger positioning and type are concerned, an identical scenario as seen in BCR’s is observed. In the homogeneous regime, sparger design is of high importance as long as the liquid is non-coalescing (Šijački et al., 2013). ALR’s that are operating in the heterogeneous flow regime however experience high bubble coalescence because of the turbulent flow. The initial bubble shape and size are therefore of low importance and have low to negligible impact on the observed k_La. The importance of sparger is further reduced if the reactor is tall, which is generally the case for industrial ALR’s. Coincidentally, the majority of industrial ALR’s growing aerobic culture operate in the heterogeneous flow regime hence the only important design criteria for a sparger is that it covers the entire cross section of the riser. This is most easily done in the draft tube and superior performance is experienced if air is sparged through it regardless (Pollard et al., 1996). The most common spargers in ALR’s are the perforated and porous plate designs (Chisti, 1989).

A more recent attempt to customise ALR’s is the presence of static impellers which are non-mechanically driven by the rising air bubbles in the reactor. Significant improvement in mass transfer and mixing has been observed in viscous systems with such systems (de Jesus et al., 2017). However, whilst such systems have been observed improving k_La even in non-viscous systems, the physical presence of the static impeller, whilst less imposing than a baffle, still slows down the flow of liquid in the system causing an increase in mixing time (Tekic et al., 2014).

2.2.4 Low Aspect Ratio Reactors

Shaken and Disposable Bioreactors

In recent years, there has been a significant push for the usage of disposable bioreactors. Such reactors make use of a disposable vessel/bag, typically constructed from a plastic film much like that used in the production of blood bags (Yang et al., 2013). The benefits of such reactors are largely based around the difficulty and cost associated with proper sterilization techniques for existing non-disposable systems in addition to the significant time saving and enhanced production upkeep as a result of not needing to re-sterilise the reaction vessel after every batch (Brecht, 2010). However, these systems are not without significant drawbacks as well. Scale is chief amongst these concerns, as disposable reactors above 1000 litres are difficult to set-up and carry a high risk of sustaining a tear which would render the system useless. Whilst manufacturers might make an initial saving in capital outlay, there is a significant increase in operational costs associated with both the disposal and procurement of disposable reactors. Finally, the cellular growth properties experienced in the system are subject to change depending on the exact material the reactor is constructed from and this is largely supplier-dependent (Brecht, 2010).

Whilst there are numerous types of disposable bioreactor available on the market, the two primary types considered in industry today are either disposable stirred tank vessels or rocker/shaker style reactors (Kaiser et al., 2013). Disposable stirred tank vessels are generally very expensive as the stirrer is magnetically driven, requiring the disposable vessel have an expensive magnetic coupling inside. The more interesting rocker/shaker style designs are the wave bioreactor and orbital shaker.

Wave Bioreactors

The wave bioreactor, first proposed by Singh (1999) is a disposable reactor system best conceptualised as a large plastic bag on a rocker mechanism, as depicted in Figure 2.6. The bag is filled with medium and aerated to generate a headspace and ensure rigidity of the bag. As the rocker moves back and forth, waves are generated in the reactor due to the motion of the medium against the walls of the bag. These waves generate turbulence which aid mixing and enhance mass transfer into the reactor (Oosterhuis et al., 2011).

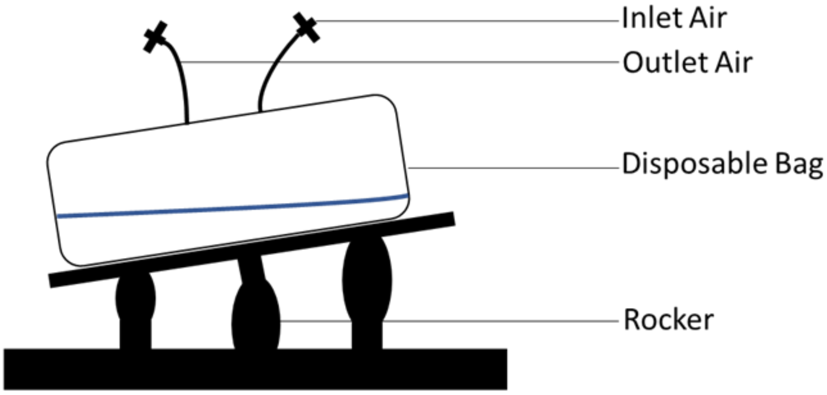

Figure 2.6 – Simplified standard wave bioreactor diagram

The advantages of the wave bioreactor extend beyond the disposable nature of the bag system. In addition to its ease of use, the transparent nature of the bag lends itself well to algal growth and the gentle wave motion generates a very low shear environment, which is ideal for mammalian cell growth (Eibl et al., 2010). Wave reactors are also more energy efficient than the more conventional bioreactors, especially as air is not bubbled through the bottom of the system but instead sparged through the headspace (Brecht, 2010). However, mass transfer, in addition to scaling issues, pose the biggest issues in the standard wave bioreactor design, leaving them generally inadequate for microbial growth. Mikola et al. (2007) tried to aerate the standard wave bioreactor using a sparger located at the bottom of the bag, however this failed to notably increase the observed mass transfer. An alternative design which overcomes this issue is the CELL-tainer® wave bag bioreactor, which enables a significantly higher mass transfer coefficient by rocking the wave bag in four directions as opposed to just back and forth and hence potential exists in using such systems for aerobic yeast growth although the aforementioned scale issues still exist (Oosterhuis et al., 2011). This design however is similar to that of an orbital shaker.

Orbital Shakers

Orbital shakers are amongst the most common of reactor types. This is because of their extensive usage in laboratory-scale research, as most experiments and even industrial productions begin with a small-scale culture or inoculum in a shaken Erlenmeyer flask. A novel approach to these reactors is in their upscaling, specifically centred around the vessel design. The success of wave bioreactors led researchers to further investigate how to enhance their performance, whilst others were already looking for a more suitable replacement. As most inoculum trains already operate using orbital shakers at the small scale, the concept of simply using larger flasks is not a new idea. However utilising larger flasks without altering their design begins to introduce significant mass transfer complications and results in the reduction of energy efficiency of mass transfer with increasing volumes (Jia et al., 2008). As a result, a significant amount of effort has been placed into the development of novel containers to work atop of orbital shakers, across a wide variety of scales. For example, Yang et al. (2013) designed a pyramid-shaped vessel which offered identical performance to conventional Erlenmeyer flasks at lower rotations per minute although this system produced more foam.

The inherent advantages of such an orbital shaker are in the similarities of the hydrodynamics in the shake flask culture versus that of the actual reactor (Anderlei et al., 2009) in addition to potentially more energy efficient mass transfer than that found in wave bioreactors. This is because the large volume of liquid is “swirled” as opposed to tipped via the rocking motion. As a result, there is less gravitational force to contend with (Jia et al., 2008). Orbital shakers are able to provide competitive levels of mass transfer compared to conventional wave bioreactors however their maximum rates are still below those required for the conventional culture of microbial organisms (Klöckner et al., 2013a).

Vessel
Shaker

Figure 2.7 – Simplified orbital shaker diagram

Tubular/loop Bioreactors

Tubular/loop bioreactors are, in principle, similar to EL-ALR’s. The general requirement for a reactor to be considered a loop reactor is that the system forms a closed loop, and that liquid circulates through this. The orientation of these systems can be either vertical, inclined, or horizontal. EL-ALR’s constitute the vertical variety and carry with it the issue of a large hydrostatic head for the compressor to overcome. Horizontal-type loop reactors do not encounter this issue. There are currently a very wide variety of different designs of loop reactor available on the market and/or being actively researched.

Travelling Wave Bioreactor

The travelling wave bioreactor as a concept attempts to merge aspects of both the wave and orbital shaker bioreactor into a single device. An annular ring is placed upon an orbital shaker and, as the orbital shaker moves, a wave is generated within the ring (Kaiser et al., 2013). The potential advantages of this system are two-fold, namely as with most orbital shakers there is no vertical movement, so the energy required to move the liquid is significantly reduced and, secondly, the annular design allows for conservation of liquid momentum.

The wave provides high liquid flow speeds, however the system experiences high mixing times which, although not unsuitable for culture growth, are below the expected range typically found in industrial bioreactors (Kaiser et al., 2016a). Much like with an orbital shaker, mass transfer is relatively energy efficient as the system makes use of surface aeration, however the maximum k_La values obtainable do not lend themselves to the growth of highly aerobic micro-organisms and the advantage of low shear and low foaming are mostly beneficial to animal cell cultivation which is their primary intended use (Kaiser et al., 2016a). Hence, the key advantage for developing a system such as this is in its easy scalability.

Raceway Bioreactor

Raceway bioreactors are large-scale bioreactors predominantly used in the algae production industry. The basic structure is that of a circle/oval, with either an exposed or covered top. Exposed systems are both easier and cheaper to construct and operate than closed systems. However, they lack the control features present in closed systems, are more easily contaminated and are more costly to harvest from owing to a lower attainable cell concentration per litre (Mendoza et al., 2013b).

A typical raceway bioreactor consists of three major design areas. The sump, the paddlewheel, and the vessel itself. Mass transfer in algal raceways is highest around the paddlewheel and sump and relatively low elsewhere in the system, with a slight increase in mass transfer being observed around the bends of the reactor (Mendoza et al., 2013b). The bends themselves are responsible for a large reduction in the energy efficiency of standard wave reactors and reflectors/baffles are generally recommended to help reduce the energy loss experienced around these corners (Liffman et al., 2013). Plug flow is experienced in raceway bioreactors, hence baffles have been considered to aid mixing in such systems. However, it has been found that even a single baffle can cause significant reductions in the circulation time in raceway bioreactors and should therefore be avoided (Mendoza et al., 2013a).

The mass transfer obtainable in raceway bioreactors is generally only high around the paddlewheel and sump and, as this constitutes only a small area of the system, is on average significantly too low (Barceló-Villalobos et al., 2018) for aerobic microbial growth. The paddlewheels also require careful design and can experience significant changes in performance/effective power input if the liquid level in the raceway changes (Mendoza et al., 2013a), making fed-batch growth difficult in raceway bioreactors with a paddlewheel. Hence, a similar system designed for aerobic growth would require significant modifications to aid with both mass transfer, liquid movement and mixing.

Tubular Loop Bioreactor

The tubular loop bioreactor can be arranged either vertically or horizontally and is distinct from an external loop bioreactor in that the liquid is pushed through the system via use of a centrifugal pump. Gas is vented into the system at up to two different positions to ensure adequate air supply throughout the reactor. The gas is then vented from the liquid when it passes through into a gas-liquid separator, which is a small tank with sufficient headspace to allow the gas to disengage. The liquid then leaves through the bottom of this tank and is pumped back into the loop where it is re-aerated (Ziegler et al., 1977). Due to the strength of the pump used, these reactors are unsuitable for shear-sensitive cell culture as such cells are ruptured when passing through it (Yazdian et al., 2009).

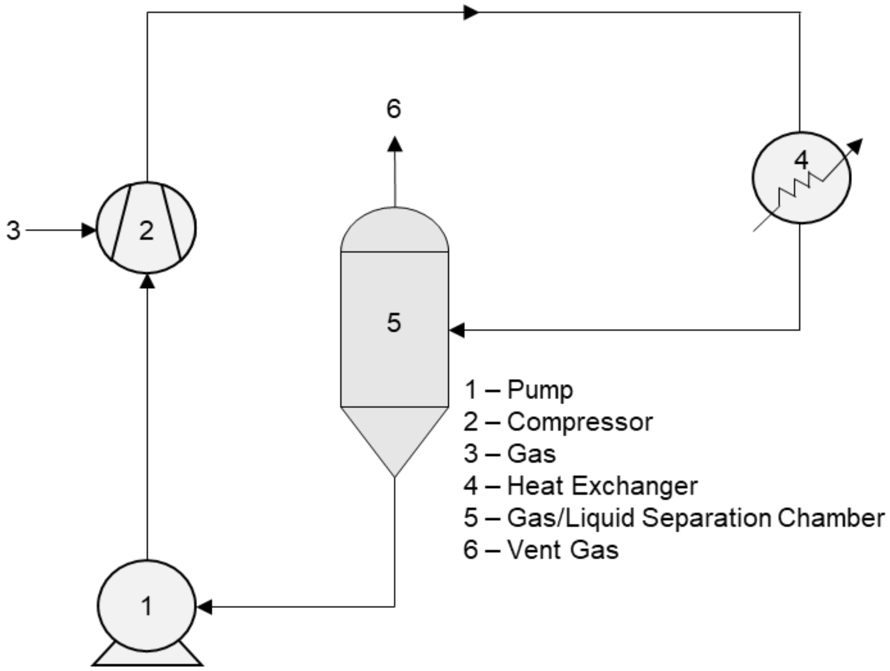

Figure 2.8 – Simplified Tubular Loop Diagram

The circular design ensures a degree of conservation of momentum, and a very lengthy gas residence time, which lends itself well to the production of aerobic micro-organisms, especially if the feedstock in question is a valuable gas. This has been successfully done with a methane consuming *Methylomonas* species. A plant running such a design was even built in 2003 in Norway, however it ultimately failed three years later citing low productivities which could not justify the expensive methane feed (Al Taweel et al., 2012).

Mass transfer in these systems is generally adequate for batch cultures, however the usage of static mixers in the tubes of the reactor can significantly improve upon this at a cost to liquid flow speed. The gas-liquid separator allows for a changing liquid height meaning that these systems can be run in fed-batch. As air is sparged in the horizontal section of the loop, the large hydrostatic head commonly encountered in HAR bioreactors is overcome. Pumping of the liquid is interestingly considered to be non-energy-intensive (Al Taweel et al., 2012). Outside of the high shear experienced due to the pump, the length of these systems makes the difficult to clean and they take up a large amount of floor space, as increasing the pipe diameter beyond a certain point is infeasible (Ziegler et al., 1977).

Helical Bioreactor

An adaption of the horizontal tubular reactor design, helical bioreactors consist of a horizontal tubular loop bioreactor that is stacked atop of itself. This design lends itself extremely well to scale up, as increasing the volume simply requires that another loop be added atop the increasing coil. As a result, the system occupies far less space than a standard horizontal tubular bioreactor (Carvalho et al., 2006). As the reactor is a singular unit, the centrifugal liquid pump needs to accommodate for the extra hydrostatic head, which can pose significant energy constraints. Unfortunately, there is a limited amount of literature available on such bioreactors. A rudimentary diagram of one (adapted from Carvalho et al. (2006)) is presented in Figure 2.9.

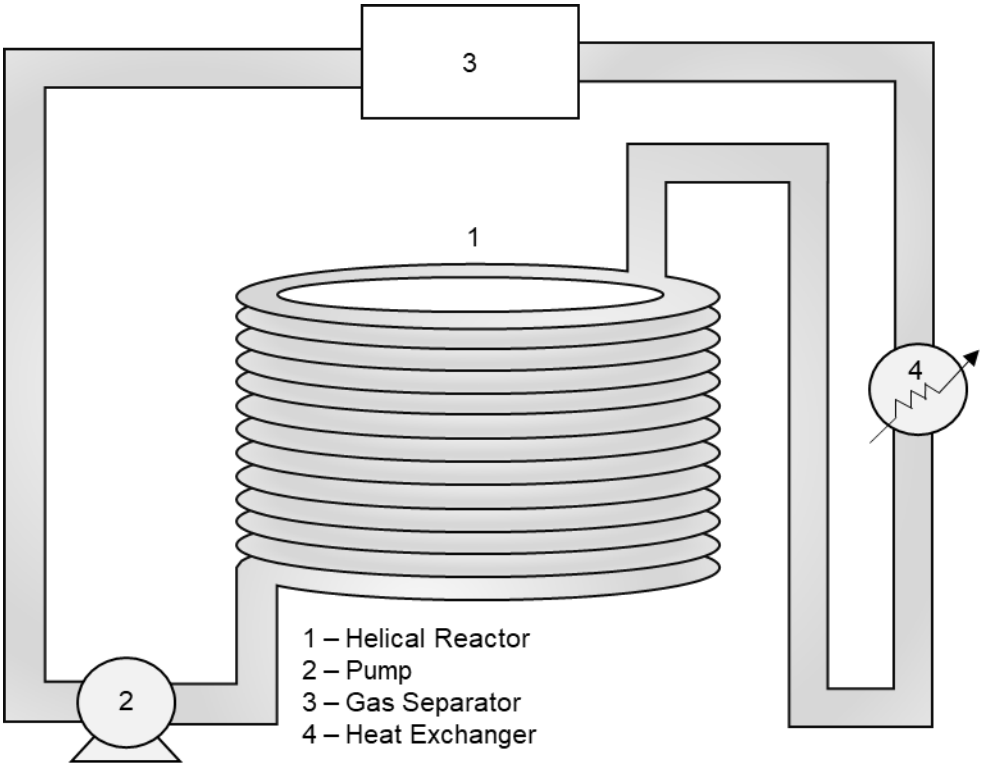

Figure 2.9 – Simplified helical reactor diagram adapted from Carvalho et al. (2006)

2.3 Reactor Performance Comparison

Whilst an empirical understanding of the available bioreactor configurations currently being used/developed is important, a more quantitative overview is of high value in this study as it allows for a direct comparison between the real-world performance of different configurations. For aerobic culture, mixing and mass transfer are among the two most important performance criteria available.

2.3.1 Mixing Time vs Power Input

In addition to mass transfer, mixing time is very useful metric in grading the performance of reactor configuration. Mixing time refers to the amount of time required for a system to reach 95% homogeneity once a disturbance is added to it such as a feed substrate/neutralising agent. Systems with high mixing times are difficult to control as the results of any addition to the reactor take a long time to reflect. This can be disastrous in an industrial operation. As a result, shorter mixing times are always desirable. This can usually be obtained by increasing the power input into the reactor system, but a balance must be struck between power draw and mixing performance.

High Aspect Ratio Reactors

Relating mixing time to power input is not a straightforward relationship. For all HAR reactors, an increase in the liquid height results in a decrease in the observed mixing time, although the magnitude of this impact will differ depending on the given reactor configuration. The efficacy at which an increase in power input alters the mixing time is highly dependent on the reactor geometry and can even result in an increase in mixing time. Further complicating the matter is the fact that consistency of mixing times between authors is lacking. This is because the result of any mixing time experiment is subject to the position of tracer addition. Depending on which system is used and where the tracer is injected in the reactor (bottom, middle or top), a significant variation in mixing time can be observed (Van’t Riet and van der Lans, 2011).

For STR’s, the most notable factors to consider outside of the liquid level are the number and type of impellers, the viscosity of the system and the level of aeration. As the number of impellers in the system increases, a noticeable decline in mixing time is observed so long as the stirrer speed is maintained at a constant value. This is due to the strong compartmentalization that occurs when a second impeller is added (Van’t Riet and van der Lans, 2011). Mixing times are observed to decrease however if axial impellers are introduced, owing to the redirection of water flow around the reactor (Houcine et al., 2000).

The viscosity of the system influences a STR in one of two ways, either by reducing the observed stirrer Reynold’s number or by hastening the onset of flooding in the STR. The former is predominantly an issue with smaller systems, as the stirrer Reynold’s number increases exponentially as the stirrer diameter increases. So long as the Reynold’s value remains above 5000, no significant impact on mixing time is observed as a result of viscosity alone (Van’t Riet and van der Lans, 2011). Impeller flooding is associated with the aeration of the STR and occurs when the flow of air is too high for the impeller system to adequately break up the bubbles as they rise to the blades. As a result, the bubbles bypass the impeller. In such scenarios the mixing time decreases, however this has a negative impact on the observed mass transfer/mass transfer energy efficiency (Van’t Riet and van der Lans, 2011).

Owing to the limited internals in a bubble column, the most significant impact on mixing time arises from the height versus diameter ratio of the system. Below a ratio of 3, the mixing time tends to remain constant regardless of the aspect ratio. As this increases beyond 3 a significant increase in mixing time can be observed (Van’t Riet and van der Lans, 2011). As with STR’s, viscosity also has a noticeable impact on the mixing performance of bubble columns and for similar reasons. As the viscosity increases, the level of turbulence in the system at a given gas flow rate will decrease. If the system enters the homogenous flow regime, the impact of a higher viscosity becomes apparent, potentially tripling the mixing time and significantly reduce the mass transfer performance (Plais and Augier, 2016).

For ALR’s, the aspect ratio/height have the greatest influence on the perceived mixing time. This is because mixing time in an ALR is dependent on the size of the flow loop(s) and can generally be approximated as 4 to 7 times the circulation time of the system depending on geometry (Van’t Riet and van der Lans, 2011). Other factors influencing the mixing time are largely based on reactor geometry. A lower downcomer to riser ratio begets a decreased mixing time and higher top/bottom clearance results in an increase in mixing time (Abdul Rahman–Al Ezzi and Faisal Najmuldeen, 2014).

As with the STR, an increase in viscosity can result in a decrease in the observed mixing time (Abdul Rahman–Al Ezzi and Faisal Najmuldeen, 2014), however, as with the bubble column this results in extremely limited mass transfer performance. A direct comparison of the mixing performances of these different systems at identical power input, volumes and liquid heights is provided by Van't Riet and van der Lans (2011).

Table 2.1 – Mixing time for different reactor configurations, volumes and aeration rates at a power input of 2 W/L, adapted from Van't Riet and van der Lans (2011).

Reactor Volume [L]		**10**		**10 000**	
Aeration Rate [m·s^{-1}]		**0.01**	**0.1**	**0.01**	**0.1**
Aspect Ratio (H_T/D_T)	**Reactor Type**	**Mixing Time (s)**			
10	**ALR**	***49***	***19***	***220***	***96***
10	**BC**	78	36	363	168
10	**STR**	270	270	1200	1200
5	**ALR**	47	18	198	78
5	**BC**	***23***	***11***	***106***	***50***
5	**STR**	79	79	364	364
2	**ALR**	46	18	192	72
2	**BC**	***11***	***5***	***52***	***24***
2	**STR**	15	15	71	71

Table 2.1 clearly demonstrates that among the HAR reactors, the bubble column maintains the best possible mixing for most scales. As the aspect ratio increases the mixing time of ALR's become increasingly competitive, until they become the superior option at high aspect ratios. Following this trend, STR's are never the best performer and their use in industry would be brought into question. However, this does not take into consideration the mass transfer performance of these systems.

Low Aspect Ratio Reactors

As with the HAR reactors, defining a true mixing time versus power input per unit volume relationship is difficult. This is due in part to the vastly different geometries of different systems as well as consistency issues between different authors. Many systems do not have power inputs which can be compared to these mixing times either, as the relationship between power input and performance gains in these systems is not always clear-cut.

Orbital Shakers

Mixing time in orbital shakers is impacted to a large extent by the relationship between the shaking diameter, vessel diameter and shaking frequency. With a constant volume, as the diameter of a vessel atop a shaker decreases the observed mixing time decreases and the inverse also holds true (Tissot et al., 2010). This can be explained via the reduced effective power input an orbitally shaken vessel receives as the liquid height increases at the same shaking frequency (Klöckner et al., 2012). Orbital shakers do not exhibit a significant change in mixing time at identical shaking frequencies as the scale of the system changes, so long as the ratio between the shaking diameter and internal diameter of the vessel is maintained (Tissot et al., 2010).

To determine the associated power input per unit volume, one can note the mixing time observed at a specific shaking frequency then determine the power draw using the following correlation proposed by Klöckner et al. (2012):

$$\frac{P}{V_L} = 9 \cdot g^{-0.42} \cdot \rho^{0.83} \cdot d^{3.34} \cdot n^{3.67} \cdot \eta^{0.17} \cdot V_L^{-0.65} \cdot d_s^{0.042} \qquad \text{Equation (2.20)}$$

Where "V_L" is the total liquid volume in m^3, "g" is the acceleration due to gravity in m/s^2, "ρ" is the liquid density in kg/m^3, "d" is the vessel diameter in metres, "n" is the shaking frequency per second, "η" is the dynamic viscosity of the liquid in kg·m^{-1}·s^{-1} and "d_s" is the shaking diameter in metres. The power input is independent of the liquid height in this correlation, which makes sense as the key advantage of such systems is the shaking motion as opposed to a rocking motion. According to Tissot et al. (2010) a 1500 L system with a 500 L working volume, a shaking diameter of 10 cm and internal diameter of 155 cm attained a mixing time of 70 seconds at a shaking frequency of 40 rpm, 15 seconds at 50 rpm and 10 seconds at 60 rpm in a water system. Using Equation (2.20), these correlate to respective power inputs per unit volume of 449, 1020 and 1990 W/m^3, respectively.

Wave Bag Bioreactors

Mixing times in wave bag reactors is dependent on the bag geometry in conjunction with the rocking speed and fill volume. The most important aspect of the bag's design for mixing is the design of the corners and edges of the bag (Junne et al., 2013). As the fill volume increases so too does the mixing time, which further emphasises the limit of 50% fill volume previously discussed. Work by Jones et al. (2017) demonstrated that, whilst important for mass transfer, the rocking angle has only a small impact on the mixing times obtained in a wave bag reactor at high rocking rates. Work by Bai et al. (2019) demonstrated that this does not always hold true noting that the exact mechanism for this is not understood. As with most systems, power input is the most straightforward method to increase the mixing time in a wave bioreactor, and this is done by increasing the rocking rate.

The power input associated with an increase in the rocking rate is not easily quantifiable and there is no currently available correlation to determine this using reactor parameters alone. As a result, power input is determined via a variety of live methods. Jones et al. (2017) determined the power input using a calorimetric method. Alternatively, Bai et al. (2019) advocate the use of a digital multi meter connected directly to the rocker's motor, measuring the voltage flowing to the rocker at any point of time and determining the power input from this. Power inputs for an associated mixing time presented by Jones et al. (2017) for a 10 L system with a rocking angle of 10 ° and a 20% filling volume were 64 and 633 W/m^3 to obtain 70 and 18 second mixing times respectively. Bai et al. (2019) compare several different filing volumes and bag sizes and demonstrate a significant deviation in trends of mixing power input versus mixing time depending on the bag size and filling volume. However, all systems tend to a sub one hundred-second mixing time once a power input of 400 W/m^3 or greater is obtained.

Raceway

Mixing times in largescale raceway reactors are very long, measuring above an hour on average for a system without a sump baffle and up to 6 hours for systems with the sump baffle as reported by Mendoza et al. (2013a). The associated power input is very low to match this, ranging between 1.5 and 8.4 W/m^3 depending on whether a baffle is present or not (baffle presence increases power draw) and the target flow velocity. These low values are indicative of the predominant usage case of raceway reactors: cheap algal growth. Studies into the repurposing of such systems for aerobic culture could not be found.

Travelling Loop

The travelling loop bioreactor is a relatively new concept and as such there is limited research into its performance and further development. Mixing time in the system is generally dependent on the shaking rate, filling volume and reactor geometry/configuration. The work by Kaiser et al. (2016b) demonstrated that the mixing time decreases both with an increase in shaking rate (power input) and an increase in fill volume, as well as a significant increase with the presence of ridge baffles along the loop. With baffles, a maximum mixing time of 50 seconds at a shaking rate of 50 rpm and an associated power input of 20 W/m^3 in a 50 L system with 70% filling volume was obtained. Larger filling volumes are more energy efficient and generally require a lower energy input to achieve similar mixing times, except at lower shaking rates, where it is likely that the added pressure from the additional water requires additional power input to generate a proper fluid flow. At lower fill volumes, the impact of baffles on the mixing time is inconsequential, however at larger fill volumes they reduce mixing times significantly. Kaiser et al. (2016b) point out that stirred tank reactors can achieve significantly shorter mixing times (below 20 seconds) at similar power inputs.

Horizontal Tubular Reactor

The mixing time in tubular loop reactors depends on the length of the loop, the power input (supplied by the liquid pump and gas aeration) and the reactor configuration itself (presence of baffles, verticality etc.). The mixing enhancement due to aeration is most impactful when the aeration is very high or when the liquid flow speed is very low. At high liquid flow speeds the contribution of the liquid flow to the mixing time outweighs that of aeration significantly.

Yazdian et al. (2009) used experimental data to generate a volume-normalized relationship between mixing time and the operating parameters of a typical horizontal tubular reactor. This is given as:

$$\frac{t_m}{V} = 1.17 U_G^{-0.40} \cdot U_L^{-0.56} \cdot \left(\frac{L}{D}\right)^{0.35} \cdot (1+S)^{-0.15}$$

Equation (2.21)

Where "t_m" is the mixing time in seconds, "V" is the system volume in m^3, "U_G" is the superficial gas velocity in m/s, "U_L" is the superficial liquid velocity in m/s, "L" is the length of the tube in metres, "D" is the tube inner diameter in metres and "S" is the ratio between the gas separator volume "V_s" to the bulk liquid volume "V_b". Yazdian et al. (2009) also provide a correlation for the determination of power input in tubular reactor systems in general (including horizontal and vertical forced circulation loop reactors in addition to standard external loop airlift reactors) as follows:

$$\left(\frac{P}{V_L}\right) = \left[\frac{Q_m \mathrm{RT}}{\mathrm{V_L}} \ln\left(1 + \frac{\rho_L g H_L}{P_{ts}}\right)\right] + \left[\frac{\Omega}{2V_L} Q_m v_0^2\right] + \left[\frac{Q_L}{2V_L} \rho_L U_L^2\right] + \left[\frac{\Delta P_s Q_L}{V_L}\right]$$

Equation (2.22)

Each square bracket in this correlation refers to a different source of power input. In order, these are the power input due to isothermal gas expansion, the kinetic energy of the injected gas, the kinetic energy of the liquid entering the reactor (if a pump is present) and finally the energy loss as a result of the sparger/static mixer present in the system. Q_m is the molar gas flow rate in kmol·s^{-1}, H_L is the liquid height in metres, P_{ts} is the pressure drop from the bottom to the top of the liquid in Pa, Ω is the efficiency factor associated with the pump, v_0 is the superficial gas velocity leaving the sparger in m·s^{-1}, Q_L is the volumetric liquid flow rate in m^3·h^{-1} and ΔP_s is the pressure drop across the sparger/static mixer in Pa.

Whilst these equations are rigorous, insufficient information is available for the generation of a general case mixing time/power input correlation as the pressure drop and volumetric liquid flow rate are both system specific.

2.3.2 Mass Transfer Coefficient vs Power Input

High Aspect Ratio Reactors

Stirred Tank Reactor

In the industrial production of Baker's Yeast, a highly aerobic process, three standard HAR reactors, the STR, BCR and ALR, have been considered. Currently, the most common reactor configuration is the BCR (Vieira et al., 2013; Bjarre and Risén, 2016), however examples of industrial scale systems making use of a STR (George et al., 1998) and ALR (El-Helow et al., 2015) are reported in literature. As has been showcased previously, this can largely be attributed to the superior mixing BC's exhibit at a large scale versus the simplicity of their construction. However, mixing performance alone is not enough a reason to decide between using any system, the mass transfer performance must be quantified.

For STR's, the relationship between power input and mass transfer coefficient differs depending on whether the system is currently being aerated. Aeration causes gas bubbles to form behind the impeller blades which reduces their effective power draw and input. The relationship between mass transfer and gassed power input is best defined with the following general equation as given by Van't Riet (1979):

$$k_L a = K\left(\frac{P_g}{V}\right)^{\alpha}(v_s)^{\beta} \qquad \text{Equation (2.23)}$$

Here, "K", "α" and "β" represent constants which are unique to every STR and their individual configuration/system conditions, "P_g" is the gassed power input in watts and "v_s" is the superficial gas velocity of the sparged air. The values of "α" and "β" range between 0.4-1 and 0-0.7 respectively whilst the value of K fluctuates greatly depending on the "α" and "β" but is generally an order of magnitude smaller than either of them. Depending on whether the system is highly ionic or not, the k_La can vary greatly, as demonstrated for single impeller systems by Van't Riet (1979) and presented in Figure 2.10.

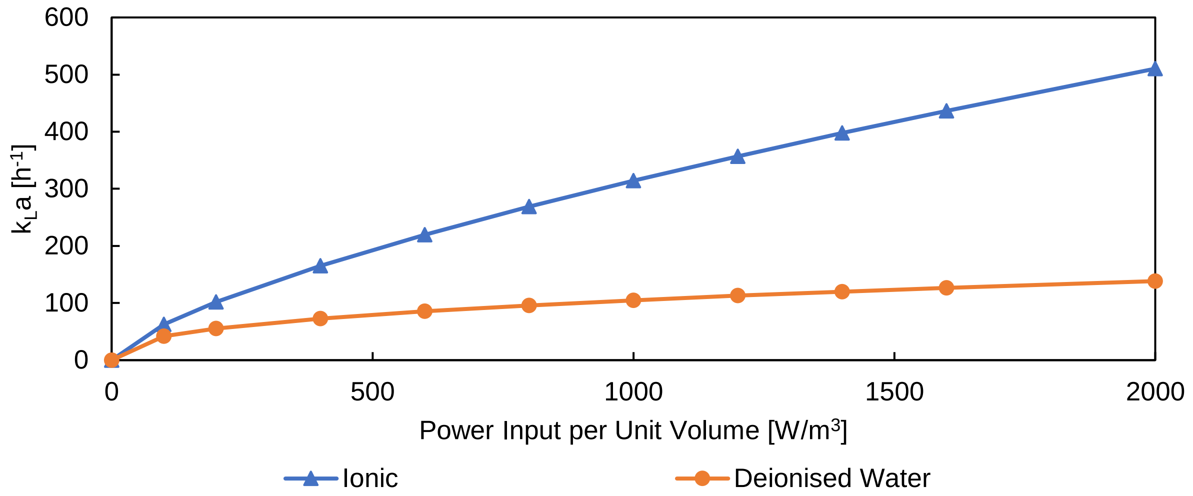

Figure 2.10 – STR power input vs observed k_La for ionic and pure water systems, correlation constants taken from Van't Riet (1979)

However, the accuracy of these correlations, as stated by Van't Riet (1979), is only between 20-40%. Resultantly, power input per unit volume on a system basis remains unpredictable until the specific ystem is individually tested. Figure 2.11 highlights these discrepancies by revealing how different STR correlations, all experimentally proven by different authors, can greatly differ.

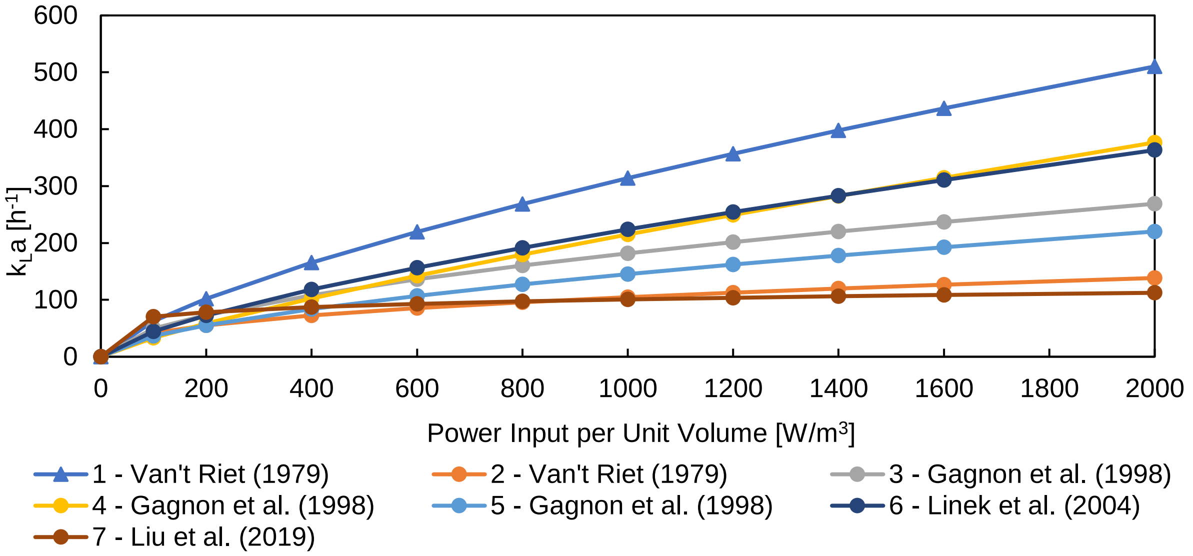

Figure 2.11 – Variation in observed k_La vs power input for different STR systems at $v_s = 0.005\ m/s$
Additional data on reactor configurations for each paper is presented in Table B.1

These discrepancies are due to the varying differences in reactor configuration available in the design of a STR, in addition to the medium being used, its viscosity and its density. These variances are listed in Table B.1 in the appendices. Of important note is the superficial gas velocity term in Equation (2.23), which is decoupled from the power input of the system. Generally speaking, the power consumption due to the pressure drop associated with the gas flow rate is neglected in power input calculations (Bouaifi et al., 2001). This is the case for the correlations presented in Figure 2.10 and Figure 2.11. However, to assume that the power consumption associated with the required compressor is negligible would be erroneous, as air compression is a significant expense in industrial cell culture (Harding, 2008). This cost, in addition to the prevalence of impeller flooding at elevated gas velocities, inhibits the aeration rate that a STR can feasibly be operated at.

Bubble Column and Airlift Bioreactors

The power input into bubble column and airlift bioreactors is entirely dependent on the gas flow rate into the system. The exact efficiency of this mass transfer is dependent on the reactor configuration. As a wide variety of different configurations are available, there are numerous correlations available in literature for the prediction of the mass transfer coefficient with rising power input. For bubble columns, these correlations typically take the following form as depicted in Equation (2.24)

$$k_L a = \alpha (v_s)^{\beta} \qquad \text{Equation (2.24)}$$

Where α and β are experimentally determined constants dependent on the specific conditions/configuration of a given bubble column. Power input correlations for airlift reactors differ in the inclusion of a downcomer to riser area ratio "$\frac{A_d}{A_r}$" where A_d is the area of the downcomer in m^2 and A_r is the area of the riser. A generic form of such a correlation is given in Equation (2.25):

$$k_L a = \alpha \left(1 + \frac{A_d}{A_r}\right)^{\beta} (v_s)^{\gamma} \qquad \text{Equation (2.25)}$$

One will note that neither of these correlations include the power input. This is because correlations associating the superficial gas velocity with the power input in airlift and bubble column reactors are readily available in literature (Chisti, 1989). For bubble columns, this correlation is given by:

$$\frac{P_G}{V_L} = \rho_L g v_s \qquad \text{Equation (2.26)}$$

Whilst for airlift reactors, this correlation is given by:

$$\frac{P_G}{V_L} = \frac{\rho_L g v_s}{1 + \frac{A_d}{A_r}} \qquad \text{Equation (2.27)}$$

Plotting the various correlations available in literature resulted in generation of Figure 2.12 and Figure 2.13 which showcase the varying mass transfer efficiencies of different bubble column and airlift bioreactors filled with non-viscous media as reported by different authors. Once again, it can be noted that significant variance in the expected performance is reported, largely because of differences in reactor configuration. These differences are detailed in both Table B.2 and Table B.3 in the appendices.

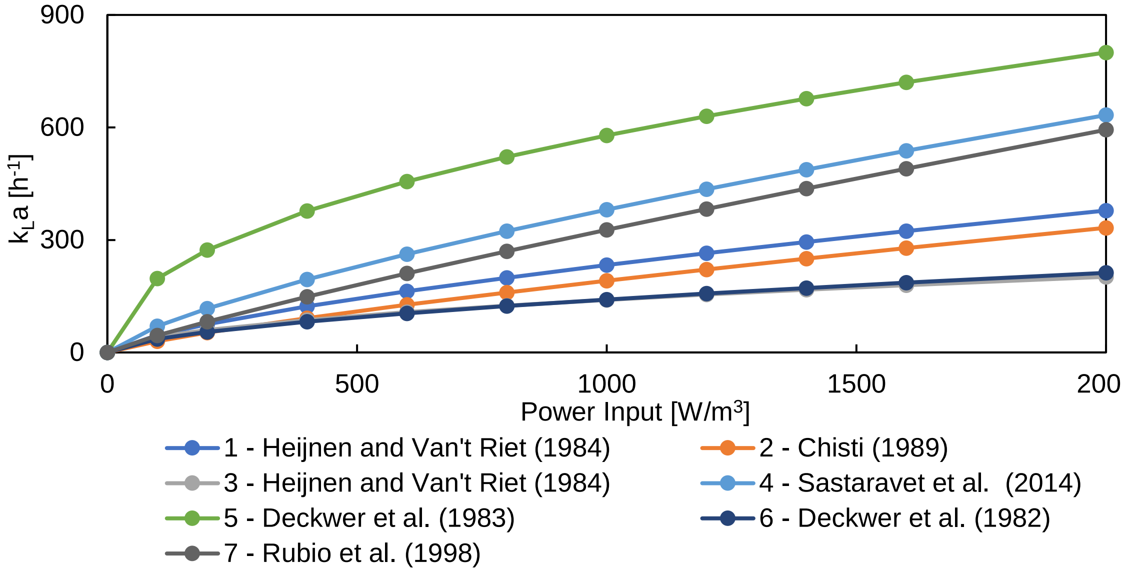

Figure 2.12 – k_La vs power input for BCR's using literature correlations
Additional data on reactor configurations for each paper is presented in Table B.2

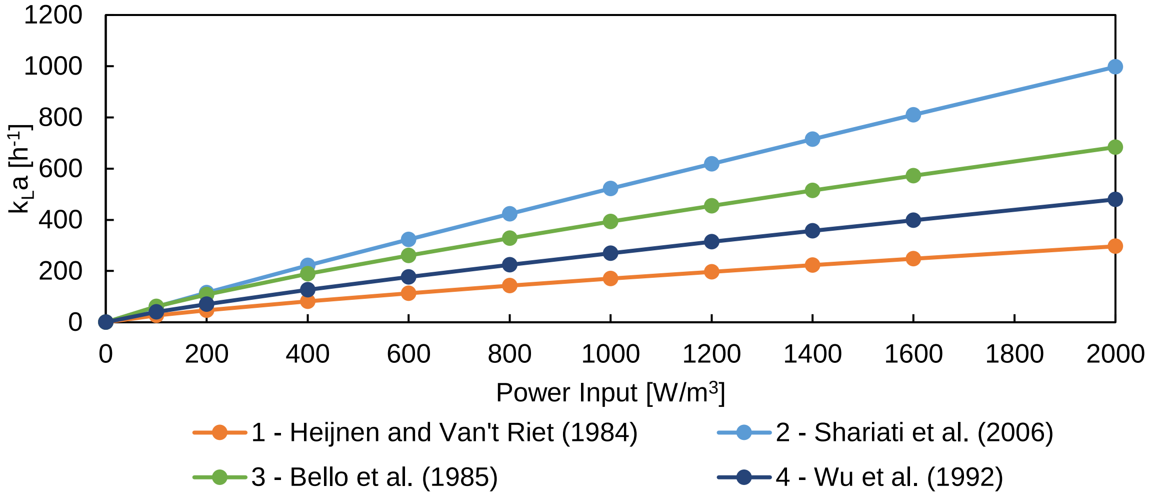

Figure 2.13 – k_La vs power input for ALR's using literature correlations
Additional data on reactor configurations for each paper is presented in Table B.3

To conclude which of these systems tends to be the most energy efficient according to the analysed literature, a mass transfer energy efficiency term is generated. This efficiency is given by the average gradient of these correlations and has units $m^3 \cdot h^{-1} \cdot W^{-1}$, with higher values indicating a higher efficiency. Alternatively, for singular points it is generated by dividing the k_La by the associated instantaneous power draw per unit volume. This metric is useful for comparison as it allows for mass transfer energy efficiency performance comparisons without having to consider the impact of oxygen concentration in the system. Hence this metric is affected exclusively by fluid hydrodynamics and the available contact surface area. This data is presented in Table 2.2 and clearly demonstrates that the highest energy efficiency in terms of achievable mass transfer among the conventional high aspect ratio reactors is enjoyed by airlift reactors.

Table 2.2 – Mass transfer energy efficiency comparison for vertical bioreactors

System	Mass Transfer Energy Efficiency	Units
STR	0.022 - 0.236	$m^3 \cdot h^{-1} \cdot W^{-1}$
BCR	0.084 - 0.317	$m^3 \cdot h^{-1} \cdot W^{-1}$
ALR	0.142 - 0.493	$m^3 \cdot h^{-1} \cdot W^{-1}$

Low Aspect Ratio Reactors

Orbital Shakers

The observed mass transfer energy efficiency for an orbital shaker is dependent on a variety of factors. These include the reactor configuration, operating parameters, and liquid properties. Whilst there is no singular defined relationship in literature correlating mass transfer and power input for orbital shakers, there are numerous correlations between mass transfer input and shaking speed (Klöckner and Büchs, 2012; Klöckner et al., 2013b; Zhu et al., 2020). In addition to shaking speed, these correlations require knowledge of the vessel diameter, total liquid volume, shaking diameter, gravitational acceleration, liquid kinematic viscosity, and the diffusivity of oxygen through the liquid medium at the operating temperature and pressure. Using the correlation between shaking speed and power input as described in Equation (2.20) in addition to assuming a 2 m^3 volume, 2 m diameter and assuming the liquid medium is pure water allowed for the generation of Figure 2.14.

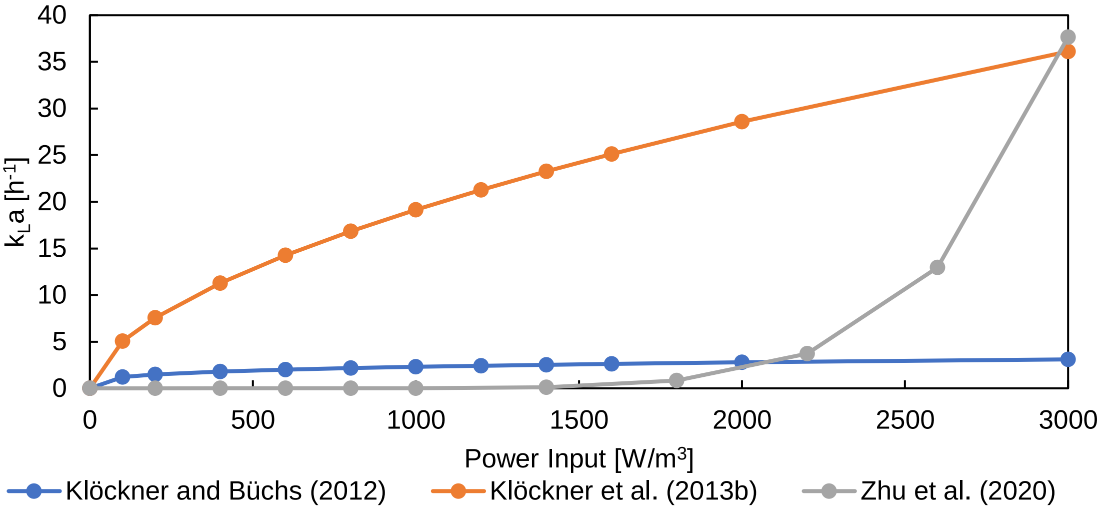

Figure 2.14 – k_La vs power input for orbitally shaken reactors

The large discrepancies in the appearance of these correlations highlights the difficulties in pinning down an exact correlation for these lesser-used systems. The differences observed in Figure 2.14 can at least in part be explained in that the correlation proposed by Klöckner and Büchs (2012) was originally intended for the prediction of mass transfer in shake flasks only. The cause for the large discrepancies found in the other two systems is however unknown, as both papers claim that the correlations are accurate for large (2 m^3) systems. In terms of mass transfer energy efficiency, the average is taken between 0 and 3000 W/m^3 for each correlation, which leaves us with a range of 0.001-0.013 $m^3 \cdot h^{-1} \cdot W^{-1}$. This range varies greatly as higher power inputs are reached according to the correlation by Zhu et al. (2020) which is an exponential function.

Wave Bag Bioreactors

Whilst the concept of the wave bioreactor is simple, there are still many variations of the design depending on the manufacturer. The expected mass transfer from such systems as a function of the associated power input can hence vary widely. Two papers were found in literature detailing the mass transfer energy efficiency as a function of the power input for typical wave bag bioreactors which tilt from side to side to generate turbulence (Jones et al., 2017; Bai et al., 2019). Only Bai et al. (2019) gave correlations for power input versus expected k_La, as Jones et al. (2017) only provide a range of power inputs and mass transfer coefficients, 10-71 h^{-1} at 64-633 W/m^3.The correlations from Bai et al. (2019) are exponential in nature, however the paper itself does not continue plotting points beyond 500 W/m^3 mark for the 8° rocking angle and 900 W/m^3 for the 12° rocking angle. This lack of data likely indicates real-world constraints with operating beyond these power-inputs negatively impacting reactor performance. A system that overcomes this issue is the Cell-tainer® wave bioreactor. Oosterhuis and van der Heiden (2010) specify mass transfers in 10 L Cell-tainer® systems attaining a maximum k_La of

750 h^{-1} at power inputs of 2800 W/m^3. The downside to this however is that the system is highly volume dependent, and this maximum drastically decreases as the volume increases, with a maximum of 300 h^{-1} being attainable in a 15 L system. As is demonstrated in Figure 2.15, the highest power efficiency is in the smaller standard wave bag reactor systems, however these are limited in how high a power input and volume they can handle. The resultant mass transfer power efficiencies however are high, with a range of 0.112 - 0.7421 $m^3 \cdot h^{-1} \cdot W^{-1}$.

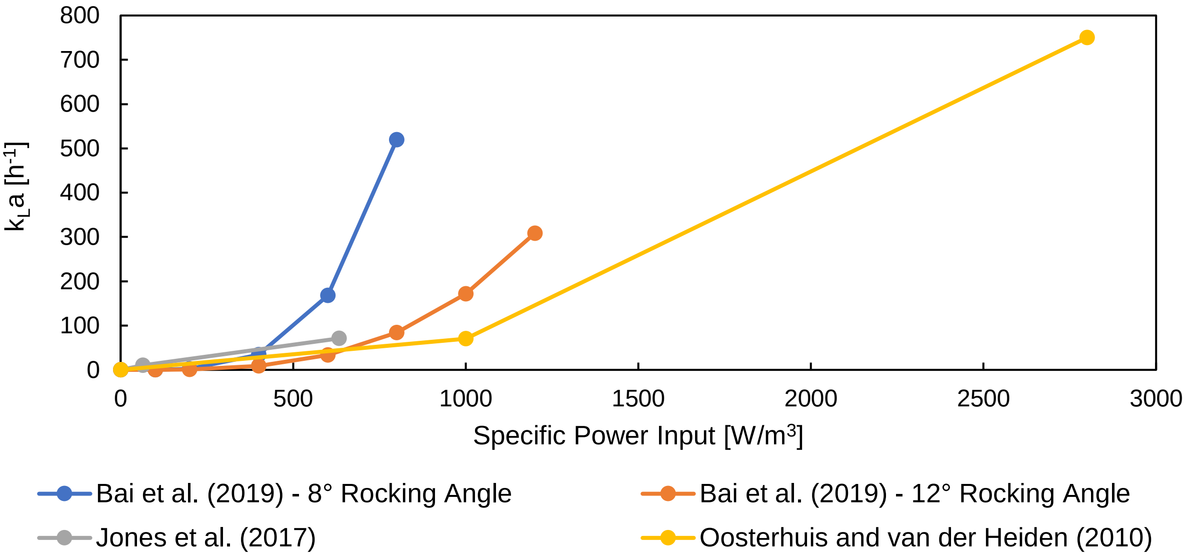

Figure 2.15 – k_La vs power input for wave bag bioreactors

Raceway Bioreactors

The mass transfer in raceway bioreactors is located primarily around the sump and paddlewheel, which makes up approximately 75% of the total mass transfer observed in raceway reactors (Barceló-Villalobos et al., 2018; Mendoza et al., 2013b). Correlations for the associated power input and observed mass transfer coefficient are given by Mendoza et al. (2013b) and differ depending on the diffuser type employed (bubble size and/or diffuser pressure drop). In their paper, the highest mass transfer coefficient attainable in the sump for their 20 m^3 system (of which the sump's volume is 0.2 m^3) was determined to be 150 h^{-1} with a power input of 1800 $W \cdot m^{-3}$. The highest mass transfer was found by the paddlewheel, but no correlation between power input and mass transfer for the paddlewheel is provided nor is any available in literature.

Literature specifies a typical range between 1.8 and 9.6 h^{-1} for the overall mass transfer coefficient (Barceló-Villalobos et al. (2018); Mendoza et al. (2013b)). However, no corresponding overall power consumption is specified for these ranges. It is mentioned that the power consumption and mass transfer performance is dependent on both the liquid velocity and the gas flow velocity in the sump. Barceló-Villalobos et al. (2018) give the overall power draw for their raceway reactor as between 4 W/m^3 for a system with no active gas flow and 13 W/m^3 for a system with an active sump. This is used in conjunction with the overall mass transfer range previously specified in the generation of Table 2.3 on the mass transfer energy efficiencies in raceway bioreactors.

It is interesting to note that whilst the efficiency of the sump is relatively low, the overall mass transfer energy efficiency in raceway bioreactors is exceptional. The flaw with this result is quickly evident, as the maximum attainable mass transfer coefficient is significantly too low for aerobic culture. Overcoming this limitation would hence be a highly promising direction for reactor design and speaks greatly of the potential of horizontal reactor systems.

Table 2.3 – Mass transfer energy efficiency in raceway bioreactors

Description	Mass Transfer Energy Efficiency	Units
Sump – Small Bubbles and High-Pressure Diffuser	0.039	$m^3 \cdot h^{-1} \cdot W^{-1}$
Sump – Small Bubbles and Low-Pressure Diffuser	0.082	$m^3 \cdot h^{-1} \cdot W^{-1}$
Sump – Medium Bubbles and Low-Pressure Diffuser	0.034	$m^3 \cdot h^{-1} \cdot W^{-1}$
Overall System	0.867	$m^3 \cdot h^{-1} \cdot W^{-1}$

Travelling Loop Bioreactor

This novel reactor design has very limited data available on its performance and no direct correlation for power input versus mass transfer coefficient has been published by the authors, although it is possible to construct one using the data published by Kaiser et al. (2016b). The derivation of such formulae can be found in (APPENDIX). Considering 15 L, 25 L and 35 L filling volumes resulted in the following correlations for the unbaffled and baffled systems respectively at shaking rates between 20 and 50 rpm:

$$Unbaffled: 0.295\left(\frac{P}{V}\right) + 2.6752 \mid R^2 = 0.9327 \qquad \text{Equation (2.28)}$$

$$Baffled: 0.286\left(\frac{P}{V}\right) + 8.3451 \mid R^2 = 0.7768 \qquad \text{Equation (2.29)}$$

These equations imply an efficiency between 0.286 and 0.295 $m^3 \cdot h^{-1} \cdot W^{-1}$ for the travelling loop bioreactor. It is important to note that whilst this efficiency is superior to that of a STR, it comes with caveats. Depending on the volume in the reactor, increasing the shaking rate causes the liquid to go “out of phase” which can potentially decrease or increase this power efficiency and the researchers were only able to attain a maximum power input of 82.2 W/m^3 and maximum k_La of 32 h^{-1}.

Horizontal Tubular Loop Bioreactor

Yazdian et al. (2009) provide a correlation for the attainable mass transfer in a horizontal tubular loop bioreactor with varying liquid and gas flow rates as follows:

$$k_L a_{O_2} = 1.25 U_G^{0.38} \cdot U_L^{1.06} \cdot \left(\frac{L}{D}\right)^{-0.69} \cdot (1+S)^{-0.025} \qquad \text{Equation (2.30)}$$

Other than indicating the elevated importance of the liquid flow velocity on the observed k_La over that of the gas flow velocity, this correlation is ultimately unhelpful. This is because it lacks a corresponding power input correlation. The authors do provide such a correlation (shown in Equation (2.22)), however they provide insufficient information for a reliable estimation to be made. Yazdian et al. (2009) do however compare the mass transfer energy efficiency for the different loop systems they test (vertical and horizonal forced circulation loop reactors and a standard external loop airlift reactor). The results of this analysis indicated that whilst the efficiency for a horizontal forced circulation system was superior to that found in a standard vertical external-loop airlift reactor, it was notably worse than that observed in the vertical forced-circulation loop bioreactor. The k_La across their range of tested parameters was between 5.14 h^{-1} and 52.3 h^{-1} for the horizontal tubular loop reactor, although it is important to note that the presence of static mixers in the system is not mentioned.

As an alternative resource, Al Taweel et al. (2012) instead mention that with static mixers present, k_La as high as 14 400 h^{-1} are obtainable at power inputs as low as 0.02 kW/tonne of media. Assuming a water medium this results in a power input of 20 W/m^3 to obtain an extremely high mass transfer coefficient and hence an efficiency of approximately 720 $m^3 \cdot h^{-1} \cdot W^{-1}$. Unfortunately, no additional information is available, and the reactor has disappointingly little literature available, indicating the need for additional research in this direction.

Conclusion

As has been detailed in this section, the mass transfer energy efficiency attainable in low aspect ratio reactors generally surpasses, or is similar to, that of even the best performing high aspect ratio reactors. The common trend however is that these systems are unable to reach the high volumes necessary to compete industrially (such is the case for the Cell-tainer®) or are unable to achieve high enough gas liquid mass transfer coefficients despite their high efficiency. Evidently, if a reactor is to be designed to replace the current industrial reactors both issues are critical although for aerobic culture the limited maximum mass transfer coefficient is likely the larger issue. To better explain why this is such an issue, an overview of a typical highly aerobic micro-organism, yeast, shall be provided.

2.4 Yeast as a Model Organism for Aerobic Culture

2.4.1 Overview

Yeasts have been used, unknowingly, since time immemorial in the production of breads and alcohol and were the very first micro-organisms to be produced on an industrial scale back in 1850 (Rosen, 1987). All yeasts are eukaryotic fungi and are well-known for the ease at which they can grow, which they can do either aerobically or anaerobically. The most prominent yeast is *Saccharomyces cerevisiae*, colloquially referred to as Baker's Yeast. It is the most produced micro-organism on the planet (Di Serio et al., 2001).

There are, however, several hundred different varieties and strains of yeast, each of which has their own unique growth characteristics which allow them to be utilised for a wide variety of industrial applications. Different species can metabolise a host of different substrates, maintain significantly different ideal operating conditions and enjoy higher tolerances to certain chemicals.

These differences can result in different oxygen requirements for sustained biological growth. A higher oxygen demand necessitates an increased mass transfer coefficient and hence the suitability of a given reactor system may be brought into question. A brief breakdown of the different oxygen utilisation rates of several yeast species at a constant growth rate of 0.1 h^{-1} is present in Table 2.4. It is important to note that depending on the phase of growth the yeast is in and several other factors, these values can fluctuate. Whilst it is not the highest, the relatively high OUR of *S. cerevisiae* in conjunction with the immense amount of literature available on it have led to its frequent usage as a model organism in aerobic systems and as such it is the micro-organism of choice for this study.

Table 2.4 – Oxygen utilisation rates for various yeast species, data from Hagman et al. (2014)

Yeast Species	**Oxygen Utilisation Rate [$\text{mmol.g}_{\text{dry weight}}^{-1}\cdot h^{-1}$]**
Saccharomyces cerevisiae	3.8 ± 0.3
Vanderwaltozyma polysporus	3.9
Torulaspora franciscae	2.5 ± 0.1
Lachancea waitii	3.3
Lachancea kluyverii	4.3 ± 0.3
Kluyveromyces lactis	4.3 ± 0.1
Kluyveromyces marxianus	1.5 ± 0.1
Eremothecium coryli	0.7 ± 0.1
Debaryomyces vanrijiae	1.9 ± 0.0
Pichia pastoris	1.9 ± 0.1

2.4.2 Growth Characteristics of Baker's Yeast

Perhaps the most important differentiating factor for yeasts is whether they are Crabtree positive or negative. The Crabtree effect details the tendency for certain yeast species to metabolise sugars via fermentation, even when air is in excess, if there is an oversupply of sugar available. This results in a significant decrease in biomass yield (Van Hoek et al., 1998). Continued ethanol production is additionally harmful to the growing yeast cells despite their resistance to it, and at concentrations equal to or above 4 vol% a notable decrease in growth rate can be observed (Piper et al., 1994). *S. cerevisiae* is a Crabtree positive yeast.

As a result of this, the optimal growth method for *S. cerevisiae* is to make use of either fed batch or continuous reactor operation as the sugar concentration in the system needs to be maintained below a critical value of 0.15 g/L glucose to avoid ethanol formation. The growth rate must also be restricted to prevent the Crabtree effect and hence the maximal growth rate attainable without activating the fermentative pathway is approximately 0.25 h^{-1}. This allows for an average dry biomass yield on glucose of 0.5 $g_{biomass}/g_{glucose}$ versus a Crabtree effect induced yield of 0.15 $g_{biomass}/g_{glucose}$ (Posten and Cooney, 1993). Batch cultivation can still be successfully performed however as the ethanol that is generated is later consumed at a relatively high growth rate of between 0.14-0.20 hr^{-1} with a yield between 0.6-0.7 $g_{biomass}/g_{ethanol}$ so long as the system is continuously aerated (Lievense and Lim, 1982).

2.4.3 Industrial Feed and Growth Conditions for Baker's Yeast

Bekatorou et al. (2006) provide a good overview of the contents of industrial media. The primary feeds are sourced from the sugar industry, specifically in the form of sugarcane- or/and beet-molasses which act as both a carbon and energy source for the growing yeast cells. This molasses typically contains between 40-55% fermentable sugars and 40% non-fermentable substances. The non-fermentable substances are eventually rejected and typically constitute a major source of pollution from the yeast production process. In addition to sugars, several vitamins and trace elements are required for effective cell growth. These include nitrogen, phosphate, magnesium, calcium, iron, zinc, copper, manganese and (as a source of vitamins) biotin. In industry and in laboratory practice it is well reported that the optimum temperature for the cultivation of *S. cerevisiae* biomass is 30 °C whilst the commonly reported pH is in the range of 4.5 and 5.0.

2.4.4 Mass Transfer Requirements for Baker's Yeast Production

To determine preliminary feasibility of an aerobic reactor configuration for the growth of a given micro-organism, it is beneficial to determine the minimum required oxygen transfer rate to sustain the expected growth. The minimum required oxygen transfer rate (OTR) is defined as being equal to the oxygen utilisation rate (OUR) of the micro-organism at any given point in time. Hence the OUR can be expressed as follows:

$$OUR = OTR = -k_L a\,(C_L^* - C_L) \qquad \text{Equation (2.31)}$$

Where C_L^* is the saturated oxygen concentration in the medium C_L is the current oxygen concentration in the medium, both in grams of oxygen per litre. To determine the k_La as a result of an increase in biomass, one needs to relate the biomass growth rate to the oxygen utilisation rate. The growth of a given micro-organism is given as follows:

$$Biomass\ Growth\ Rate = \mu X \qquad \text{Equation (2.32)}$$

Where X is the dry biomass weight in grams per litre and μ is the specific growth rate in h^{-1}. This growth rate can additionally be expressed as the product of the OUR (in $g_{oxygen}/L\cdot h$) and the biomass yield on oxygen ($g_{biomass}/g_{oxygen}$):

$$\mu X = OUR \cdot Y_{\frac{x}{o}} = -k_L a (C_L^* - C_L) \cdot Y_{\frac{x}{o}} \qquad \text{Equation (2.33)}$$

Rearranging the formula to make $k_L a$ the subject and setting C_L to zero to simulate the maximum potential concentration gradient between the liquid and air supply results in the following correlation for the minimum mass transfer coefficient required to sustain yeast growth at a given dry weight and growth rate:

$$k_L a_{min} = \left(\frac{\mu X}{C_L^* \cdot Y_{\frac{x}{o}}} \right) \qquad \text{Equation (2.34)}$$

As previously mentioned for *S. cerevisiae*, the maximum viable growth rate without causing the Crabtree effect (0.25 h^{-1}) is regarded as the maximum growth rate one would aim to achieve. The yield on oxygen is given by Nagai (1979) as 0.97 $g_{biomass}/g_{oxygen}$. Making use of a fixed dry mass concentration, the final unknown is the saturated oxygen concentration, C_L^*. For a water system at 30 °C this value is given by Doran (2013b) as 8.05 mg/L. These values lead to the generation of Figure 2.16.

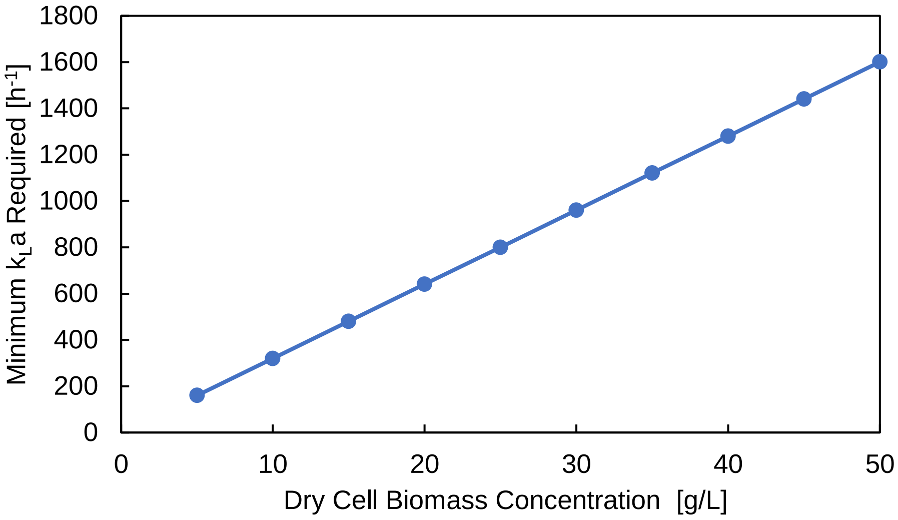

Figure 2.16 – Relationship Between Minimum k_La Required and Dry Yeast Cell Biomass at $\mu = 0.25\ h^{-1}$

Figure 2.16 represents the absolute minimum k_La required to support the maximal growth rate (while avoiding oxygen limitation) at any point in time and does not take into consideration the reduction in oxygen solubility typically observed in fermentation media. It additionally does not consider the critical oxygen limit which needs to be avoided in any industrial fermentation to ensure the system remains fully aerobic. For Baker's Yeast production DO is typically kept above 15% of the saturated oxygen value (Di Serio et al., 2003). As a result, the actual k_La demand at any given biomass concentration for this growth rate will be higher than the trend shown in Figure 2.16. Referring to Section 2.3.2, this exceeds the k_La ranges of many bioreactors and is hence why oxygen is considered the limiting component in most industrial operations. Therefore, a feeding strategy that limits the glucose supply and hence restricts the growth rate as the biomass concentration increases is generally effective. Industrially, a combination of feeding profiles and reactor configurations are used to grow Baker's Yeast.

2.4.5 Typical Industrial Reactor Configurations for Baker's Yeast Production

The industrial fermentation process for *S. cerevisiae* production is very well-defined (Bekatorou et al. (2006); Di Serio et al. (2001)). An overview of this process is given in Figure 2.17. The general process involves a series of reactors, starting with a pure cell culture that is prepared in a laboratory. The first fermentation is typically an anaerobic batch process focused on growing as much biomass as possible as quickly as possible (despite the low yield as this is still a small cultivation at this stage). Each stage after the initial batch phase implements increasing volume and aeration, which reaches a maximum in the Trade Fermenter.

The exact reactor configuration for each of the steps demonstrated in Figure 2.17 will differ depending on the exact choices of the engineering team behind the industrial plant although, generally, the larger vessels are either BCR’s or ALR’s owing to the superior mixing and mass transfer energy efficiency at high volumes.

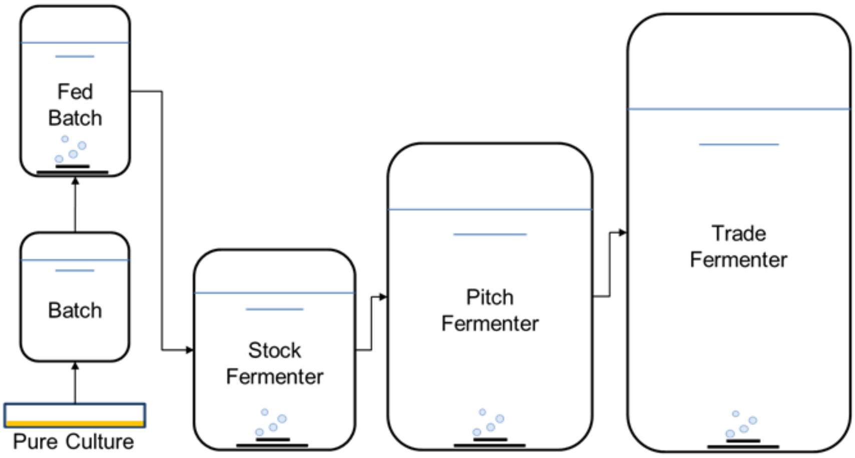

Figure 2.17 – Typical Industrial Yeast Fermentation Pathway adapted from Bekatorou et al. (2006)

It is interesting to note that as each fermenter is dealing with a unique final mass of yeast, the oxygen requirements will be different at each step of the chain. As a result, reactors with a low maximum k_La (but higher mass transfer energy efficiency) could potentially be used to replace some of the smaller systems/earlier steps displayed in Figure 2.17.

2.5 Concluding Remarks

Contained within this literature review, an overview of the fundamentals of mass transfer in conjunction with reactor overviews has provided an understanding of how mass transfer occurs and how best to optimise it in each reactor configuration. Performance assessments of existing HAR and LAR reactors in terms of gas-liquid mass transfer, mixing time and power efficiency have provided a useful tool for comparing reactors so that their advantages and disadvantages can be better interpreted and applied to the design of the novel reactor. Finally, an overview of the industrial production of Baker’s Yeast (the model organism for this study) has provided insight into the various performance criteria that the novel reactor will have to meet to sustain aerobic culture. This information has provided an important baseline for the design and later assessment of the novel reactor.

3 Project Definition

3.1 Problem Statement

As revealed through the literature review, despite their high energy requirements, there are still two key benefits to HAR reactors that LAR reactors need to meet before any meaningful replacement of these systems can occur on an industrial scale, these being the maximum attainable mass transfer rate and system scalability. The challenge in overcoming these criteria can be directly correlated with the hydrodynamics of low-aspect-ratio reactors. As the size or power-input increases the performance efficiency begins to deteriorate due to changing system hydrodynamics. Additionally, the system needs to be capable of a short mixing time to ensure sufficient nutrient transfer is provided support the rapid growth of aerobic cultures. Hence, a novel reactor is to be proposed with three key aspects in mind:

1) The system requires a high potential for mass transfer whilst maintaining the high energy efficiency low-aspect-ratio reactors are known for.

2) The system needs to be easy to scale, this will aid in the transition from laboratory-scale to industrial scale in addition to ensuring that performance is maintained across different scales.

3) The system needs to be capable of providing adequate mixing to support a high cell-growth rate.

The objective of this Master’s dissertation lies in attempting to realise a system capable of meeting all three of these criteria. To this end an initial design potentially capable of covering all three key aspects is proposed, making use of the information present in the literature review to inform the design. A preliminary system has been constructed and its performance in terms of all three criteria assessed.

3.2 Hypothesis

It is hypothesised that the novel LAR reactor will prove to have a higher mass transfer energy efficiency than that found in generic HAR reactors used in industry, owing to removing the need to introduce the air against a high-pressure head typical in HAR reactors. Further, by careful sparger and fluid flow design, the gas liquid mass transfer rate is maintained sufficient to support high aerobic growth rates in the novel LAR reactor, but not to exceed those in HAR reactors.

3.3 Key Questions

- Which LAR reactor design lends itself best to energy efficient oxygen mass transfer?
- Which LAR reactor design lends itself best to reliable scalability?
- What modifications can be imposed to existing LAR reactors to improve their gas-liquid mass transfer and mixing performance?
- Can the designed LAR reactor provide a sufficient OTR such that fed-batch aerobic biomass growth can be supported?
- Will the designed LAR reactor have superior energy efficiency and scalability over existing LAR reactor designs?
- Would the performance of such a system change over cultivation time as the physicochemical conditions of the microbial culture suspension changes?
- How would the mixing and gas-liquid mass transfer performance of this LAR reactor compare to typical HAR reactors?

4 Research Approach, STR Methods and Methodology

4.1 Experimental Approach to Research

The experimental work done for this dissertation was broken up into two key segments. The first consisted of background experimental work. To have a baseline with which to compare the designed reactor, the following experimentally verified information was sought: the mass transfer performance as a function of power input of the STR as the most commonly used HAR reactors discussed in the literature review, growth data and oxygen demand from a *S. cerevisiae* fed-batch growth cycle and the change in rheological properties of the microbial culture over time (viscosity and density). The HAR chosen was a STR, owing to its prevalence in both industry and laboratory studies. Using this information, a comparison of mass transfer energy efficiency and capacity between the HAR reactor and the designed reactor could be made. Data obtained from the fed-batch growth would indicate suitability of the designed reactor towards aerobic culture and determine the extreme oxygen transfer rate requirements of production of dense aerobic cultures. Rheological data would give the required operating range for the growing microbial suspension. If performance of the designed reactor remained consistent at similar rheological conditions to those found in the fed-batch growth in the HAR reactor, it could be implied that the reactor’s performance would be stable for the duration of a typical fermentation.

The second segment of experimental research consisted of the reactor design itself and the experimental testing of the chosen design in terms of the necessary performance indicators. This is explained in detail in Chapter 6. Here the experimental work included determination of k_La, mixing time and circulation time. These were performed under varying operating conditions to explore various design aspects for the purpose of prototyping and analysis of the reactor, in addition to generating comparable metrics for the system. Microbial growth experiments were not performed in the novel reactor.

4.2 STR Methodology, Materials and Methods

4.2.1 Reactor Description

Stirred tank reactor experiments including batch growth, fed-batch growth and k_La experiments were all conducted in a 14 L New Brunswick BioFlo 110 Fermenter with a maximum working volume of 10.5 L. The design of the reactor matches that shown in Figure 2.3. The reactor was 0.61 m high, with a diameter of 0.29 m. A dual-Rushton impeller system was employed in the reactor. Each of the six blades had a length of 2.3 cm, height of 1.7 cm and thickness of 1.25 cm. The default blade positions were 235 mm from the headplate for the upper impeller and 305 mm from headplate for the lower impeller. The impeller shaft had a length of approximately 0.39 m.

A ring sparger was located directly below the impeller blades, with five equidistant holes of approximately 1 mm diameter, spaced approximately 2 cm apart. An Ingold polarographic electrode was used for the DO detection, whilst pH was detected using an Ingold gel-filled pH probe. The motor was attached to the impeller shaft at the top of the reactor and supports an agitation range of 50-1200 rpm. An air outlet fitted with an ethylene glycol-cooled condenser was also located at the top. Ethylene glycol fed via an external chiller was used for reactor cooling. The air outlet was kept sterile via the use of a vent filter. The pH in the medium was maintained via a controller unit. It was monitored using an in situ probe and adjusted through automated titration of 12.5% ammonium hydroxide.

For the fed-batch experiments, feeding of the concentration feed solution was done using a peristaltic pump for which the calibration curve generated is shown in Figure 4.1 so that the feed rate could be manually adjusted in accordance with the calculated feeding profile, found in the Fed-Batch Feeding Profile and Cell Growth Predictions sub-section. To heat the reactor and aid with temperature control, an external heating jacket, connected to the control unit for automated control, was used.

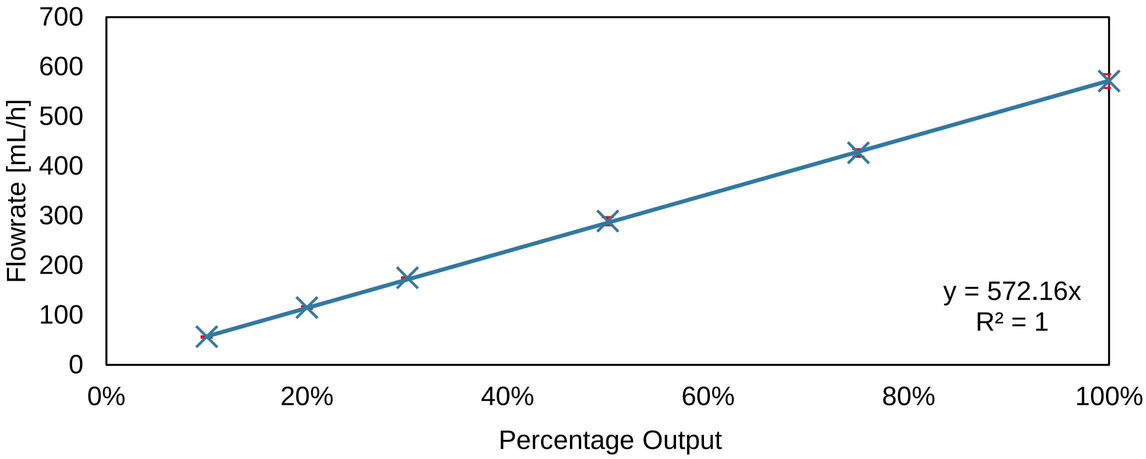

Figure 4.1 – Peristaltic pump calibration curve

4.2.2 k_La Measurement Techniques

Response Time Measurement - STR

Prior to any k_La experiments, the response time of the STR's DO probe needed to be established. This was determined by filling a beaker with a saturated sodium sulphite solution which was prepared to act as a "zero" for the experiment. The STR was then aerated at a flow rate of 1 vvm at a volume of 10 L and agitation was enabled at a speed of 800 rpm. The DO probe was then placed in the sodium sulphite solution until a reading of zero was noted on the measuring device whereupon the DO probe's zero was calibrated. Once 10 minutes had passed, the probe was moved to the aerated reactor and left for another 10 minutes after which the DO probe's saturated DO concentration was calibrated. The DO probe was then returned to the sodium sulphite solution and left until a zero value was noted. The DO probe was then shifted to the reactor and a timer was simultaneously started on entry. This timer was stopped once the DO reached 63.2% of the saturated DO value and the value was recorded. The experiment was then repeated twice more in order to determine the probe response time, which was found to be 5.9 seconds.

Baseline k_La Measurement - STR

Experiments in a pure water system served as an important baseline. Determination of the k_La in the STR needed to consider the response time of the DO probe as for highly aerobic conditions a response time of 5.9 seconds is too high to be ignored. As k_La can be expected to change when dealing with media as opposed to pure water, a similar baseline was established for sterile media for comparison to the pure water system. In testing the k_La, the following method was employed:

For the first baseline measurement, an STR volume of 6 L water was investigated. Additional experiments were performed at 7 L, 8 L, 9 L and 10 L for a comprehensive understanding of the mass transfer at all volumes. Once the STR was filled, agitation was initiated at a speed of 400 rpm. The STR was then sparged with nitrogen gas to calibrate a zero for the DO probe. Once the zero had been set, the STR was then aerated until the DO stopped increasing, and this value was calibrated as the saturation point. The STR was sparged with nitrogen again until the DO valued reached 0%. At this point, the set-up was now ready for the experiment to take place. The experiments began at an aeration rate of 1 vvm, with a timer being started in tandem with the air flow. Due to lack of an automatic logging system, the DO percentage versus time was manually recorded. Once the DO reached the saturation point, the experiment was terminated, and airflow cut off. Each experiment was repeated in triplicate for reliability, for every volume tested. Additionally, agitations rates of 600 rpm and 800 rpm were tested.

Once the baseline for the water system had been established via the above experimental method, the same process was repeated for sterile media, owing to changes in rheological properties from water versus the prepared media. All DO and time results were then used to determine the k_La via the application of both Equation (2.13) and Equation (2.18) in a Microsoft Excel spreadsheet.

Growing Systems - STR

Mass transfer experiments in the growing system took place during fed-batch operation, hence the mass transfer coefficient could be simultaneously inferred both experimentally and from the growth rate data obtained. The process involved first recording the STR's agitation rate and current volume. At this point the STR's agitation rate control was turned off and the motor powered down. Simultaneously, the supply of air was cut off and a timer was started. This enabled the determination of the OUR by recording the DO% as the DO decreased in 5 second intervals. Once the DO reached approximately 30%, measurement was paused and both aeration and agitation (at their previous rates) restarted to avoid reaching the critical oxygen concentration. The timer was then reset such that recordings could be made in 5 second intervals as the DO increased. Once the DO stopped increasing, measurements were no longer taken.

These experiments were carried out at approximately 2 hour intervals during the reactor run between sample collection and other experiments. The experiments were stopped once oxygen demand was sufficiently high in the reactor that the DO could not be maintained comfortably above the critical DO limit of 15%. The k_La was determined from the data using two different methods such that a comparison could be made. The first as proposed by Tribe, Briens and Margaritis (1995) entailed use of a solver and is described in the Dynamic Method sub-section of the literature review. The second, also described in the Dynamic Method sub-section, made use of Equation (2.12) and Equation (2.18).

Post Fed-Batch - STR

Additional mass transfer experiments were performed post-fermentation for all runs excluding the first STR run, which ended prematurely. The exact method employed varied across runs owing to changes in the desired results and ongoing discussion at the time.

For STR run 2, and all STR runs, the final volume at the end of the run was recorded before any additional experimentation was performed. As the system was still respiring, the method as described in the Growing Systems - STR section was employed except with a few altercations. Rather than noting the current agitation rate, the agitation rate was manually set 800 rpm for the first experiment, then 400 rpm for the second experiment. These experiments were performed in duplicate. Afterwards, 30% of the reactor volume was drained and then the 800 rpm and 400 rpm experiments were repeated once again. The system was then filled to the 10 L mark to dilute the system (altering the rheological properties of the medium), at which point the process was once again repeated.

For STR run 3, as with the previous run, the system was still respiring on conclusion of the experiment. For these mass transfer experiments, only an agitation rate of 800 rpm was tested, and a total of two standard k_La experiments were performed before 1.5 L of media were removed from the system. At this point an additional two experiments were performed and a further 1.5 L of media removed. Two final mass transfer experiments were then performed before the run was considered entirely concluded.

For STR run 4, once again, respiration was still ongoing despite no additional media having been added. No dilutions or draining took place once the initial fed-batch run had ended. Instead, the k_La experiments were performed at the recorded final volume at agitation rates of 400 rpm, 600 rpm and 800 rpm. Each agitation rate was investigated in duplicate.

Finally, for STR run 5, to attempt to neutralise the respiration of the cells, the reactor was heated to 60 °C using the heating jacket for a period of 30 minutes. The k_La determination method as described in the Baseline k_La Measurement - STR sub-section was then employed, with a few changes. As the final reactor volume was not equal to 10 L, the reactor was topped off with deionised water. At this point the viscosity and density of the liquid were experimentally determined. Volumes of 10 L, 8 L and 6 L were investigated, with the reactor being drained between volume tests. Once the 6 L experiments concluded, the system was topped off back to 10 L with additional deionised water and the viscosity and density once again determined. At this point the experimental procedure was repeated. One final dilution was made after this, and again the same procedure was employed.

4.2.3 Power Input Measurement

To determine the ungassed power input into the STR, the method described by Doran (2013b) was employed. This required use of Equation (4.1):

$$P = N_p \rho N^3 D^5 \qquad \text{Equation (4.1)}$$

where "P" is the ungassed power input in watts, "N_p" is the dimensionless power number of the reactor, calculated as a function of the Reynold's number and multiplied by a factor of two for the two-impeller system, "N" is the impeller rotational speed in rotations per second and "D" is the impeller diameter in meters.

Power draw by the impeller decreases with aeration (Doran, 2013b), hence for all aerated experiments the gassed power input needs to be calculated instead. Following the method as described by Michel and Miller, (1962), the gassed power input was determined using Equation (4.2):

$$P_g = 0.706 \left(\frac{P^2 N D^3}{Q^{0.56}} \right)^{0.45} \qquad \text{Equation (4.2)}$$

where "P_g" is the gassed power input in watts and "Q" is volumetric flow rate of air in m^3/s. In addition to this gassed power calculation, the power input due to aeration was considered. This was calculated as specified by Doran, (2013b) using Equation (4.3):

$$P_a = \rho g h \cdot Q \qquad \text{Equation (4.3)}$$

where "P_a" is the power draw due to aeration and "h" is the reactor height in meters. The sum of the gassed power input and power draw due to aeration divided by the total volume in the reactor gave the total power input per unit volume at a given moment.

4.2.4 Yeast Fermentation

The yeast fermentation experiments required a substantial amount of planning and research. This work can be divided into five segments: feeding profile, inoculation procedure, media preparation, reactor operation and analytical techniques. A total of 5 full fed-batch STR runs were completed.

Fed-Batch Feeding Profile and Cell Growth Predictions

The fed-batch feeding profile was generated via a combination of literature research and trial and error. The inspiration for this plan was found in a paper by Gueguim Kana et al. (2007). The feeding plan for each STR run used required the manual setting of the desired cell growth rate at every hour and a targeted final cell concentration. Using this cellular growth rate, the new total dry mass of cells within the next hour could be predicted. This information could also be used to predict the expected cellular productivity by dividing the generated mass by the elapsed time. This would be repeated for every hour until the target final biomass concentration was reached. Assuming an optimal growth yield of 0.5 $g_{biomass}/g_{glucose}$ allowed for the predicting of the required mass of glucose to be added within the 1 hour timeframe to support the targeted growth rate. A growth rate of 0.20 h^{-1} was chosen as the experiment's maximum growth rate. This placed it comfortably below the threshold for the Crabtree effect (0.25 h^{-1}). For the first STR run, no final cell density was targeted, only a constant growth rate 0.19 h^{-1}. For the second and third runs, a final density of 50 g/L was targeted and for the fourth and fifth runs a density of 60 g/L was targeted. Literature indicates that the maximum growth rate cannot be maintained as an exponential increase in cell density causes a similar increase in oxygen demand. Instead, the minimum k_La requirements for each hour of operation were calculated using Equation (2.34) and the growth rates in the feeding plan were altered to ensure the OUR did not exceed the OTR (this was not the case for the first and second STR runs). In the third run, data obtained from the baseline experiments was to be used to determine the k_La thresholds. However, this was found to be an underestimate, discussed later in Chapter 5, and instead thresholds as determined from the first two runs were used for the final three STR runs. These thresholds were implemented into the feeding profile by using a solver to ensure that the growth rate in conjunction with the dry biomass did not result in a minimum k_La demand that exceeded the planned thresholds at every hourly period.

Once the final predicted cell density had been reached via the hourly calculation, the total mass of glucose was summed. This mass of glucose had to be dissolved in a reservoir along with various supplementary nutrients, the composition and making of which is detailed in the Media Composition and Preparation sub-section. The concentration of glucose in the final media was used to determine the volume of media that needed to be fed every hour. The feed rate could then be adjusted via use of the calibration curve (depicted in Figure 4.1).

Inoculation Procedure

Inoculation of the reactor prior to the fed-batch run was a four-step process. This consisted of plating, a pre-inoculum, an inoculum and then a batch growth cycle wherein the target starting biomass cell concentration would be reached.

An *S. cerevisiae* sample was taken from cold storage and aseptically spread upon three petri dishes in a fume hood. Whilst only one plate was required, the additional plates served as back-ups in case of contamination. The plates were then moved to a 30 °C room for a period of 72 hours to allow for colony growth. Once 48 hours had passed, the media for the pre-inoculum was prepared. The pre-inoculum consisted of two 250 mL Erlenmeyer flasks with a final volume of 15 mL each. Once the *S. cerevisiae* plates were ready, a single *S. cerevisiae* colony from one of the plates was added to each flask. The flasks were then placed on a shaker rotating at 120 rpm in a 30 °C room for 24 hours. After the 24 hours, the pre-inoculum was then transferred to the two inoculum flasks which comprised a total volume of 150 mL each. These flasks were then put in the 30 °C room for 24 hours. The inoculation flasks were then transferred to the prepared STR and a batch growth cycle was initiated. The cycle for each run lasted approximately 10.5 hours and targeted an approximate starting cell density of 3.5 g/L for the fed-batch growth phase.

A batch growth run was a necessary precursor to the running of fed-batch experiments as this would allow for the timing of the batch growth cycle. The reactor could then be started in batch overnight, allowing for the culture to reach a target concentration before fed-batch operation began in the morning.

Media Composition and Preparation

Two different media compositions were used in the STR experiments. The first was yeast peptone dextrose (YPD) media. The composition of this media can be described as follows:

- 10 g/L glucose
- 5 g/L peptone
- 3 g/L yeast extract
- 3 g/L malt extract

This was used for its high accessibility and ease of use in the preparation of *S. cerevisiae* agar plates and the reactor pre-inoculum. The media is prepared depending on the volume required in accordance with the above compositions. The exact preparation procedure used differs depending on whether the YPD is for use in petri dishes or as pre-inoculum. For petri dishes, an additional 15 g/L of agar powder are added to the mixture in a Schott bottle. The Schott bottle is then autoclaved and left to cool, following which the mixture is aseptically poured into the petri dishes in a fume hood. They are then allowed to set in the fume hood before being used/stored. For the pre-inoculum, the peptone, yeast extract and malt extract were dissolved in 14.25 mL of de-ionised water in an Erlenmeyer flask then autoclaved. Glucose had to be autoclaved separately to avoid the Maillard reaction. Hence, 100 mL of a 200 g/L glucose solution were prepared in a 500 mL Schott bottle. 0.75 mL of this solution were then added to the Erlenmeyer flasks just before they were inoculated.

For the inoculum and STR, complex YPD media was replaced with a minimal media adapted from O'Connor et al. (1992). The composition is presented in Table 4.1. The decision to use this media in particular was made on the basis that all the chemicals constituents were readily available in the laboratory, in addition to finding its use in the work of different authors (Gueguim Kana et al., 2007; Ejiofor et al., 1994). Furthermore, the media does not include fermentable sugars by default. Hence, it was possible to modify the media to have a custom initial glucose concentration depending on the needs of the experiment.

The media consisted of three components: a mineral salts medium, a trace salt solution, and a supplement solution. Preparation of the trace salt and supplement solutions was identical for both the inoculum, batch phase and feed reservoir. The solutions had to be prepared and sterilised separately to the bulk of the mineral salts medium to prevent precipitation of the dissolved metals. To this extent, these solutions were each prepared in 250 mL Schott bottles in a bulk quantity (100 mL) and at 10 times the concentration to speed up later mineral salts medium preparation. In order aid dissolution, 1M H_2SO_4 was added via pipette 1 drop at a time to both solutions until the metals were completely dissolved.

Preparation of the mineral salts medium differed depending on its usage case. As with the pre-inoculum, glucose could not be added until after sterilisation of the bulk media to avoid the Maillard reaction. To prepare the inoculum, the following procedure was followed:

First, 250 mL of a 1.5 times concentrated version of the mineral salts medium was prepared in a 250 mL volumetric cylinder, excluding any of the trace salt solution, supplement solution and glucose. 100 mL of this solution were then decanted into each of two 1 L Erlenmeyer flasks. The solution was then diluted in each flask with 19.55 mL of deionised water. And the flasks sealed and autoclaved. Prior to transferring of the pre-inoculum to the inoculum flasks, 0.30 mL of the concentrated trace salt solution were injected into each flask using a 0.22 µm cellulose syringe filter, in addition to 0.15 mL of the concentrated supplement solution and 15 mL of the previously prepared 200 g/L glucose solution.15 mL of pre-inoculum were then transferred to the Erlenmeyer flasks for a total volume of 150 mL in each flask.

For the batch phase of the reactor the following procedure was followed instead:

A 6 times concentration of the mineral salts solution was prepared in a 1 L volumetric flask then transferred into the STR, at which point 4 432 mL of deionised water were then added to dilute the solution. Once this was done, 250 mL of a 120 g/L glucose solution were prepared in a 500 mL Erlenmeyer flask with a rubber tube attached targeting a batch phase glucose concentration of 5 g/L in the STR. The STR was then sealed and autoclaved along with the separate glucose solution. Prior to the commencement of reactor operation, 12 mL of the concentrated salt solution and 6 mL of the concentrated supplement solution were injected using a 0.22 µm cellulose syringe filter into the STR. At this point, the glucose was then aseptically added to the STR via a feeding port using the attached tube. Both 150 mL inoculum flasks were then poured into the STR to make up the final starting volume of 6 L and commence the experiment.

For the feed reservoir the mass of glucose required by the fed-batch run, as previously calculated, needed to be dissolved in a 4 L reservoir. This mass differed for each run depending on the growth plan utilised. Using a higher feed volume than 4 L would cause the 11 L STR to overflow during operation. Additional nutrients would also need to be provided to ensure that no nutrient would be limiting. The feed reservoir included a concentrated variant of the mineral salts medium. The mass of chemical/volume of solution required to fill a 10 L reactor (the target final volume of the STR) was condensed into a 4 L volume. A mass balance was performed to ensure that nitrogen would not be limiting, and an ammonium hydroxide solution was used for pH control in order to provide an additional nitrogen source. The process of making the reservoir itself was as follows:

The required mass of glucose was weighed and added to a 5 L Schott bottle, after which 3 L of de-ionised water were added to the Schott bottle. The bottle was then closed and placed in a warm water bath, at which point it was swirled repeatedly to aid in the dissolution of the glucose. Separately to this, a 10 times concentration of the mineral salts medium solution was prepared in a 1 L volumetric flask (excluding the trace salt and supplement solutions) and transferred to a 2 L Schott bottle. Both the concentrated mineral salts medium and glucose solution were then autoclaved. Once autoclaved, the contents of the 2 L Schott bottle were aseptically added to the 5 L Schott bottle. 20 mL of concentrated trace salt solution and 10 mL of supplement solution were then both filtered into the feed reservoir. Additionally, three 2 mL Eppendorf tubes were filled from the completed reservoir and placed in a freezer for later HPLC analysis to confirm the initial glucose concentration.

Table 4.1 – Media composition for STR fed-batch operation growing *S. cerevisiae*

Component	Chemical Name	Concentration	Units
Mineral Salts Medium	Ammonium Sulphate	10	g/L
	Potassium Dihydrogen Phosphate	5	g/L
	Calcium Chloride Bi-hydrate	0.5	g/L
	Sodium Chloride	0.5	g/L
	Magnesium Sulphate Heptahydrate	0.3	g/L
	Yeast Extract	5	g/L
	Trace Salt Solution	20	mL/L
	Supplement Solution	10	mL/L
Trace Salt Solution	Iron Sulphate Heptahydrate	0.278	g/L
	Zinc Sulphate Heptahydrate	0.299	g/L
	Copper Sulphate Pentahydrate	0.080	g/L
	Sodium Molybdate	0.242	g/L
	Cobalt Dichloride Hexahydrate	0.238	g/L
	Magnesium Sulphate Monohydrate	0.169	g/L
Supplement Solution	Iron Sulphate Heptahydrate	5	g/L
	Zinc Sulphate Heptahydrate	5	g/L
	Magnesium Sulphate Heptahydrate	5	g/L

Reactor Operation and Scheduling

Reactor operation was different depending on the run owing to the knowledge gained from prior runs. It is important to note that the current reactor operating conditions including agitation rate, temperature, dissolved oxygen level, pH and liquid level were manually recorded due to the lack of software support for the reactor.

The first two runs did not include any density or viscosity measurements due to equipment availability. The following general operating procedure was followed for fed-batch experiments three to five:

First, a template feeding profile was generated on Microsoft Excel with instructions for adjustment of the feed rate throughout the run, with reactor operation commencing at 22h30 with the initiation of the batch growth phase via inoculation. At the moment of inoculation, the reactor conditions were recorded, and a 20 mL sample was taken from the reactor and used to conduct four standard experiments: an optical density reading, cell dry weight preparation/measuring, density measuring and viscosity measuring.

Once the batch phase had ended the next morning (10.5 hours on average), the four standard experiments were repeated once again, and the fed-batch phase was initiated via the commencement of substrate addition in accordance with the predetermined feeding plan. At this moment an oxygen mass transfer experiment was performed. A general procedure was then followed until the end of the fed-batch run, which went as follows:

The substrate feeding rate was adjusted every hour to match with the feeding profile. Alternatively, if a reading/feed adjustment couldn't be made within an hour due to other time constraints, the feed rate was averaged over the period then set. To minimise excessive sampling, the four standard experiments were only performed in full at key points in the run, such as where oxygen limitation became a major factor or when cell density was at its highest. For minor sampling points, taken every hour, instead only a 10 mL sample was removed for dry weight and later HPLC analysis. Note that in later runs the number of minor sampling points is higher as a better understanding of the experiment had been obtained and the "critical points" were known.

Furthermore, at certain key points, mass transfer coefficient experiments were performed, however these ceased once the DO was unable to remain above 30% despite the system being at its maximum agitation rate of 800 rpm.

The fed-batch portion of the run generally lasted between 48 and 60 hours, and terminated when the reservoir was empty, and the DO was once again increasing despite no changes to the agitation rate. At this point the reactor was then left to operate without additional feed until the next day. An exception to this occurred in STR run five, where sodium benzoate was added up to a concentration of 2 g/L to kill the cells and prevent additional respiration. This proved to be unsuccessful, and this was instead obtained by heating the reactor to 60 °C the next day. At the start of the next day, the current volume in the STR was recorded and the post-fermentation mass transfer experiments were performed.

Analytical Techniques

Throughout reactor operation several analytical techniques were employed to obtain the following information: viscosity, density, cell dry weight, optical density (OD) and glucose and ethanol concentration in the fermentation broth. The method for these techniques was as follows:

Fermentation Broth Density Measurement

To obtain the density, two empty 5 mL volumetric cylinders were weighed with their caps on in advance. 5 mL of sample from the STR was then placed in each of the volumetric cylinders using an Eppendorf P5000 micropipette. The volumetric cylinders were then sealed and later weighed on an analytical balance. The recorded weight was then divided by the volume of 5 mL to determine the approximate density of the broth.

Fermentation Broth Viscosity Measurement

For this experiment, a size 50 Cannon-Fenske viscometer tube and water bath at 30 °C were set up. Once the bath was ready, 5 mL of sample from the STR were then poured into the viscometer. The viscometer was then submerged in the water bath for 5 minutes to ensure the temperature of the broth was at 30 °C.

At this point, the air inside of a three-way rubber suction ball was pushed out, then the ball was attached to the narrow end of the viscometer. The junction of the three-way rubber suction ball was then firmly pressed such that the liquid in the viscometer began to rise. Once the liquid extended passed the demarcated top-most experiment line on the viscometer, pressure was released from the three-way rubber suction ball and the liquid was allowed to fall back down. A timer was prepared and started the moment the liquid level dropped to the top-most line on the viscometer, then stopped once the liquid reached the bottom-most line on the viscometer. Finally, the recorded time was converted to seconds and used in conjunction with a manufacturer-supplied calibration correlation to determine the kinematic viscosity in centistokes. This kinematic viscosity was then converted into the dynamic viscosity in centipoise by multiplying the kinematic viscosity by the previously determined sample density.

Cell Dry Weight Measurement

To accurately record cell dry weights, some of the work involved need to be performed before the STR experiment began. Namely, a large batch of 2 mL plastic Eppendorf tubes (with the exact amount depending on the number required for the experiment) had to have their weights recorded. To this end, they were first autoclaved at 121 °C for 20 minutes. The Eppendorf tubes were then labelled using a permanent marker on the top of their caps, then dried in an oven operating at 80 °C over a period of 48 hours. Following this, the Eppendorf tubes were then placed in a desiccator until they were cool, then removed. At this point, the mass of each individual Eppendorf tube was determined with an analytical balance and recorded. The tubes were then ready for use in the STR experiment.

Once a liquid sample was removed from the STR, 6 mL of it were pipetted into three of the prepared 2 mL Eppendorf tubes using an Eppendorf P1000 micropipette. The Eppendorf tubes were then placed in a Sigma 1-14 microfuge and rotated at 13000 rpm for 5 minutes, then removed so that the liquid inside could be carefully poured out. 1 mL of de-ionised water was then pipetted into the Eppendorf tubes and they were once again rotated at 13000 rpm for 5 minutes in the microfuge. The water was then carefully removed, and the Eppendorf tubes sealed. The sealed tubes were then transported to the oven (still operating at 80 °C) and placed in an upright container so that they could completely dry over a period of 72 hours. After this waiting period, the tubes were then removed from the oven and weighed again. These weights were then compared to the original weights of each individual tube. The cell dry weight concentration per litre could was then determined by dividing the calculated mass by the sample volume of 2 mL.

Optical Density Measurement

Optical density measurements were made by first taking 3 mL of sample from the STR. 1 mL of this sample was then pipetted into a test tube using an Eppendorf P1000 micropipette. This sample was then diluted using deionised water up to 10x (depending on the predicted dilution requirements). The contents of the test tube were then well-mixed using a test tube shaker. At this point, the sample was transferred into a cuvette, which was in turn placed in a Thermo Scientific™ - Genesys 20-VIS spectrophotometer using 660 nm wavelength (as stipulated in the CeBER Labs Method Manual) where the OD could be taken.

If the OD was greater than 0.6, it was deemed too high to be reliable and a serial dilution of the original sample was implemented, up to 100x. However, if the OD was still greater than 0.6, another serial dilution was implemented, up to a total of 250x.

On conclusion of the STR run, the OD was compared to the recorded dry weights at each time point. Plotting a graph of OD vs. dry weight (with each point corresponding to the same sample from which both measurements were taken) allowed for the determination of a linear relationship between the two data points (with an associated R^2). This linear correlation could then be applied to future runs to estimate the actual dry mass cellular concentration present in the STR without having to wait for dry weight results to be ready.

Analysis of Glucose and Ethanol Concentrations

Glucose and ethanol concentrations present in the fermentation broth and feed reservoir were determined via the use of high-pressure liquid chromatography (HPLC). An HPLC unit fitted with a Bio Rad Aminex HPX-87H column was used for analysis. The mobile phase used was 0.005 M H_2SO_4, prepared via the addition of H_2SO_4 to ultra-filtrated water. This column and mobile phase were suitable for both glucose and ethanol determination, hence no change in column or mobile phase needed to occur (Bio-Rad Laboratories, 2012). As per Bio-Rad Laboratories (2012), a temperature of 50 °C, a flow rate of 0.60 mL/min and 210 nm UV detection were employed. The general procedure followed to obtain results was as follows:

First, 6 mL of sample taken from the STR were pipetted into three unlabelled 2 mL Eppendorf tubes, which were then labelled with permanent marker. These Eppendorf tubes were then placed in a freezer room operating at -11 °C until the conclusion of the experiment to preserve them and prevent possible degradation of the sugars/ethanol within.

Once the department's HPLC unit was available, mobile phase was then prepared in addition to several 2 mL clear glass vials with silicon screw caps which were sonicated. To establish a control/baseline, glucose and ethanol standards of 0.25, 0.50, 0.75, 1.0 g/L were prepared using glucose monohydrate and pure ethanol. These were diluted with mobile phase and filter sterilised into the glass vials using a 0.22 μm cellulose syringe filter.

The previously frozen samples were then retrieved from the freezer room and thawed. Predictions regarding the current concentration of glucose/ethanol in the samples were made such that the concentration in the samples would always be below 1 g/L glucose/ethanol respectively once diluted, then the relevant dilutions with mobile phase were performed. The diluted samples were then filter sterilised into glass vials which were then labelled. The HPLC was then fed all of the standards and samples. The resultant peak data was logged automatically by software, then this peak data was manually inspected before being recorded manually in a Microsoft Excel spreadsheet for later analysis.

Cell Growth Data Manipulation

Determination of Cellular Growth Rate

The cellular concentration in a reaction system at any point, assuming a constant growth rate, is given by the following Equation (4.4), as given by (Doran, 2013c):

$$x = x_0 e^{\mu t} \qquad \text{Equation (4.4)}$$

Where "x" is the instantaneous cellular concentration in g/L, "x_0" is the initial cellular concentration for the period being considered, "μ" is the average cellular growth rate for the period with units h^{-1} and "t" is the current amount of time elapsed from the start to the end of the period in hours. This equation can be applied to the fed-batch growth system with variable growth rate by assuming that the growth rate remains relatively constant in distinct time periods. Rearranging Equation (4.4) to make "μ" the subject results in Equation (4.5):

$$\mu = \frac{\ln\left(\frac{x}{x_0}\right)}{t} \qquad \text{Equation (4.5)}$$

Equation (4.5) was used to determine the average growth rate between two time points during the fed-batch run once dry cell weight data for the two time points had been obtained.

Determination of Cellular Productivity

Cellular productivity across a given time period in the system was calculated via Equation (4.6):

$$P = \frac{x - x_0}{t} \cdot V \qquad \text{Equation (4.6)}$$

Where "P" is the average cellular productivity across a time period in g/h, "x" is the instantaneous cellular concentration in g/L, "x_0" is the initial cellular concentration for the period being considered, "t" is the current amount of time elapsed from the start to the end of the period in hours and "V" is the average volume in the system across the period of time in litres.

5 STR Results and Discussion

5.1 Baseline STR Results

The preliminary experiments concerned STR operation in absence of any micro-organisms. The results here served as a baseline for further analysis, namely the maximum k_La that should be expected from the system at varying agitation rates. This would allow approximation of the maximum supportable growth rate in the system as well as serve as a general performance indicator. Two systems were tested in this regard. The first was filled entirely with deionised water, the second was filled entirely with the chosen media for the growth experiments.

Referring to Figure 5.1, the maximum mass transfer coefficient observed in the STR was 160 h^{-1} in the pure water system. The mass observed mass transfer drops noticeably when the water is replaced with media, with the new maximum instead at 140 h^{-1}, representing a 12.5% decrease in k_La. This is to be expected, as media is more viscous than deionised water and an increase in viscosity is associated with a decrease in mass transfer coefficient. A difference is observed in the k_La with varying liquid volume. These differences are caused by several factors. The liquid height will result in a lower bubble residence time for shallower systems. The power input per unit volume, with constant agitation rate, will decrease with increasing volume, which will in turn result in a lower mass transfer coefficient. There is a greater spread of results in the water system than in the media system, however it is likely that this is due to natural variance within the data. Only two runs were performed per data point, hence standard deviation around these points is omitted in Figure 5.1.

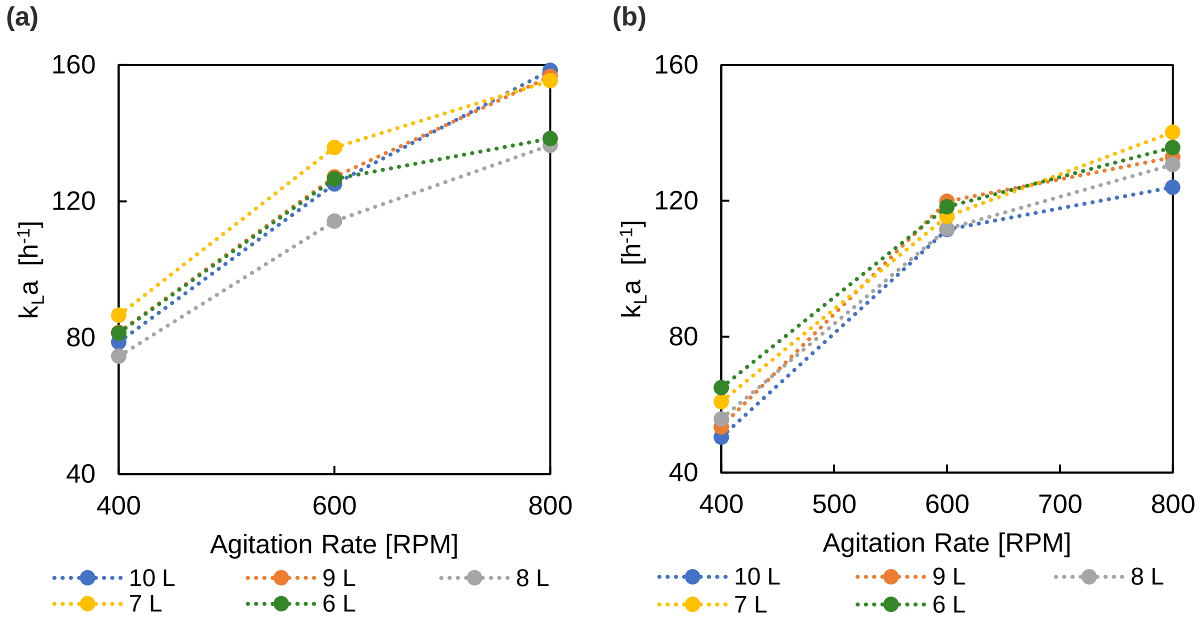

Figure 5.1 – Observed k_La vs. agitation rate in a STR at different volumes in (a) deionised water and (b) media systems at 30 °C and an aeration rate of 1 vvm.

5.2 STR Batch Results

For the initial batch growth experiment, a 5 g/L starting glucose concentration was utilised. Mass transfer experiments were not performed in this run as its sole purpose was to determine the length of time required for the batch phase to end for fed-batch experimentation.

Referring to Figure 5.2, both the diauxic growth of *S. cerevisiae* and Crabtree effect can be clearly observed. As the glucose concentration starts well above the critical limit of 0.15 g/L, the production of ethanol is observed immediately. As the consumption rate of glucose increases, so too does the production of ethanol, as observed between 3 and 5 hours. Once the glucose is almost entirely utilised, the consumption of ethanol can be observed slowly beginning. The rate of ethanol consumption then begins speeding up in conjunction with an increase in the cellular growth rate, further lending credence to the diauxic growth trend. The experiment completes in a period of 10.5 hours, with a yield on glucose of approximately 0.667 $g_{biomass}/g_{glucose}$. This yield is higher than expected as Posten and Cooney (1993) indicated a maximum of 0.5 $g_{biomass}/g_{glucose}$. This is possibly a result of an underestimation of the starting glucose concentration (determined as 5.18 g/L via HPLC analysis) and/or an underestimation/overestimation of the relevant cell concentrations (measured as 0.17 g/L at experiment start and 3.62 g/L at experiment end).

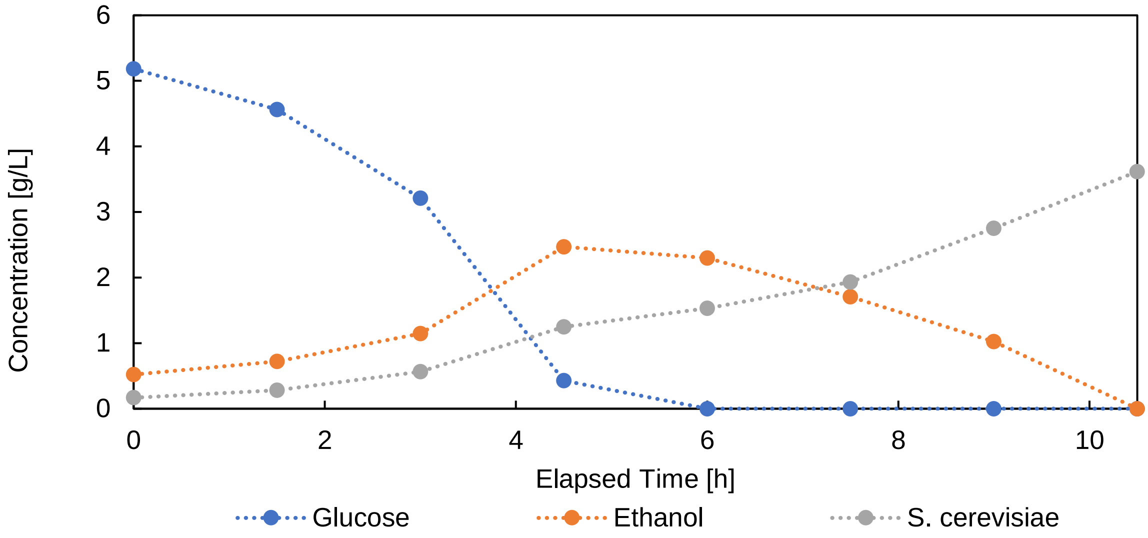

Figure 5.2 – Glucose, ethanol and cell concentration vs. time for a single batch STR fermentation growing *S. cerevisiae*

5.3 STR Fed-Batch Results

The fed-batch reactor results constitute the bulk of the STR experimentation. Fed-batch experiments can be broken down into several sub-categories, namely cell growth, mass transfer and power input.

5.3.1 Cell Growth Trends

No two runs were truly identical during STR fed-batch operation. This is a result of a variety of factors, ranging from reactor stability owing to age of the rig as well as continuous editing of the fed-batch feeding profile in accordance with information learned from prior runs. As such, an average of the five successful runs performed is not possible. As the feeding strategy was further optimised with every iteration, the final, fifth run, is the truest reflection of the performance of the feeding strategy. As a result, only growth and HPLC data from the fifth run will be shown here, with data from earlier runs included in Appendix C.1 for reference.

Cell and Substrate Concentration Profiles

Figure 5.3 illustrates the observed growth trend over the course of the experiment, with the dashed black line representing the moment that fed-batch operation began (at 10.5 hours, as demonstrated in Figure 5.2). The efficacy of the feeding plan lies in the ability to maintain a low glucose concentration to ensure that ethanol formation is minimised, and a preliminary look demonstrates that the plan is successful in this regard, with the ethanol concentration remaining low throughout the experiment with an exception occurring at 38.5 hours into the experiment. The most likely cause would be either the invocation of the Crabtree effect via a higher-than-expected glucose concentration, or the DO concentration dropping too low to sustain aerobic growth.

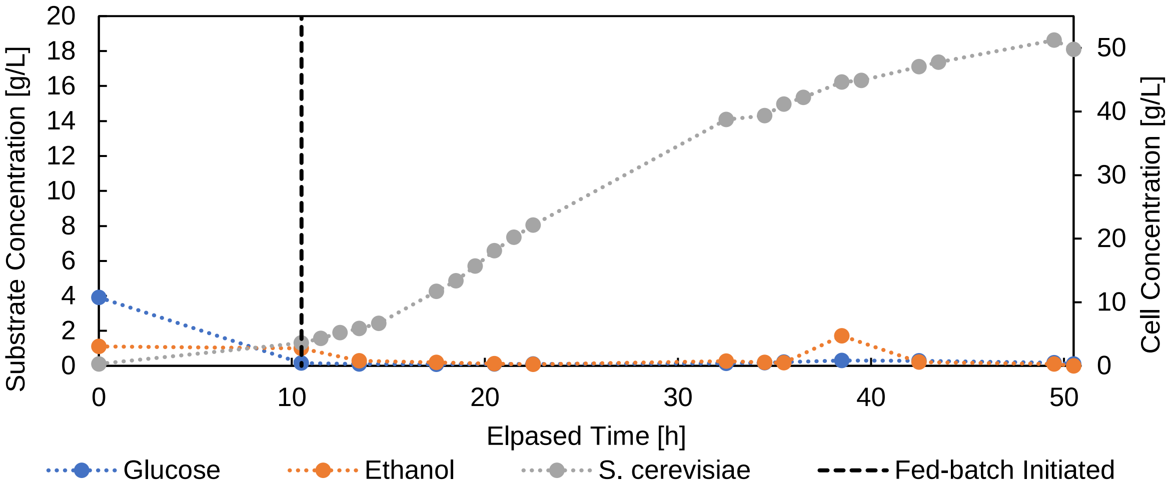

Figure 5.3 – Fed-batch STR run 5 ethanol, glucose, and cell concentration profiles over time

Referring to Table 5.1, there are two points at which the DO drops below at the critical DO of 15% (Di Serio et al., 2003). These occur at the 34.5 hour mark and the 38.5 hour mark. Unfortunately, as the reactor's logging system was faulty, more detailed trends around these points are unavailable.

Table 5.1 – Temperature, pH, and DO data for fed-batch STR run 5

Time [hours]	Temperature [°C]	pH	Dissolved Oxygen [%sat]
0	30.0	4.99	100
10.5	30.0	4.72	65.8
11.5	30.0	4.52	60.5
12.5	30.0	4.51	60.3
13.5	28.9	4.50	59.9
14.5	29.9	4.51	60.5
17.5	30.0.	4.37	60.1
18.5	30.0	4.42	32.4
19.5	29.9	4.38	45.6
20.5	30.0	4.47	48.9
21.5	30.1	4.47	43.4
22.5	29.9	4.46	51.1
32.5	30.0	4.46	35.6
34.5	**30.1**	**4.37**	**0.20**
35.5	30.0	4.40	40.1
36.5	30.0	4.38	43.4
38.5	**30.1**	**4.44**	**8.60**
39.5	29.9	4.39	47.9
42.5	29.8	4.40	32.2
43.5	29.9	4.35	51.9
49.5	29.8	4.54	59.9
50.5	30.0	4.60	60.3

The dip in DO concentration at 34.5 hours does not reflect any observable change in Figure 5.3 at the same point in time. However, the dip at 38.5 hours reflects the observed ethanol concentration spike. This discrepancy might be due to the length of time that these lows were experienced, but without additional information it is difficult to say with certainty why this is the case. The DO does appear to be the most likely culprit of the spike, as the temperature was very near the 30 °C optimum and the pH was similarly close the 4.5 pH optimum. To be certain, a closer inspection of the glucose concentration profile in the reactor is required.

Figure 5.4 illustrates the glucose concentration profile for the fed-batch portion of the fifth fed-batch run. Observing the profile, it can be seen that the glucose concentration remained below the critical glucose concentration of 0.15 g/L, required to prevent the Crabtree effect from engaging (Posten and Cooney, 1993), up until the 34.5 hour mark. From this point onwards, the glucose concentration remained above the critical threshold until the end of the experiment, peaking at the 38.5 hour mark. Exceeding this critical concentration for such a long period of time resulted in a significant amount of ethanol production. This indicates that the ethanol production was caused by an oversupply of glucose to the system. This oversupply was likely caused by insufficient oxygen mass transfer to sustain a sufficiently high consumption rate, as observed by the increasing glucose concentration coinciding with the exact point in time that the DO first dropped below the critical level of 15%.

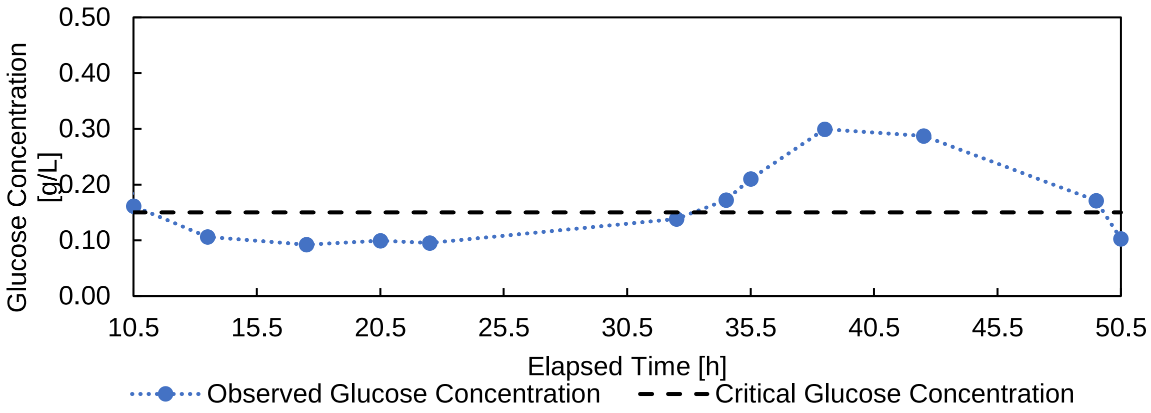

Figure 5.4 – Glucose concentration vs. time for fed-batch STR run 5

Changes in Viscosity and Density

Viscosity and density are both important factors to consider during STR operation, as they have a direct influence on mixing characteristics and power input (as discussed in the literature review). Density and viscosity calculations were started on the third fed-batch run and continued until the final, fifth run.

Observing Figure 5.5 for the associated density data, a definite trend for an increasing system density with increasing cell concentration can be observed. However, the accuracy of the overall correlation is questionable with an R^2 of 0.68. Two factors were likely to have caused this. The first is the differences in fermentation broth composition across runs due to growth and feeding profiles. This can be observed in the generally higher accuracy observed in Figure 5.5 (b) and Figure 5.5 (d). The second cause is the measuring method. As described in the methodology, density was taken by using a 5 mL micropipette to transfer 5 mL of sample into 5 mL volumetric flasks, which had been pre-weighed. This was not the case however for the third and fourth runs, where the flasks had not yet been procured and as a result a single 10 mL glass measuring cylinder was used instead. Therefore, the highest correlation is observed for Figure 5.5 (d). Additionally, whilst every effort was made to ensure accuracy, the fermentation broth is sticky and difficult to pipette entirely accurately, hence the volume dispersed was not always fully consistent. This particularly noticeable in Figure 5.5, where the spread is higher, and some definite outliers can be observed.

Figure 5.6 instead details the change in viscosity versus time. As expected, the viscosity can definitively be observed to be increasing with cell density. As a viscometer was employed, with lower likelihood of human error due to a lack of reliance on volume size, the trends are better defined. Once again, the R^2

value is lower for the overall compilation than for the per-run trends. The reasons for this are identical: differences in fermentation broth composition and human error. An important data point to note is the maximum viscosity obtained: 1.32 cP at a cell density of 47.7 g/L. This will be used for the novel reactor design as a basis for the maximum viscosity the system will need to be capable of operating at.

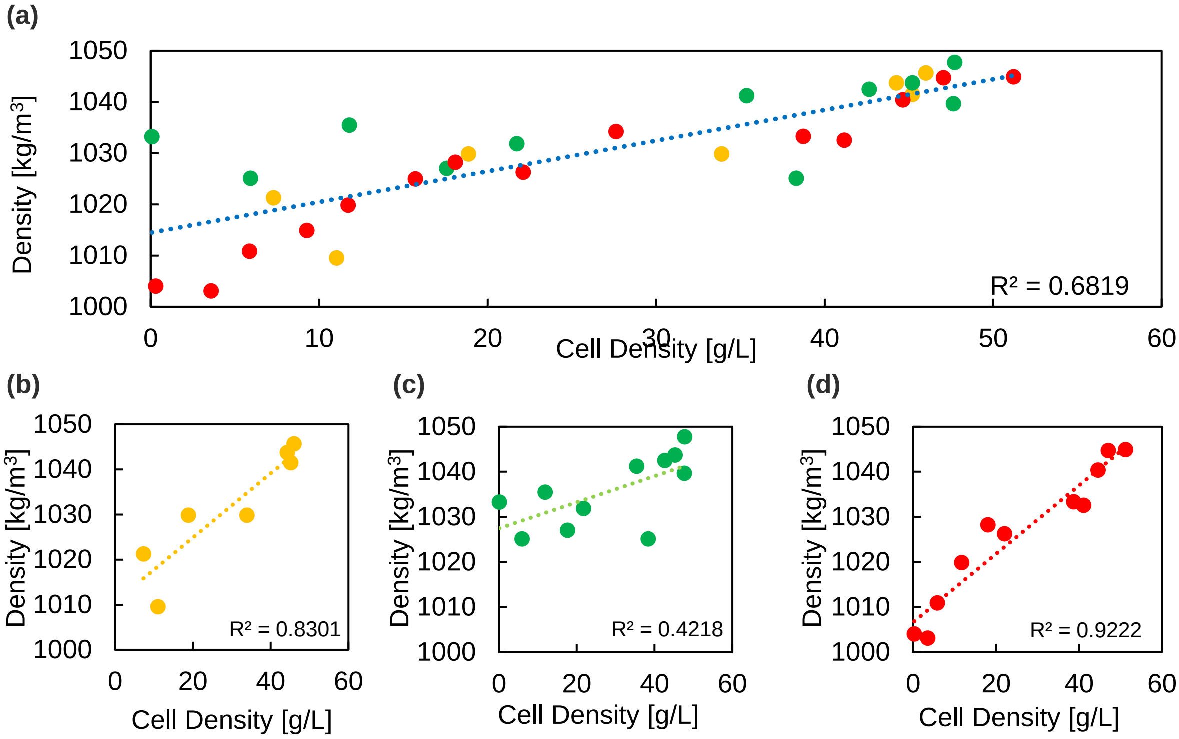

Figure 5.5 – Fermentation broth density vs. cell density profiles for fed-batch STR runs for the (a) overall system, (b) 3rd run, (c) 4th run, and (d) 5th run

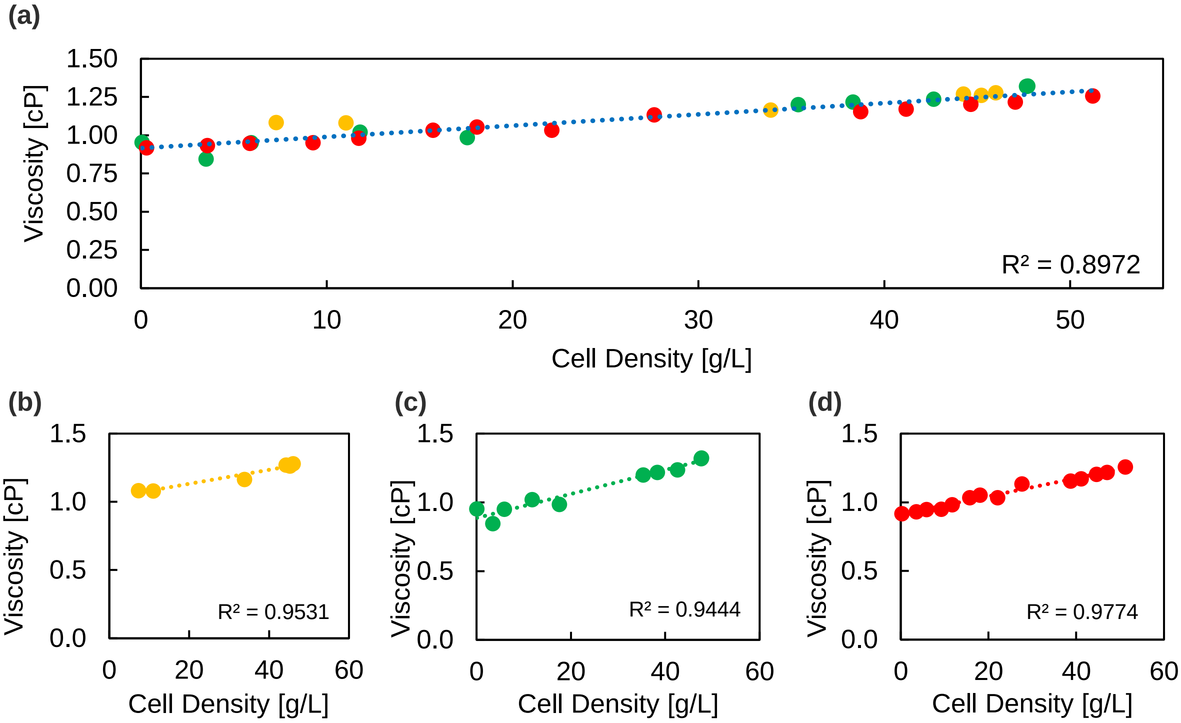

Figure 5.6 – Fermentation broth viscosity vs. cell density profiles for fed-batch STR runs for the overall system (a), 3rd run (b), 4th run (c), and (d) 5th run

Key Fed-batch Results

Table 5.2 refers to the key results from the final fed-batch STR run. Once again, as all runs were unique and run 5 represents the best iteration of the fed-batch feeding strategy, the final data for run 1, run 2, run 3, and run 4 can be found in Appendix C.2 and only the data from run 5 will be discussed.

Table 5.2 – Key Results from fed-batch STR run 5

Item	Value	Units
Overall Yield on Glucose (Excluding Death Phase)	0.465	$g_{biomass}/g_{glucose}$
Maximum Observed Growth Rate	0.202	h^{-1}
Minimum Theoretical k_La Required @ Max O_2 Demand	372	h^{-1}
Average Observed Growth Rate	0.093	h^{-1}
Minimum k_La Required on Average	190	h^{-1}
Average Productivity	9.44	g/h
Final Cell Density	49.8	g/L

Comparing the overall yield on glucose from Run 5 to that observed during batch operation (0.465 to 0.667), the fed-batch yield is more in line with what the literature reported yield of 0.5 g/g (Posten and Cooney, 1993). The difference between literature and experimental yields is likely a result cell stress/maintenance energy requirement and the varying performance of the fed-batch feeding strategy. For example, if an excess of glucose were provided at any point, the Crabtree effect would be engaged, and the observed yield would be impacted. The maximum growth rate was 0.202 h^{-1}, which is below the maximum growth rate threshold for the Crabtree effect of 0.25 h^{-1} (Posten and Cooney, 1993). The maximum growth rate however is a poor performance indicator. The average growth rate is a more interesting data point, at 0.09 h^{-1}. It will be noted that this average is significantly lower than the Crabtree maximum. This is because to realistically obtain the maximum growth rate of 0.25 h^{-1}, an extremely high mass transfer coefficient is required.

The “minimum theoretical k_La required at maximum oxygen demand” listed in Table 5.2 specifies the minimum k_La requirement, assuming that the DO in the reactor is at 0%, to have sustained the observed dry cell weight increase (growth rate). Hence this value, at the maximum oxygen demand, indicates the minimum k_La any reactor system would have to provide to be capable of supporting the growth that the STR can support. As a result, this serves as an important baseline for the novel reactor. If the novel reactor cannot reach a theoretical k_La output of 372 h^{-1}, it will not be able to sustain similar growth rates/productivities to those observed in an STR. To further stress this result, the average minimum k_La required was calculated across the entirety of the fed-batch experiment. To have attained the average productivity of 9.44 g/h as obtained by the STR, a reactor of equivalent volume would need to prove a minimum k_La of 190 h^{-1}.

In addition to functioning as a baseline, these theoretical k_La results are interesting in that they exceed the experimentally determined maximum k_La observed in Figure 5.1 for both the pure water and media systems. Whilst an enhancement of mass transfer performance is not irregular, as mentioned by Ju and Sundararajan (1995), it was not expected to be this extreme. Looking at the STR run data in Appendix C.2 it can be noted that this exceeding of the experimentally determined maximum k_La for the STR is a consistent occurrence. Originally, the response time data had been ignored up until the completion of the second fed-batch run. However, this issue was identified when attempting to set up k_La thresholds for the fed-batch feeding profiles and noticing the discrepancy between the two data sets. Evidently, the probe response time was worse than originally thought and response time corrections were applied to k_La experimental data for all the fed-batch runs. The unmodified initial runs are left as-is to better illustrate this disparity.

The final key results presented in Table 5.2 are the average productivity and the final cell density. The productivity is the most important metric for comparing reactor performance in an industrial setting in conjunction with energy efficiency. If the novel reactor can support aerobic growth, this productivity will be targeted to see whether it can compete realistically compete with the STR. The final cell density of 49.7 g/L was 10 g/L below the targeted density of 60 g/L for this run. As has been discussed in the previous subsection, this is likely due to the system breaching its mass transfer threshold/oversupply of glucose causing the yield to drop.

5.3.2 Accuracy/Reliability of the Fed-batch Feeding Strategy

The key outcome of the STR runs was to obtain baseline mass transfer, productivity, and energy efficiency results from aerobic fed-batch bioreactor operation. However, an additional outcome was the development of a successful fed-batch feeding strategy. As described in the Fed-Batch Feeding Profile sub-section, an approximation of the required feeding rate was made by targeting a specific growth rate at hourly time intervals. This predicted growth rate could then be directly compared to the actual growth rate as obtained via the cell dry weight measurements. As each run had different feeding profiles due to different final cell concentration targets and growth rate approximations, a valid comparison of the runs is not possible. Instead, the data for fed-batch STR run 5 is presented and discussed here (as a basis for the merit of the final version of the feeding profile) with all prior run data presented in C.3. Figure 5.7 presents the predicted and observed trends, as dictated by the feeding profile, for cell concentration, growth rate and productivity.

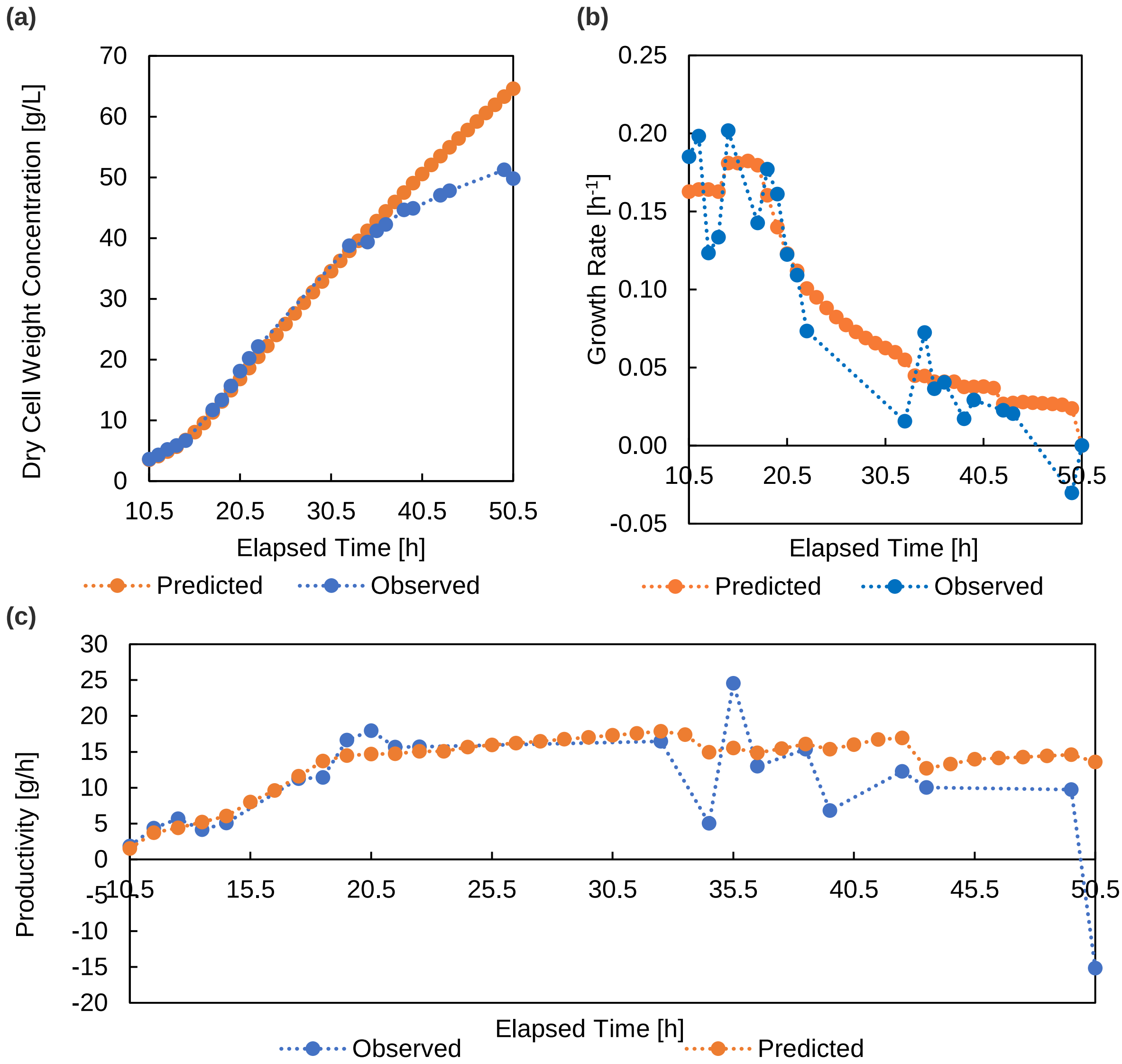

Figure 5.7 – Observed vs. predicted (a) cell concentration, (b) growth rate, and (c) productivity for fed-batch STR run 5

A cursory look indicates that the overall trends are similar, however a statistical evaluation is more useful. Regression analysis was performed to compare the predicted trend to the observed trend. This led to R^2 values of 0.92, 0.86, and 0.49 for the cell concentration, growth rate and productivity, respectively. Whilst these overall values are not indicative of high accuracy, this is an issue of cascading effects. When a deviation from the expected cell concentration was observed, the feeding profile was not changed to account for the new cell concentration. As a result, the larger the deviance of predicted vs. observed cell concentration, the larger the deviance in the observed growth rate/productivity vs. the predicted one. This, when combined with periods of oxygen limitation, would explain the decrease in accuracy as the experiment progressed.

For example, prior to the 34.5 hour mark, accuracy of the dry weight approximations is very high (an R^2 of 0.99 is observed). Similarly, the productivity correlations see a drastic accuracy increase (an R^2 of 0.93 is observed). The growth rate correlation however does not experience a similar accuracy increase (an R^2 of 0.84 is observed), this is because the growth rate is significantly more sensitive to changes in the cell concentration and varied far more throughout the run. Additionally, the growth rate determined at each point is the average growth rate, using the cell concentration from that time point and comparing it to the new cell concentration found at the next time point. The overall growth rate is perhaps more informative. The predicted overall growth rate was 0.099 h^{-1}, whilst the observed overall growth rate was 0.093 h^{-1}. Considering only data from before the 24 hour mark, the predicted overall growth rate was 0.142 h^{-1}, whilst the overall observed growth rate was 0.137 h^{-1}, indicating higher accuracy at an earlier time point in the experiment. Irrespective of the accuracy of the growth predictions, another means of analysing the performance of the feeding strategy is via analysis of the theoretical k_La demand with regards to the threshold values for k_La demand used in the generation of the fed-batch feeding profile.

Figure 5.8 demonstrates the minimum k_La threshold values used to develop the feeding plan. Note that upon closer inspection of the data it was found that an erroneous growth rate calculation had been performed in the Excel spreadsheet, hence Equation (4.5) had not been correctly implemented. This resulted in a decrease of all calculated growth rates (both predicted and from experimental data). As both the experimental and predicted data were both calculated using the same incorrect calculation, replacing the formula resulted in no change in the relationship between these two. Additionally, as the feed rates were based on predicted cell dry mass and not growth rate, the feeding profiles remained unchanged.

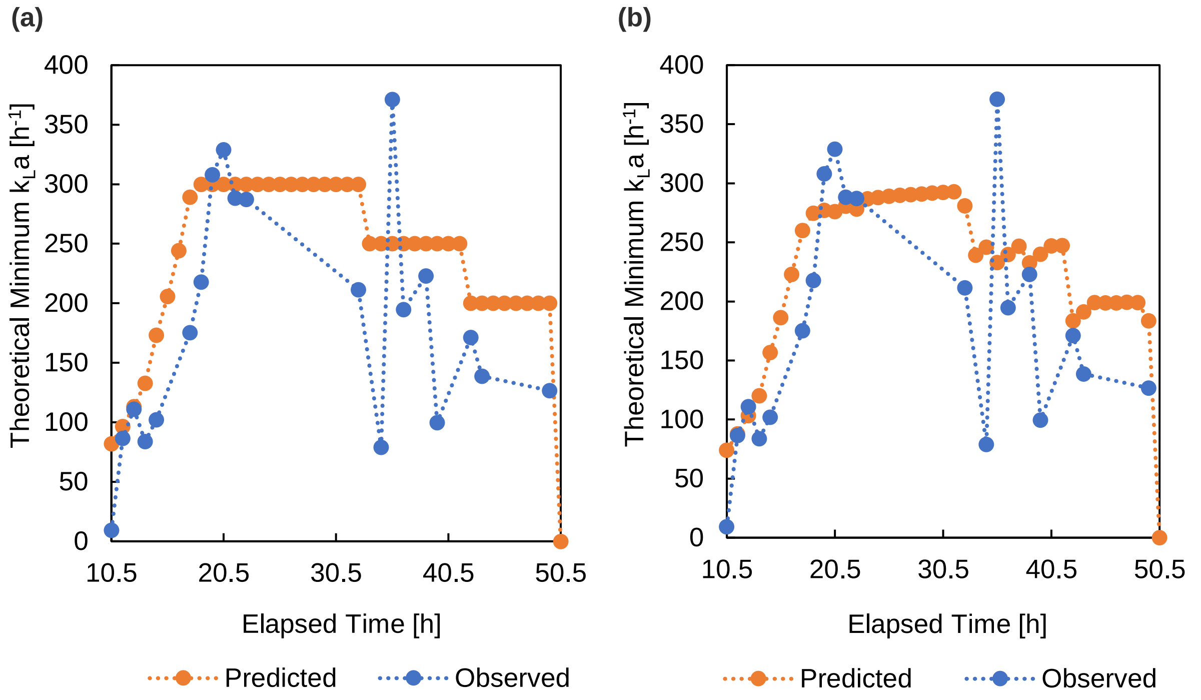

Figure 5.8 – Theoretical minimum k_La requirement vs observed minimum k_La requirement over time for fed-batch STR run 5 using (a) initial growth rates and (b) corrected growth rates

The only consequence to this incorrect calculation was an incorrect approximation of the minimum k_La required to sustain cell growth at the target growth rate once the growth rate had been corrected using the correct formula.

Referring to Figure 5.8 it can be noted that, at first, the observed minimum k_La demand increases along with the predicted growth rate. However, it exceeds the threshold value given. The profile is successful whenever the observed k_La is below the threshold value as the purpose of this threshold is to prevent oxygen limitation. Ideally however, the observed values should be very close to the predicted ones.

The discrepancy observed is likely a result of two factors, the first of which was the frequency of sampling (more frequent sampling would result in more accurate growth rate prediction). The second factor is the way the feeding profile operated. The static nature of the profile meant that any deviation from the original plan would be exacerbated as the run continued. Additionally, as the feeding rate was only adjusting every hour at first, and every other hour as the run continued, the glucose feeding rate was averaged over a period. At the start of such periods, one would observe a higher than allotted for oxygen demand (due to increased glucose feed), followed by a decrease in said oxygen demand towards the end of the feeding period. Fed-batch STR run 5 was the final iteration of the fed-batch feeding profile and therefore represents the most accurate version prior to commencement of the design of the novel reactor.

5.4 k_La vs. Power Input per Unit Volume Results

5.4.1 Fed-batch STR Results

The power input into the system for the STR experiments was calculated as described in sub-section 4.2.3. However, the k_La was determined using a combination of two methodologies as discussed in sub-section 2.1.4. The first method applied made use of Equation (2.16) and Equation (2.17), with the k_La determined using a solver. The second method bypassed the need for a solver and instead Equation (2.18), Equation (2.12), and Equation (2.13) were used. A Microsoft Excel spreadsheet was used to interpret DO data using both methodologies. Deciding which method was valid was done as follows:

The default method used was the solver method, and the alternative method was only employed when select criteria were met. The first was if the solver returned an illogical or erroneous value, such as a zero or near zero k_La. This was typically caused by an incorrect recording of the time at which re-aeration began, or early termination of the re-aeration part of the experiment. After this check, when possible (if growth data was available), k_La results were compared to the minimum k_La required for the achieved cell growth during the fed-batch run. The method providing a k_La closest to this value was accepted in this scenario.

A graph of the results for fed-batch STR run 1 are omitted in Figure 5.9, as only two data points were available. In addition to generating lines of best fit to determine how well this data correlates with expected trends as described in literature, a key outcome of this data is the energy efficiency at which the mass transfer coefficient is obtained. This can be obtained as either a single point (given by the gradient between that point and the point 0,0), as the average of all points of data or the gradient of the best fit line. For each run, this data is presented in Table 5.3.

Table 5.3 – Mass transfer energy efficiency across fed-batch STR runs

Run Number	Max. Mass Transfer Energy Efficiency [$m^3 \cdot h^{-1} \cdot W^{-1}$]	Av. Mass Transfer Energy Efficiency [$m^3 \cdot h^{-1} \cdot W^{-1}$]	Best Fit Gradient [$m^3 \cdot h^{-1} \cdot W^{-1}$]
1	0.245	0.180	N/A
2	0.224	0.078	0.020
3	0.165	0.073	0.026
4	0.198	0.065	0.013
5	0.130	0.044	0.012

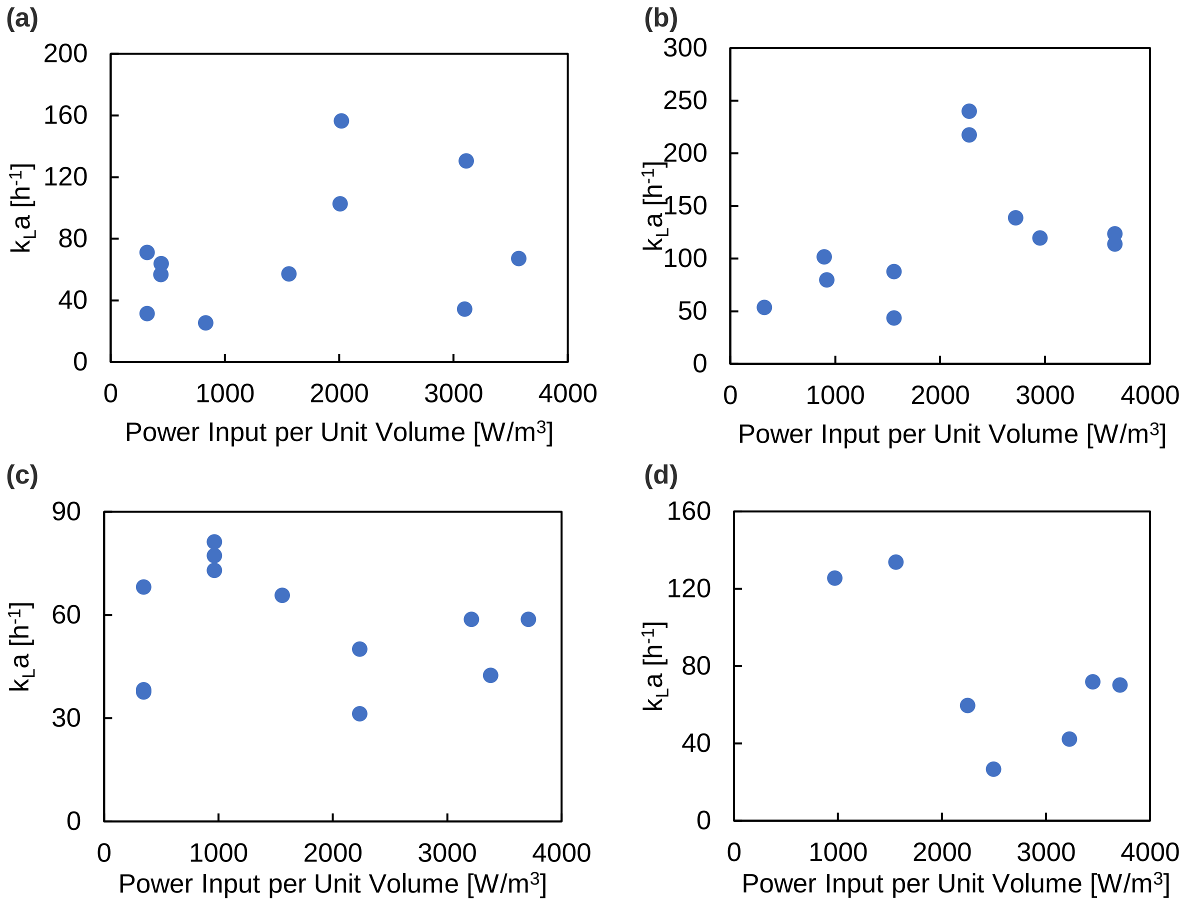

Figure 5.9 – k_La vs. power input per unit volume for fed-batch STR (a) run 2, (b) run 3, (c) run 4 and (d) run 5

The maximum efficiency data detailed in Table 5.3 is useful as a metric for comparison of the novel reactor. Referring to the STR mass transfer energy efficiency range listed in Table 2.2 (0.022 - 0.236 $m^3 \cdot h^{-1} \cdot W^{-1}$), the obtained maximum efficiency of 0.245 $m^3 \cdot h^{-1} \cdot W^{-1}$ compares well to the maximum observed literature efficiency. However, for the fed-batch runs the efficiency would be expected to be lower than this maximum, owing to the varying rheological properties of the fermentation broth. Observing the full efficiency data set shown in Appendix C.4, these maxima are always observed at low power inputs. This indicates a decreasing efficiency as power input increases. This is further backed by the average efficiency values.

The average efficiency across all runs was always higher than the minimum efficiency found via literature correlations. The average efficiency is always substantially lower than the maximum efficiency. This can partly be explained by the large amount of scatter present in the data sets. The other explanation for this is the decreasing efficiency observed with increasing power input. These average efficiencies are of particular interest as they serve as a metric to which the novel reactor can be compared.

An attempt was made to provide a “best fit” line for each figure in Figure 5.9 based on Equation (2.23) and the gradient as used in Table 5.3 was obtained by averaging the gradient of these lines. The lines were non-smooth in nature because of the different gas flow velocities used in the recording of different data points, as a constant vvm of 1 was targeted in all instances instead of a constant superficial gas velocity. Unfortunately, as can be seen from the high scatter evident in the data, these lines were very poor fits. The resultant coefficients and residuals for each of these lines are presented in Table 5.4. The energy efficiency as described by the gradient line is in theory an indicator of the overall system efficiency, such that one could potentially predict the efficiency at a power input even higher than those tested. However, the significant scatter associated with these data sets has made the gradient difficult to utilise.

Table 5.4 – Constants and R^2 for fed-batch STR runs 2-5

Run Number	K	α	β	R^2
2	0.00078	0.4	0.0998	0.16
3	0.00117	0.4	0.0998	0.29
4	0.00056	0.4	0.0997	N/A
5	0.00061	0.4	0.0997	N/A

R^2 values for runs 4 and 5 were negative and therefore nonsensical. The poor R^2 values for these lines of best fit are an indicator of underlying issues with the DO probe during fed-batch operation and highlight the degree to which the data is scattered. Attempting to sort data out by identical volumes (and hence identical gas flow rate) yields similarly scattered data, as shown in Figure 5.10.

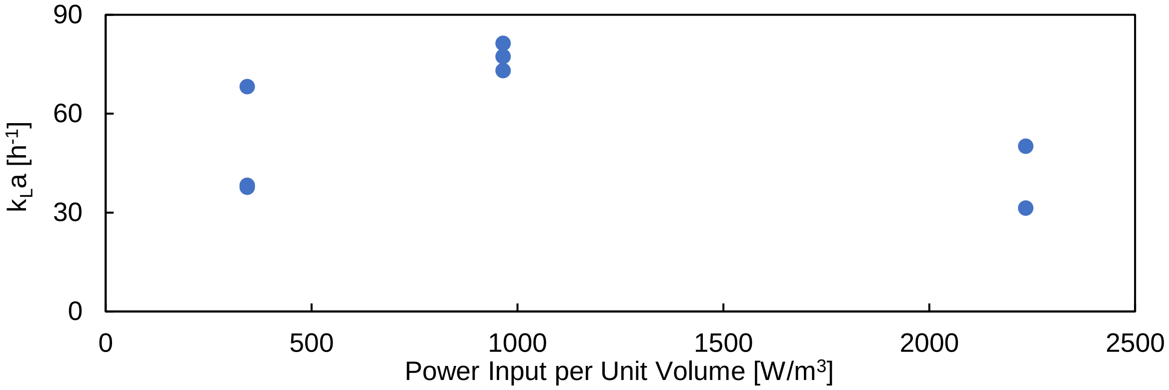

Figure 5.10 – k_La vs power input per unit volume at a constant volume of 9.4 L from post fermentation experiments from fed-batch STR run 4

Culminating all data points across all experiments yields similar results, as displayed in Figure 5.11. The resultant coefficients for the best fit line (not shown) for the data presented in Figure 5.11 are 0.0001, 0.4 and 0.7 for K, α and β respectively, whilst the R^2 for this fit is 0.10. This is an extremely poor fit which effectively implies little to no correlation of the data to the predicted trend.

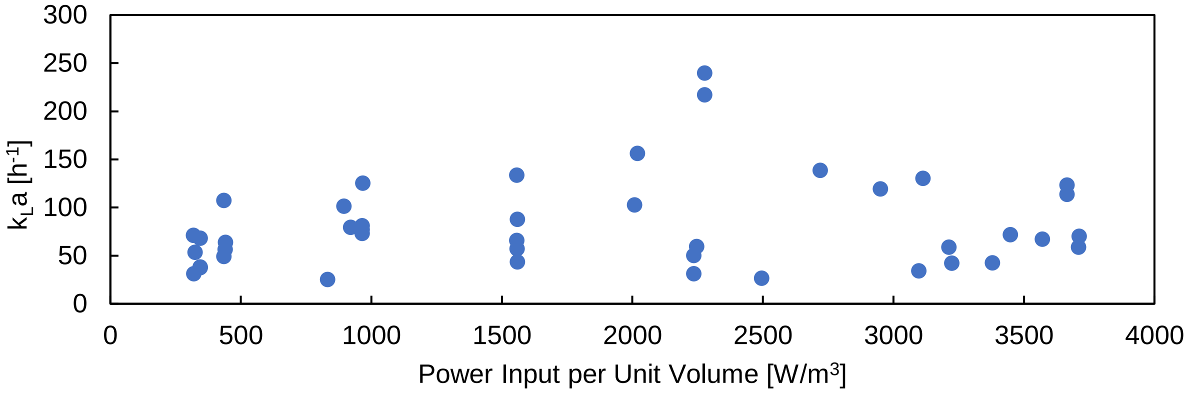

Figure 5.11 – All fed-batch STR k_La results vs. respective power input per unit volume

Regardless of the method employed, the mass transfer coefficients never correlate with the high “minimum” mass transfer rates theoretically achieved as indicated by the growth data. As these values are “minima” (calculated with the assumption of 0% DO) the actual mass transfer coefficient would be expected to be even higher than them depending on the DO level in the reactor at a given point. This issue was quickly realised, hence the development of the two-method approach used in the determination of the k_La. However, this failed to correct the issue. Attempting to artificially inflate the response time (on the assumption that the 5.9 second response time was incorrect) to obtain higher k_La values resulted in highly inconsistent data and even worse fits and did not completely explain the poorness of the data. It must be recalled that if the mass transfer coefficient is sufficiently high and the probe response time sufficiently high as well that the dynamic method is highly unrecommended (Gaddis, 1999). However, it is unlikely that the probe response time is this high, as the system tested was laboratory-scale and commercially produced for research.

5.4.2 Adjusted Baseline STR Results

To investigate this further, the initial baseline STR data was re-investigated with the 5.9 second response time data via use of Equation (2.15). As power input calculations require density data and density data was not gathered initially for the baseline experiments with media, only the deionised water system could be considered.

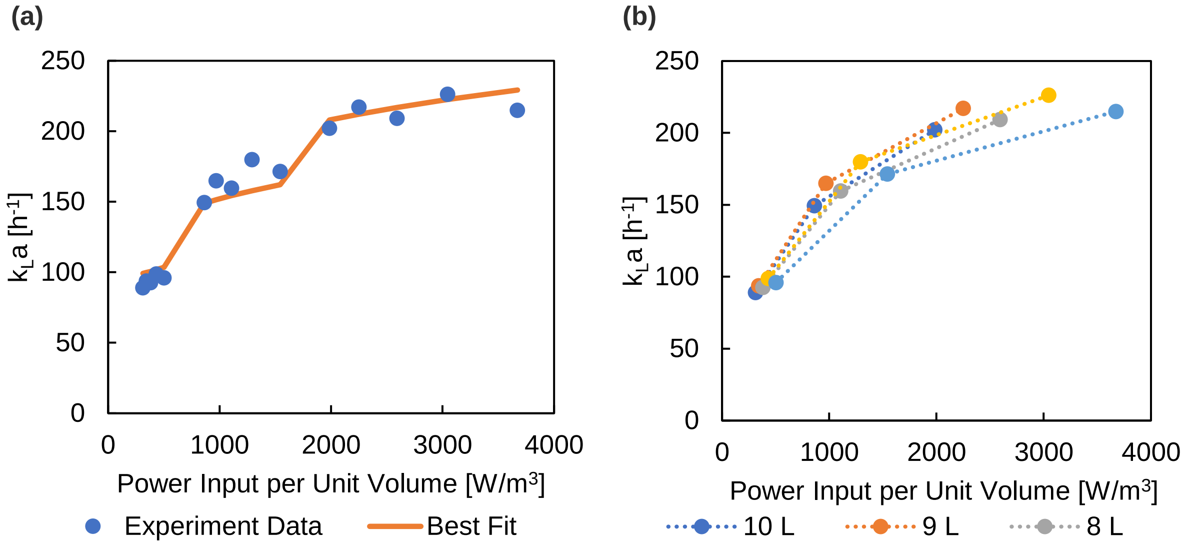

Figure 5.12 – Response time corrected data for a (a) deionised water STR set-up, with (b) fill volume comparisons from the same experiment

A far more believable "best fit" line, relative to those attempted in the fed-batch experiments, is observed in Figure 5.12 for the water system data. These corrections increase the maximum observed k_La in the baseline system to 226 h^{-1}, a substantial improvement when compared to the results in Figure 5.1. However, this is still below the minimum theoretically required k_La as determined via the growth data. The associated R^2 with the best fit line is 0.96, indicating a good level of correlation between the proposed power input correlations (given by Equation (2.23)) and this data set. Figure 5.12 does not have error bars associated with each data point as each data point is made from duplicates, not triplicates. Therefore, little commentary can be given on the relationship between the fill volume and mass transfer energy efficiency/maximum k_La outside of what can be directly observed. Key observations are compiled in Table 5.5.

Table 5.5 – Key observations from response time corrected deionised water STR experiment data

Observation	Value	Unit	Fill Volume [L]	Power Input [W/m^3]
Maximum Mas Transfer Energy Efficiency	0.285	[$m^3 \cdot h^{-1} \cdot W^{-1}$]	10	312
Minimum Mass Transfer Energy Efficiency	0.059	[$m^3 \cdot h^{-1} \cdot W^{-1}$]	6	3670
Average Mass Transfer Energy Efficiency	0.158	[$m^3 \cdot h^{-1} \cdot W^{-1}$]	-	-
Best Fit Gradient	0.044	[$m^3 \cdot h^{-1} \cdot W^{-1}$]	-	-
Maximum k_La	226	h^{-1}	7	3045

Table 5.5. reveals that the highest energy efficiency is attained at the highest fill volume and at the lowest agitation rate (and therefore lowest effective energy input). This is an expected result, a larger volume will result in the power input being divided by a greater amount, hence reducing the overall power input per unit volume. As with the fed-batch data, at higher power inputs the energy efficiency decreases. This is exacerbated by the fact that at 6 L the STR appears to perform more poorly than at any other fill volume tested. This is likely because of the placement of the impeller blades relative to the liquid height, which influences the STR hydrodynamics.

With regards to the fed-batch data, this at least implies that the probe is functional and that response time corrections can indeed be successfully applied to the data. However, this also indicates that the issue with the fed-batch data may lie in an issue with the probe upon autoclaving/change in probe performance of the duration of the fed-batch experiments. No growth could be observed on the probe membrane and no nicks were observed to indicate damage; hence it is suspected that an issue existed with the supplied DO module itself. This might simply be a case of an aging machine, however no additional information to troubleshoot this issue could be found. A note was instead made to avoid the use of membrane probes in the novel system to obtain more consistent results.

6 Novel Reactor Design

The designing of the novel reactor was an involved process. It can be broken down into two key segments: ideation and prototyping. The ideation phase involved consultation between supervisors, industry experts and literature to determine the best possible design to go ahead with. The prototyping phase involved the construction of a precursor to the final laboratory-scale reactor, where the fundamentals on whether the ideated reactor would work could be tested. This chapter shall elaborate on both these segments.

6.1 Literature Discussion and Reactor Ideation

As was stressed in the literature review, HAR reactor designs have a fundamental issue in the large pressure head they must overcome. As a result, the design of the novel reactor needed to take inspiration from LAR reactor designs. To this end, the various strengths and weaknesses of the various LAR reactor designs investigated in the literature review were compared. This resulted in the generation of Table 6.1.

Table 6.1 – LAR reactor performance comparison

Reactor Configuration	Lowest Mixing Time	Typical k_La Range [h^{-1}]	k_La Energy Efficiency [$m^3 \cdot h^{-1} \cdot W^{-1}$]	Reactor Scalability [Qualitative]	References
Orbital Shaker	10 s	0 – 38	0.001 – 0.013	Poor	Tissot et al. (2010) Klöckner and Büchs (2012) Klöckner et al. (2013b) Zhu et al. (2020)
Wave	18 s	0 – 750	0.112 – 0.7421	Poor	Jones et al. (2017) Bai et al. (2019) Oosterhuis and van der Heiden (2010)
Raceway	6.0 h	1.8 – 9.6	0.034 – 0.867	Good	Mendoza et al. (2013a) Barceló-Villalobos et al. (2018) Mendoza et al. (2013b)
Travelling Loop	50 s	0 – 32	0.286 – 0.295	Poor	Kaiser et al. (2016b)
Horizontal Tubular Reactor	?	5.1 – 52* (0-14 400)	?* (720)	Good	Yazdian et al. (2009) Al Taweel et al. (2012)
Helical Reactor	?	?	?	Good	Carvalho et al. (2006)

Note that the question marks represent areas where insufficient credible information could be found for inclusion in this table. The asterisks for the horizontal tubular reactor represent information from Al Taweel et al. (2012). These values are so high that it is likely that the energy efficiency calculation performed in this dissertation is erroneous because of additional energies not stipulated by the authors of the paper, hence why it is in brackets.

6.1.1 LAR Reactor Mixing Time and k_La Range

Referring to Table 6.1, only two systems appear to be capable of attaining a k_La above 100 h^{-1}: the wave reactor and the horizontal tubular reactor. Of these, the horizontal tubular reactor's k_La range lacks additional backing outside of a single source owing to scarcity of literature information. This highlights the issues with LAR reactors. They struggle to obtain high enough mass transfer rates to sustain aerobic growth. Mixing times are fortunately more promising, with all designs where such information is available indicating mixing times below 1 minute.

6.1.2 LAR Reactor Energy Efficiency

The best and most reliable mass transfer energy efficiency is achieved by the raceway reactor. This is unsurprising in that the main benefit of the raceway is its low energy usage. The energy efficiency of the wave reactor, specifically owing to the performance of the Cell-tainer® system is additionally impressive. Both systems comfortably surpass the maximum efficiency obtained by any of the three primary HAR reactor types as observed in Table 2.2.

Insufficient information is available on the horizontal tubular and helical reactors to provide reliable energy efficiencies. The lowest mass transfer energy efficiency is obtained in the orbital shaker. This is because the data used to generate the range is for scaled-up orbital shakers which, as previously stated, have poor scalability. As a result, it is not surprising to see that the travelling loop reactor, which is a loop system driven by an orbitally shaken base, does not perform as well as the wave bag reactor and raceway reactor in terms of energy efficiency and is comparable to the HAR reactors in this regard. It is interesting to note however, that the loop design has resulted in a significant increase in energy efficiency over standard orbitally shaken systems. This illustrates an inherit benefit of the loop design.

6.1.3 LAR Reactor Scalability

Reactor scalability is a qualitative score and is based on how well a design lends itself to scaling to larger volumes whilst maintaining reactor performance. For orbital shakers and wave bioreactors, these systems are severely limited in their maximum attainable volumes without significant alterations to energy efficiency and performance and hence have poor scalability for large scale aerobic culture. Raceway reactors have good scalability as their energy efficiency and performance remain consistent throughout their scaling and they can reach extremely large volumes. The travelling loop reactor is interesting with its good mass transfer energy efficiency; however, it is let down by a low k_La range and questionable scalability. The scalability is questionable as it relies on a shaking motion, which historically has poor scalability (as seen with the orbital shaker). The horizontal tubular reactor's scalability is judged on the fact that factories using this technology at a large scale have already been built (Al Taweel et al., 2012). However, concern for the pump power consumption with increasing volume causes doubts with regards to the associated energy efficiency and whether it would remain sufficiently high at larger scales for aerobic culture. The helical reactor design has very little literature available (as mentioned in the literature review), however the concept has very good scaling. Despite being horizontal in nature (it consists of horizontal loops), it can be scaled vertically. This means that significant floor space can be saved and scale-up is easy.

6.1.4 The Proposed Design

Considering the discussion up until this point, the following design was proposed: the horizontal air-injected loop (HAIL) reactor. Inspiration for this system comes predominantly from five key points:

1. The scalability of the helical reactor design.
2. The mass transfer energy efficiency obtainable in the raceway reactor.
3. The performance increase observed in the travelling loop reactor over the similarly operated orbital shakers.
4. The potential for high mass transfer coefficient seen in the horizontal tubular reactor.
5. The desire to design a low aspect ratio reactor to minimise pressure head for aeration

Attempting to model the design over the wave bag reactor would prove fruitless, as the wave reactor is well explored at this point and any possible changes to the design would likely provide minor improvements over those already offered by the Celltainer® configuration if possible. Scaling of the wave reactors remains a key concern as well, as there is no viable way of doing this outside of increasing the bag size, which has a limit. The orbital shaker design clearly offered too low an energy efficiency and suffered poor scaling, without the high k_La possible in the wave reactor. This steered the design towards the loop reactors.

The vertical scaling of the helical reactor is appealing in concept. However, the reactor itself is a continuous loop, which complicates scale-up/design. This brought out the idea of a compartmentalised reactor configuration. If the designed reactor could be stacked, the vertical scaling benefit of the helical reactor could be preserved. Scale-up would be a simple matter of stacking additional “compartments” atop each other and the hydrodynamics of each “compartment” and their associated power draw would remain consistent. In this manner, despite the net system having a high aspect ratio the actual liquid height on a per-compartment basis would remain low. For this approach, the travelling loop reactor was a promising candidate. Its design can easily be stacked so long as the orbitally shaken base plate is removed. The two key concerns then were the maximum attainable k_La and mass transfer energy efficiency.

To enable a high rate of mass transfer, the proposed reactor design would require some form of agitation. As the orbital shaker baseplate was ruled out as a scalable possibility, and the efficacy of paddlewheels in raceways is not ideal, an air-injection approach like that used for horizontal tubular reactors was considered. Air-injection into a low liquid level system results in a significantly reduced energy draw (as the required pressure head is lower), hence overcoming the key issue with HAR reactors. However, a key question remained whether sufficiently high mass transfer rates could be obtained in this manner. Experimentation would need to take place.

With regards to the mass transfer energy efficiency, the following was considered: The typical operating range for the travelling loop reactor was found to be between 0.286-0.295 $m^3 \cdot h^{-1} \cdot W^{-1}$. Comparing this to the efficiencies for the HAR reactors, displayed in Table 2.2, reveals that this is close (but lower) than the maxima found for BCR’s and ALR’s, although it is already superior to that of a STR. However, it is important to note that these ranges do not consider the actual associated power draw for the system, simply the power input. This means that the actual power consumption of the compressor is not accounted for in the correlations. For BCR’s and ALR’s, this power draw for the power input is almost exclusively sourced from the air compressor, however the power input correlations for BCR’s (shown in Equation (2.26) and Equation (2.27)) consider only the pressure head, not the compressor efficiency/power draw. At best for the largest of compressors (2.83-47.2 m^3/s gas flow rates) an energy efficiency of between 76-78% can be obtained (Coker, 2007). Hence, a significant decrease in the observed mass transfer energy efficiency for BCR’s and ALR’s is observed. In the best-case scenario (78% compressor efficiency) the mass transfer energy efficiency is reduced to 0.066-0.247 $m^3 \cdot h^{-1} \cdot W^{-1}$ and 0.111-0.385 $m^3 \cdot h^{-1} \cdot W^{-1}$ for BCR’s and ALR’s respectively. For LAR reactors such as the proposed horizontal loop design, significantly less power is drawn by the compressor as the liquid head is significantly lower for the same volume.

As a result, actual power draw would be expected to be lower for the HAIL reactor. As a final note, not all ALR’s would be expected to capable of operating at the maximum efficiency, hence this does not discourage the concept of the HAIL reactor. A proof-of-concept prototype was therefore approved for construction to investigate whether the concept was functional before more in-depth testing was performed.

6.2 Proof-of-Concept Prototype

6.2.1 Specifying the prototype

The proof-of-concept prototype of the HAIL reactor is displayed in Figure 6.1. The prototype was constructed out of a clear braided PVC hose with an internal diameter of 50 mm and length of 3.17 m. Opposite ends of the tube were connected using a 50 mm PVC connector. The maximum volume of the system was 6.2 L. Three small holes approximately 6 mm in diameter were initially drilled into the top of the reactor, one for the sparger, one to act as an air outlet and one to act as a feed port. A fourth, identical, hole was later added to test the functioning of a dual-sparger set-up. The opposite ends of the reactor were connected using a standard 50 mm PVC pipe connector. Spargers used in this prototype were modelled using TinkerCad and 3D printed with PLA filament using a LulzBot Mini 3D Printer. An example sparger for this prototype system is given in Figure 6.2.

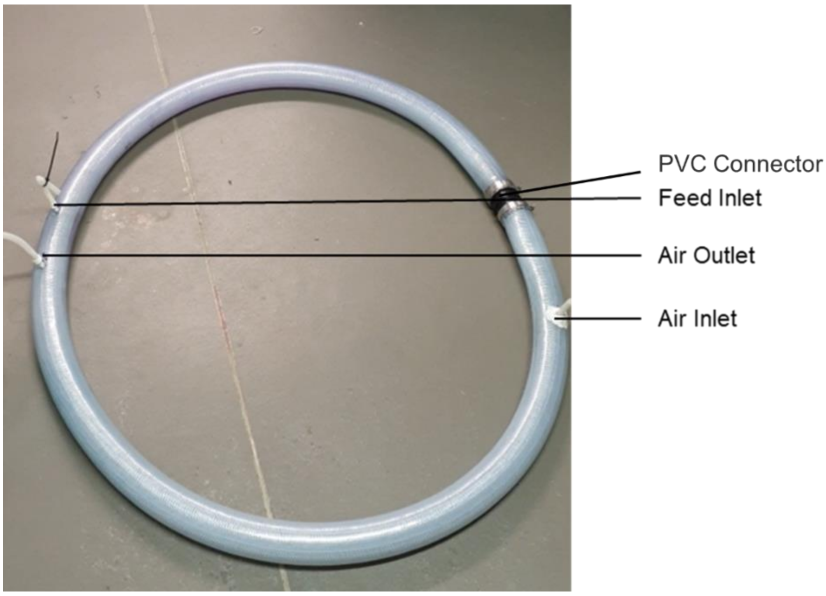

Figure 6.1 – Proof-of-concept prototype HAIL reactor

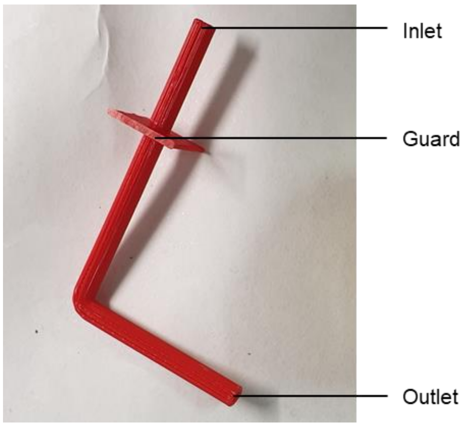

Figure 6.2 – Prototype sparger

Each sparger had a consistent outlet inner diameter of 3.6 mm, corresponding to an area of 10 mm^2, and an outer diameter of 6 mm. The guard had a length and width of 20 mm, with a thickness of 1.2 mm. The function of the guard was to prevent the sparger from falling further into the tube than the desired height in addition to preventing leaks and providing a surface with which to apply adhesive.

6.2.2 Potential Configuration Changes – Sparger Design

Whilst literature has shown that for HAR reactors the sparger design is not of high importance at high agitation and aeration rates (Karimi et al., 2013; Šijački et al., 2013; Thorat et al., 1998), this was not necessarily the case for the HAIL reactor, as sparger design is important for non-heterogenous flow (Šijački et al., 2013). As this was a proof-of-concept prototype, changes to the design were limited exclusively to the sparger design and sparger placement. The following design considerations were considered for the spargers: nozzle depth, number of spargers and nozzle angle.

Nozzle depth was considered important as a lower sparger faces more head pressure, although it maximises the bubble contact time with the liquid. Three depths were tested in this regard: 30 mm, 40 mm, and 50 mm. Nozzle angle was considered important due to preliminary calculations on momentum and energy transfer because of bubble motion (found in Appendix F) indicating that a difference in energy transferred to the liquid would be observed at different angles, with greater horizontal/axial force (and hence a faster liquid velocity) being observed at an angle of 90° (from vertical, relative to 270°) and more vertical/radial force being applied as the angle decreased.

A greater liquid velocity as a result of a 90° sparger angle would result in the liquid travelling through the loop more quickly and hence passing the sparger more quickly, which could lead to improved mixing. Alternatively, whilst the liquid might travel more slowly if the sparger is angled, there would be greater turbulence around the sparger exit area due to an increase in radial flow. This increased turbulence could potentially offset the decrease in velocity, hence the need for multiple angles to be investigated in the proof-of-concept prototype HAIL reactor. Detailed calculations concerning mathematical predictions of the final liquid velocities were not performed as the science of bubble physics is complex and outside the scope of this dissertation. To this extent the following sparger angles were tested in the proof-of-concept prototype: 45°, 60°, 75°, and 90°. Finally, the number of spargers was tested to see whether multiple inlets might improve turbulence in the system and so the k_La. A diagram of the sparger set-up, as well as 3D models of all the tested sparger designs are presented in Appendix E.

6.2.3 Methodology, Materials and Methods

The primary objective of the proof-of-concept build was to verify whether the design demonstrated potential or carried a fundamental flaw that would prevent it from functioning. The secondary objective was to perform a preliminary investigation into the impact of sparger design on performance. Both objectives were accomplished via the use of a food colourant tracer as an indicator for circulation time in the semi-transparent system. Due to the scale and focus of the system, no large probes were inserted in the system so as not to obstruct the liquid flow.

Dye Tracer Circulation Time Test

The dye tracer test was performed exclusively at a reactor volume of 4 L, corresponding to a liquid height of 30.5 mm in the reactor. For each experiment, the sparger/s being tested was/were inserted into the air inlet hole/s situated on the reactor roof and then angled to be straight. They were then secured in place with Prestik.

The air flow rate was then set to 2 vvm (8 LPM) and the flow in the reactor was given 10 minutes to establish itself properly. Once the system was ready, a 5 mL syringe was used to transfer a 1 mL pulse of red food colourant into the reactor via the feeding port at the same time a timer was started. The flow of dye through the system was then observed, whilst checking for any potential dead-zones in the flow. Once the tracer had completed an entire loop of the system, the timer was paused, and the circulation time was recorded. This process as then repeated once again with additional red food colourant, then finally with blue food colourant (at which point the bulk liquid was too dark to continue adding more dye).

At this point, the sparger/s being currently tested was/were removed and the reactor drained. This allowed for the reactor be reconfigured for the next experiment. This procedure was repeated for every sparger configuration designed.

6.2.4 Results and Discussion

The results of the proof-of-concept prototype, while operated at a gas flow rate of 8 LPM, were initially promising as no dead zones could be observed within the system using the food colourant, indicating no major flaws with the system. The results of these preliminary experiments are summarised in Figure 6.3.

Inspection of the data reveals that the fastest circulation times were observed when the sparger outlet was positioned at a depth of 30 mm in the reactor (just below the liquid surface) and at a depth of 50 mm (the bottom of the reactor). The sparger with the most consistent fast circulation times was the 60° sparger, followed by the 45° sparger, then the 75° sparger and finally the 90° sparger. These results were surprising as it was expected that a 90° angle would result in the maximum horizontal energy transfer to the system, supported by the preliminary bubble calculations in Appendix F. Furthermore, the large discrepancy between circulation times at 30 mm and 50 mm versus those at 40 mm also disagrees with the preliminary calculations, as the bubbles should stop motion nearly instantly upon entering the water and so depth should not be an issue (which was a desired outcome for this experiment). These results gave way to suspicion about the integrity of the proof-of-concept reactor. This placed greater emphasis on the need for additional experimentation in the laboratory-scale prototype reactor.

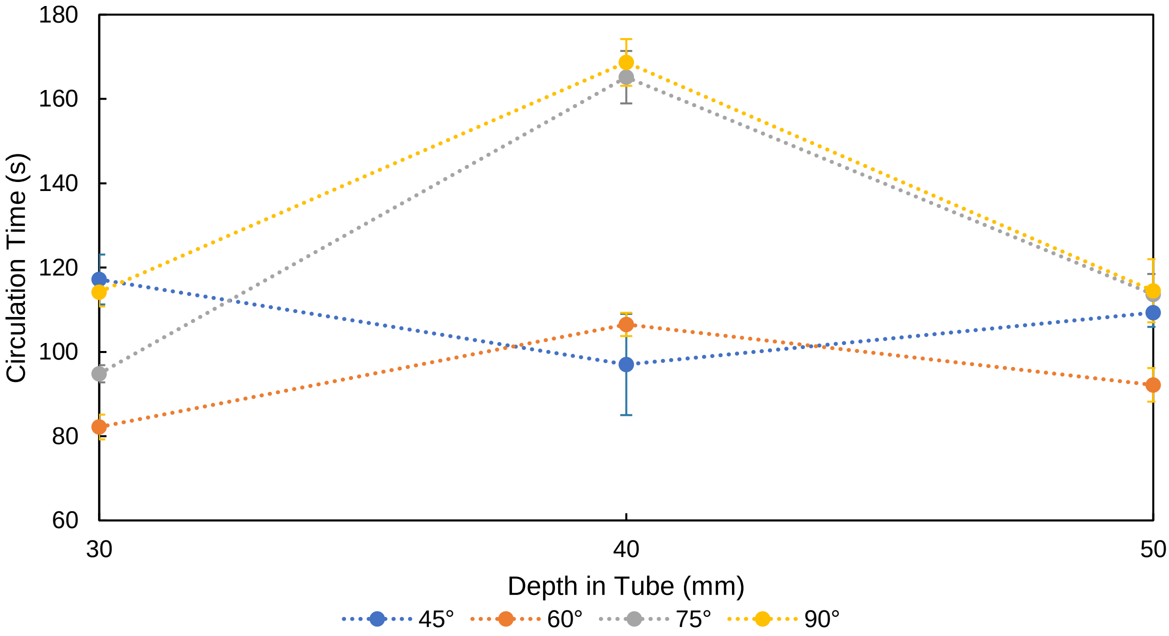

Figure 6.3 – Circulation time at different depths for different sparger designs on aeration at 8 LPM in a HAIL reactor filled with 4 L of tap water

Error bars represent the 95% confidence interval for each data point as determined via t-test.

6.3 Laboratory-scale Prototype

6.3.1 Prototype Reactor Design

To improve the reliability and reproducibility of the data, a levelled table was constructed for the laboratory-scale prototype. Outside of reactor scale, no changes to the physical design of the reactor were considered at this stage, as the result of the proof-of-concept prototype required verification in the laboratory-scale system. Because the laboratory-scale system, with a maximum working volume of 31.4 L, was significantly larger than the proof-of-concept prototype with a maximum working volume of 6.4 L and had an increased inner diameter of 100 mm, the material of construction was altered. Clear braided PVC hose is incapable of supporting such a large diameter without collapsing on itself, so instead Heliflex tubing was used. The completed system is presented in Figure 6.4. The laboratory-scale design had a length of 4.0 m. A small kink was present in the reactor because the tube was heated to connect the opposite ends to the stainless-steel connector. To reduce the number of sensors blocking flow in the reactor, a very narrow pH probe was used in the system for pH measurement and "dot" sensors were employed for DO measurements. These dots are non-autoclavable PreSens oxygen sensor spots (SP-PSt7-NAU) and work in conjunction with a PreSens OXY-1 SMA compact fibre optic oxygen meter. The operation of this equipment is discussed later in this chapter. The dots are not visible in Figure 6.4 as they are internal although the location of the "front" dot is shown (this DO dot was placed in front of the sparger outlet). A second, "back" DO dot (located behind the sparger nearby the temperature port) was also present.

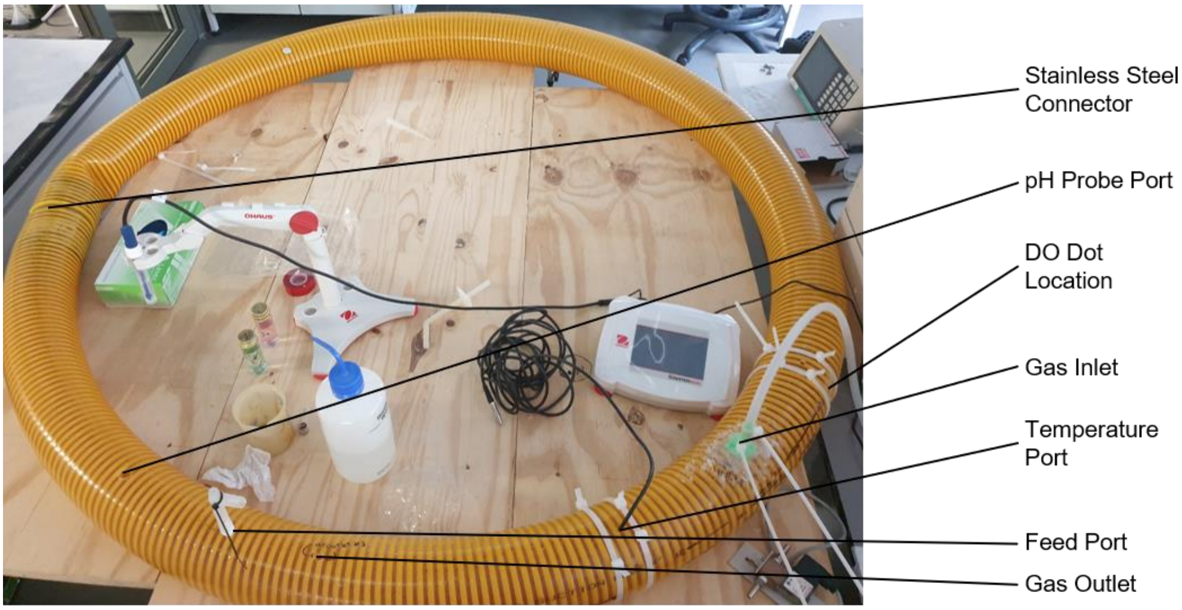

Figure 6.4 – HAIL reactor

6.3.2 Potential Configurations to Test

Sparger designs for the proof-of-concept prototype dealt exclusively with depth of the sparger and angle of the sparger.

Following from Figure 6.3, the difference in performance between having the sparger situated near the surface, versus near the bottom was not significant enough to expect the rising liquid level during fed-batch operation to negatively impacting reactor performance. As a result, all the new spargers' designs were limited to the maximum depth within the laboratory-scale system.

Angle data from Figure 6.3 indicated that the 60° sparger was the best overall performer, however the 90° sparger performed unexpectedly poorly considering the preliminary bubble calculations in Appendix F. As a result, both angles were investigated in the laboratory-scale system. As the system had increased in size, the spargers' thickness was increased proportionately, resulting in an outer diameter of 9.6 mm. The guard was improved upon, made thicker to provide more rigidity (4 mm thick) and a triangle attached to the front end for easier alignment of the sparger with the tube. This allowed for consistent sparger placement to help reduce potential error. An example of one such upgraded sparger is depicted in Figure 6.5.

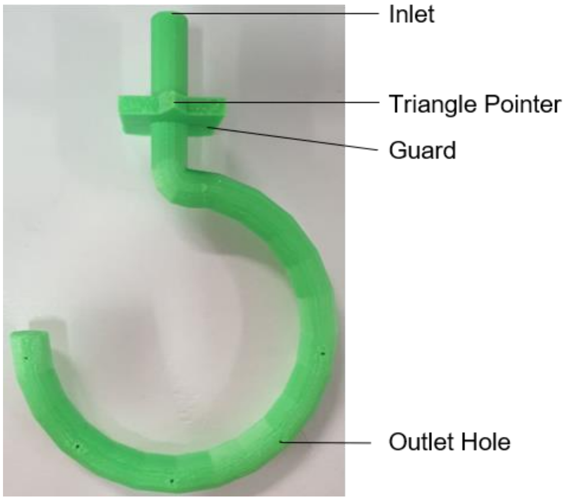

Figure 6.5 – Circle sparger with improved guard design

Figure 6.5 represents one of the new sparger designs tested in the laboratory-scale prototype, with a semi-circle shape. The purpose of this sparger design was to determine whether a flow dispersed over a greater area of the tube would prove to have a more beneficial impact on mixing time, circulation time and/or mass transfer than a sparger focus on a single jet.

Additional sparger designs were based on the initial single nozzle sparger. One such design included the inclusion of five outlet orifices at the end of the sparger as opposed to one, making up constant total area of 10 mm^2 to not increase the associated pressure. The purpose of this was to shrink the bubble size, whilst maintaining the same effective sparger area. An additional design included the reduction of the total outlet area to 2 mm^2 from 10 mm^2 to purposefully increase the pressure and associated gas velocity. These two designs were applied to both the 60° and 90° spargers. The complete list of tested configurations is presented in Table 6.2 and 3D models of all the sparger designs used in the laboratory-scale HAIL reactor can be found in Appendix E.3.

Table 6.2 – List of tested spargers in laboratory-scale prototype HAIL reactor

Sparger Name	**Sparger Angle**	**Number of Outlets**	**Hole Diameter [mm]**	**Total Outlet Area [mm^2]**
60d	60°	1	3.6	10.20
90d	90°	1	3.6	10.20
60dm	60°	5	1.6	10.05
90dm	90°	5	1.6	10.05
60s	60°	1	1.6	2.036
90s	90°	1	1.6	2.036
c1	N/A	5	1.6	10.05

Note that the letters “d”, “m”, “s”, and “c” are personal naming conventions representing the words “default” (as this was the jet spargers were the first sparger designs considered), “multiple” (for multiple holes as opposed to a single hole with respect the angled jet spargers), “small” (as the total outlet area of these spargers is smaller than the rest) and “circular” (as this was the only circular sparger design).

6.3.3 Methodology, Materials and Methods

For each reactor configuration tested, the sparger was inserted into the air inlet with the triangle facing the direction of the tube. To ensure no air leaks would be present and to fix the sparger in place, silicon glue was used around the sparger guard. When a sparger needed to be changed, a knife was used to cut away the silicon glue and allow for removal of the sparger. A new sparger could then be placed.

Fill volume was an important characteristic to consider in these experiments. Due to the shape of the HAIL reactor, a change in volume results in a varying exposed surface area relative to the total volume. The liquid level also changes with increased volume, resulting in a larger pressure head due to the spargers’ location at the bottom of the reactor. The increased liquid height also has an impact on the observed wave formation/turbulence in the reactor. The volumes tested and their corresponding liquid heights were different depending on the goals of each experiment, as more in-depth analyses were performed on more promising sparger designs. However, the entire range of volumes tested over all laboratory-scale HAIL reactor experiments was as follows: 12 L, 14 L, 16 L, 20 L, 23 L, 26 L, 27 L and 28 L. The corresponding heights were 41 mm, 46 mm, 51 mm, 61 mm, 69 mm, 77 mm, 80 mm, and 84 mm. Figure 6.6 demonstrates this relationship between volume and height, as well as the resultant fill percentage, in the HAIL reactor.

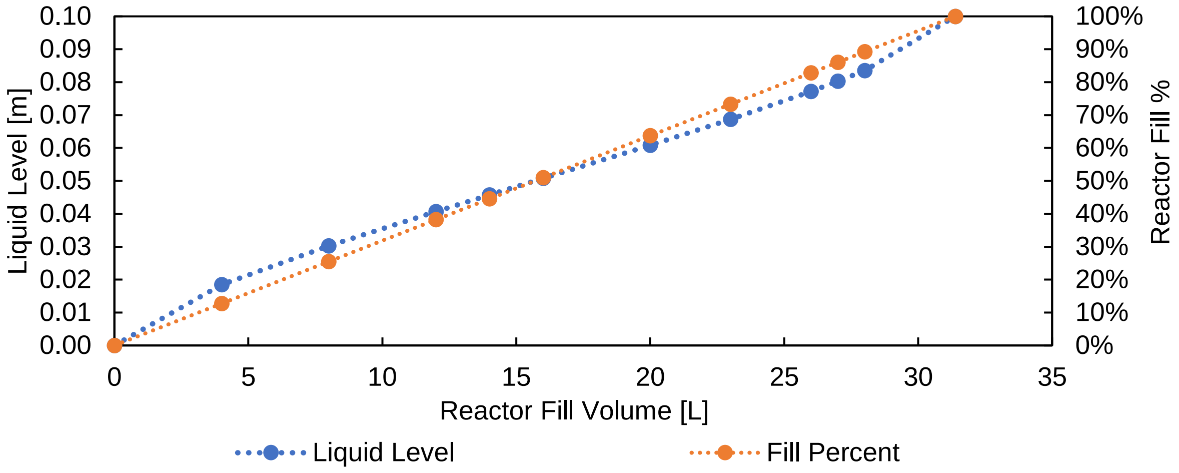

Figure 6.6 – Laboratory-scale HAIL reactor fill volume vs. liquid height

Mixing and Circulation Time Experiments

Mixing and circulation time in the system were both determined with a pH tracer method. This method was carried out in the following manner:

At first, a 1 L 1M solution of HCl was prepared for lowering the pH, in addition to a 1 L 1M solution of NaOH for raising the pH. At this point, the reactor configuration was set up. First by inserting the appropriate sparger into the reactor a day in advance and sealing it with silicone glue (which was given the day to harden). Once the sparger was in properly, the reactor was then filled to the target volume for the experiment that was being conducted. At this point the pH probe/monitor (an Ohaus ST5000-B that was calibrated once daily) was inserted into the reactor via the pH probe inlet. Air flow to the reactor was then enabled and set to 2.0 vvm to aid in mixing.

For the tracer portion of the experiment, at first approximately 4 mL of HCl was added to drop the pH to approximately 4.5 using an Eppendorf P5000 micropipette. The system was then given time to stabilise around its new pH value. The point of this pH reduction was to add stability to the readings once the full experiment commenced. If the pH was still greater than 5 after the acid addition, more HCl was added, and the reactor was left until the pH stabilised once again.

At this point, the true experiment could begin. For each experiment the air flow to the reactor was initially changed to the flow rate being tested. The system was then left for 15 minutes to allow for the liquid speed and flow pattern to stabilise with the new air flow rate. 2 mL of 1M HCl were then added to the system and the pH probe's recorder functionality was enabled to observe the change in pH over time. Measurements continued until the pH stabilised, whereupon pH recording was paused. Acid additions followed by measurements were repeated until such a point as the "stable" pH dropped below 3.5. At this point 1M NaOH was added instead of the 1M HCl in identical volumes. A minimum of 3 repeats of the experiment were performed for each sparger configuration.

This method was first applied in absence of any mass transfer analysis (owing to the DO dots not having arrived from Germany yet). The 60d configuration that had achieved the fastest circulation times in the proof-of-concept prototype was the first configuration to be used in the laboratory-scale HAIL reactor prototype. As a result of it being the first tested configuration, preliminary experiments on the impact of liquid height on the circulation time were conducted using the 60d sparger as opposed to the "best" sparger, which had not yet been found. The 90d sparger was tested immediately after this. However, it was found that the circulation and mixing times were better than the 60d sparger, hence similar tests were conducted on the 90d sparger at different volumes. For all other configurations, excluding the best performing configuration, the only volume/liquid height tested was 20 L/61 mm at gas flow rates of 15 LPM, 20 LPM and 30 LPM, except where the sparger was incapable of supporting such a gas flow rate. The experiments conducted on each sparger are tabulated in Appendix F. Once the DO dots had arrived and been inserted, mixing time/circulation time analysis took place in parallel with an associated

k_La measurement (during the gassing-in phase) whenever possible to save time. The method was otherwise unchanged.

An example of experimental data from the mixing studies is presented in Figure 6.7. Data analysis was conducted by means of an automated Microsoft Excel spreadsheet. The spreadsheet's input consisted of the raw pH data from the pH probe/monitor. This data was then converted into H^+ ion concentration versus time. A series of data manipulations were then applied to automatically identify peaks in the system and determine the average final pH. The circulation time was given by the average time between peaks, whilst the mixing time was given by the amount of time it took for the peaks to fall within 5% of the final concentration value. The final concentration value was determined by taking the average of all values over the experiment, however when this method failed a visual eye test, the concentration line was manually adjusted.

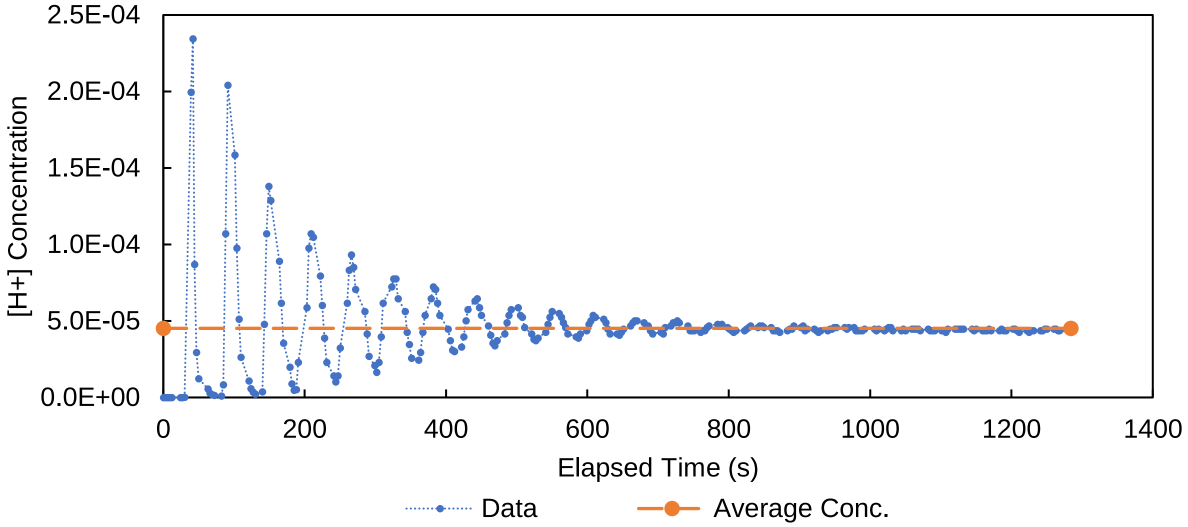

Figure 6.7 – Sample mixing and circulation time data

k_La Measurement Technique

DO measurements were performed using a PreSens OXY1-SMA compact fibre optic measuring meter. This meter allowed for the insertion of very small and thin sensor spots to be placed in the designed reactor which would not inhibit flow. A cable attached to the measuring meter shines a light on the sensor spot, which provides the device with a DO reading. The response time for the probe was below 2-3 seconds, hence as per Riet and Tramper (1991) this value could be ignored during k_La calculations. As a result, k_La could be determined via Equation (2.13).

To take k_La measurements in the HAIL reactor a set procedure had to be followed. First, the reactor was filled to a target volume, specific to the requirements of the experiment being conducted. The reactor was then sparged with nitrogen so that a zero DO calibration point could be established. Following from this the reactor was sparged with air until the DO stopped increasing so a saturated DO calibration point could be established. The reactor was then once again sparged with nitrogen, until the DO had dropped sufficiently low for the experiment to commence (DO% at least below 30%). The reactor aeration rate was then set to the experiment's target gas flow rate and recordings were taken automatically via software. Aeration was cut off once the DO reading stopped increasing, marking the end of an experiment run, and the experiment was repeated twice more.

This method was applied to all sparger configurations listed in Table 6.2 at a constant volume of 20 L (corresponding to a liquid height of 61 mm) and a gas flow rate of 20 LPM (1 vvm). As only one position could be read at a time, for these experiments the mass transfer was observed behind the sparger outlet (the expected worst-case scenario performance). The best performing sparger was then determined from this data, and a series of additional experiments were performed using the same method with alterations to various conditions to better understand the system.

The first such batch of experiments tested the circle sparger's performance at gas flow rates of 0.75 vvm, 1.50 vvm and 2.00 vvm such that a trend could be established. The second such batch of experiments targeted a fill volume of 20 L at gas flow rates of 0.75 vvm, 1.00 vvm, 1.50 vvm and 2.00 vvm with the optical sensor attached to a DO dot situated directly in front of the sparger (as opposed to the typical position behind the sparger). The final set of additional experiments were performed at volumes of 23 L and 26 L (corresponding to liquid heights of 69 mm and 77 mm respectively) at a fixed gas flow rate of 30 LPM to determine the change in reactor performance vs liquid height (as the 20 L 1.50 vvm experiment corresponded to a gas flow rate of 30 LPM).

It was noted that the mass transfer coefficient due to surface aeration was a desirable value for the analysis of the HAIL reactor. To obtain this information, a modification of the 90d sparger was made such that the sparger rested well above the liquid line in the reactor. Volumes of 12 L, 20 L and 26 L were chosen, corresponding to fill percentages of 38%, 64% and 83%. These volumes were chosen as they gave a good indication of a low, average, and high fill volume. The aeration was set at 20 LPM owing to the large number of sparger experiments conducted at 20 L and 1 vvm. Steps 1 through 7 were then followed for these experiments.

Determination of Power Input per Unit Volume

Ideally, power input into the HAIL reactor would be determined using an experimental technique. However, designing a technique to determine this experimentally was outside the scope of this dissertation. A calorimetric method might have been used instead, but insufficient insulation for the system and a complete lack of temperature control in the laboratory-scale prototype made this difficult. Therefore, due to the novelty of the reactor design, the power input per unit volume for the HAIL reactor was determined mathematically.

This was done using the assumption that the associated compressor power draw with a given gas flow velocity and sparger size would approximate the power input. This would be an overestimate of the actual power input, as the compressor would not transfer energy into the liquid with 100% efficiency and not all imparted energy would go towards mixing and mass transfer. As a result, all mass transfer power efficiencies are expected to be higher than the values calculated in this dissertation. The calculation went as follows:

On the assumption that the reactor is operating at atmospheric pressure (as it is open to the atmosphere), the pressure required to feed air at atmospheric pressure to the reactor was determined using the Bernoulli Equation:

$$P_{compressor\ outlet} + \frac{1}{2}\rho_{air}v_{initial}^2 + \rho_{liquid}gh_{outlet} = P_{outlet} + \frac{1}{2}\rho_{air}v_{final}^2 + \rho_{liquid}gh_{liquid} \quad \text{Equation (6.1)}$$

All pressures are calculated in pascals, heights are recorded in meters, velocities are recorded in m/s, gravity has units m/s^2 and the densities are recorded in kg/m^3. The pressure at the compressor outlet is the unknown, the initial gas velocity is assumed to be zero and the liquid density can be determined either experimentally or via literature (in the case of water). The height at the sparger outlet is assumed to be 0 (as it is situated at the bottom of the system). The pressure at the outlet of the sparger is assumed to be 1 atm (101 325 Pa) as the system is operating at atmospheric pressure. The liquid height is dependent on the fill volume of the reactor, and the final velocity of the gas can be determined using the total area of the sparger outlet and the volumetric gas flow rate.

Once the pressure has been obtained, the associated compressor power draw is determined. Two resources were used to this extent, the first being Coker (2007) and the second being Green and Southard (2019). The equation specified by Coker (2007) is as follows:

$$P_{compressor} = (SCFM) \cdot \frac{T_1}{8130\left(\frac{k-1}{k}\right)}\left[\left(\frac{P_2}{P_1}\right)^{\frac{k-1}{k}} - 1\right] \quad \text{Equation (6.2)}$$

Where “$P_{compressor}$” is the compressor power in horsepower, “$SCFM$” is the gas flow rate in ft^3/min, “T_1” is the compressor inlet temperature in Rankine (assumed for a standard case of 25 °C and converted to °R), “k” is the ratio of specific heat of the gas (air in this scenario, which is a value of 1.4), “P_1” is the compressor inlet pressure (assumed to be atmospheric in this scenario) in kPa and “P_2” is the compressor outlet pressure in kPa. The equation specified by Green and Southard (2019) is instead as follows:

$$P_{compressor} = 2.78 \times 10^{-4} \left(\frac{k}{k-1}\right) Q_1 P_1 \left[\left(\frac{P_2}{P_1}\right)^{\frac{k-1}{k}} - 1\right] \qquad \text{Equation (6.3)}$$

Where “$P_{compressor}$” is the compressor power in kW, “Q_1” is the gas flow rate in m^3/h, “k” is the ratio of specific heat of the gas, “P_1” is the compressor inlet pressure (assumed to be atmospheric) in atm and “P_2” is the compressor outlet pressure in atm. Both are approximations and differ slightly in their output, with Equation (6.2) resulting in slightly higher values than Equation (6.3). Due to this work being a preliminary investigation, results from Equation (6.2) are used in the discussion of data as it is a “worst-case” scenario.

Live Cell Fermentation and Viscosity Experiments

Aerobic cultivation of yeast was a goal of the HAIL reactor. However, the mixing time and mass transfer results (as detailed in Chapter 7), in addition to time constraints, meant that any cultivation which might be performed in the system would prove uninformative, based on the preliminary performance information obtained from the STR runs. However, assessing the impact of viscosity on the system’s performance was still of importance. This is because the viscosity in a typical aerobic fed-batch process tends to increase with increasing cell density.

To increase the viscosity without growing cells, glycerol was added to the reactor as a viscosity modifier. Calculations were performed using correlations between glycerol concentration as wt% and liquid viscosity in glycerol/water systems at specific temperatures to determine the mass of glycerol to be added. Glycerol used in this calculation was 99.5% pure, to match the specification of the Sigma-Aldrich ≥ 99.5% glycerol available in the laboratory. The maximum viscosity to be tested was the maximum viscosity obtained in the fed-batch STR runs. If the performance of the system did not change noticeably at this viscosity, it could be concluded that the system was not sufficiently sensitive to viscosity for it to be included as a design factor.

Once a glycerol solution of the desired concentration had been prepared, the viscosity was double checked using a viscometer. If the measured value were less or greater than expected, the viscosity was corrected with water or glycerol depending on the requirements. Viscosity experiments were limited to the best performing sparger design as determined from the mixing time and k_La measurement experiments. Once the target viscosity had been reached and manually verified, both mixing time and mass transfer experiments were conducted. The method followed for both was identical to that previously described.

As the laboratory-scale HAIL reactor prototype lacked temperature control, the viscosity needed to be taken prior to every experimental run if the temperature had varied by more than 1°C from a prior run.

7 HAIL Reactor Results and Discussion

7.1 Initial Test Results

The first tests conducted upon initial construction of the HAIL reactor were mixing and circulation time experiments using the 60d sparger configuration, owing to its success in the proof-of-concept prototype. The focus of these initial tests was to verify that the system was functional. Further, the system's mixing performance was investigated at different fill volumes and aeration rates.

Figure 7.1 illustrates the circulation time data from the 60d sparger configurations, with gas flow rates both in LPM and in terms of vvm. Using LPM data accounts for the actual gas flow rate (which is tied to the power input) and provides a superior understanding of the systems performance. The vvm data has been used as a parameter for scaling in HAR reactors in the past (Nauha et al., 2015), as it is useful in that it maintains the ratio of air fed to a system per litre; this provides a relationship to P/V and compares reactors across a similar availability of oxygen supply per unit volume. Nauha et al. (2015) explicitly mention that power input per unit volume is a better mechanism for scaling than vvm in HAR reactors.

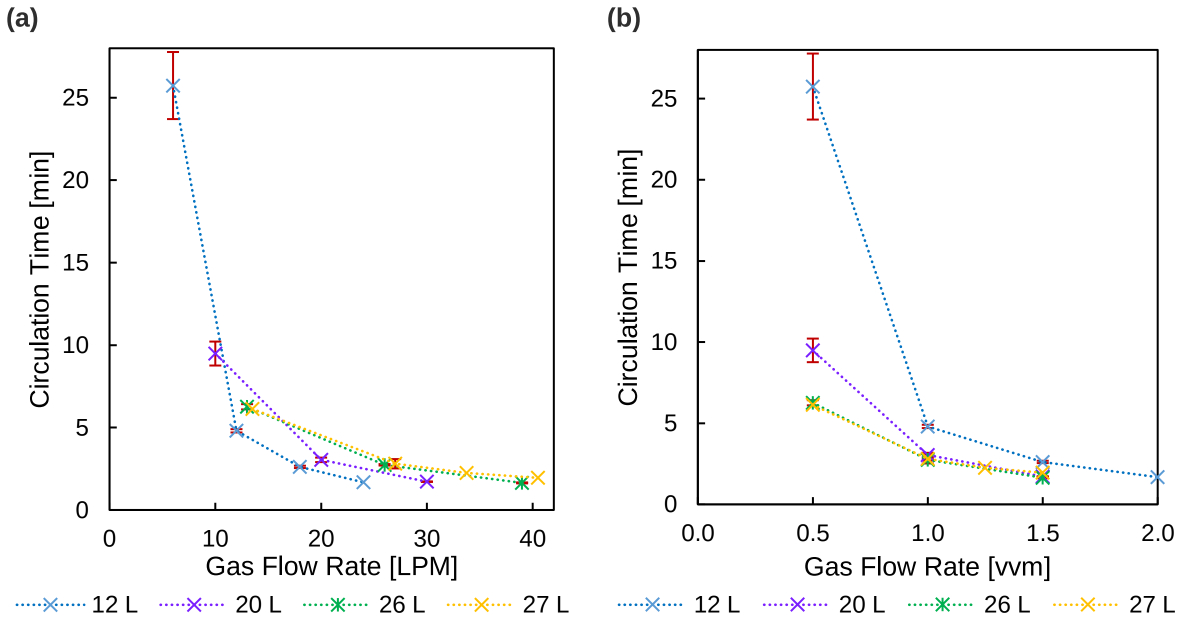

Figure 7.1 – Circulation time vs gas flow rate in LPM (a) and vvm (b) for the 60d sparger configuration operated at four fill volumes

Error bars represent the 95% confidence interval for each data point as determined via a t-test.

The circulation time data is useful in that it indicates the liquid velocity in the system. Converting the circulation time to seconds and dividing the reactor length (4 m) by this time gives a range of liquid velocities between 0.003-0.039 m/s for circulation times between 25.7-1.7 minutes. From Figure 7.1 (a), the increase in the circulation time is strongly dependent on gas flow rate at any gas flow rate lower than 10 LPM. The impact of increasing the gas flow rate beyond approximately 24 LPM appears to have limited benefits, with a very reduced change in circulation time in this region. This decrease in the improvement of circulation time is better illustrated in Figure 7.1 (b), where at 1.50 vvm it can be visibly seen that despite the differences in volumes, almost all systems have a similar circulation time (with notable overlap between the observable error bars for the 95% confidence intervals). This is not improved further on increasing to 2 vvm.

Circulation time data alone is not comparable to literature information on HAR reactors, as they do not have a direct comparison (liquid travel speed is not measured in HAR reactors as mixing time is the more useful metric). Figure 7.2 shows the obtained mixing times (with their associated 95% confidence intervals) in the HAIL reactor with the 60d sparger configuration. It can be observed, as with the circulation time, that there is a drastic decrease in the mixing time with increasing gas flow rate in the range 6 to 20 LPM. This negative exponential trend highlights the importance of not operating the HAIL reactor at very low gas flow rates. Hence regardless of the actual oxygen demand at a point, the results from the 60d sparger configuration indicate that the reactor must be maintained above a certain gas flow rate to maintain operable mixing and circulation times; in this reactor a flow rate of 10 LPM or greater is proposed. Increasing the gas flow rate decreases the mixing time up to a point, after which the reduction is much more gradual. This eventually appears to level off at gas flow rates in the range 20 to 38 LPM, at a mixing time between 14 and 18 minutes for the 60d sparger.

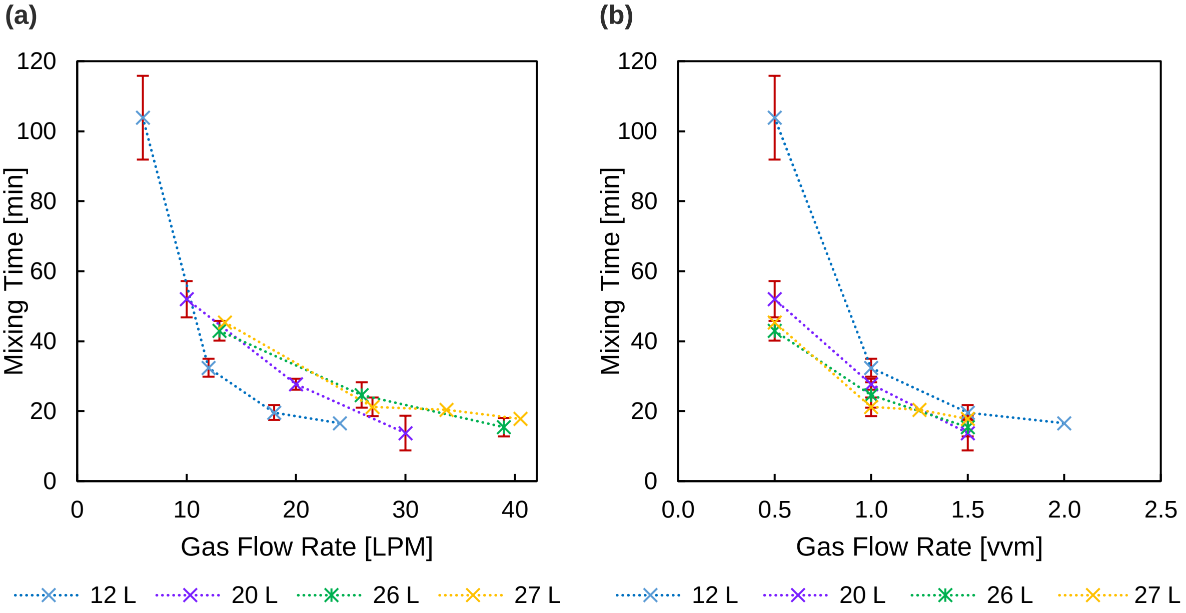

Figure 7.2 – Mixing time vs gas flow rate in LPM (a) and vvm (b) for the 60d sparger configuration at different fill volumes

Error bars represent the 95% confidence interval for each data point as determined via a t-test.

As most mixing occurs at the sparger outlet, a faster circulation time will result in liquid passing the sparger more frequently, resulting in faster mixing. Referring to Figure 7.2, the mixing time indicates agreement with this. This relationship is further elaborated on in Figure 7.3, where an R^2 of 0.96 can be observed, indicating a high level of correlation between the two. As these two are linked due to the frequency of passes through the sparger, it is therefore theoretically possible to improve the mixing time further by introducing air into the reactor at two different points as opposed to one.

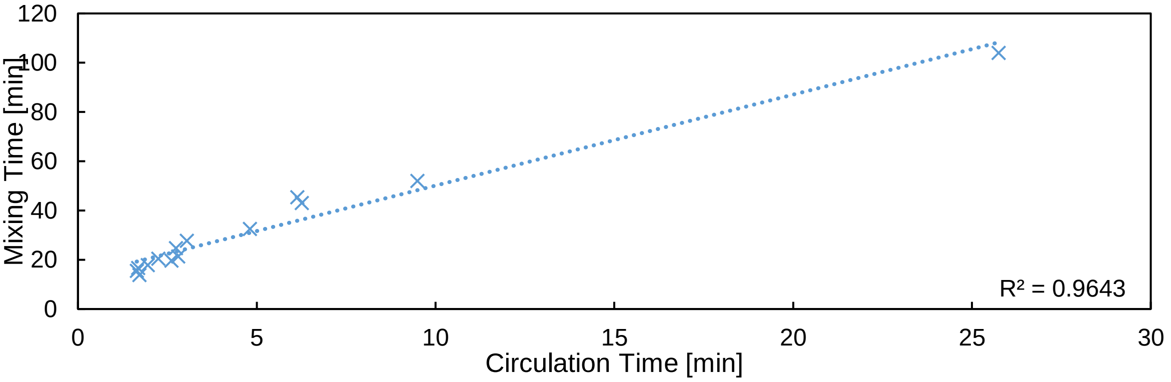

Figure 7.3 – Comparison between mixing time and circulation time for all volumes using the 60d sparger configuration

It is evident from the above results that the mixing time of this configuration of the HAIL reactor (14-107 minutes) is uncompetitive with the mixing times typically expected in HAR reactors (or even other LAR reactors), referring to both Table 2.1 and Table 6.1. From these it can be observed that STR's, BCR's and ALR's having mixing times below a minute depending on configuration and the only LAR reactor incapable of reaching mixing times below a minute is the raceway reactor.

The purpose of the 60d sparger design was to serve as a preliminary baseline for comparison for the additional sparger designs to be tested. For this reason, mass transfer experiments were performed with the 60d configuration at a volume of 20 L. Two zones of interest were identified for these experiments: directly in front of the sparger and directly behind the sparger. These two zones would represent the lowest and highest mass transfer rates in the reactor. Behind the sparger represents the furthest possible point away from the primary source of mass transfer (the sparger outlet). The area directly in front of the sparger experiences the most turbulence and direct contact with the bubbling air and should instead have the highest mass transfer coefficient. The results of this study demonstrate the different mass transfer coefficients observed in different regions of the HAIL reactor while operating at a specific power input. They are presented in Figure 7.4.

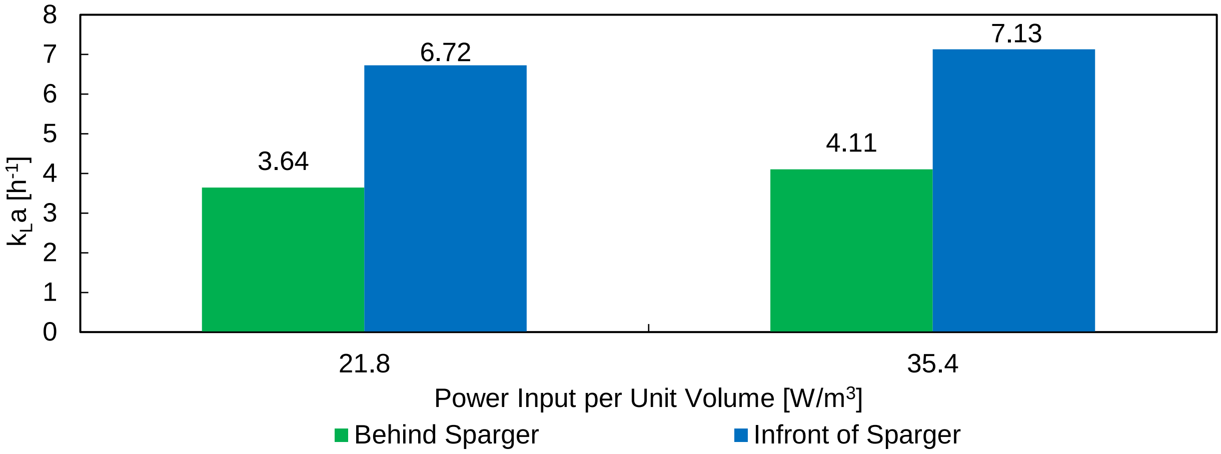

Figure 7.4 – Mass transfer coefficient vs. power input per unit volume at 20 L fill volume for the 60d sparger configuration

The mass transfer coefficient is higher in front of the sparger than behind the sparger, as theorised above. Comparing these k_La values to those specified in Table 2.2 for HAR reactors, it is apparent that the performance of the 60d sparger in terms of mass transfer capacity is lower by an order of magnitude. Additionally, increasing the power input from 22 W/m^3 to 35 W/m^3 does not have a large impact on the mass transfer coefficient. The power inputs correspond to gas flow rates of 20 and 25 LPM, which is in the same range that the circulation time ceases to drastically improve with increasing gas flow rate (20-38 LPM as observed in Figure 7.2). Study across a wider range of gas flow rate and associated P/V is required to draw rigorous conclusions. Additional testing was evidently necessary.

7.2 Sparger Comparisons

As was mentioned in sub-section 6.3, a total of seven different sparger designs were designed and tested, the exact specifications of which can be found in Table 6.2. Comparisons between these spargers are broken up between mixing/circulation time and mass transfer.

7.2.1 Mixing and Circulation Time Performance

Figure 7.5 and Figure 7.6 detail the observed circulation and mixing times across a range of gas flow rates for all the sparger configurations tested. Referring to both figures, it can be seen that (as with the 60d design) the mixing and circulation time are connected, with spargers performing similarly in both aspects, i.e. there is no sparger that has a circulation time lower than another sparger that does not also have a mixing time lower than that sparger at a given gas flow rate.

Referring to the mixing times presented in Figure 7.6, it is observed that the lowest mixing time at the lowest gas flow rate is held by the 90s sparger configuration, followed by the 60s configuration and then finally the c1 configuration. Circulation times range between 1.0-1.6 minutes and 0.4-0.9 minutes for the 60s and 90s spargers respectively, with associated mixing times ranging between 16-11 minutes and 13-8 minutes respectively. This better supports the bubble calculations shown in Appendix D, as the additional forward momentum owed to the 90° sparger increases the circulation time and hence enhances the mixing time over the 60° spargers. This trend can be observed across all the angled sparger permutations, with the mixing and circulation time for the 60° spargers being outclassed by their 90° equivalent. Following from this, the best performance of mixing time as a function of gas flow rate is held by the 90s configuration; however, P/V must also be considered.

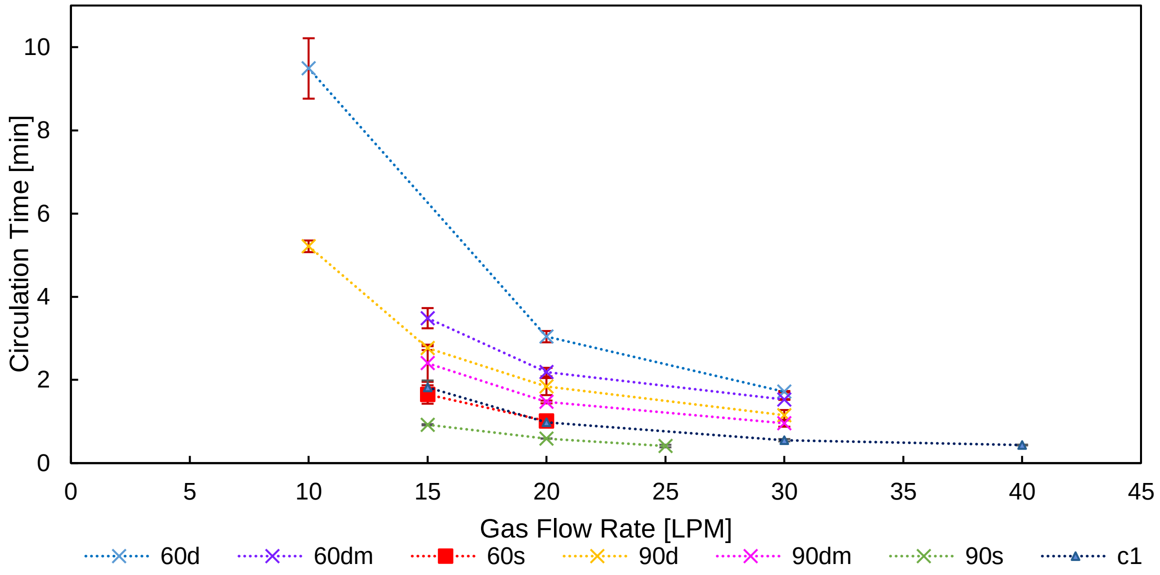

Figure 7.5 – Circulation time vs. gas flow rate at 20 L fill volume in HAIL Reactor across all sparger designs

Error bars represent the 95% confidence interval for each data point as determined via a t-test.

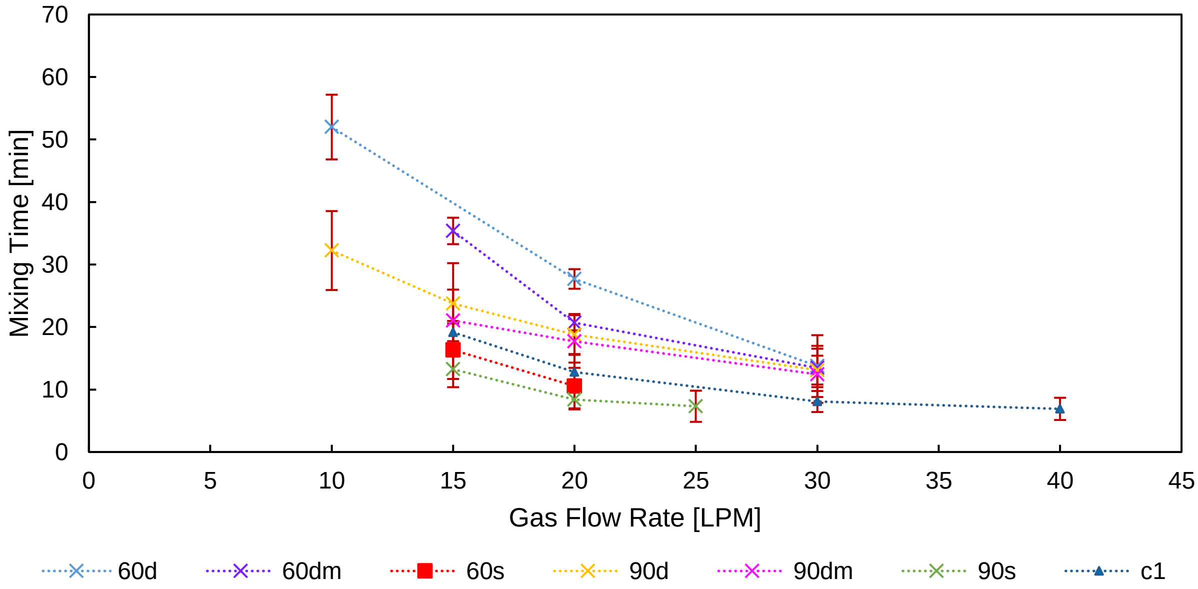

Figure 7.6 – Mixing time vs. gas flow rate at 20 L fill volume in HAIL Reactor across all sparger designs

Error bars represent the 95% confidence interval for each data point as determined via a t-test.

The 60s and 90s spargers both have smaller outlet areas of 2 mm^2 as opposed to the 10 mm^2 outlet area present on all other spargers. This has a direct impact on the observed power input per unit volume, as it increases the superficial gas flow velocity. The relationship between mixing time and P/V across the three favoured spargers is presented in Figure 7.7. Note that all power inputs displayed here are calculated using Equation (6.2) as it results in the largest values (hence, a worst-case scenario for power efficiency). It is immediately apparent from Figure 7.7 that the energy efficiency of mixing for the c1 sparger is superior to both the 60s and 90s spargers. The 95% confidence intervals at the 4th data point for the c1 sparger do not overlap with the 95% confidence intervals for the 60s and 90s spargers at a higher power input of 123 W/m^3, indicating that this observation is significant. The importance of considering power input per unit volume as opposed to gas flow rate is highlighted by this, supporting the findings of Nauha et al. (2015). Extending the power input analysis to the other spargers yields a similar observation, as can be seen in Figure 7.8.

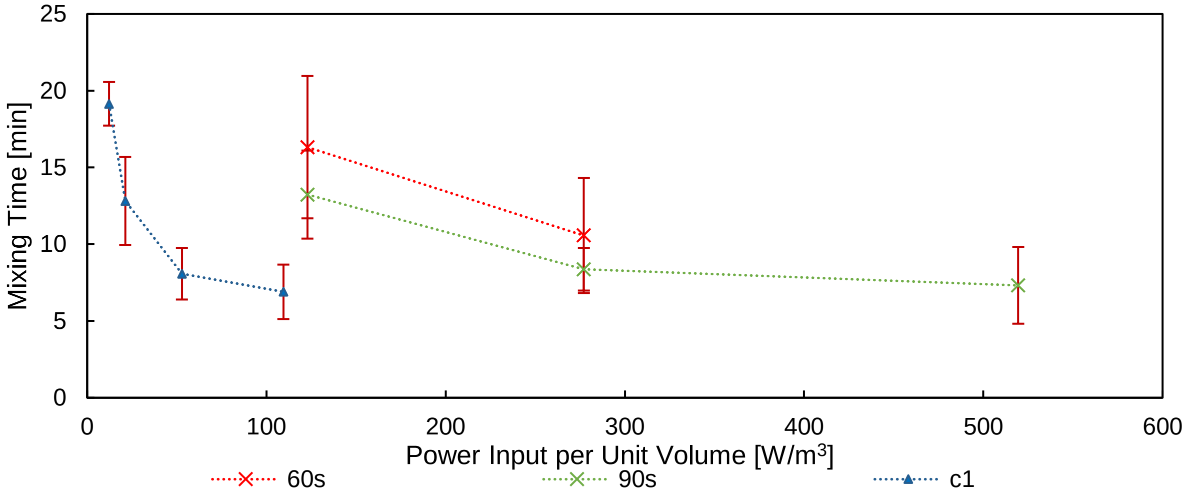

Figure 7.7 – Mixing time vs. power input per unit volume for the c1, 60s and 90s sparger designs at a fill volume of 20 L in the HAIL reactor

Error bars represent the 95% confidence interval for each data point as determined via a t-test.

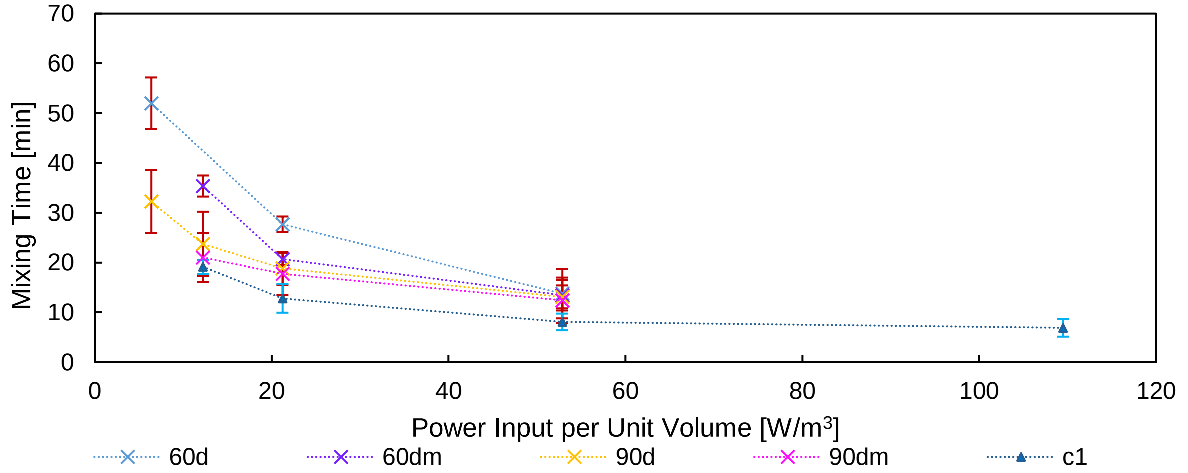

Figure 7.8 – Mixing time vs. power input per unit volume for all 10 mm2 sparger designs at a fill volume of 20 L in the HAIL reactor

Error bars represent the 95% confidence interval for each data point as determined via a t-test. Confidence intervals for c1 have been coloured in teal for enhanced clarity.

From the above mixing time data, it is apparent that the HAIL reactor has a significantly longer mixing time on average than the HAR reactors typically used for aerobic fermentations. Comparing these mixing times to those specified in Table 6.1 for other LAR reactor designs, the mixing time is found to be between that of the travelling loop reactor (under a minute) and raceway reactor (360 minutes and more). The design of the HAIL reactor bares a large resemblance to these two reactor types, so finding the mixing time to be between these values is not non-sensical. The superior mixing time of the travelling loop reactor is likely a result of the orbital shaking providing more momentum to the liquid than the gas jet used in the HAIL reactor. However, as the mixing time and circulation time are related, it is theoretically possible to decrease the mixing time in the HAIL reactor by adding a second feeding port opposite to the primary one. As the HAIL reactor resembles a plug flow reactor in design, there will be two "plugs" to be disrupted by the sparger as opposed to one.

With regards to the optimal sparger design for the current iteration of the HAIL reactor, the c1 sparger is evidently the best performer in terms of mixing and circulation time. However, to ensure that it is the optimal sparger design for the HAIL reactor, the mass transfer energy efficiency of each sparger needs to be discussed.

7.2.2 Mass Transfer Performance

Referring to Figure 7.4, the mass transfer coefficient is evidently lower behind the sparger than in front of it. This indicated that the area behind the sparger could be used for a "worst-case scenario" of mass transfer performance for the HAIL reactor. It was with this in mind that the mass transfer capacity of all spargers was tested behind the sparger.

Table 7.1 details the preliminary mass transfer analysis results. It is immediately apparent that regardless of the sparger design employed, the mass transfer coefficient remains significantly lower than that observed in the STR, both as described in literature (Van't Riet, 1979; Gagnon et al., 1998; Linek et al., 2004; Liu et al., 2019) and in the experimental work of this dissertation. This indicates that the reactor in its current form is unsuitable for aerobic cultures at high growth rates.

Table 7.1 – HAIL reactor mass transfer coefficient results behind the sparger at a fill volume of 20 L and gas flow rate of 20 LPM for all tested spargers

Sparger	**Power Input [W/m^3]**	**k_La [h^{-1}]**	**k_La 95% Confidence Interval**	**Efficiency [m^3·h^{-1}·W^{-1}]**
60d	21.8	3.64	-	0.17
60dm	21.8	3.90	± 0.51	0.18
60s	285	7.39	± 1.67	0.03
90d	21.8	3.25	± 0.28	0.15
90dm	21.8	3.82	± 0.59	0.18
90s	285	10.13	± 0.70	0.04
c1	21.8	4.68	± 1.17	**0.21**

However, it is important to note that the energy efficiency of the HAIL reactor remains competitive against the HAR reactors, as these values at least fall within the performance ranges specified in Table 2.2. As the area behind the sparger is also the "worst-case" scenario mass transfer, the efficiency directly in front of the sparger should yield even greater efficiencies. Comparing the efficiencies here to the other LAR reactors specified in Table 6.1, the efficiency of this design is close to that of the travelling loop, but generally (for this "worst-case" scenario) lower than the efficiencies found in other LAR reactor designs, excluding the orbital shaker. Evidently, to assess the true performance of the HAIL reactor the mass transfer in front of the sparger needed to be investigated. This was explored for the optimal sparger design.

Comparing the angled spargers, the superior mass transfer performance is not as clearly held by the 90° spargers as was seen in the mixing time results. This is supported by the bubble calculations shown in Appendix D, as a lower angle results in a portion of the energy being imparted upwards. This causes additional turbulence at the sparger outlet which aides mass transfer. This relationship is complicated however, because a faster circulation time also results in the liquid passing the sparger more frequently. As with the mixing time, c1 once again is the best performer amongst the tested spargers with a mass transfer energy efficiency of 0.21 m^3·h^{-1}·W^{-1}. As a result of its strong performance in both mixing and mass transfer, c1 was chosen as the optimal sparger design for the HAIL reactor. As the maximum mass transfer coefficient measured under the current operating conditions was low, it is unfeasible to perform either batch or fed-batch aerobic culture at this stage of the HAIL reactor design. As a result, no micro-organisms were grown in the HAIL reactor for the content of this dissertation.

7.3 Investigating the Optimal Sparger Configuration

7.3.1 Mixing and Circulation Time Performance

Additional experimentation on mixing and circulation time for the optimal sparger design (c1) was performed to explore the impact of an increase in volume with a constant gas flow rate, and therefore an approximately equal power input, albeit a lower power input per unit volume.

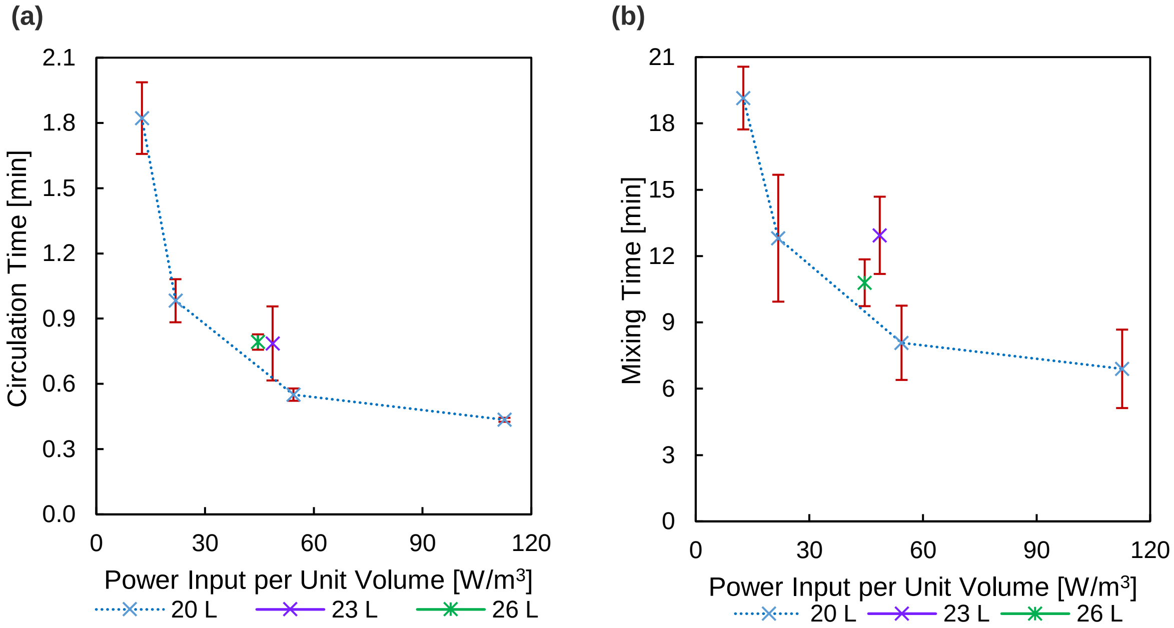

Figure 7.9 – (a) Circulation and (b) mixing time vs. power input data for c1 sparger for 20 L, 23 L and 26 L volumes

Error bars represent the 95% confidence interval for each data point as determined via t-test.

Figure 7.9 is a re-expression of the mixing time data already shown in Figure 7.7 albeit with the addition of two new data points for tests performed at 23 L and 26 L. The 95% confidence intervals of the two new data points do not appear to have significant overlap with the trend observed at 20 L. This implies that performance of the system changes with varying fill volume. Figure 7.10 highlights this observation. Whilst there is overlap between the three 95% confidence intervals for each of the data points, the deviation of these points from one another suggests that there is a notable change in system performance with varying fill volume. This is partly because of a reduction in power input per unit volume as the system volume increases (hence the same power is spread over a larger volume). This trend is observed between 20 and 23 L. However, from 23 L to 26 L there is a decrease in the mixing time, despite there being a decrease in the power input per unit volume. This is likely a result of the increased volume resulting in a larger liquid height, enabling the bubbles ejected from the sparger to stay underwater for a longer period. This would increase the turbulence at the sparger which would result in the generation of larger waves at the surface of the HAIL reactor (which was observed during experimentation).

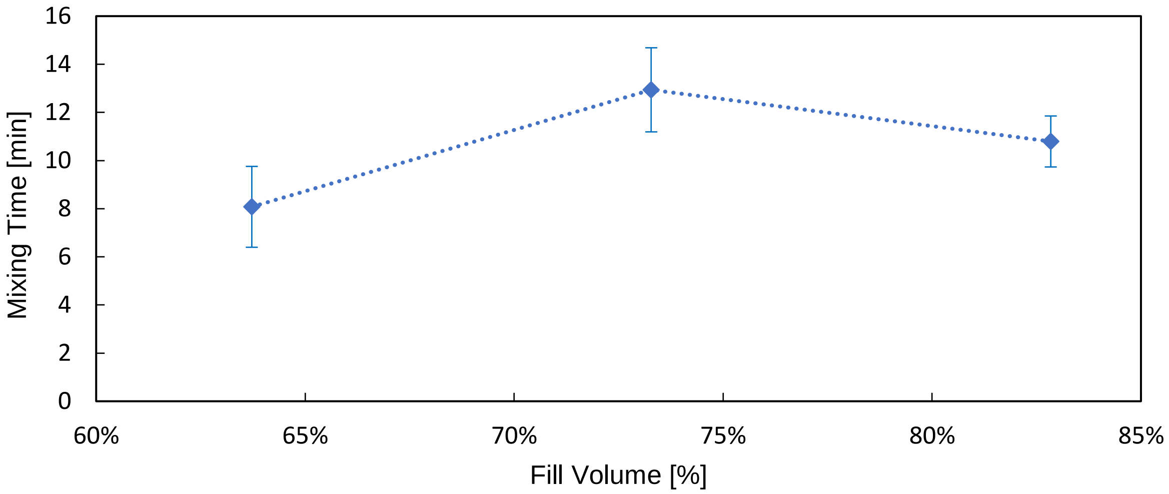

Figure 7.10 – Mixing time vs reactor fill percentage at a gas flow rate of 30 LPM for c1 HAIL reactor configuration.

Error bars represent the 95% confidence interval for each data point as determined via a t-test.

7.3.2 Mass Transfer Performance

Impact of Surface Aeration

Whilst the mass transfer in the HAIL reactor is driven primarily by the gas jet produced by the sparger, it would be erroneous to neglect the impact of surface aeration. As the HAIL reactor operates, air bubbles to the surface quickly from the sparger outlet and then travels through the headspace of the reactor. Due to the reactor design, there is a significant amount of surface area for surface aeration to occur. Additionally, the jet leaving the sparger tends to cause waves to appear at the surface of the reactor (the turbulence of which is dependent on the liquid fill volume). However, as these waves were generated by the aeration itself, they could not be considered in conjunction with surface aeration analysis. Figure 7.11 indicates the relationship between the amount of liquid in the system and the available surface area in the laboratory-scale HAIL reactor.

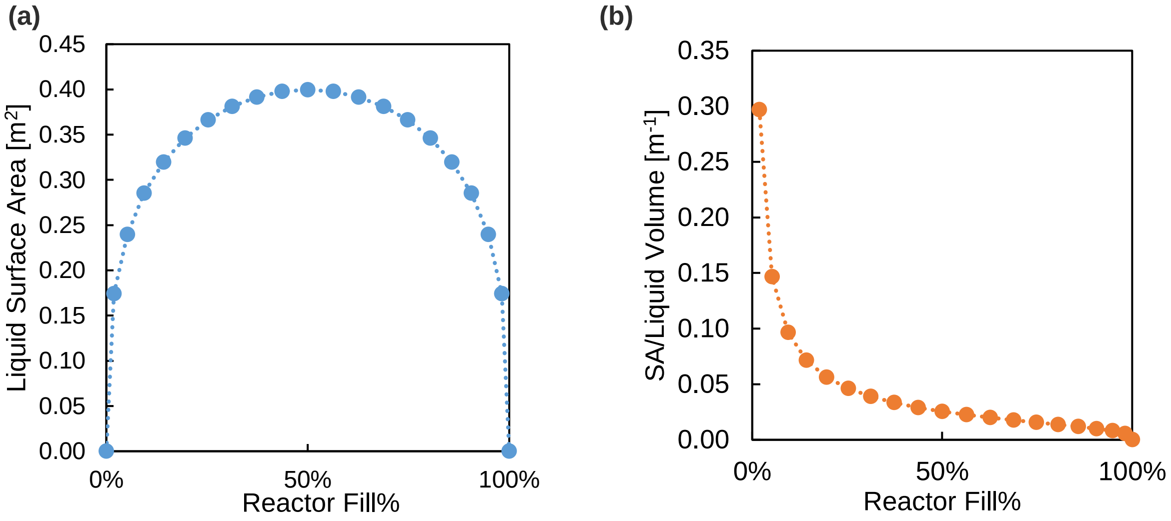

Figure 7.11 – (a) Liquid surface area vs. liquid level and (b) the ratio between surface area and liquid volume in the laboratory-scale HAIL reactor

The available surface area is at a maximum at a fill volume of 50%, which corresponds with a liquid level at the halfway mark (50 mm). However, the ratio between surface area and liquid volume, i.e., the amount of surface available for mass transfer relative to the volume of liquid in the reactor, is highest when the fill volume is lowest.

The results shown in Table 7.2 for surface aeration only can be partially explained by the trend observed in Figure 7.11. When the liquid volume is low, despite the surface area not being at a maximum, the available surface area per unit liquid volume is high. Therefore, the transfer of oxygen across this surface into this liquid and its dispersion throughout it impacts volumetric concentration more strongly, allowing for it to be detected by the DO probe. This explains why the mass transfer due to surface aeration is highest at 12 L and decreases with increasing volume.

Table 7.2 – k_La due to surface aeration in the HAIL reactor with 20 LPM aeration at varying volumes in absence of below-surface liquid sparging

Volume [L]	k_La [h^{-1}]	95% Confidence Interval
12	0.37	± 0.02
20	0.19	± 0.09
26	0.29	± 0.07

An outlier in this dataset is observed at 26 L. Here, the k_La is higher than at 20 L, despite a lower surface area/volume ration and lower overall surface area. This is very likely the result of an error in the experiment design, as the sparger used was very close to the surface of the liquid at 26 L and very far from the surface at 12 L and 20 L. As the sparger was so close the surface, an increased amount of turbulence was caused, enhancing surface aeration more so than at 20 L.

Comparing the data in Table 7.2 to the mass transfer data already presented thus far, it is evident that the impact of the spargers provides a notable improvement over the mass transfer due to surface aeration alone, with surface aeration accounting for less than 6% of the oxygen mass transfer for all spargers at a fill volume of 20 L.

Detailed Mass Transfer Analysis for c1

Figure 7.12 illustrates the obtained mass transfer coefficients with the c1 sparger at varying gas flow rates (and therefore power inputs). By measuring the mass transfer coefficient over a wider range of power inputs, two new observations can be made. Firstly, for power inputs as low as those currently tested, the trend for kLa vs. power input per unit volume can be approximated via a linear correlation, with an R^2 of 0.98. This would be expected to decrease as the power input increases further, although it is unknown by how much it would do so. Secondly, as the power input increases, the difference between the performance observed at the back and front of the system is reduced. This is likely a result of the decreased circulation time, allowing the freshly aerated liquid to complete a circuit more frequently.

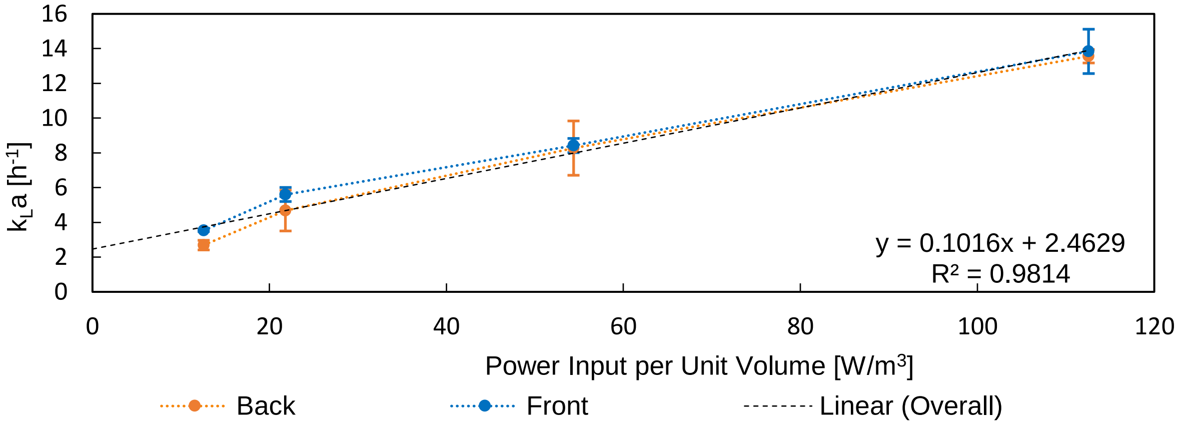

Figure 7.12 – Mass transfer coefficient vs. power input per unit volume at 20 L fill volume in the laboratory-scale HAIL reactor using the c1 sparger

Error bars represent the 95% confidence interval as determined via t-test. Note that the power inputs for each of the four data points, in order, correspond to gas flow rates of 15 LPM, 20 LPM, 30 LPM and 40 LPM.

As noted in the previous section, the mass transfer coefficient for the HAIL reactor is an order of magnitude lower than that required for aerobic fermentations in HAR reactors, and this has not changed with the c1 sparger. Further reactor optimisation will be required. Instead, the hopes of this reactor design lie in the efficiency information, which is detailed in Table 7.3 and Table 7.4.

Table 7.3 – Mass transfer efficiencies for c1 sparger taken from Figure 7.12

Power Input [W/m^3]	**Efficiency – Back [m^3·h^{-1}·W^{-1}]**	**Efficiency 95% Confidence Interval (Back)**	**Efficiency – Front [m^3·h^{-1}·W^{-1}]**	**Efficiency 95% Confidence Interval (Front)**
12.6	0.214	± 0.022	0.281	± 0.004
21.8	0.214	± 0.054	0.257	± 0.019
54.4	0.152	± 0.029	0.155	± 0.008
112.6	0.120	± 0.003	0.123	± 0.011

Table 7.4 – Overall mass transfer energy efficiency results for HAIL reactor with c1 sparger

Result	**Value**	**Unit**
Average Efficiency (Back)	0.175	[m^3·h^{-1}·W^{-1}]
Average Efficiency (Front)	0.204	[m^3·h^{-1}·W^{-1}]
Combined Average Efficiency	0.190	[m^3·h^{-1}·W^{-1}]
Trend Gradient Efficiency	0.102	[m^3·h^{-1}·W^{-1}]

Referring to Table 7.3, it can be observed that the mass transfer energy efficiency experienced both in front of and behind the sparger asymptotes as the power input increases. Table 7.4 contains the overall information, which illustrates a strong average efficiency for both the back and front positions in the reactor. The combined average efficiency value is a more accurate representation of the system, as the mass transfer experienced throughout the entire system will dictate the operating capacity of the reactor. The trend efficiency is the expected efficiency as the power input continues to increase, although this may very likely not hold and is simply a prediction. A more detailed comparison of these values to those presented throughout this dissertation is detailed later in this sub-section.

Figure 7.13 shows the mass transfer energy efficiency in the HAIL reactor as a function of fill volume. As can be observed from the depicted points, the energy efficiency of the mass transfer changes by an insignificant amount, as opposed to the mixing time (as shown in Figure 7.10). The 95% confidence intervals for the 20 L and 23 L data points overlap significantly, hence it cannot be stated that they are significantly different from one another. It can be observed that the efficiency increases, albeit slightly, with an increasing volume although this is within error and cannot be stated with certainty.

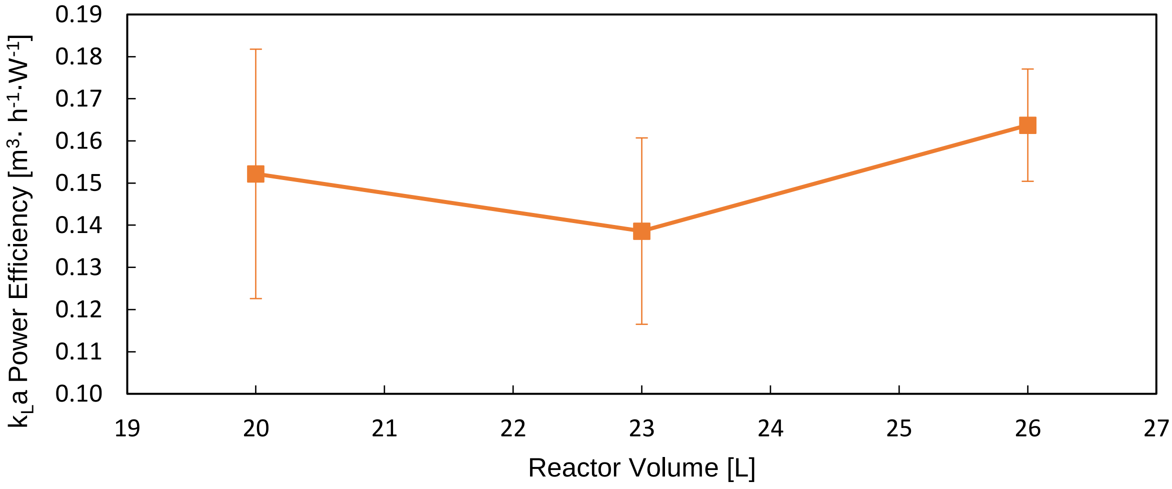

Figure 7.13 – k$_L$a power efficiency vs. reactor fill volume at an aeration rate of 30 LPM in the HAIL reactor using the c1 sparger

Error bars represent the 95% confidence interval as determined via t-test.

HAIL Reactor Mass Transfer Performance Assessment and Comparison

The efficiency data obtained for the best configuration of the HAIL reactor presented in Table 7.3 and Table 7.4 must be compared to the efficiency data for HAR and LAR reactors taken from literature (Table 2.2 and Table 6.1) and the STR experiment data presented in Table 5.3 and Table 5.5. This is summarised in Table 7.5.

Table 7.5 – Summary of k_La data from literature review and experimental work results

Reactor Type	Maximum k_La [h^{-1}]	Mass Transfer Energy Efficiency [$m^3 \cdot h^{-1} \cdot W^{-1}$]	Source
HAIL	13.8	0.120-0.214	This work
STR-Experiments	240	0.059-0.285	This work
STR	High*	0.022-0.236	Van’t Riet (1979) Gagnon et al. (1998) Linek et al. (2004) Liu et al. (2019)
BCR	High*	0.084-0.317	Chisti (1989) Deckwer et al. (1982) Deckwer et al. (1983) Heijnen and Van’t Riet (1984) Rubio et al. (1999) Sastaravet et al. (2014)
ALR	High*	0.142-0.493	Bello et al. (1985) Heijnen and Van’t Riet (1984) Shariati et al. (2007) Wu et al. (1992)
Orbital Shaker	38.0	0.001-0.013	Tissot et al. (2010) Klöckner and Büchs (2012) Klöckner et al. (2013b) Zhu et al. (2020)
Wave	750	0.112-0.742	Jones et al. (2017) Bai et al. (2019) Oosterhuis and van der Heiden (2010)
Raceway	9.60	0.034-0.867	Mendoza et al. (2013a) Barceló-Villalobos et al. (2018) Mendoza et al. (2013b)
Travelling Loop	32.0	0.286-0.295	Kaiser et al. (2016b)

*The mass transfer coefficient of these HAR reactors can reach as high as (or even higher than) 1000 h^{-1} depending on the power input into the system.

The highest efficiency amongst the HAR reactors is held by the ALR and sits at a maximum of 0.493 $m^3 \cdot h^{-1} \cdot W^{-1}$ (Bello et al., 1985; Heijnen and Van’t Riet, 1984; Shariati et al., 2007; Wu et al., 1992). The highest efficiencies of the commonly used STR and BCR’s are 0.236 $m^3 \cdot h^{-1} \cdot W^{-1}$ and 0.317 $m^3 \cdot h^{-1} \cdot W^{-1}$. In comparison, the highest efficiency in the HAIL reactor prior to rigorous optimisation is 0.281 $m^3 \cdot h^{-1} \cdot W^{-1}$.

This is however an underestimate as previously discussed and demonstrates that the HAIL reactor can be on-par with the performance of the best HAR reactors. Further studies are required to ascertain whether it can surpass them. This maximum does surpass the literature values for STR’s (0.236 $m^3 \cdot h^{-1} \cdot W^{-1}$) as determined from a variety of sources (Van’t Riet, 1979; Gagnon et al., 1998; Linek et al., 2004; Liu et al., 2019) and is close to the maximum value obtained for BCR’s in literature (0.317 $m^3 \cdot h^{-1} \cdot W^{-1}$) as taken from (Chisti, 1989; Deckwer et al., 1982; Deckwer et al., 1983; Heijnen and Van’t Riet, 1984; Rubio et al., 1999; Sastaravet et al., 2014).

On another note, the minimum energy efficiency obtained by the HAIL reactor with the c1 sparger equipped far outpaces that of any of the HAR reactors, a benefit likely a result of the LAR design. It can be noted that the power input for the HAIL reactor is very low in its current form and this trend might not be observed at higher power inputs, requiring additional testing.

Comparing the system to the LAR reactor data in Table 7.5, the maximum mass transfer energy efficiency is extremely close to that observed in the travelling loop reactor, indicating potential for this system to compete. However, the average combined mass transfer energy efficiency of the HAIL reactor is much lower, and the k_La attainable in the horizontal tubular loop reactor is higher. Evidently more work must go into the design of the HAIL reactor for it to be a viable alternative even to the travelling loop reactor. The mass transfer obtainable in the HAIL reactor is comparable to that of a raceway reactor, which is likely a result of the high similarity between its design and that of a closed raceway reactor. The energy efficiency is however far lower than that obtained in a raceway reactor, although a higher k_La is obtained in the HAIL reactor. In its current state the system is uncompetitive with the Cell-tainer® Wave bioreactor design in terms of mass transfer coefficient, mass transfer energy efficiency and mixing time (Oosterhuis and van der Heiden 2010). However, the HAIL reactor's superior scalability remains.

Comparing the efficiency results obtained to those obtained during the fed-batch STR experiments is significantly more promising for the HAIL reactor in terms of energy efficiency. However, these results need to be met with a level of scepticism due to potential issues with the DO probe/DO module of the STR. The maximum efficiency observed across all fed-batch STR runs was 0.245 $m^3 \cdot h^{-1} \cdot W^{-1}$, which is lower than the maximum for the HAIL reactor. The highest average efficiency was 0.180 $m^3 \cdot h^{-1} \cdot W^{-1}$, once again lower than the HAIL reactor. Additionally, these values coincide with the first fed-batch run, of which only two data points were taken hence the potential for these STR results to be an overestimate is non-negligible. The best fit gradients are significantly lower than the best fit gradient obtained for the HAIL reactor. The only area in which the experimental STR results do beat the HAIL reactor is the maximum attainable k_La.

The final comparison to be made is between the deionised water STR experiment data. This STR data is far less scattered than the fed-batch runs, making it substantially more reliable for comparison. The maximum attainable mass transfer energy efficiency in the deionised water system was 0.285 $m^3 \cdot h^{-1} \cdot W^{-1}$, which very narrowly surpasses that observed in the HAIL reactor. The average efficiency of the STR is however lower than the HAIL reactor, with the best fit gradient also being substantially lower (indicating that at higher power inputs, this efficiency will drastically decrease). However, as with all HAR reactors, the k_La attained in these experiments surpassed the k_La obtained by the unoptimized HAIL reactor.

7.3.3 Impact of Viscosity

As a final criterion for analysis of the laboratory-scale prototype HAIL reactor, the viscosity of the system was chemically altered via the addition of glycerol to the system. The highest viscosity obtained during the STR fed-batch experiments with yeast was 1.4 cP as previously stated, hence a viscosity of 1.4 cP was targeted for the viscosity experiments. The added glycerol caused the density of the glycerol system to reach 1029 kg/m^3 compared to the 1000 kg/m^3 density of a pure water system.

Figure 7.14 illustrates the observed trends in circulation time and mixing time with an increase in viscosity from 1.0 cP (that of a pure water system) to 1.4 cP (correlating with a cell dry weight concentration of approximately 50 g/L). Whilst the circulation time can definitively be observed to be lower for the lower viscosity system (there is no overlap of the 95% confidence intervals), the same cannot be said for the mixing time. This variation in the circulation time is potentially caused due to the increase in density and viscosity causing the liquid to move more sluggishly through the system. The mixing time would then be expected to change, but does not in this case, possibly as the increased density results in a marginal increase in the power input per unit volume. This would increase turbulence at the point of mixing (the sparger outlet) which could make up for the reduced circulation time experienced.

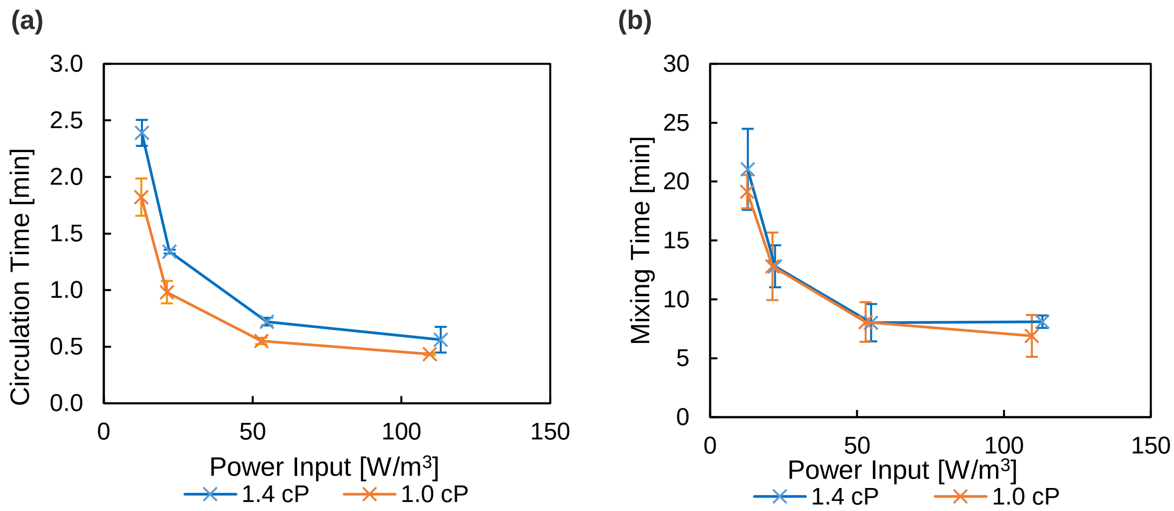

Figure 7.14 – Circulation and mixing time vs. power input at 20 L volume in the HAIL reactor at 1.0 cP and 1.4 cP using the c1 sparger

Error bars represent the 95% confidence interval for each data point as determined via a t-test.

Figure 7.15 illustrates the observed mass transfer coefficient versus power input in the system. The mass transfer data presented here was gathered behind the sparger as a “worst case” scenario. As with Figure 7.12 a linear correlation has a good fit with the data, with an R^2 of 0.989. The gradient of this line is 0.152, which is higher than that found for the non-viscous system. This drastic shift in gradient is a result of the final data point in Figure 7.15 having a higher efficiency (due to error/variance) than that for the circle sparger. The average efficiency across all data points is 0.171 $m^3 \cdot h^{-1} \cdot W^{-1}$, which is marginally lower than for the non-viscous system (when considering the area behind the sparger). These results are expected considering the marginally different circulation and mixing time results displayed in Figure 7.14. They imply that an increase of viscosity from 1.0 cP to 1.4 cP has limited to no impact on the mass transfer and mixing performance of the HAIL reactor.

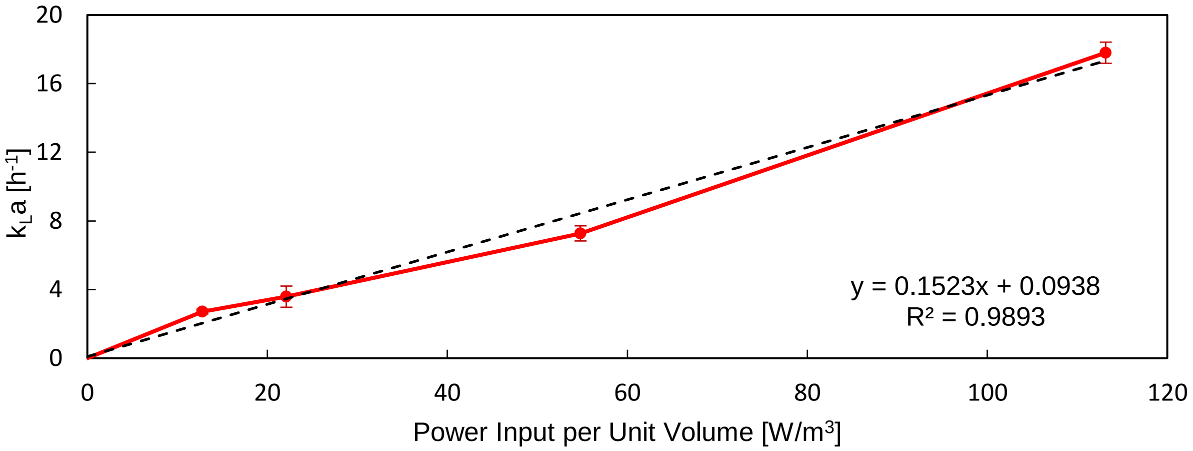

Figure 7.15 – kLa vs. power input per unit volume at 20 L fill volume in laboratory-scale HAIL reactor at 1.4 cP viscosity

Error bars represent the 95% confidence interval for each data point as determined via a t-test.

8 Conclusion and Recommendations

8.1 Conclusion

The objective of this work was to investigate existing literature and to design a novel reactor that could potentially compete with the existing industrial aerobic HAR reactor designs while enhancing the energy efficiency of gas-liquid mass transfer and mixing. Such a design needed to have a sufficiently high mass transfer coefficient such that it could sustain a high productivity to maintain a high cell density culture, such as required in yeast fermentation. The mixing time in such a system also needed to be suitably low to support the quick mixing of substrate necessary to maintain a stable and sufficient concentration range throughout the system. To be competitive, the design would also need to be more energy efficient than the HAR systems. Literature research dictated that LAR reactor design might hold the solution to this problem.

After a review of the relevant literature, a prototype reactor was developed to potentially meet this objective. The developed HAIL reactor prototype merges the concept of a raceway, a helical reactor, and a loop reactor into one. The design is theoretically stackable, hence removing the scaling issue frequently encountered by similar LAR reactor designs.

It was initially hypothesised that the HAIL reactor prototype would not be able to compete with the HAR reactors used industrially in terms of minimal mixing time and maximum mass transfer coefficient, although it was hoped that the difference here would be sufficiently low to meet the cultivation needs, paving the way for additional research and development. The primary concern for the testing of the HAIL reactor was to ascertain whether it was notably more energy efficient to operate than any of the currently used industrial HAR reactors. The term mass transfer energy efficiency was introduced to assess mass transfer potential as a function of energy requirement through determining the quotient of k_La and power input per unit volume. Data collected through the literature review indicated that the mass transfer energy efficiency of typical HAR reactors ranged from 0.022-0.236 $m^3 \cdot h^{-1} \cdot W^{-1}$ for STR's, 0.084-0.317 $m^3 \cdot h^{-1} \cdot W^{-1}$ for BCR's and 0.142-0.493 $m^3 \cdot h^{-1} \cdot W^{-1}$ for ALR's. Typical maximum k_La values for these systems ranged between 500-1000 h^{-1} (although this entirely dependent on the usage case and power input). Mixing times for these systems varied greatly depending on which system (and what scale) was being used. At the highest scales (10 m^3) and aspect ratios (10), they were 1.5-20 minutes, whereas at the lowest scales (10 L) and aspect ratios (2) they were always under a minute.

Part of the work in this dissertation included experiments to verify the mass transfer data at laboratory-scale for comparison to the HAIL reactor, both with and without active fermentation. Ignoring potential issues with the DO probe, the mass transfer energy efficiency during fed-batch experiments for the 10 L laboratory-scale STR was found to be 0.044-0.245 $m^3 \cdot h^{-1} \cdot W^{-1}$ with a maximum observed k_La of 240 h^{-1}. For the base case in deionised water, this efficiency range was instead found to be 0.059-0.285 $m^3 \cdot h^{-1} \cdot W^{-1}$, with a maximum k_La of 226 h^{-1}. The STR work also served to establish a baseline for oxygen demand during fed-batch culture of *S. cerevisiae*. To this end, a minimum theoretical k_La of 372 h^{-1} would be required by the HAIL reactor to maintain similar growth performance to the STR.

In addition to comparing the HAIL reactor to HAR systems, mass transfer and mixing data for other LAR reactors was gathered for assessment (and design) of the HAIL reactor. The most notable efficiencies are held by the travelling loop, raceway, and wave reactors with ranges of 0.286-0.295 $m^3 \cdot h^{-1} \cdot W^{-1}$, 0.034-0.867 $m^3 \cdot h^{-1} \cdot W^{-1}$, and 0.112-0.742 $m^3 \cdot h^{-1} \cdot W^{-1}$. For the wave and travelling loop reactors, mixing times below 1 minute were attainable, with mixing times in raceway reactors being substantially longer by an order of magnitude (6 hours or more) due to their typically substantially larger scale.

Prior to an in-depth comparison of the HAIL reactor to its alternatives, the design of the reactor needed to be finalised. In this first study, only the sparger designs were investigated. The first system tested was the proof-of-concept prototype. It was 3.2 m in length with an internal diameter of 50 mm and maximum volume of 6.2 L. In this system, the sparger design was investigated through the impact of sparger angle and depth. These preliminary results demonstrated proof of concept and indicated that optimal sparger performance could be found either near the surface or near the bottom of the system. To further the investigation, the more precise laboratory-scale prototype was constructed.

In the laboratory-scale prototype, seven different sparger configurations were tested. Six of these designs made use of a single jet, of which half were angled at 60° and half at 90°. Two had a reduced orifice area. It was shown that mixing time in the HAIL reactor is significantly better with a jet sparger at 90° as opposed to 60° due to the associated decrease in circulation time. This is a result of greater horizontal momentum transfer from the bubbles to the liquid. Mass transfer performance is not as clear cut between the two angles. The increased vertical momentum generates increased turbulence at the sparger outlet (aiding mass transfer), but the reduced horizontal momentum reduces the circulation time, causing the liquid to pass the sparger outlet less frequently. However, irrespective of the angled spargers, a circular sparger design proved to be the most energy efficient of the designed spargers, hence future iterations of the HAIL reactor prototype should make use of this circular sparger design.

Analysing the optimal sparger HAIL reactor configuration, the mixing time was found to have a range of 7-19 minutes depending on the power input. This is substantially higher than most HAR reactors at large scale and is also higher than the LAR reactors explored in the literature review, with the exception of the raceway. The power efficiency of the HAIL reactor was estimated to range between 0.120-0.281 $m^3 \cdot h^{-1} \cdot W^{-1}$, although owing to the calculation method used to get the power inputs this is recognised as an underestimate. This efficiency is of the same order of magnitude as the HAR and LAR reactors, being superior to the efficiency found for STR's in literature but lower than the efficiency observed in the best performing BCR's and ALR's. The efficiency is also lower than that obtained in other LAR reactors. Improvement of the mass transfer energy efficiency is expected with further optimisation. The major challenge found with the HAIL reactor was the low gas-liquid mass transfer coefficient; the maximum obtained mass transfer coefficient in the HAIL reactor was 13.84 h^{-1}. This value is an order of magnitude lower than the values typically obtained in HAR reactors for industrial aerobic culture. However, little effect of viscosity on this performance was noted in the range 1-1.4 cP. Design optimisation is required to explore whether this can be meaningfully increased. Currently the value of the HAIL reactor is limited to application of either very slow growing or micro-aerobic systems.

The research concluded to date provides partial support of the hypothesis with respect to the mass transfer energy efficiency but puts into question the hypothesis with respect to magnitude of mass transfer rate attainable.

The mass transfer energy efficiency of the HAIL reactor is better than or at least on par with the typical industrial HAR reactors in its currently unoptimized state. This demonstrates its potential to exceed these once optimised, thereby upholding the hypothesis. Further research is required to finalise this. While it is unlikely that the k_La achieved with optimisation of the HAIL will exceed the maximums of the industrial HAR reactors based on the "order of magnitude" lower performance recorded to date, the HAIL reactor's potential uses and potential to support a sufficiently high productivity of microbial biomass remains to be quantified. Additional modifications to the HAIL reactor's design which might greatly enhance its overall performance are detailed in the recommendations.

8.2 Recommendations

The HAIL reactor is a prototype and hence the fact that the results do not outcompete existing reactor designs, optimised over many years, must not come entirely as a surprise. While the first prototype reactor has displayed the potential for energy efficiency, further work is needed to enhance gas-liquid mass transfer. There were many different avenues to be explored for the prototype. These could substantially improve the mixing time, mass transfer coefficient and/or the mass transfer energy efficiency.

To improve the mixing time, a viable option to explore would be the addition of a second, or even third and fourth, feeding inlet. As the mixing is greatly enhanced based on how frequently the initial pulse of substrate passes the sparger, splitting the pulse into smaller pulses will increase the rate at which the system reaches homogeny. This could be done by having a tube system connected to each feeding inlet leading to the centre of the reactor. Injecting into a single tube that then splits the feed across the feeding inlets would then result in the improved mixing time.

An additional avenue to explore further is the presence of two or more spargers as opposed to one. Due to time constraints and unpromising data from the proof-of-concept prototype, a dual sparger system was abandoned. However, it was later found that the data from the proof-of-concept prototype was not reliable. As a result, the dual sparger system may have erroneously been set aside and still have potential. Two sparger outlets provide more areas where agitation can occur, which could potentially enhance both mixing and mass transfer results. As both sparger outlets would generate shear, it is important that the shear forces applied via the sparger jets are investigated in future as well.

In terms of the design of the HAIL reactor itself, baffles were not tested in the system but are a highly recommended avenue for future research. The horizontal tubular loop reactor found in literature made use of internal baffles in the pipe wall and these appeared to massively increase the mass transfer coefficient in the system. The baffles used in that system were however based on a fully submerged pipe. If the semi-filled pipe design is to be maintained, baffles that make use of ridges at the top and bottom of the reactor would be preferred. If the ridges at the top are long enough and touch the liquid, it will cause a pressure build up in the reactor. However, if there is also wave action, the air will have brief moments where it can escape to the next pocket. This will cause the air to remain in the system longer and improve surface aeration. The added pressure would also enhance mass transfer.

A final recommendation on the design of the HAIL reactor is to potentially operate in a similar manner to the horizontal tubular loop reactor, where the tube portion of the reactor is fully submerged, and a chamber exists for venting air. The sparger would be inserted in the tube, driving liquid flow and the gas would be entrained in the liquid until it reaches the ventilation chamber. This long contact time could greatly improve the observed mass transfer and a LAR design could still be maintained. The design could also remain stackable.

Regarding general experiment improvements for the STR section of this dissertation, it is recommended that future work take note of the probe response time in media of various compositions (for example, with inactive yeast cells/high sucrose concentration etc.)

References

Abdul Rahman–Al Ezzi, A., Faisal Najmuldeen, G., 2014. Gas Hold-Up, Mixing Time and Circulation Time in Internal Loop Airlift Bubble Column. J. Eng. Res. Appl. 4, 286–294.

Abufalgha, A.A., Clarke, K.G., Pott, R.W.M., 2019. The liquid–liquid homogeneity of a four-phase simulated hydrocarbon-based bioprocess in a bubble column reactor. J. Chem. Technol. Biotechnol. 94, 2034–2039. https://doi.org/10.1002/jctb.5989

Al Taweel, A.M., Shah, Q., Aufderheide, B., 2012. Effect of Mixing on Microorganism Growth in Loop Bioreactors. Int. J. Chem. Eng. 2012, 1–12. https://doi.org/10.1155/2012/984827

Anderlei, T., Cesana, C., Bürki, C., De Jesus, M., Kühner, M., Wurm, F., Lohser, R., 2009. Shaken bioreactors provide culture alternative. Genet. Eng. Biotechnol. News 29, 19–21.

Bai, Y., Moo-Young, M., Anderson, W.A., 2019. Characterization of power input and its impact on mass transfer in a rocking disposable bioreactor. Chem. Eng. Sci. 209, 115183. https://doi.org/10.1016/j.ces.2019.115183

Bandyopadhyay, B., Humphrey, A.E., Taguchi, H., 1967. Dynamic measurement of the volumetric oxygen transfer coefficient in fermentation systems. Biotechnol. Bioeng. 9, 533–544. https://doi.org/10.1002/bit.260090408

Barceló-Villalobos, M., Guzmán Sánchez, J.L., Martín Cara, I., Sánchez Molina, J.A., Acién Fernández, F.G., 2018. Analysis of mass transfer capacity in raceway reactors. Algal Res. 35, 91–97. https://doi.org/10.1016/j.algal.2018.08.017

Bekatorou, A., Psarianos, C., Koutinas, A.A., 2006. Production of food grade yeasts. Food Technol. Biotechnol. 44, 407–415.

Bello, R.A., Robinson, C.W., Moo-Young, M., 1985. Prediction of the volumetric mass transfer coefficient in pneumatic contactors. Chem. Eng. Sci. 40, 53–58. https://doi.org/10.1016/0009-2509(85)85046-6

Bio-Rad Laboratories, I., 2012. Aminex® HPLC Columns.

Birch, D., Ahmed, N., 1997. The influence of sparger design and location on gas dispersion in stirred vessels. Chem. Eng. Res. Des. 75, 487–496. https://doi.org/10.1205/026387697523994

Bjarre, J., Risén, S., 2016. Aeration in fed batch cultivations of Saccharomyces cerevisiae within Industrial Biotechnology. Royal Institute of Technology.

Bouaifi, M., Hebrard, G., Bastoul, D., Roustan, M., 2001. A comparative study of gas hold-up, bubble size, interfacial area and mass transfer coefficients in stirred gas–liquid reactors and bubble columns. Chem. Eng. Process. Process Intensif. 40, 97–111. https://doi.org/10.1016/S0255-2701(00)00129-X

Brecht, R., 2010. Disposable Bioreactors: Maturation into Pharmaceutical Glycoprotein Manufacturing, in: Eibl, R., Eibl, D. (Eds.), Disposable Bioreactors. Springer Berlin Heidelberg, Berlin, Heidelberg, pp. 1–31. https://doi.org/10.1007/10_2008_33

Buffo, M.M., Corrêa, L.J., Esperança, M.N., Cruz, A.J.G., Farinas, C.S., Badino, A.C., 2016. Influence of dual-impeller type and configuration on oxygen transfer, power consumption, and shear rate in a stirred tank bioreactor. Biochem. Eng. J. 114, 130–139. https://doi.org/10.1016/j.bej.2016.07.003

Carvalho, A.P., Meireles, L.A., Malcata, F.X., 2006. Microalgal Reactors: A Review of Enclosed System Designs and Performances. Biotechnol. Prog. 22, 1490–1506. https://doi.org/10.1021/bp060065r

Chen, N.Y., 1990. The design of airlift fermenters for use in biotechnology. Biotechnol. Genet. Eng. Rev. 8, 379–396. https://doi.org/10.1080/02648725.1990.10647875

Chisti, M.Y., 1989. Airlift Reactors: Current Technology, in: Airlift Bioreactors, Elsevier Applied Biotechnology Series. Elsevier Applied Science, pp. 33–86.

Coker, A.K. (Ed.), 2007. RULES OF THUMB: SUMMARY, in: Ludwig’s Applied Process Design for Chemical and Petrochemical Plants. Elsevier, Burlington, pp. xviii–xxvi. https://doi.org/10.1016/B978-075067766-0/50007-5

de Jesus, S.S., Moreira Neto, J., Maciel Filho, R., 2017. Hydrodynamics and mass transfer in bubble column, conventional airlift, stirred airlift and stirred tank bioreactors, using viscous fluid: A comparative study. Biochem. Eng. J. 118, 70–81. https://doi.org/10.1016/j.bej.2016.11.019

Deckwer, W.-D., Nguyen-Tien, K., Kelkar, B.G., Shah, Y.T., 1983. Applicability of axial dispersion model to analyze mass transfer measurements in bubble columns. AIChE J. 29, 915–922. https://doi.org/10.1002/aic.690290607

Deckwer, W.-D., Nguyen-Tien, K., Schumpe, A., Serpemen, Y., 1982. Oxygen mass transfer into aerated CMC solutions in a bubble column. Biotechnol. Bioeng. 24, 461–481. https://doi.org/10.1002/bit.260240215

Di Serio, M., Aramo, P., de Alteriis, E., Tesser, R., Santacesaria, E., 2003. Quantitative Analysis of the Key Factors Affecting Yeast Growth. Ind. Eng. Chem. Res. 42, 5109–5116. https://doi.org/10.1021/ie030078z

Di Serio, M., Tesser, R., Santacesaria, E., 2001. A kinetic and mass transfer model to simulate the growth of baker’s yeast in industrial bioreactors. Chem. Eng. J. 82, 347–354. https://doi.org/10.1016/S1385-8947(00)00353-3

Doran, P.M., 2013a. Mass Transfer, in: Doran, P.M. (Ed.), Bioprocess Engineering Principles. Academic Press, London, pp. 379–444. https://doi.org/https://doi.org/10.1016/B978-0-12-220851-5.00010-1

Doran, P.M., 2013b. Mixing, in: Doran, P.M. (Ed.), Bioprocess Engineering Principles. Elsevier, London, pp. 255–332. https://doi.org/10.1016/B978-0-12-220851-5.00008-3

Doran, P.M., 2013c. Homogeneous Reactions, in: Bioprocess Engineering Principles. Elsevier, pp. 599–703. https://doi.org/10.1016/B978-0-12-220851-5.00012-5

Eibl, R., Werner, S., Eibl, D., 2010. Bag Bioreactor Based on Wave-Induced Motion: Characteristics and Applications, in: Eibl, R., Eibl, D. (Eds.), Disposable Bioreactors. Springer Berlin Heidelberg, Berlin, Heidelberg, pp. 55–87. https://doi.org/10.1007/10_2008_15

Ejiofor, A.O., Posten, C.H., Solomon, B.O., Deckwer, W.D., 1994. A robust fed-batch feeding strategy for optimal parameter estimation for baker’s yeast production. Bioprocess Eng. 11, 135–144. https://doi.org/10.1007/BF00518735

El-Helow, E.R., Elbahloul, Y., El-Sharouny, E.E., Ali, S.R., Ali, A.A.-M., 2015. Economic production of baker’s yeast using a new Saccharomyces cerevisiae isolate. Biotechnol. Biotechnol. Equip. 29, 705–713. https://doi.org/10.1080/13102818.2015.1038302

Elibol, M., 2001. Improvement of antibiotic production by increased oxygen solubility through the addition of perfluorodecalin. J. Chem. Technol. Biotechnol. 76, 418–422. https://doi.org/10.1002/jctb.389

Gaddis, E.S., 1999. Mass transfer in gas–liquid contactors. Chem. Eng. Process. Process Intensif. 38, 503–510. https://doi.org/10.1016/S0255-2701(99)00046-X

Gagnon, H., Lounès, M., Thibault, J., 1998. Power consumption and mass transfer in agitated gas-liquid columns: a comparative study. Can. J. Chem. Eng. 76, 379–389. https://doi.org/10.1002/cjce.5450760306

Garcia-Ochoa, F., Gomez, E., 2009. Bioreactor scale-up and oxygen transfer rate in microbial processes: An overview. Biotechnol. Adv. 27, 153–176. https://doi.org/10.1016/j.biotechadv.2008.10.006

García-Ochoa, F., Gómez, E., 1998. Mass transfer coefficient in stirred tank reactors for xanthan gum solutions. Biochem. Eng. J. 1, 1–10. https://doi.org/10.1016/S1369-703X(97)00002-8

Garcia-Ochoa, F., Santos, V.E., Gomez, E., 2011. 2.15 - Stirred Tank Bioreactors, in: Moo-Young, M. (Ed.), Comprehensive Biotechnology (Second Edition). Academic Press, Burlington, pp. 179–198. https://doi.org/https://doi.org/10.1016/B978-0-08-088504-9.00108-2

George, S., Larsson, G., Olsson, K., Enfors, S.-O., 1998. Comparison of the Baker’s yeast process performance in laboratory and production scale. Bioprocess Eng. 18, 135. https://doi.org/10.1007/s004490050423

Green, D.D.W., Southard, D.M.Z., 2019. Perry’s Chemical Engineers’ Handbook, 9th Edition, 9th editio. ed. McGraw-Hill Education, New York.

Gueguim Kana, E.B., Oloke, J.K., Lateef, A., 2007. Novel feeding strategies for Saccharomyces cerevisiae DS2155, using glucose limited exponential fedbatch cultures with variable specific growth rates (µ). African J. Biotechnol. 6, 1122–1127.

Hagman, A., Säll, T., Piškur, J., 2014. Analysis of the yeast short-term Crabtree effect and its origin. FEBS J. 281, 4805–4814. https://doi.org/10.1111/febs.13019

Haque, M.W., Nigam, K.D.P., Joshi, J.B., 1986. Optimum gas sparger design for bubble columns with a low height-to-diameter ratio. Chem. Eng. J. 33, 63–69. https://doi.org/10.1016/0300-9467(86)80035-1

Harding, K., 2008. A generic approach to environmental assessment of microbial bioprocesses through life cycle assessment (LCA). University of Cape Town.

Heijnen, J.J., Van't Riet, K., 1984. Mass transfer, mixing and heat transfer phenomena in low viscosity bubble column reactors. Chem. Eng. J. 28, B21–B42. https://doi.org/10.1016/0300-9467(84)85025-X

Ho, C.S., Ju, L.-K., Baddour, R.F., 1990. Enhancing penicillin fermentations by increased oxygen solubility through the addition ofn-hexadecane. Biotechnol. Bioeng. 36, 1110–1118. https://doi.org/10.1002/bit.260361106

Houcine, I., Plasari, E., David, R., 2000. Effects of the Stirred Tank's Design on Power Consumption and Mixing Time in Liquid Phase. Chem. Eng. Technol. 23, 605–613. https://doi.org/10.1002/1521-4125(200007)23:7<605::AID-CEAT605>3.0.CO;2-0

Jakobsen, H.A., Bourg, I., Svendsen, H.F., Hjarbo, K.W., 2001. Interaction Between Reaction Kinetics and Flow Structure in Bubble Column Reactors, in: Jenssen, C.B., Andersson, H.I., Ecer, A., Satofuka, N., Kvamsdal, T., Pettersen, B., Periaux, J., Fox, P. (Eds.), Parallel Computational Fluid Dynamics 2000. North-Holland, Amsterdam, pp. 543–550. https://doi.org/https://doi.org/10.1016/B978-044450673-3/50134-2

Jia, Q., Li, H., Hui, M., Hui, N., Joudi, A., Rishton, G., Bao, L., Shi, M., Zhang, X., Luanfeng, L., Xu, J., Leng, G., 2008. A bioreactor system based on a novel oxygen transfer method. Bioprocess Int. 66–71.

Jones, S.M.J., Louw, T.M., Harrison, S.T.L., 2017. Energy consumption due to mixing and mass transfer in a wave photobioreactor. Algal Res. 24, 317–324. https://doi.org/10.1016/j.algal.2017.03.001

Ju, L. -K, Lee, J.F., Armiger, W.B., 1991. Enhancing Oxygen Transfer in Bioreactors by Perfluorocarbon Emulsions. Biotechnol. Prog. 7, 323–329. https://doi.org/10.1021/bp00010a006

Ju, L.K., Sundararajan, A., 1995. The effects of cells on oxygen transfer in bioreactors. Bioprocess Eng. 13, 271–278. https://doi.org/10.1007/BF00417639

Junne, S., Solymosi, T., Oosterhuis, N., Neubauer, P., 2013. Cultivation of Cells and Microorganisms in Wave-Mixed Disposable Bag Bioreactors at Different Scales. Chemie Ing. Tech. 85, 57–66. https://doi.org/10.1002/cite.201200149

Kadic, E., Heindel, T.J., 2014. An Introduction to Bioreactor Hydrodynamics and Gas-Liquid Mass Transfer. John Wiley & Sons, Inc., Hoboken, NJ, USA. https://doi.org/10.1002/9781118869703

Kaiser, S.C., Kraume, M., Eibl, D., 2016a. Development of the Travelling Wave Bioreactor. Part I: Design Studies Based on Numerical Models. Chemie-Ingenieur-Technik 88, 77–85. https://doi.org/10.1002/cite.201500092

Kaiser, S.C., Kraume, M., Eibl, D., 2013. Development of the Travelling Wave Bioreactor - A Concept Study. Chemie Ing. Tech. 85, 136–143. https://doi.org/10.1002/cite.201200127

Kaiser, S.C., Perepelitsa, N., Kraume, M., Eibl, D., 2016b. Development of the Travelling Wave Bioreactor. Part II: Engineering Characteristics and Cultivation Results. Chemie-Ingenieur-Technik 88, 86–92. https://doi.org/10.1002/cite.201500091

Karimi, A., Golbabaei, F., Mehrnia, M., Neghab, M., Mohammad, K., Nikpey, A., Pourmand, M., 2013. Oxygen mass transfer in a stirred tank bioreactor using different impeller configurations for environmental purposes. Iranian J. Environ. Health Sci. Eng. 10, 6. https://doi.org/10.1186/1735-2746-10-6

Kawase, Y., Moo-Young, M., 1990. The effect of antifoam agents on mass transfer in bioreactors. Bioprocess Eng. 5, 169–173. https://doi.org/10.1007/BF00369581

Klöckner, W., Büchs, J., 2012. Advances in shaking technologies. Trends Biotechnol. 30, 307–314. https://doi.org/10.1016/j.tibtech.2012.03.001

Klöckner, W., Diederichs, S., Büchs, J., 2013a. Orbitally Shaken Single-Use Bioreactors, in: Advances in Biochemical Engineering/Biotechnology. pp. 45–60. https://doi.org/10.1007/10_2013_188

Klöckner, W., Gacem, R., Anderlei, T., Raven, N., Schillberg, S., Lattermann, C., Büchs, J., 2013b. Correlation between mass transfer coefficient kLa and relevant operating parameters in cylindrical disposable shaken bioreactors on a bench-to-pilot scale. J. Biol. Eng. 7, 28. https://doi.org/10.1186/1754-1611-7-28

Klöckner, W., Tissot, S., Wurm, F., Büchs, J., 2012. Power input correlation to characterize the hydrodynamics of cylindrical orbitally shaken bioreactors. Biochem. Eng. J. 65, 63–69. https://doi.org/10.1016/j.bej.2012.04.007

Kováts, P., Thévenin, D., Zähringer, K., 2020. Influence of viscosity and surface tension on bubble dynamics and mass transfer in a model bubble column. Int. J. Multiph. Flow 123, 103174. https://doi.org/10.1016/j.ijmultiphaseflow.2019.103174

Krishna, R., Van Baten, J.M., 2003. Mass transfer in bubble columns. Catal. Today 79–80, 67–75. https://doi.org/10.1016/S0920-5861(03)00046-4

Labík, L., Petricříček, R., Moucha, T., Brucato, A., Caputo, G., Grisafi, F., Scargiali, F., 2018. Scale-up and viscosity effects on gas–liquid mass transfer rates in unbaffled stirred tanks. Chem. Eng. Res. Des. 132, 584–592. https://doi.org/10.1016/j.cherd.2018.01.051

Lievense, J.C., Lim, H.C., 1982. The Growth and Dynamics of Saccharomyces Cerevisiae, in: Annual Reports on Fermentation Processes. ACADEMIC PRESS, INC., pp. 211–262. https://doi.org/10.1016/B978-0-12-040305-9.50010-8

Liffman, K., Paterson, D.A., Liovic, P., Bandopadhayay, P., 2013. Comparing the energy efficiency of different high rate algal raceway pond designs using computational fluid dynamics. Chem. Eng. Res. Des. 91, 221–226. https://doi.org/10.1016/j.cherd.2012.08.007

Linek, V., Kordač, M., Fujasová, M., Moucha, T., 2004. Gas–liquid mass transfer coefficient in stirred tanks interpreted through models of idealized eddy structure of turbulence in the bubble vicinity. Chem. Eng. Process. Process Intensif. 43, 1511–1517. https://doi.org/10.1016/j.cep.2004.02.009

Linek, V., Moucha, T., Sinkule, J., 1996. Gas-liquid mass transfer in vessels stirred with multiple impellers—II. Modelling of gas-liquid mass transfer. Chem. Eng. Sci. 51, 3875–3879. https://doi.org/10.1016/0009-2509(96)00015-2

Liu, C., Liang, B., Tang, S., Min, E., 2013. Effects of Orifice Orientation and Gas-Liquid Flow Pattern on Initial Bubble Size. Chinese J. Chem. Eng. 21, 1206–1215. https://doi.org/10.1016/S1004-9541(13)60630-8

Liu, K., Phillips, J.R., Sun, X., Mohammad, S., Huhnke, R.L., Atiyeh, H.K., 2019. Investigation and Modeling of Gas-Liquid Mass Transfer in a Sparged and Non-Sparged Continuous Stirred Tank Reactor with Potential Application in Syngas Fermentation. Fermentation 5, 75. https://doi.org/10.3390/fermentation5030075

Manica, R., Klaseboer, E., Chan, D.Y.C., 2015. Force Balance Model for Bubble Rise, Impact, and Bounce from Solid Surfaces. Langmuir 31, 6763–6772. https://doi.org/10.1021/acs.langmuir.5b01451

Mehrnia, M.R., Bonakdarpour, B., Towfighi, J., Akbarnejad, M.M., 2004. Design and operational aspects of airlift bioreactors for petroleum biodesulfurization. Environ. Prog. 23, 206–214. https://doi.org/10.1002/ep.10024

Mendoza, J.L., Granados, M.R., de Godos, I., Acién, F.G., Molina, E., Banks, C., Heaven, S., 2013a. Fluid-dynamic characterization of real-scale raceway reactors for microalgae production. Biomass and Bioenergy 54, 267–275. https://doi.org/10.1016/j.biombioe.2013.03.017

Mendoza, J.L., Granados, M.R., de Godos, I., Acién, F.G., Molina, E., Heaven, S., Banks, C.J., 2013b. Oxygen transfer and evolution in microalgal culture in open raceways. Bioresour. Technol. 137, 188–195. https://doi.org/10.1016/j.biortech.2013.03.127

Michel, B.J., Miller, S.A., 1962. Power requirements of gas-liquid agitated systems. AIChE J. 8, 262–266.

Mikola, M., Seto, J., Amanullah, A., 2007. Evaluation of a novel Wave Bioreactor® cellbag for aerobic yeast cultivation. Bioprocess Biosyst. Eng. 30, 231–241. https://doi.org/10.1007/s00449-007-0119-y

Mohd Sauid, S., Krishnan, J., Huey Ling, T., Veluri, M.V.P.S., 2013. Enhancement of oxygen mass transfer and gas holdup using palm oil in stirred tank bioreactors with xanthan solutions as simulated viscous fermentation broths. Biomed Res. Int. 2013. https://doi.org/10.1155/2013/409675

Nagai, S., 1979. Mass and energy balances for microbial growth kinetics. pp. 49–83.

https://doi.org/10.1007/3-540-08990-X_22

Nauha, E.K., Visuri, O., Vermasvuori, R., Alopaeus, V., 2015. A new simple approach for the scale-up of aerated stirred tanks. Chem. Eng. Res. Des. 95, 150–161. https://doi.org/10.1016/j.cherd.2014.10.015

Nishikawa, M., Nishioka, S., Kayama, T., 1984. Gas absorption in an aerated mixing vessel with multi-stage impellers. J. Chem. Eng. Japan 17, 541–543. https://doi.org/10.1252/jcej.17.541

O'Connor, G.M., Sanchez-Riera, F., Cooney, C.L., 1992. Design and evalution of control strategies for high cell density fermentations. Biotechnol. Bioeng. 39, 293–304. https://doi.org/10.1002/bit.260390307

Oosterhuis, N.M.G., Hudson, T., D'Avino, A., Zijlstra, G.M., Amanullah, A., 2011. Disposable Bioreactors, in: Comprehensive Biotechnology. Elsevier, pp. 249–261. https://doi.org/10.1016/B978-0-08-088504-9.00098-2

Oosterhuis, N.M.G., van der Heiden, P., 2010. Mass Transfer in the CELL-tainer® Disposable Bioreactor, in: Noll, T. (Ed.), Cells and Culture. Springer Netherlands, Dordrecht, pp. 371–373.

Piper, P.W., Talreja, K., Panaretou, B., Moradas-Ferreira, P., Byrne, K., Praekelt, U.M., Meacock, P., Recnacq, M., Boucherie, H., 1994. Induction of major heat-shock proteins of Saccharomyces cerevisiae, including plasma membrane Hsp30, by ethanol levels above a critical threshold. Microbiology 140, 3031–3038. https://doi.org/10.1099/13500872-140-11-3031

Plais, C., Augier, F., 2016. Effect of liquid viscosity on mixing times in bubble columns. Theor. Found. Chem. Eng. 50, 969–974. https://doi.org/10.1134/S0040579516060142

Pollard, D.J., Ayazi Shamlou, P., Lilly, M.D., Ison, A.P., 1996. Saccharomyces cerevisiae fermentations in a pilot scale airlift bioreactor: Comparison of air sparger configurations. Bioprocess Eng. 15, 279–288. https://doi.org/10.1007/BF02391590

Posten, C.H., Cooney, C.L., 1993. Growth of Microorganisms, in: Rehm, H.-J., Reed, G. (Eds.), Biotechnology: Biological Fundamentals. Wiley-VCH Verlag GmbH, Weinheim, Germany, pp. 111–162. https://doi.org/10.1002/9783527620821.ch3

Prins, A., van't Riet, K., 1987. Proteins and surface effects in fermentation: foam, antifoam and mass transfer. Trends Biotechnol. 5, 296–301. https://doi.org/10.1016/0167-7799(87)90080-1

Richardson, J.F., Harker, J.H., Backhurst, J.R., Coulson, J.M., 2002. Coulson and Richardson's chemical engineering. Vol. 2, Vol. 2,.

Rosen, K., 1987. Production of baker's yeast, in: Berry, D.R., Russell, I., Stewart, G.G. (Eds.), Yeast Biotechnology. Springer Netherlands, Dordrecht, pp. 471–500. https://doi.org/10.1007/978-94-009-3119-0_15

Rubio, F.C., Garcia, J.L., Molina, E., Chisti, Y., 1999. Steady-state axial profiles of dissolved oxygen in tall bubble column bioreactors. Chem. Eng. Sci. 54, 1711–1723. https://doi.org/10.1016/S0009-2509(98)00540-5

Ruzicka, M.C., Drahoš, J., Fialová, M., Thomas, N.H., 2001. Effect of bubble column dimensions on flow regime transition. Chem. Eng. Sci. 56, 6117–6124. https://doi.org/10.1016/S0009-2509(01)00215-9

Sastaravet, P., Chuenchaem, C., Thaphet, N., Chawaloesphonsiya, N., Painmanakul, P., 2014. Comparative Study of Mass Transfer and Bubble Hydrodynamic Parameters in Bubble Column Reactor: Physical Configurations and Operating Conditions. Environ. Eng. Res. 19, 345–354. https://doi.org/10.4491/eer.2014.S1.013

Schaschke, C., 2014. Henry's law. Dict. Chem. Eng.

Shah, Y.T., Kelkar, B.G., Godbole, S.P., Deckwer, W.-D., 1982. Design parameters estimations for bubble column reactors. AIChE J. 28, 353–379. https://doi.org/10.1002/aic.690280302

Sharaf, S., Zednikova, M., Ruzicka, M.C., Azzopardi, B.J., 2016. Global and local hydrodynamics of bubble columns - Effect of gas distributor. Chem. Eng. J. 288, 489–504. https://doi.org/10.1016/j.cej.2015.11.106

Shariati, F.P., Bonakdarpour, B., Mehrnia, M.R., 2007. Hydrodynamics and oxygen transfer behaviour of water in diesel microemulsions in a draft tube airlift bioreactor. Chem. Eng. Process. Process Intensif. 46, 334–342. https://doi.org/10.1016/j.cep.2006.07.003

Šijački, I.M., Tokić, M.S., Kojić, P.S., Petrović, D.L., Tekić, M.N., Lukić, N.L., 2013. Sparger type influence on the volumetric mass transfer coefficient in the draft tube airlift reactor with diluted alcohol solutions. Ind. Eng. Chem. Res. 52, 6812–6821. https://doi.org/10.1021/ie303211u

Singh, V., 1999. Disposable bioreactor for cell culture using wave-induced agitation. Cytotechnology 30, 149–158. https://doi.org/10.1023/a:1008025016272

Stenberg, O., Andersson, B., 1988. Gas-liquid mass transfer in agitated vessels-II. Modelling of gas-liquid mass transfer. Chem. Eng. Sci. 43, 725–730. https://doi.org/10.1016/0009-2509(88)87032-5

Tatterson, G.B., 1991. Fluid mixing and gas dispersion in agitated tanks, Fluid mixing and gas dispersion in agitated tanks. McGraw-Hill, New York.

Tekic, M., Sijacki, I., Tokic, M., Kojic, P., Petrovic, D., Lukic, N., Popovic, S., 2014. Hydrodynamics of a self-agitated draft tube airlift reactor. Chem. Ind. Chem. Eng. Q. 20, 59–69. https://doi.org/10.2298/CICEQ120627102T

Thorat, B.N., Joshi, J.B., 2004. Regime transition in bubble columns: Experimental and predictions. Exp. Therm. Fluid Sci. 28, 423–430. https://doi.org/10.1016/j.expthermflusci.2003.06.002

Thorat, B.N., Shevade, A.V., Bhilegaonkar, K.N., Aglawe, R.H., Parasu Veera, U., Thakre, S.S., Pandit, A.B., Sawant, S.B., Joshi, J.B., 1998. Effect of Sparger Design and Height to Diameter Ratio on Fractional Gas Hold-up in Bubble Columns. Chem. Eng. Res. Des. 76, 823–834. https://doi.org/10.1205/026387698525577

Tissot, S., Farhat, M., Hacker, D.L., Anderlei, T., Kühner, M., Comninellis, C., Wurm, F., 2010. Determination of a scale-up factor from mixing time studies in orbitally shaken bioreactors. Biochem. Eng. J. 52, 181–186. https://doi.org/10.1016/j.bej.2010.08.005

Tribe, L.A., Briens, C.L., Margaritis, A., 1995. Determination of the volumetric mass transfer coefficient (kLa) using the dynamic “gas out–gas in” method: Analysis of errors caused by dissolved oxygen probes. Biotechnol. Bioeng. 46, 388–392. https://doi.org/10.1002/bit.260460412

Turner, A.P.F., White, S.F., 2002. Process Monitoring, in: Encyclopedia of Bioprocess Technology. American Cancer Society. https://doi.org/10.1002/0471250589.ebt171

Van’t Riet, K., 1979. Review of Measuring Methods and Results in Nonviscous Gas-Liquid Mass Transfer in Stirred Vessels. Ind. Eng. Chem. Process Des. Dev. 18, 357–364. https://doi.org/10.1021/i260071a001

Van’t Riet, K., Tramper, J., 1991. Basic Bioreactor Design. CRC Press, New York. https://doi.org/10.1201/9781482293333

Van ’t Riet, K., van der Lans, R.G.J.M., 2011. Mixing in Bioreactor Vessels, in: Comprehensive Biotechnology. Elsevier, pp. 63–80. https://doi.org/10.1016/B978-0-08-088504-9.00083-0

Van Hoek, P., Van Dijken, J.P., Pronk, J.T., 1998. Effect of Specific Growth Rate on Fermentative Capacity of Baker’s Yeast. Appl. Environ. Microbiol. 64, 4226–4233. https://doi.org/10.1128/AEM.64.11.4226-4233.1998

Vendruscolo, F., Rossi, M.J., Schmidell, W., Ninow, J.L., 2012. Determination of Oxygen Solubility in Liquid Media. ISRN Chem. Eng. 2012, 1–5. https://doi.org/10.5402/2012/601458

Vieira, É.D., Andrietta, M. da G.S., Andrietta, S.R., 2013. Yeast biomass production: a new approach in glucose-limited feeding strategy. Brazilian J. Microbiol. 44, 551–558. https://doi.org/10.1590/S1517-83822013000200035

Whitman, W.G., 1923. The two film theory of gas absorption. Chem. Metall. Eng. 29, 146–148.

Wu, W.T., Wu, J.Y., Jong, J.Z., 1992. Mass transfer in an airlift reactor with a net draft tube. Biotechnol. Prog. 8, 465–468. https://doi.org/10.1021/bp00017a015

Yang, T., Huang, Y., Han, Z., Liu, H., Zhang, R., Xu, Y., 2013. Novel disposable flexible bioreactor for Escherichia coli culture in orbital shaking incubator. J. Biosci. Bioeng. 116, 452–459. https://doi.org/10.1016/j.jbiosc.2013.04.004

Yazdian, F., Shojaosadati, S.A., Nosrati, M., Mehrnia, M.R., Vasheghani-Farahani, E., 2009. Study of geometry and operational conditions on mixing time, gas hold up, mass transfer, flow regime and biomass production from natural gas in a horizontal tubular loop bioreactor. Chem. Eng. Sci. 64, 540–547. https://doi.org/10.1016/j.ces.2008.09.031

Yen, H.-W., Hu, I.-C., Chen, C.-Y., Nagarajan, D., Chang, J.-S., 2019. Chapter 10 - Design of photobioreactors for algal cultivation, in: Pandey, A., Chang, J.-S., Soccol, C.R., Lee, D.-J., Chisti, Y. (Eds.), Biofuels from Algae (Second Edition), Biomass, Biofuels, Biochemicals. Elsevier, pp. 225–256. https://doi.org/https://doi.org/10.1016/B978-0-444-64192-2.00010-X

Zhu, L., Xu, B., Wu, X., Lei, J., Hacker, D.L., Liang, X., Wurm, F.M., 2020. Analysis of volumetric mass transfer coefficient (kLa) in small- (250 mL) to large-scale (2500 L) orbitally shaken bioreactors. 3 Biotech 10, 397. https://doi.org/10.1007/s13205-020-02352-9

Ziegler, H., Meister, D., Dunn, I.J., Blanch, H.W., Russell, T.W.F., 1977. The tubular loop fermentor: Oxygen transfer, growth kinetics and design. Biotechnol. Bioeng. 19, 507–525. https://doi.org/10.1002/bit.260190406

Appendix A – Equation Derivation

The derivation of Equation (2.28) and Equation (2.29) for the travelling loop reactor was performed by compiling data values for k_La and power input as provided by Kaiser et al. (2016b). These values were then plotted on a plot of k_La vs. power input per unit volume. As only a rudimentary correlation was desired for the sake of determining mass transfer energy efficiency, a linear relationship was assumed. For the baffled and unbaffled systems, this resulted in the generation of Figure A.1 and Figure A.2. The resultant lines of best fit were then used as the generic equation for the determination of k_La with increasing power input.

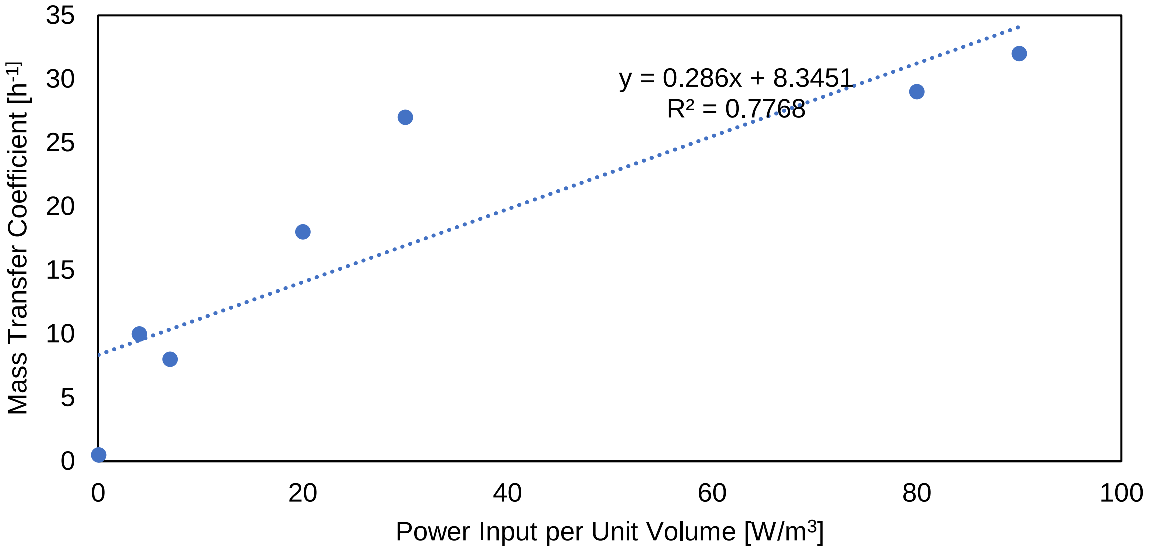

Figure A.1 – Plot of k_La vs. power input per unit volume for the baffled travelling loop reactor, adapted from Kaiser et al. (2016b)

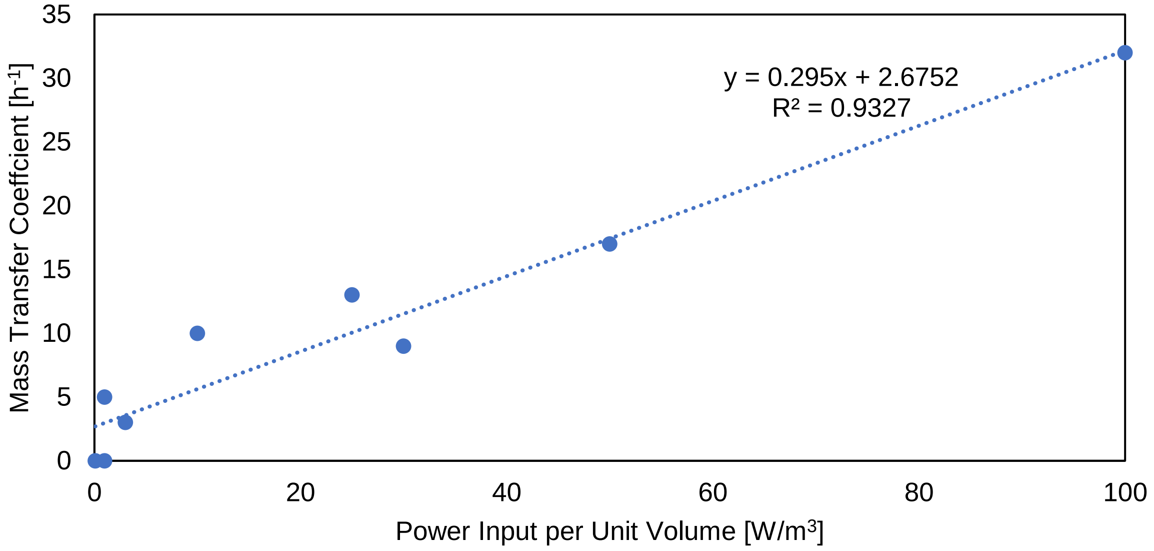

Figure A.2 – Plot of k_La vs. power input per unit volume for the unbaffled travelling loop reactor, adapted from Kaiser et al. (2016b)

Appendix B – Reactor Configurations

The following tables depict the reactor configurations (when specified by the author/s) used to generate the k_La vs. power input per unit volume trendlines observed in Figure 2.11 to Figure 2.13 (HAR reactor systems).

Table B.1 – STR reactor configurations used in Figure 2.11

Trend Number	Reactor Specifications/Notes	Liquid Medium	Reference
1	**No Reactor Specifications Provided:** Coefficients/trends are aggregated from many other papers.	Ionic water	Van't Riet (1979)
2	**No Reactor Specifications Provided:** Coefficients/trends are aggregated from many other papers.	Deionised water	Van't Riet (1979)
3	**Working volume:** 17 L **Diameter:** 0.228 m **Height:** 0.550 m **Impeller Type:** Rushton **Number of Impellers:** 1	Water	Gagnon et al. (1998)
4	**Working volume:** 17 L **Diameter:** 0.228 m **Height:** 0.550 m **Impeller Type:** Rushton **Number of Impellers:** 2	Water	Gagnon et al. (1998)
5	**Working volume:** 17 L **Diameter:** 0.228 m **Height:** 0.550 m **Impeller Type:** Rushton **Number of Impellers:** 3	Water	Gagnon et al. (1998)
6	**Working volume:** Not given **Liquid height:** 0.58 m **Diameter:** 0.29 m **Height:** Not given **Impeller Type:** Rushton **Number of Impellers:** 2	Water	Linek et al. (2004)
7	**Working volume:** 7 L **Diameter:** 0.146 m **Height:** 0.419 m **Impeller Type:** Rushton **Number of Impellers:** 2	Deionised water	Liu et al. (2019)

Table B.2 – BCR reactor configurations used in Figure 2.12

Trend Number	**Reactor Specifications/Notes**	**Liquid Medium**	**Reference**
1	**No Reactor Specifications Provided:** Coefficients/trends are aggregated from many other papers.	Water	Heijnen and Van't Riet (1984)
2	**Liquid Height:** 1.8 m **Reactor Height:** None given **Reactor Diameter:** 0.152 m **Superficial Gas Velocity Range:** 0.0137-0.086 $m \cdot s^{-1}$	Water/aqueous salt solution	Chisti (1989)
3	**Note:** The correlation for this trendline was for a viscous system. However, to compare this to water systems a viscosity of 1 cP was used in the correlation. **No Reactor Specifications Provided:** Coefficients/trends are aggregated from many other papers.	Water	Heijnen and Van't Riet (1984)
4	**Note:** 3 different configurations were tested, the correlation used in the paper is an aggregate between the three. **Liquid Heights:** 30 cm/100 cm/100 cm **Reactor Diameters:** 5 cm/10 cm/15 cm	Water	Sastaravet et al. (2014)
5	**No Reactor Specifications Provided:** Coefficients/trends are aggregated from many other papers.	Water	Deckwer et al. (1983)
6	**No Reactor Specifications Provided:** The relationship established in this paper was determined by analysing and modifying relationships from other papers. **Note:** The correlation for this trendline was for a viscous system. However, to compare this to water systems a viscosity of 1 cP was used in the correlation.	Water	Deckwer et al. (1982)
7	**Liquid Height:** 3.995 m **Reactor Height:** 8.05 m **Reactor Diameter:** 0.243 m	Tap water	Rubio et al. (1999)

Table B.3 – ALR reactor configurations used in Figure 2.13

Trend Number	Reactor Specifications	Liquid Details	Reference
1	**No Details Provided:** Coefficients/trends are aggregated from many other papers. **Reactor Configuration:** Internal loop	Water	Heijnen and Van't Riet (1984)
2	**Reactor Height:** None given **Liquid Height:** 1.35 m **Draft Tube Height:** 1.1 m **Draft Tube Internal Diameter:** 0.14 m **Downcomer to Riser Ratio:** 0.906 **Reactor Configuration:** Internal loop	Distilled water (Although water diesel mixtures were also tested)	Shariati et al. (2007)
3	**Reactor Height:** None given **Liquid Height:** 1.8 m **Draft Tube Height:** 1.55 m **Total Reactor Diameter:** 0.152 m **Reactor Configuration:** Internal loop **Downcomer to Riser Ratio:** 0.13-0.35	Water	Bello et al. (1985)
4	**Reactor Height:** 2 m **Reactor Working Volume:** 15 L **Reactor Diameter:** 0.13 m **Draft Tube Height: 1 m** **Draft Tube Diameter:** 6.5 cm/8.0 cm/9.0 cm/10.4 cm **Reactor Configuration:** Internal loop **Downcomer to Riser Ratio:** Ratio not specified	Water	Wu et al. (1992)

Appendix C – STR Data

C.1 STR Fed-batch Concentration Data

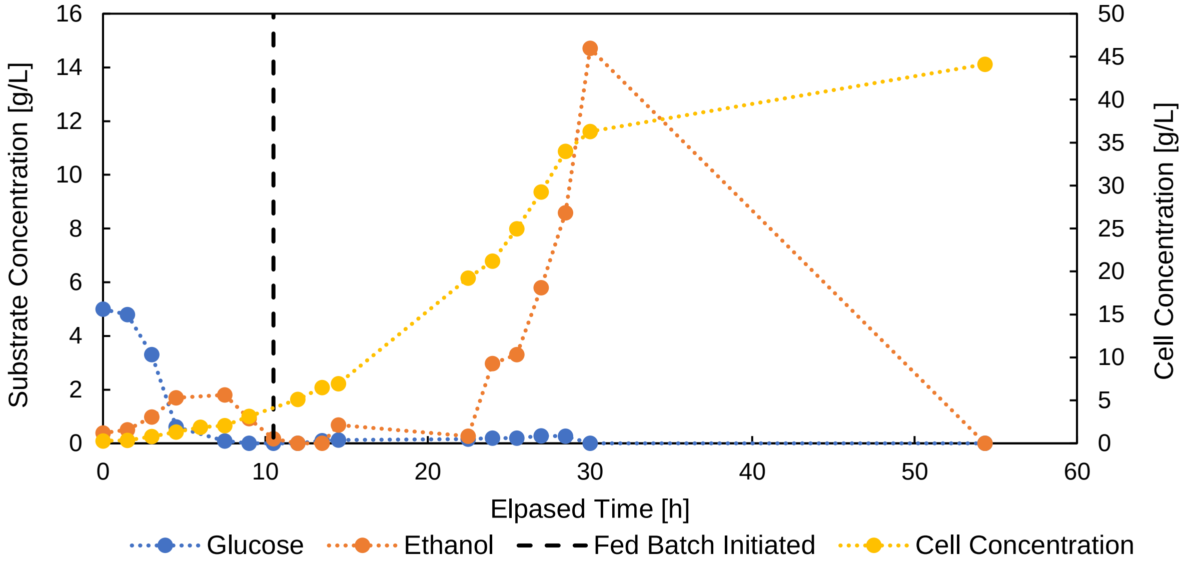

Figure C.1 – Substrate and cell concentration data for fed-batch STR run 1

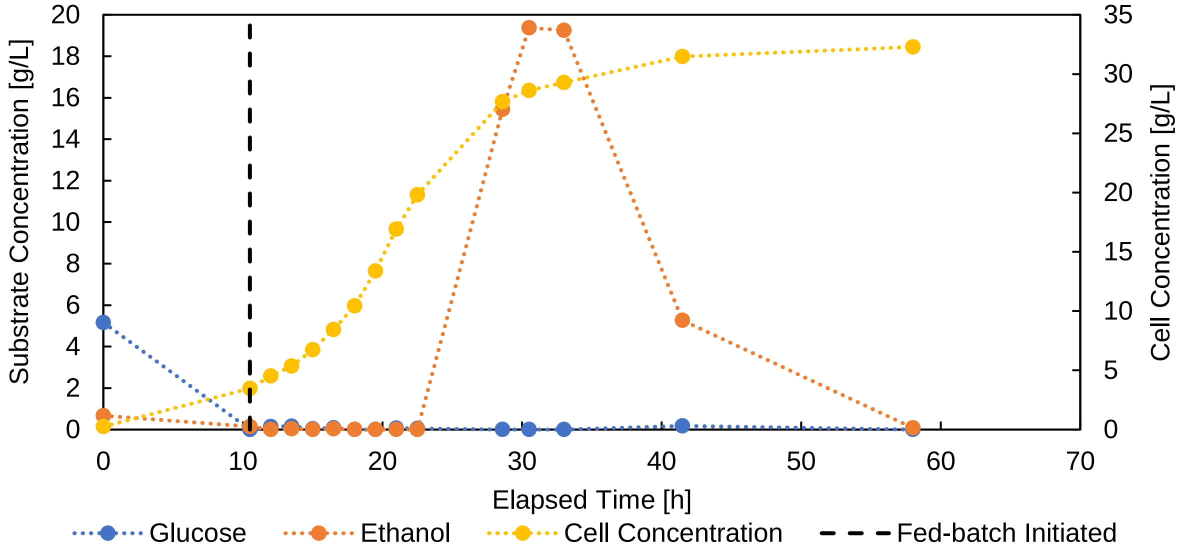

Figure C.2 – Substrate and cell concentration data for fed-batch STR run 2

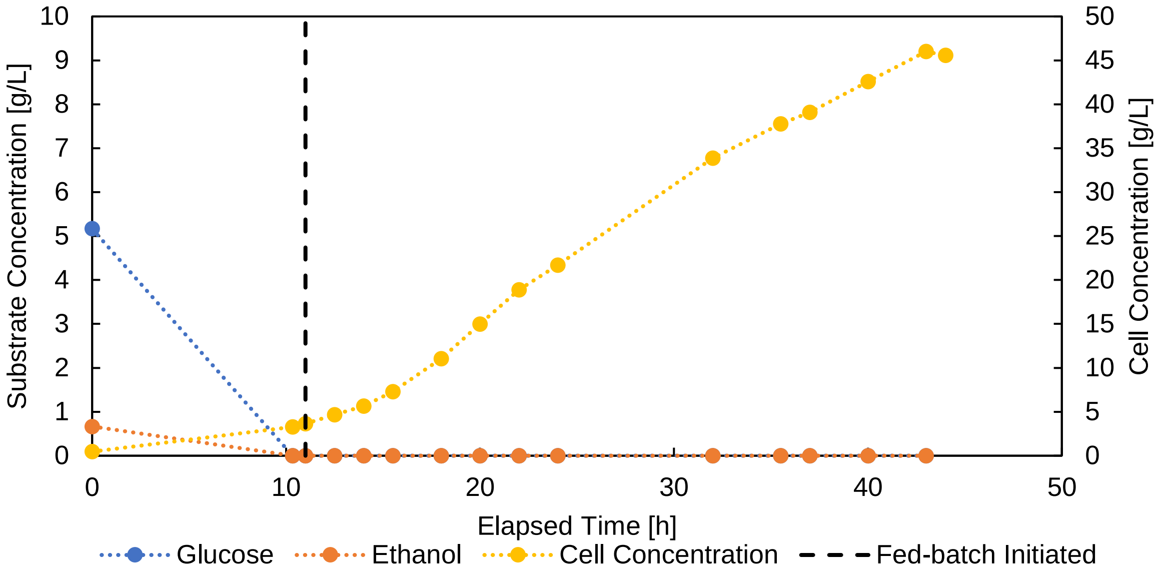

Figure C.3 – Substrate and cell concentration data for fed-batch STR run 3

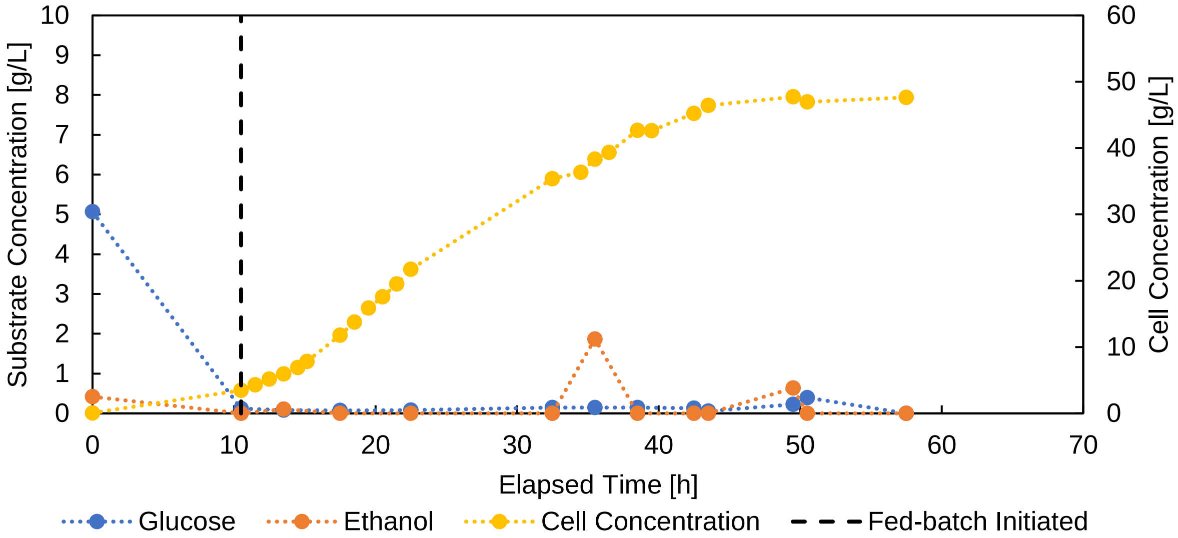

Figure C.4 – Substrate and cell concentration data for fed-batch STR run 4

C.2 STR Fed-batch Key Results Tables

Table C.1 – Key fed-batch data from fed-batch STR run 1

Item	Value	Units
Overall Yield on Glucose (Excluding Death Phase)	Insufficient Data	$g_{biomass}/g_{glucose}$
Maximum Observed Growth Rate	0.16	h^{-1}
Minimum Theoretical k_La Required @ Max O_2 Demand	Insufficient Data	h^{-1}
Average Observed Growth Rate	0.09	h^{-1}
Minimum k_La Required on Average	Insufficient Data	h^{-1}
Average Productivity	Insufficient Data	g/h
Final Cell Density	44.1	g/L

Table C.2 – Key fed-batch data from fed-batch STR run 2

Item	Value	Units
Overall Yield on Glucose (Excluding Death Phase)	0.31	$g_{biomass}/g_{glucose}$
Maximum Observed Growth Rate	0.18	h^{-1}
Minimum Theoretical k_La Required @ Max O_2 Demand	291	h^{-1}
Average Observed Growth Rate	0.11	h^{-1}
Minimum k_La Required on Average	173	h^{-1}
Average Productivity	9.90	g/h
Final Cell Density	32.3	g/L

Table C.3 – Key fed-batch data from fed-batch STR run 3

Item	Value	Units
Overall Yield on Glucose (Excluding Death Phase)	0.51	$g_{biomass}/g_{glucose}$
Maximum Observed Growth Rate	0.18	h^{-1}
Minimum Theoretical k_La Required @ Max O_2 Demand	269	h^{-1}
Average Observed Growth Rate	0.10	h^{-1}
Minimum k_La Required on Average	162	h^{-1}
Average Productivity	12.0	g/h
Final Cell Density	45.6	g/L

Table C.4 – Key fed-batch data from fed-batch STR run 4

Item	Value	Units
Overall Yield on Glucose (Excluding Death Phase)	0.44	$g_{biomass}/g_{glucose}$
Maximum Observed Growth Rate	0.20	h^{-1}
Minimum Theoretical k_La Required @ Max O_2 Demand	401	h^{-1}
Average Observed Growth Rate	0.10	h^{-1}
Minimum k_La Required on Average	186	h^{-1}
Average Productivity	10.6	g/h
Final Cell Density	47.7	g/L

C.3 STR Fed-batch Prediction Trends

Note that for fed-batch STR runs 1, 2 and 3, no prediction trends for productivity were made, hence they are not present in these appendices.

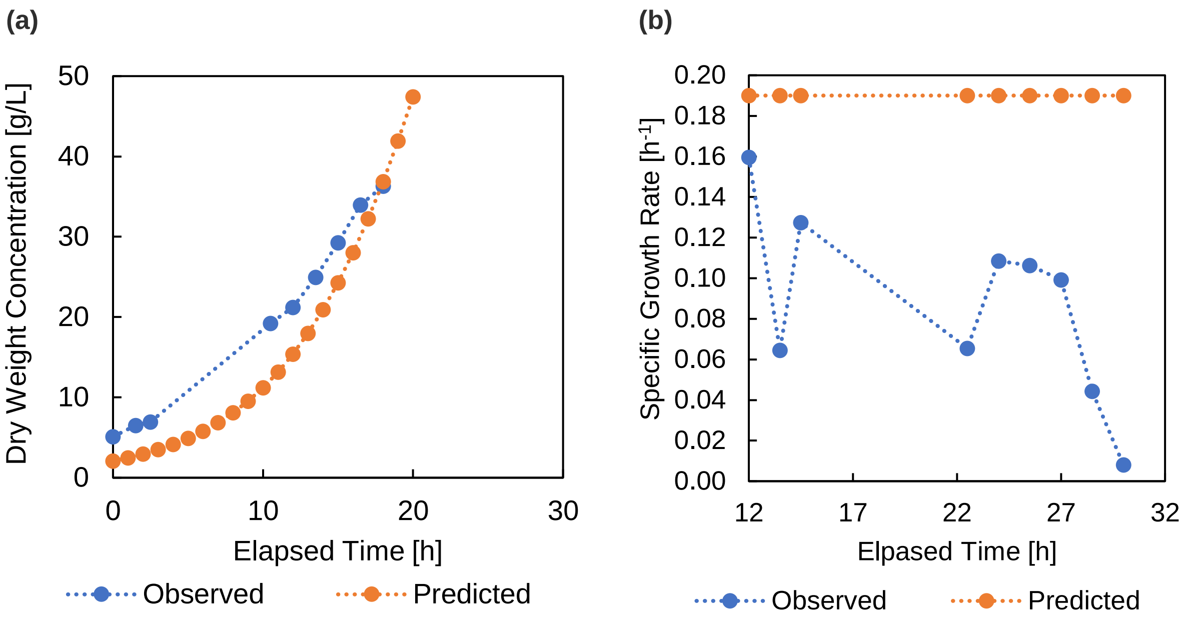

Figure C.5 – Observed vs. predicted (a) cell concentration and (b) fed-batch growth rate for fed-batch STR run 1

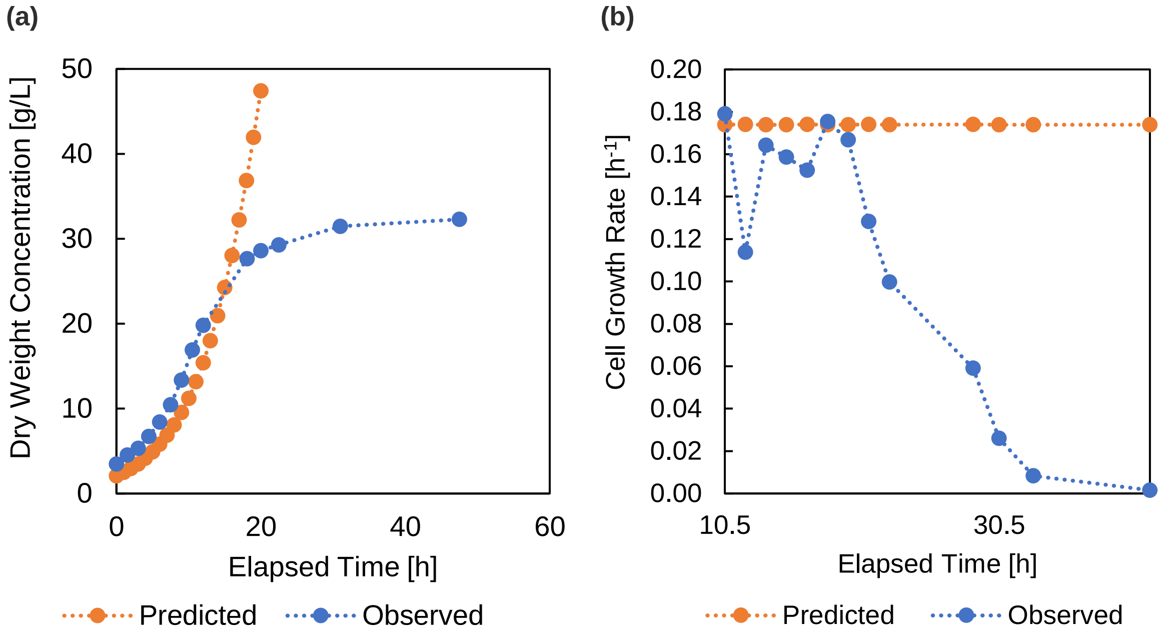

Figure C.6 – Observed vs. predicted (a) cell concentration and (b) fed-batch growth rate for fed-batch STR run 2

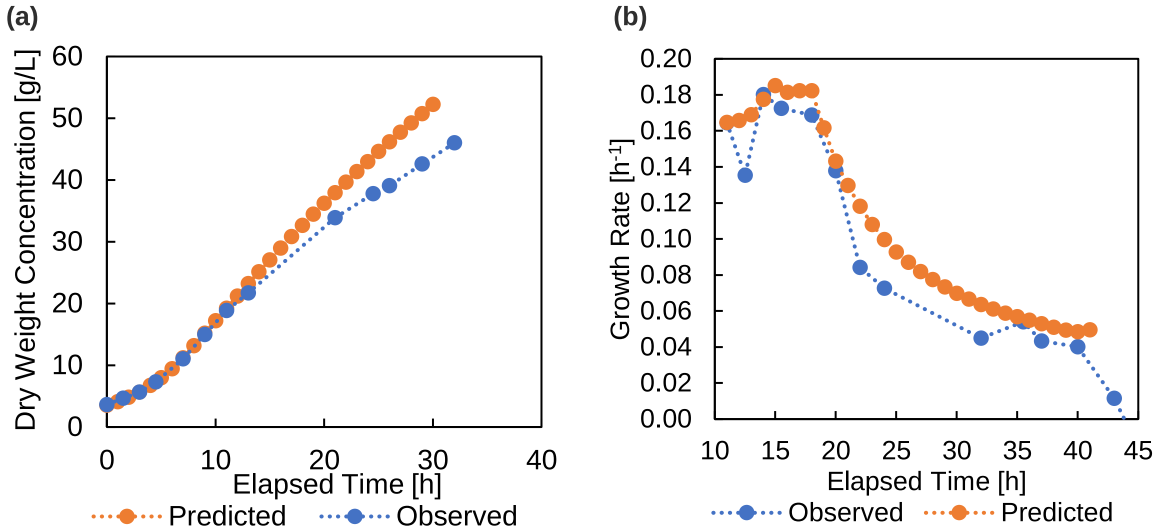

Figure C.7 – Observed vs. predicted (a) cell concentration and (b) fed-batch growth rate for fed-batch STR run 3

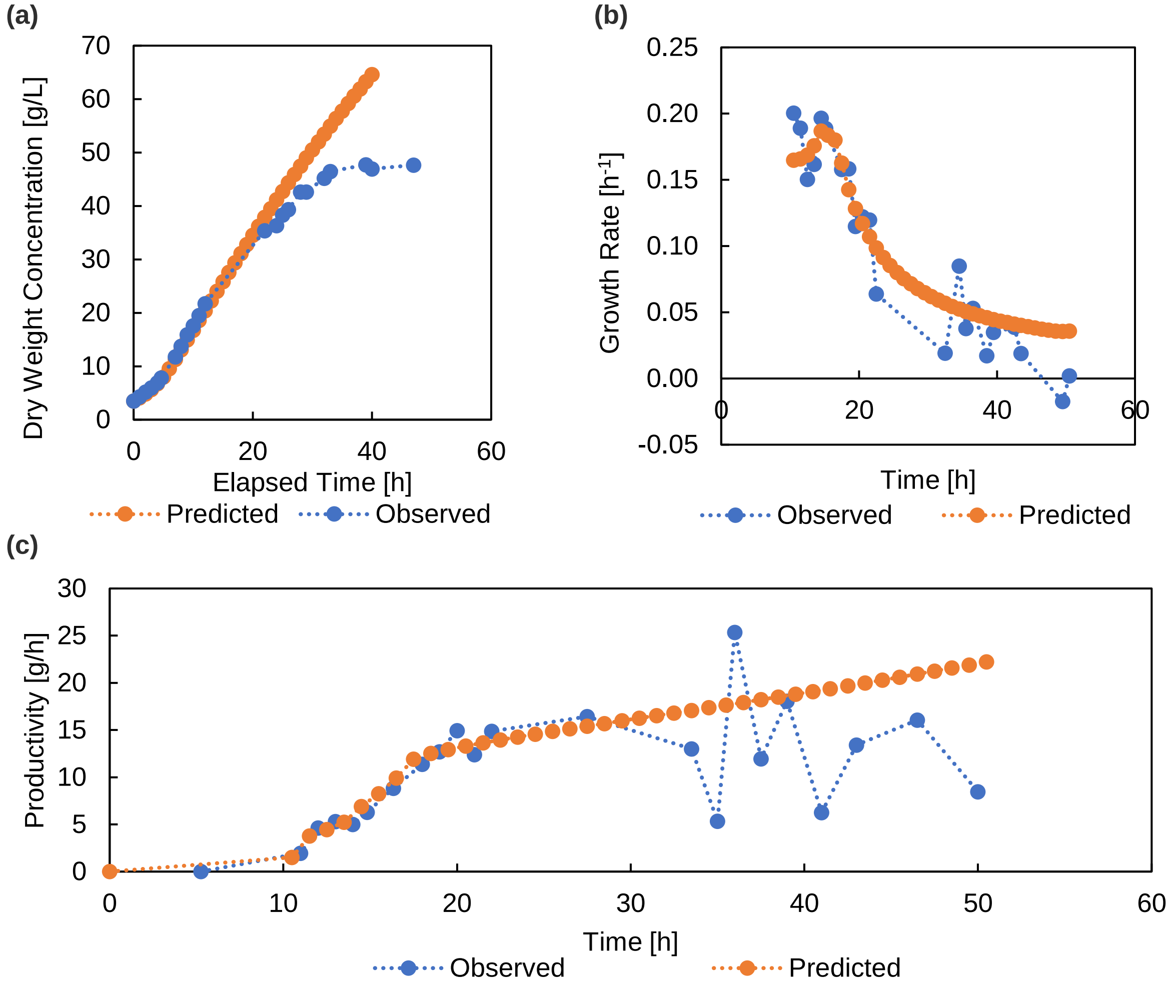

Figure C.8 – Observed vs. predicted (a) cell concentration, (b) fed-batch growth rate and (c) productivity for fed-batch STR run 4

C.4 STR Fed-batch Efficiency Data

Table C.5 – Run 1 mass transfer energy efficiency data

Power Input [W/m^3]	Efficiency [m^3·h^{-1}·W^{-1}]
434	0.25
435	0.11

Table C.6 – Run 2 mass transfer energy efficiency data

Power Input [W/m^3]	Efficiency [m^3·h^{-1}·W^{-1}]
318	0.22
319	0.10
439	0.13
441	0.14
832	0.03
1558	0.04
2008	0.05
2019	0.08
3098	0.01
3112	0.04
3571	0.02

Table C.7 – Run 3 mass transfer energy efficiency data

Power Input [W/m^3]	Efficiency [m^3·h^{-1}·W^{-1}]
324	0.16
895	0.11
920	0.09
1559	0.06
1559	0.03
2276	0.11
2276	0.10
2720	0.05
2950	0.04
3664	0.03
3664	0.03

Table C.8 – Run 4 mass transfer energy efficiency data

Power Input [W/m^3]	Efficiency [m^3·h^{-1}·W^{-1}]
344	0.11
344	0.11
344	0.20
965	0.08
965	0.08
965	0.08
1556	0.04
2234	0.02
2234	0.01
3213	0.02
3380	0.01
3710	0.02

Table C.9 – Run 5 mass transfer energy efficiency data

Power Input [W/m^3]	Efficiency [m^3·h^{-1}·W^{-1}]
967	0.13
1557	0.09
2245	0.03
2495	0.01
3223	0.01
3448	0.02
3711	0.02

Appendix D – Bubble Calculations

The following calculations are performed based on a 26 L HAIL reactor, with a superficial gas velocity from the sparger of 42.6 m/s (corresponding to a gas flow rate of 1 vvm). To determine the impact of the jet sparger on the liquid circulation rate and turbulence in the system, two approaches were considered. The first approach considered a simple force diagram over a bubble leaving a sparger:

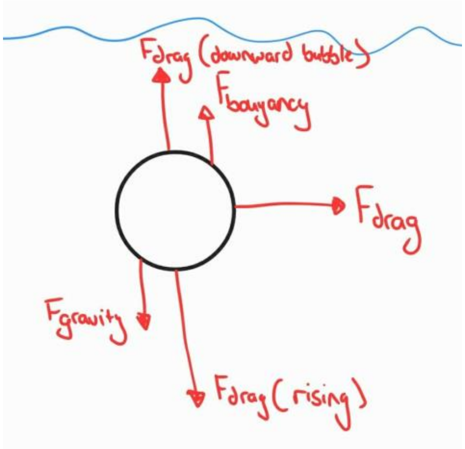

Figure D.1 – Force diagram over bubble

From Figure D.1 above, one will note that there are three drag forces that act on the bubble over the course of its motion. If the sparger is angled downwards, there will be a drag force counteracting the bubble’s downward motion. This will act until the velocity of the bubble reaches zero. Once the bubble stops descending, the buoyancy force will overcome the gravitational force and cause the bubble to rise. Drag once again acts on the bubble as it rises. The horizontal motion experiences no force outside of drag until the moment the bubble stops moving horizontally.

The drag force on the bubble clearly plays a big role in the force imparted by it on the liquid. To attempt to approximate this force, the bubble was assumed to be a spherical particle This is a simplification, as the bubble will deform as it moves which would greatly complicate the calculation (Manica et al., 2015). To determine the drag force on a spherical particle, the method outlined by Richardson et al., (2002) was followed. The first step is to determine the particle Reynold’s number, given by:

$$Re' = \frac{vd\rho}{\mu}$$ Equation D.1

Where “Re'” is the particle Reynolds number, “v” is the particle velocity in m/s, “d” is the particle diameter in meters, “ρ” is the liquid density in kg/m^3 and “μ” is the liquid viscosity in cP. Depending on the magnitude of the particle Reynolds number, the particle will then be placed in one of four zones for determining the drag force. The maximum particle Reynolds number for the tested system was found to be 1.72×10^5, which would place the particle in the 3rd region ($Re'<2\times10^5$). As the velocity of the sphere decreases, so to would the region. However, a general correlation for a particle in the first three regions is available:

$$F = \frac{\pi}{4} d^2 \rho v^2 (1.84Re'^{-0.31} + 0.293Re'^{0.06})^{3.45}$$ Equation D.2

Where “F” is the total drag force experienced by the particle. For a non-perpendicular angle, the velocity can be broken down into a vertical and horizontal component using basic trigonometry. Using Equation D.2 with these velocities allows for the net vertical and horizontal drag force to be determined. For an angle of 60° this results in a net, instantaneous, drag force of 0.956 N vertically and 3.04 N horizontally. At an angle of 90°, this results in no vertical force and a horizontal force of 4.13 N. The vertical force contributes to radial mixing in the system, whereas the horizontal force contributes more to the liquid velocity and hence aids in reducing the circulation time. The drag force would change rapidly as the velocity of the particle decreases, but for the purpose of these preliminary bubble calculations no further work calculation needs to be done.

Appendix E – Sparger Designs

E.1 Sparger Layout

All spargers were tested in the same location in the reactor. In the proof-of-concept prototype the spargers were kept straight by looking through the transparent tubing and “eyeing” the sparger. For the laboratory-scale prototype, the guard rail was enhanced with a triangle such that the direction of the sparger could be observed briefly and more easily maintained. A cross section of a typical experiment is presented in Figure E.1.

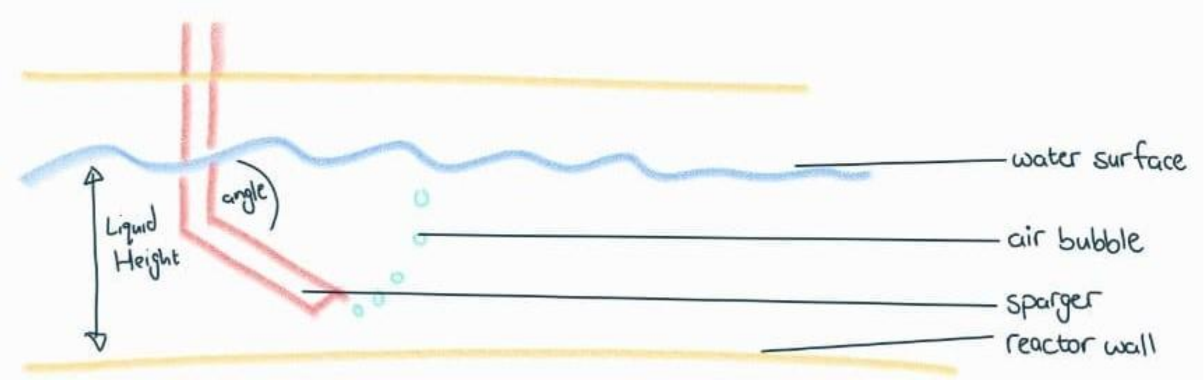

Figure E.1 – Typical sparger experiment cross-section

The depth of the angled spargers (used in the proof-of-concept reactor experiments) is given by the vertical distance between the sparger outlet and the roof of the reactor. This depth was obtained by altering the height of the sparger guard, as can be observed in Appendix E.2.

E.2 Proof-of-concept Reactor Sparger 3D Models

Table E.1 – 45° proof-of-concept reactor sparger designs

Sparger Name	**P45-30**	**P45-40**	**P45-50**
Sparger Image	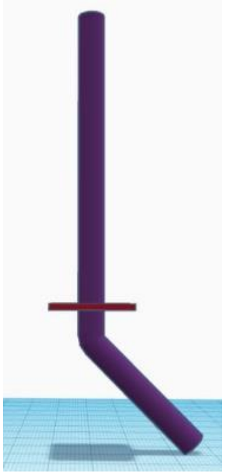 Figure E.2 – Sparger P45-30	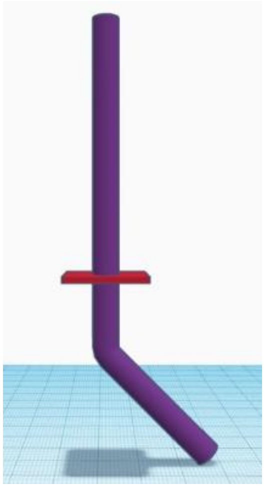 Figure E.3 – Sparger P45-40	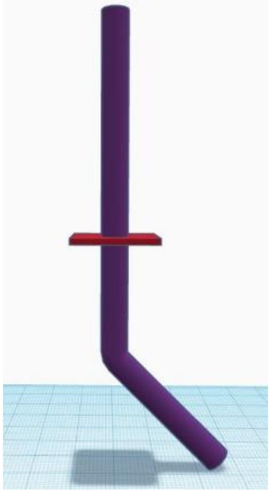 Figure E.4 – Sparger P45-50
Sparger Depth [mm]	30	40	50

Table E.2 – 60° proof-of-concept reactor sparger designs

Sparger Name	**P60-30**	**P60-40**	**P60-50**
Sparger Image	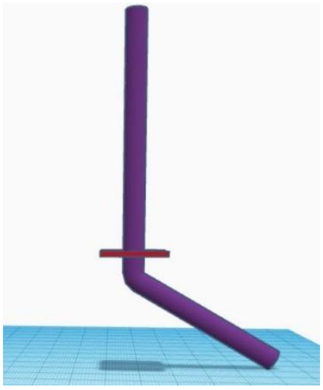 Figure E.5 – Sparger P60-30	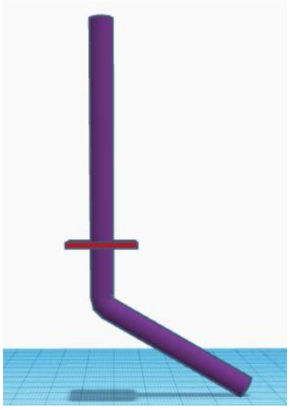 Figure E.6 – Sparger P60-40	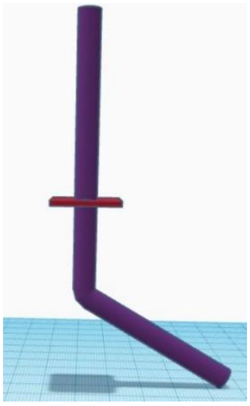 Figure E.7 – Sparger P60-50
Sparger Depth [mm]	30	40	50

Table E.3 – 75° proof-of-concept reactor sparger designs

Sparger Name	**P75-30**	**P75-40**	**P75-50**
Sparger Image	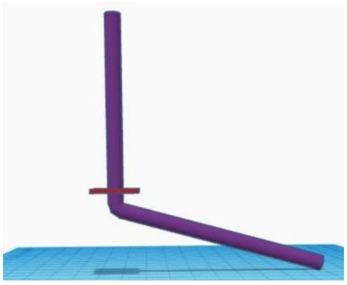 Figure E.8 – Sparger P75-30	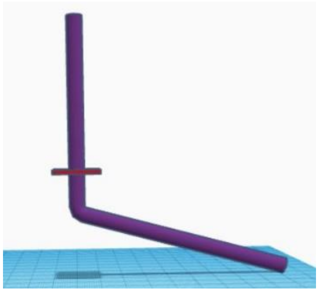 Figure E.9 – Sparger P75-40	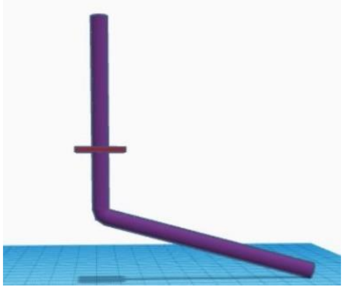 Figure E.10 – Sparger P75-50
Sparger Depth [mm]	30	40	50

Table E.4 – 90° proof-of-concept reactor sparger designs

Sparger Name	**P90-30**	**P90-40**	**P90-50**
Sparger Image	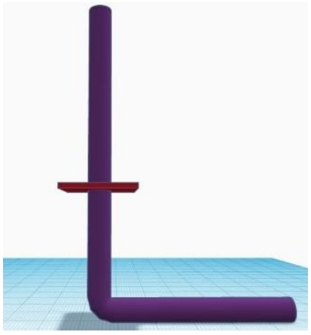 Figure E.11 – Sparger P90-30	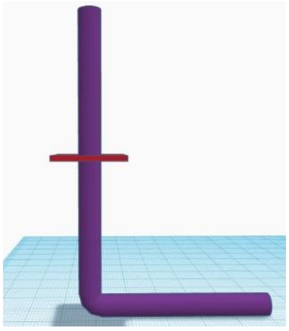 Figure E.12 – Sparger P90-40	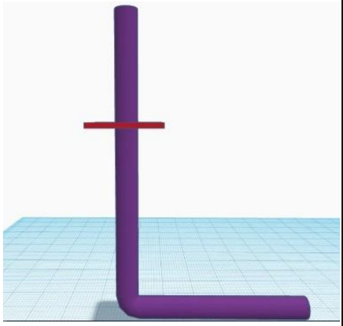 Figure E.13 – Sparger P90-50
Sparger Depth [mm]	30	40	50

E.3 Laboratory-scale Reactor Sparger 3D Models

Design specifications for the spargers listed in this section of the appendix are listed in Table 6.2. Only the 3D models are described as a result.

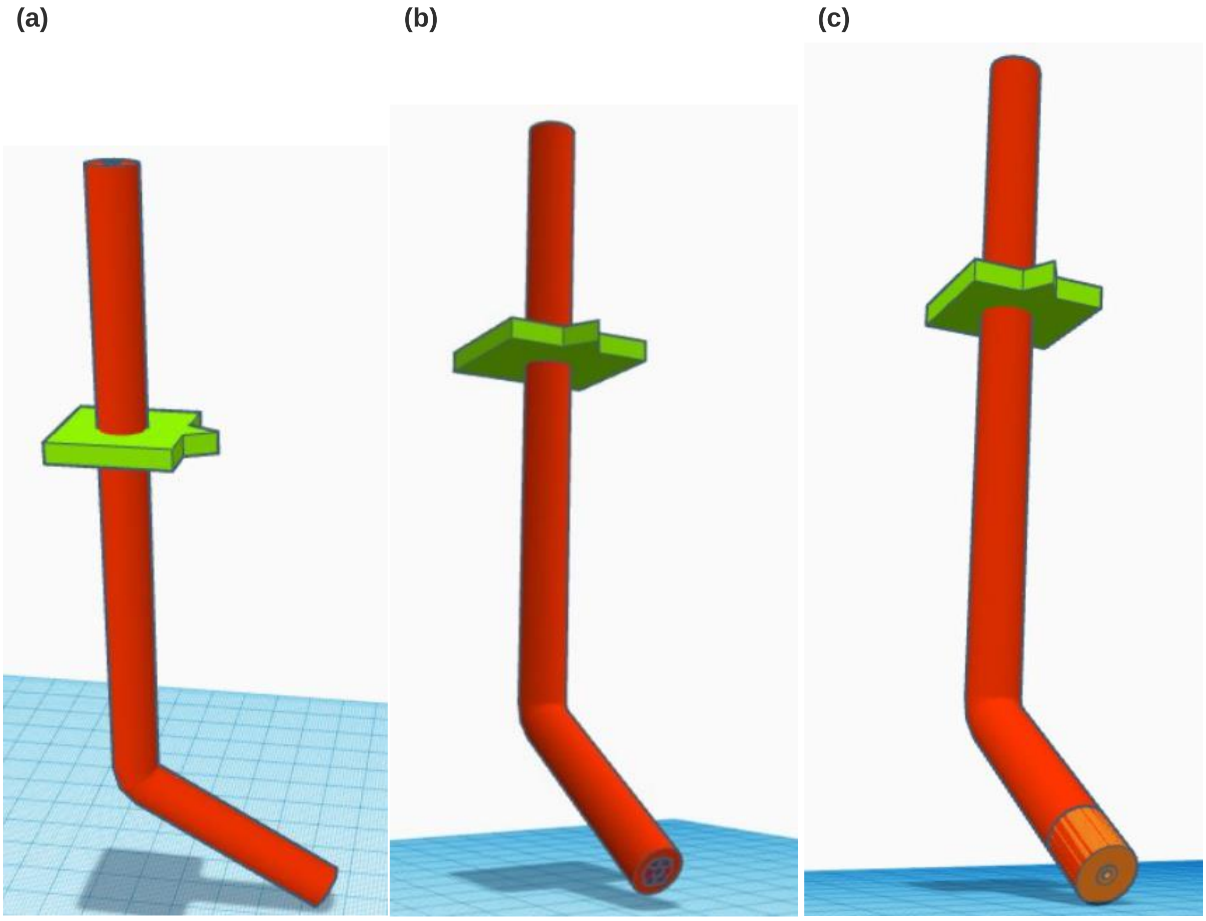

Figure E.14 – 60° laboratory-scale HAIL reactor sparger designs (a) 60d, (b) 60dm, and (c) 60s

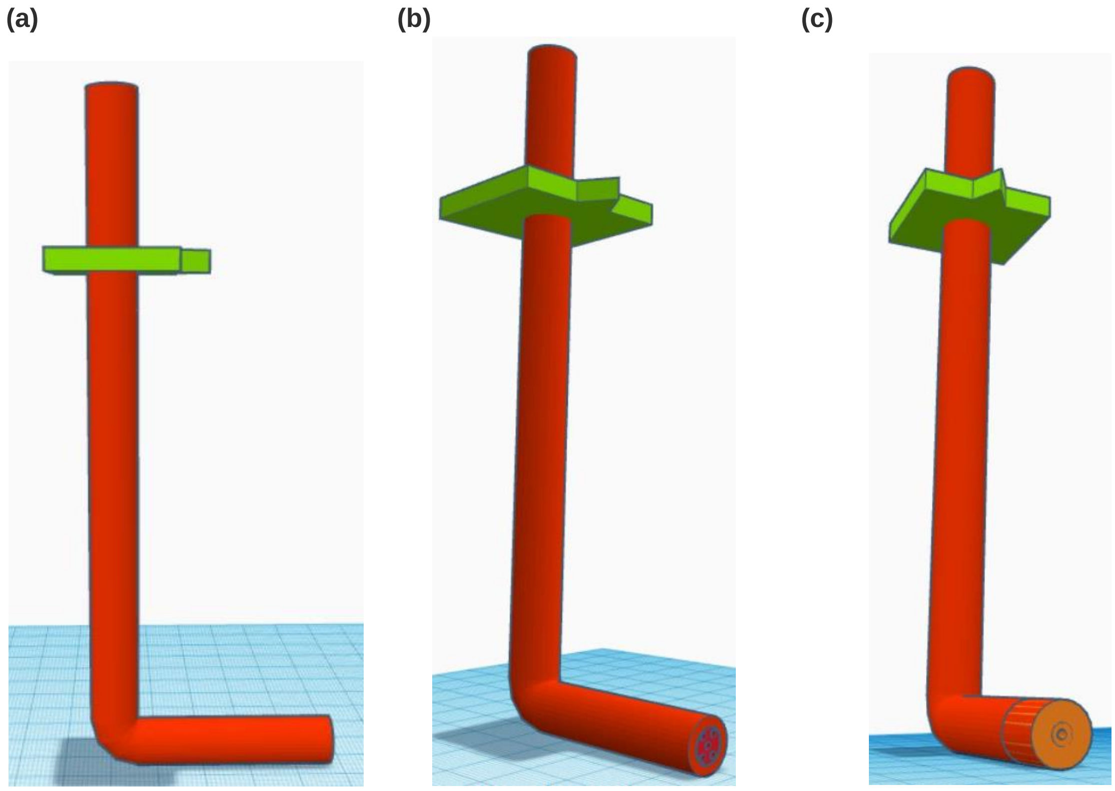

Figure E.15 – 90° laboratory-scale HAIL reactor sparger designs (a) 90d, (b) 90dm, and (c) 90s

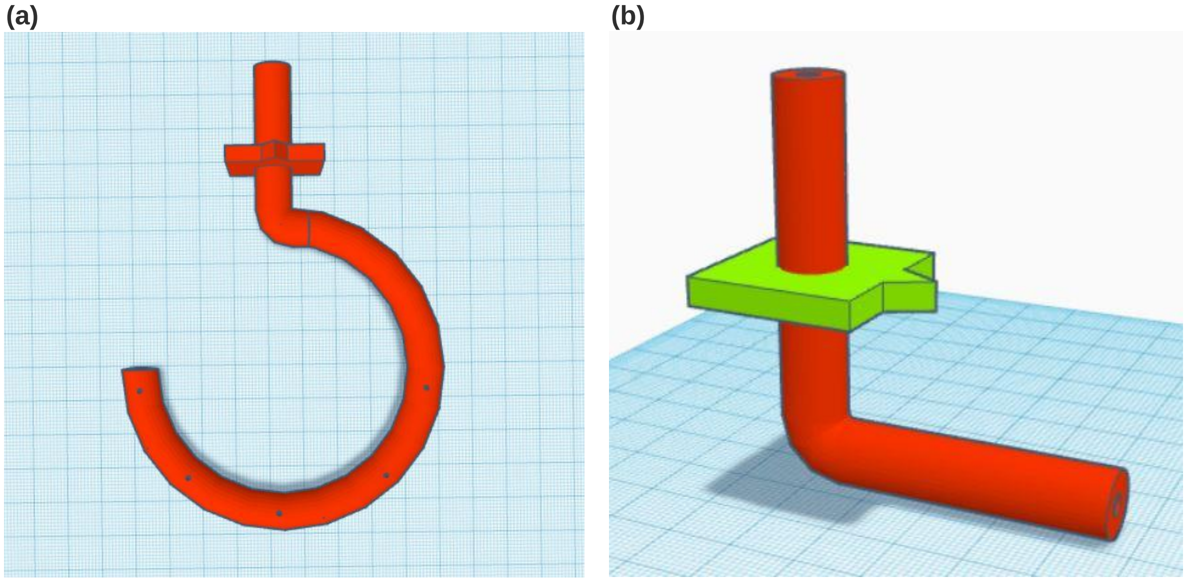

Figure E.16 – Non-standard laboratory-scale HAIL reactor sparger designs (a) c1 and (b) surface aerator

Appendix F – HAIL Reactor Experiment List

Table F.1 – HAIL reactor circulation/mixing time experiment list

Sparger Name	Fill Volume [L]	Liquid Height [mm]	Aeration Rate [LPM]
60d	12	40.7	6
			12
			18
			24
	20	60.9	10
			20
			30
	26	77.2	13
			26
			39
	27	80.3	14
			27
			34
			40
60dm1	20	60.9	15
			20
			30
60s1	20	60.9	15
			20
90d	16	50.8	12
			16
			24
	20	60.9	10
			15
			20
			30
	27	80.3	27
90dm1	20	60.9	15
			20
			30
90s1	20	60.9	15
			20
			25
circle1	20	60.9	15
			20
			30
			40
	23	68.7	30
	26	77.2	30